

ABSTRACT

SWEET III, WILLIAM JOHN. Application of Conductive Thin Films and Selectively Patterned Metal Oxide Coatings on Fibers by Atomic Layer Deposition. (Under the direction of Professor Gregory N. Parsons).

Next generation device technologies such as flexible electronics will require new materials to be developed that meet a broad set of device performances metrics including strength, flexibility, and electrical conductivity. Atomic Layer Deposition (ALD) is a thin film deposition technique used to manufacture the current state-of-the-art integrated circuits because it is capable of producing highly conformal, pin-hole free films on ultra high aspect ratio features, while providing sub-nanometer level thickness control. Surface modification using coating methods like ALD, provides a route to imparting desired material properties onto a variety of substrates. By applying ALD coatings to flexible polymer substrates, new hybrid materials can be created, the properties of which are a function of the substrate material, the coating material, and the deposition conditions under which the coating was applied.

We utilize the ALD coating method to deposit a variety of thin films including metal, semiconducting metal oxides, and insulating metal oxide films, on polymer and crystalline substrates. Materials development is done with an eye towards electronic devices, and therefore films are characterized for electrical conductivity; the impact of deposition conditions on conductivity is thoroughly investigated as well. A new method is developed to measure and characterize conductivity for electrically conductive fiber substrates, and conductive ALD coated fibers are compared to conductive fibers produced by other methods.

The conductivity of metal and semiconducting coatings applied to nonwoven fiber mats is systematically investigated and characterized using the aforementioned technique

developed for measuring the conductivity of conductive fibers. The impact of mechanical deformation on these coatings is also characterized by measuring conductivity before and after stretching and bending tests. The mechanical properties of the ALD coated fibers are studied by tensile testing the coated nonwovens, and an increase in tensile strength after ALD coating is demonstrated.

A method to pattern ALD coatings onto flexible fibrous substrates by localized physical compression is developed, which can be used to pattern flexible metal or semiconducting electrodes onto nonwoven substrates by ALD. Patterning of various nonwoven substrates by ALD is demonstrated, and the factors controlling pattern resolution are examined. A full quantitative transport model is developed that describes the impact of fiber structure and mechanical compression on patterning resolution.

Furthermore, in situ conductance measurements are taken during ZnO ALD onto nonwoven substrates, and the process is used to study ZnO film growth on quartz and polymer fibers. Differences in ZnO film growth on Al₂O₃ ALD and TiO₂ ALD coatings is shown using in situ conductance measurements. The change in conductance behavior as a function of ZnO cycle number is investigated for quartz, nylon-6 and polypropylene substrates. The transition through ALD growth modes is observed for ZnO deposition on polypropylene where the transition from film nucleation/coalesces, sub-surface growth and eventually self-limited ALD growth is observed, and the in situ conductance measurements correspond well to literature results.

© Copyright 2014 William John Sweet III

All Rights Reserved

Application of Conductive Thin Films and Selectively Patterned Metal Oxide Coatings on
Fibers by Atomic Layer Deposition

by
William John Sweet III

A dissertation or thesis submitted to the Graduate Faculty of
North Carolina State University
in partial fulfillment of the
requirements for the degree of
Doctor of Philosophy

Chemical Engineering

Raleigh, North Carolina

2014

APPROVED BY:

Dr. Gregory Parsons
Committee Chair

Dr. Michael Dickey

Dr. Jesse Jur

Dr. Saad Khan

DEDICATION

To my loving family and fiancé, whose support has made all my work possible.

BIOGRAPHY

William John Sweet III was born in Baltimore Maryland and is the oldest of three children, a sister Maureen and brother, Michael. He attended the Friends School of Baltimore, where he spent his formative years from nursery school through high school. While a junior in high school, he began dating Brigit Bowers, to whom, some 10 years later he would propose. After graduation, he attended Vanderbilt University in Nashville, TN, where he was enrolled in the chemical engineering program. While at Vanderbilt he began his research career under the guidance of Professor Bridget Rogers, studying low pressure chemical vapor deposition of metal oxides. While attending the American Vacuum Society International Symposium his senior year, he was introduced to the work of Professor Gregory Parsons, who he would later study under. Both he and Brigit would graduate from Vanderbilt in 2009. After graduation he attended North Carolina State University, where he would pursue a Ph.D. in chemical and biomolecular engineering under the guidance of Professor Gregory Parsons. While at NC State, he pursued his research interest in vacuum science, as well as his interests in entrepreneurship, business, and finance through the coursework in the Poole College of Management. He spent part of his final summer prior to graduation as an intern at Northrop Grumman in the Advanced Concepts and Technology Division, where he gained experience in semiconductor manufacturing processes. Upon graduation, he will return to Northrop Grumman. He and Brigit Bowers are scheduled to be married on September 13th, 2014, after 11 blissful years together.

ACKNOWLEDGMENTS

First and foremost, I would like to thank Dr. Gregory Parsons for his help and mentorship over the years. I would also like to thank all past and present Parsons Group members that have helped me during my time at NC State, including Dr. Bo Gong, Dr. Christina McClure, Berç Kalanyan, Sarah Atanasov, Moataz Mousa, Junjie Zhao, Erinn Dandley, Paul Lemaire, and Zach Mundy. I would also like to thank Dr. Richard Padbury for our incredibly interesting and informative discussions over the years. I would especially like to thank Dr. Christopher Oldham and Dr. Jesse Jur, for their mentorship and guidance during our shared time in the Parsons Research Group during my formative years of graduate school research.

I would also like to thank Casey Galvin, Dr. Christopher Oldham, Dr. Qing Peng, and Dr. Phillip Williams for their advice, guidance, input, and collaboration on all things related to finance and the stock market. I look forward to sharing ideas for years to come.

Last but not least, I would like to thank all of my friends for making Raleigh a great place to be for the last five years, I'll always remember those nights out on the town!

TABLE OF CONTENTS

LIST OF TABLES	viii
LIST OF FIGURES	ix
CHAPTER 1. Introduction	1
References.....	6
CHAPTER 2. Experimental Tools.....	13
2.1 Atomic Layer Deposition	13
2.2 Ellipsometry.....	14
2.3 Four point probe	14
2.4 Four Electrode Probe	14
2.5 Optical Imaging	17
2.6 Scanning Electron Microscope	17
2.7 Transmission Electron Microscope	18
2.8 Ultra Violet – Visible Light Spectrophotometer	19
2.9 X-Ray Diffraction.....	19
2.10 Tensile Testing	19
2.11 References	21
CHAPTER 3. Bi-layer Al₂O₃/ZnO Atomic Layer Deposition for Controllable Conductive Coatings on Polypropylene Nonwoven Fiber Mats	22
3.1 Abstract.....	23
3.2 Introduction	24
3.3 Experimental.....	26
3.4 Results and Discussion	31
3.5 Conclusions	40
3.6 Acknowledgments	41
3.7 References	53
CHAPTER 4. Atomic Layer Deposition of Metal Oxide Patterns on Nonwoven Fiber Mats using Localized Physical Compression.....	55
4.1 Abstract.....	56
4.2 Introduction	57
4.3 Experimental.....	59
4.4 Results	64
4.5 Modeling Reaction-Diffusion for ALD in a Nonwoven	70
4.6 Conclusions	76
4.7 Acknowledgments	77
4.8 Appendix – Supplemental Items Not Published.....	92
4.9 References	102

CHAPTER 5. The Conductivity and Touch-Sensor Application for ALD ZnO and Al:ZnO on Nylon Nonwoven Fiber Mats.....	106
5.1 Abstract.....	107
5.2 Introduction	108
5.3 Experimental.....	109
5.4 Results and Discussion	113
5.5 Conclusion	120
5.6 Acknowledgements	122
5.7 References	138
CHAPTER 6. In Situ Nucleation Analysis during Zinc Oxide Atomic Layer Deposition on Polymers using Real-time Conductance Measurements.....	142
6.1 Introduction	142
6.2 Experimental.....	143
6.3 Results and Discussion	153
6.4 Conclusions	163
6.5 Acknowledgements	164
6.6 Appendix - Supplemental Items Not Published	175
6.7 References	184
CHAPTER 7. Atomic Layer Deposition on of Zinc Oxide on Nylon-6 Nanofibers and Microfibers: A Comparison of Conductivity and Tensile Properties	186
7.1 Introduction	186
7.2 Experimental.....	187
7.3 Results and Discussion	188
7.4 Conclusions	194
7.5 References	202
APPENDIX	204
APPENDIX A1. Co-Authored Work	205
Appendix A1.1 Highly Conductive and Flexible Nylon-6 Nonwoven Fiber Mats Formed using Tungsten Atomic Layer Deposition	205
A1.1.1 Abstract	206
A1.1.2 Introduction.....	207
A1.1.3 Experimental.....	208
A1.1.4 Results and Discussion	213
A1.1.5 Summary and Conclusions	220
A1.1.6 Acknowledgment	221
A1.1.7 Appendix - Supplemental Items Not Published.....	231
A1.1.8 References.....	235

Appendix A1.2 Atomic Layer Deposition of Conductive Coatings on Cotton, Paper, and Synthetic Fibers: Conductivity Analysis and Functional Chemical Sensing using

“All-Fiber” Capacitors 239

- A1.2.1 Abstract 240
- A1.2.2 Introduction 241
- A1.2.3 Results and Discussion 244
- A1.2.4 Conclusions 259
- A1.2.5 Experimental 260
- A1.2.6 Acknowledgments 263

LIST OF TABLES

Table 4.1. The effective diffusion coefficients and calculated tortuosity values for the model curves plotted in Figure 4.13.	75
---	----

LIST OF FIGURES

- Figure 3.1.** Percent mass gain for Al₂O₃ ALD deposition on polypropylene nonwoven fiber mats (at 50°C) as a function of Al₂O₃ cycle number. Mass gain was measurable at 50 Al₂O₃ cycles, and increased as more cycles were applied. This data provides a reference mass to determine the mass gain after ZnO ALD onto Al₂O₃-coated fibers. A linear trend is fitted to the data with an R-squared value of 0.99; it is noted that non-linear growth maybe occurring at low cycle numbers, although this was not investigated further due to sensitivity limitations of the measurement technique. 42
- Figure 3.2.** (a) The percent mass gain of 500 ZnO ALD cycles (at 155°C) is plotted as a function of deposition temperature for: 1) deposition on virgin polypropylene; 2) deposition on polypropylene first coated with 200 Al₂O₃ ALD cycles at 50°C. The samples are labeled ZnO/PP and ZnO/AlO/PP respectively; (b) The corresponding film thickness for ZnO growth on silicon corresponding to the deposition on polypropylene fibers from Fig. 3.2(a), and are signified by labels ZnO/Si or ZnO/AlO/Si. 43
- Figure 3.3.** ZnO mass gain (%) plotted as a function of ZnO cycle number for ZnO ALD on 1) virgin polypropylene; 2) polypropylene coated with 50, 100, and 200 Al₂O₃ ALD cycles (at 50°C) prior to ZnO deposition. By first coating the polypropylene with Al₂O₃, the ZnO nucleates more quickly on the Al₂O₃ coating than on virgin polypropylene, reducing the cycles before linear mass gain is achieved. 44
- Figure 3.4.** TEM images of polypropylene after 300 cycles of ZnO ALD at 110°C for (a) untreated polypropylene and (b) polypropylene pre-treated with 150 cycles of Al₂O₃ ALD at 50°C. The untreated polypropylene fiber shows small granular formation towards the center, growing larger towards the edge of the fiber. For the pre-treated fiber (b), two distinct layers can be seen, the Al₂O₃ pretreatment and the ZnO coating..... 45
- Figure 3.5.** (a) Percent mass gain of ZnO ALD at 155°C is plotted as a function of DEZ dose time for 1) 200 ZnO cycles on untreated polypropylene (ZnO/PP); and 2) 200 ZnO cycles on polypropylene pre-coated with 200 Al₂O₃ cycles at 50°C (ZnO/AlO/PP). (b) Film growth on simultaneously deposited silicon substrates shows ZnO deposition on bare Si, and Al₂O₃ coated Si, is achieved quickly. Similar to the silicon substrates, Al₂O₃ coated polypropylene shows saturation is achieved with short precursor doses..... 46
- Figure 3.6.** Conductivity of polypropylene after a 300 cycle ZnO ALD coating deposited at various temperatures on 1) virgin polypropylene, and 2) polypropylene with a 200 cycle Al₂O₃ ALD barrier layer deposited at 50°C, and corresponding silicon samples, respectively. The Al₂O₃ barrier results in ZnO with higher conductivity; presumably because higher quality ZnO is deposited on the Al₂O₃ barrier layer. Fig. 3.4 shows higher density ZnO is deposited on top of the Al₂O₃ barrier coated polypropylene. Higher temperature ZnO ALD leads to higher conductivity, most likely due to a shift in preferred crystalline orientation of the deposited ZnO. 47

Figure 3.7. (a) Conductivity of ZnO deposited at 155°C on 1) thermal oxide silicon; and 2) virgin polypropylene, as a function of DEZ dose time. The conductivity of ZnO on silicon plateaus with a 1 second dose. Conductivity of ZnO on virgin PP increases with dose times up to 3 seconds. (b) Conductivity of ZnO deposited at 155°C on 1) Al₂O₃ coated thermal oxide silicon; and 2) ZnO on PP first treated with 200 Al₂O₃ cycles at 50°C; both samples show saturation with a 1 second dose. This shows that Al₂O₃ is eliminating some of the non-ideality of ZnO ALD on PP that is shown in (a)..... 48

Figure 3.8. (a) Conductivity as a function of ZnO cycle number for 1) ZnO on virgin polypropylene at 155°C; and 2) ZnO (at 155°C) on polypropylene first coated with a 200 cycle Al₂O₃ barrier. (b) Conductivity as a function of zinc oxide ALD cycles for 1) zinc oxide deposited on a 150 nm thermal oxide silicon, and 2) zinc oxide deposited on 200 Al₂O₃ ALD cycles on top of a 150 nm thermal oxide silicon wafer. Conductivity of ZnO deposited on Al₂O₃ is noticeably higher than ZnO without the Al₂O₃ layer. A peak exists at 200 ZnO cycles (~360 Å of ZnO), after which conductivity decreases towards a bulk value of ~150 S/cm, in line with the value for ZnO deposited directly on thermal oxide. 49

Figure 3.9. Conductivity is plotted as a function of the number of ZnO ALD cycles, for ZnO/AlO/PP samples deposited at two different temperatures. As demonstrated in Fig. 3.6, conductivity is higher for ZnO samples deposited at higher temperatures. This shows that conductivity exhibits similar behavior as a function of ZnO thickness, for two different deposition temperatures. Both samples show low conductivity for < 200 ZnO cycles, and then exhibit “plateau” like behavior for thicker ZnO depositions. 50

Figure 3.10. (a) A picture and (b) a schematic of a ZnO coated polypropylene sample as it is being bent around a glass cylinder with 1.13cm radius. As the cylinder is rolled over the sample, the sample becomes sandwiched between the cylinder wall and the paper support adhered to the cylinder. This causes the sample to roll up the side as the cylinder is rotated forward; the cylinder is then rolled in reverse, the sample is removed and the conductivity is measured. 51

Figure 3.11. The conductivity of ZnO/Al₂O₃ coated polypropylene samples (from Fig. 3.8(a)) as function of the inverse of the diameter of bending. The samples were tested prior to bending (“unbent”), as well as after bending around cylinders of decreasing diameters. Trend lines were fit for samples with 100, 200, 300, and 500 ZnO cycles (deposited at 155°C on 200 cycle Al₂O₃ coated polypropylene). Data is shown for other samples, but was not fit, in order to reduce clutter in the figure. Because the samples sat in ambient for up to 16 months before testing, the unbent conductivity is lower than initially measured from Fig. 3.8(a). 52

Figure 4.1. Scanning electron microscope images of (a) polypropylene nonwoven, (b) nylon-6 nonwoven, and (c) nylon woven mats used in this study; all SEM scale bars are 20 microns. Insets are low magnification optical microscopy images of the respective substrates to show context for the SEM images, the scale bars for the inset images are 300 microns. Optical images are of the fibers as received; a 5 nm Au/Pd coating was sputtered onto the substrates prior to the SEM images. 78

Figure 4.2. ZnO ALD on nonwoven polypropylene deposited at 155°C, with different numbers of ALD cycles. The color change reflects the thickness of the ALD coating..... 79

Figure 4.3. Schematic cross-section showing ALD coating on a nonwoven mat (a,b) without a mask; and (c,d) with a compression mask in place. The mask limits lateral diffusion of the precursors within the nonwoven, producing a pattern that is restricted to exposed portions of the mask. This example shows a solid backing plate. The solid plate allows the extent of growth in the vertical direction to also be controlled by adjusting the precursor dose time per cycle. 80

Figure 4.4. (a) Aluminum solid back plate and pattern mask with mask with slits 10 mm wide and lengths of 1.6 mm, 3.2 mm, 6.4 mm, and 12.7 mm, spaced at least 5 mm apart and 5 mm from the edge. (b) Both sides of a nylon-6 nonwoven patterned with 400 cycles of ALD ZnO at 155°C show a pattern, demonstrating that the precursors vertically permeate through the nonwoven to also produce a pattern on the side that was covered by the solid metal back plate. The patterned color of the oxide is visible, with some coating also on the edge of the samples. 81

Figure 4.5. (a) An SEM image and EDS scans of a ZnO patterned feature on a polypropylene nonwoven. The numbers on the image correspond to locations where the EDS scans were taken. (I) The patterned region is not covered by the mask; (II) the compressed region near the opening where DEZ diffuses during dosing; (III) compressed region beyond where DEZ diffuses. The zinc signal is strongest relative to carbon in the patterned feature, location (I). Carbon signal is strongest in the region that is not patterned, and no zinc signal is detected. (b) Optical absorption data vs. photon energy for ZnO (400 cycles at 155°C) on quartz disks, for as-deposited and after annealing at 800°C in air for 3 hours. Inset shows the same films deposited on quartz fibers. The visible color on the as-deposited fibers is ascribed to ZnO with oxygen vacancy or other related defects. 82

Figure 4.6. Optical microscopy in reflection (top images) and transmission mode (bottom) of patterned ZnO ALD on polypropylene and nylon-6 nonwoven fiber mats. The pattern edge is readily visible in reflection, and the average extent of coating under the pattern is observed transmission. 83

Figure 4.7. Machine direction cut nylon-6 was patterned with 400 cycles of ZnO ALD using various DEZ dose times. Short dose times produce a feature that is well defined with minimal diffusion distance beyond the boundary of the compressive mask. Longer dose times result in longer diffusion lengths. This process was repeated for cross direction cut nylon-6 and polypropylene substrates; the results of which are compared and discussed in later sections of this work..... 84

Figure 4.8. Patterned layers made by compression of porous substrates. 4.8(a) shows a stack of 10 nonwoven nylon-6 mats stacked (a,i) before and (a,ii) after compression and patterning. 4.8(b) shows (b,i) a cross section schematic of precursor diffusing through a sample, where L and V indicate lateral and vertical diffusion, respectively; and (b,ii-iv) stacks patterned with increasing DEZ dose times. For longer exposure times per ALD cycle, the

coating penetrates completely in the vertical direction while maintaining the lateral pattern through the stack. 4.8(c) shows the top three and bottom three layers of a 10 nylon-6 mat tall stack patterned with a 2 second dose time, the numbers signify the position within the stack. The top-most sample (1) is coated uniformly, but the bottom-sample (10) shows minimal coating. ALD can achieve patterned growth with controlling depth on a fiber substrate. 85

Figure 4.9. ZnO ALD on (a) nylon-6 nonwoven fiber mats cut in the machine direction, and (b) polypropylene nonwoven mats. For deposition on nylon, the extent of diffusion under the masked area is the same for 400 vs 800 ALD cycles, whereas for the polypropylene substrate the 800 cycle deposition is more spread out than the 400 cycle sample. For more deposition cycles, precursor diffusion into the polypropylene polymer may extend growth further under the mask region. The images were digitally enhanced to increase contrast by 50%. 86

Figure 4.10. Nonwoven nylon-6 and polypropylene were patterned at 125°C and 155°C to determine the impact of deposition temperature on the pattern. (a) Nylon-6 shows a darker color pattern is created when deposited at higher temperature, but the diffusion length, as indicated by the arrows, remains the same. (b) Polypropylene also shows a darker feature when coated at higher temperature, however, the sample also shows significantly lower extent of diffusion of the coating at higher temperatures. Deposition on polypropylene at 155°C while under compression may cause the polypropylene to deform, fusing fibers and increasing tortuosity of diffusing precursor molecules. The contrast of the images was increased 50% to make the coated region more apparent. 87

Figure 4.11. ZnO patterns on nonwoven nylon-6 after coating with 400 cycles at 155°C. The extent of deposition under the exposed mask depends on the amount of compression used. In this case, ‘full compression’ indicates masking blocks are fully tightened with self tightening screws using a hexagonal wrench, and ‘partial compression’ are tightened to finger tight; for consistency, digital calipers were used to measured height of the combined mask and nonwoven samples to verify tightening was consistent throughout a data set. 88

Figure 4.12. Optical images of (a) nonwoven nylon; and (b) woven nylon fiber substrates after pattern-coating with ZnO ALD. Optical microscopy images from each sample show the physical structure of each material. The random orientation of the fibers in the nonwoven compared to the oriented fibers in the woven yarns restricts lateral reactant transport to achieve better feature definition. The images were digitally enhanced to increase contrast by 40%. 89

Figure 4.13. Data from experimental measurements of visible diffusion length for different substrates deposited using various DEZ dose times are shown; polypropylene (blue triangles) and nylon cut in the machine direction (black squares) and cross direction (red circles). Samples were patterned while under both full compression (solid symbols) and partial compression (hollow symbols). Distance measurements were taken using an optical microscope, four micrographs were taken per sample and the maximum and minimum diffusion distances were measured for each. The average distance is plotted, and the error bars shown are for the highest standard deviation sample for each of the data sets. The curves

shown are derived from the solutions to equation 4.4 and 4.5, which are solved using $\beta_0=0.01$, $\theta_c=0.5$, each substrates physical parameters (\bar{s} , T), but allowing the effective diffusion coefficient (D_{eff}) to vary to fit the data. The tortuosity can then be found for each substrate using equation 4.6. 90

Appendix Figure A.4.1. (a) Growth per cycle for ZnO ALD on silicon, as a function of DEZ dose time, for 400 ZnO cycles deposited at 155°C where a cycle is DEZ/purge/H₂O/purge = X/40s/2s/40s. The observed pressure change during a DEZ dose is ~0.07 Torr, and during an H₂O dose is ~0.28 torr. (b) Coverage profile curves as a function of normalized distance (z/L) for various dose times, using an initial reaction probability of $\beta_0=0.01$; lower initial reaction probabilities produce less abrupt changes in the coverage profile. The coverage curves shown here are related to the experimentally data plot of coating distance vs. dose time, by θ_c the critical coverage value, which is the amount of coverage required to produce a visible coating, which we estimate to be $0.25 \leq \theta_c \leq 0.5$ 97

Appendix Figure A.4.2. ZnO patterns in nonwoven nylon and polypropylene after coating with 400 cycles at 155°C on nylon, and 125°C on polypropylene. For both substrate materials, the extent of deposition under the exposed mask depends on the amount of compression used. In this case, ‘full compression’ indicates masking blocks are fully tightened using self tightening screws using an hexagonal wrench, and ‘partial compression’ are tightened to finger tight; for consistency, digital calipers were used to measured height of the combined mask and nonwoven samples to verify tightening was consistent throughout a data set. 98

Appendix Figure A.4.3. The NCSU logo patterned on a polypropylene nonwoven mat using ZnO ALD. The insets show SEM images, where the ZnO coating appears lightly colored and the uncoated polypropylene appears dark. The sample was coated with 400 cycles of ZnO at 155°C using dose times of DEZ/purge/H₂O/purge = 1s/40s/1s/40s. This demonstrates the ability to pattern complex designs using ALD and compressive masking. Shorter dose times, smaller diameter fibers and higher compression could be used to increase the resolution of patterned features. 99

Appendix Figure A.4.4. Patterning is easily performed using Al₂O₃ ALD, and can be achieved using anything that can compress the substrate. (a) Perforated aluminum plates are used to compress a polypropylene mat, and is held together using nuts and bolts. 200 cycles of aluminum oxide ALD are deposited at 60°C on the substrate. No color change is observed but the aluminum coating changes the surface energy of the polypropylene to produce a transition from hydrophobic to hydrophilic. (b) The Al₂O₃ patterned substrate is floated on water; the sample selectively wets where the Al₂O₃ coating was deposited, but remains hydrophobic where the substrate was covered by the mask. Uniformity of the compressive force is the key to obtaining well defined pattern replication. The force distribution of the screws is not uniform, resulting in variable pattern quality; a large weight could be used instead of screws to apply force, as long as it permitted sufficient transport of the precursors during ALD. (c) Large scale patterning can be achieved with the technique, and is only limited to the ability to apply sufficient compressive force, the uniformity of which

determines pattern quality; (d) the pattern created from ZnO ALD onto polypropylene the location of which is indicated in Figure A.4.4(c). 100

Figure 5.1. The nylon-6 nonwoven substrate used in this work, as shown in (a) picture, (b) optical microscopy image, (c) scanning electron micrograph. The orientation distribution of fibers that comprise the nonwoven is shown in (d), which plots the percentage of fibers aligned relative to the cross direction; in this histogram the ‘machine direction’ orientation is in the center. 123

Figure 5.2. (a) Zinc oxide film thickness is plotted as a function of cycle number for deposition on silicon and spuncast nylon-6 films. ZnO films appear to grow well on native silicon, exhibiting ~1.7 Angstroms/cycle growth, whereas deposition on nylon-6 film appears to initially inhibit ZnO deposition. (b) The mass gain measured after ZnO deposition on nylon-6 fibers is plotted as a function of cycle number. 124

Figure 5.3. Mass gain for 300 cycles of ZnO deposited at 150°C, as a function of DEZ/H₂O dose time for deposition on Allasso Winged Fiber™ nylon-6 nonwoven (black squares); ZnO film thickness on silicon (grey circles) is plotted for reference. Saturation is easily achieved on silicon, where a 0.5 second dose is sufficient to achieve ~90% of the film thickness of a 6 second dose, whereas the PA6 fibers require a 2 second dose to meet this requirement. The nylon-6 is a higher surface area material and therefore requires more precursor to reach saturation. 125

Figure 5.4. The mass gain of ZnO coated nylon nonwoven samples is plotted as a function of deposition temperature. ALD on polymers is a function of both the coating chemistry (such as properties of the ALD window) as well as properties of the polymer. Thermal expansion of the polymer as a function of temperature may influence the deposited coating by effecting diffusion. The limiting characteristic such as reactivity or diffusivity may shift over the deposition window. At higher temperatures, reactivity of the coating may decrease diffusion into the polymer, which may explain the observed lower mass gain at higher deposition temperatures. 126

Figure 5.5. TEM images of 300 cycles of ZnO ALD deposited on nylon-6 fibers at (a,c) 100°C and (b,d) 190°C. The lobe structure of the Winged Fibers™ can be seen in the low magnification images. The high magnification images show abrupt ZnO/nylon-6 interfaces for both 100°C and 190°C deposition with no significant diffusion region or subsurface nucleation. 127

Figure 5.6. XRD scans of 300 ZnO ALD cycles deposited at various temperatures on (a) thermal oxide silicon, and (b) nylon-6 fibers. In the nylon-6 fiber XRD, higher surface area material leads to more clearly defined peaks, but most of the same features are visible in the silicon XRD as well. A scan of the silicon substrate that was used is shown for reference, as is an uncoated piece of nylon-6 fibers. The XRD scans are normalized to the highest peak value. Peak identification was determined by the use of ICDD (PDF 2009) 00-036-1451 and 00-054-2323 material data files. 128

Figure 5.7. Conductivity of 300 cycle ZnO ALD coated substrates as a function of DEZ dose time on thermal oxide silicon (black squares), spuncast nylon-6 film (hollow squares), nonwoven fibers oriented in the machine direction (hollow circle) and the cross direction (hollow triangles). Machine direction fibers preferentially aligned perpendicular to the measurement electrodes, whereas cross direction fibers are preferentially oriented parallel to the measurement electrodes. As a result, cross direction fibers have higher inter-fiber transfer of current, which introduces additional fiber-fiber resistances, resulting in lower effective conductivity for the same ZnO coating..... 129

Figure 5.8. Conductivity of various planar and fibrous substrates, plotted as a function of ALD cycle number, for (a) ZnO ALD and (b) AZO ALD coatings. ZnO conductivity is dependent on film thickness for thin films (< 400 ALD cycles); only moderately so for films on silicon for spuncast PA6 films, but the conductivity of coated fibers shows a strong dependence. The conductivity of AZO films appear dependent on film thickness for all substrates, over the range of thicknesses investigated. Interestingly, thinner AZO coatings on fibers do not exhibit a decrease in conductivity to the same extent as the ZnO coated fibers in (a). Both ZnO and AZO films were deposited at 150°C. The AZO film was deposited using a 19:1 ZnO:Al₂O₃ doping ratio..... 130

Figure 5.9. Conductivity of (a) ZnO and (b) AZO coatings, deposited on MD nylon-6 and thermal oxide silicon as a function of deposition temperature. The samples were coated with 300 cycles of ZnO or AZO, using recipes of two second precursor doses (ZnO: DEZ,H₂O and AZO: DEZ, H₂O, TMA) and 40 second N₂ purges inbetween. The laminate structure for AZO was 19 ZnO – 1 Al₂O₃..... 131

Figure 5.10. (left) The conductivity of ZnO and AZO coated cross direction nylon-6 fibers was measured intermittently, and is plotted on a log scale as a function of time since being exposed to ambient lab conditions upon removal from the ALD reactor at t=0 hours. (middle) The conductivity data for the ZnO and AZO samples from (a) was normalized to the initial measurement after deposition (taken 0.1 hours after removal); (right) Conductivity of the corresponding ZnO and AZO films deposited on thermal oxide silicon..... 132

Figure 5.11. Conductivity after mechanical strain is applied for MD PA6 coated with (a) 400 cycles of AZO deposited at 115°C, 150°C, and 200°C; (b) 100, 200, 400 cycles of AZO deposited at 200°C. The as-deposited conductivity (at 0% strain) of the AZO coated fibers in (a) increases with deposition temperature, but their decrease in conductivity upon straining appears to follow the same trend. Similarly, increasing the AZO coating thickness increases the as-deposited conductivity of the fibers as shown in (b), but the trend upon straining appears to remain the same..... 133

Figure 5.12. Nylon-6 nonwoven substrates with preferential fiber orientation in the machine direction and the cross direction were coated with AZO and subject to tensile testing. A fixed mechanical strain was applied using a universal tensile tester, and the conductivity of the samples was measured afterwards. Machine direction oriented fibers align parallel to the deformation force, whereas cross direction fibers align perpendicular to the deformation

force. The coating applied was 400 cycles of AZO ALD at 150°C using a 19:1 ZnO:Al₂O₃ doping ratio. 134

Figure 5.13. Conductivity for AZO coated machine and cross direction nylon is plotted as a function of the inverse radius of curvature, to show how the conductivity of the two substrates orientations changes from initially as-deposited (unbent, 0 cm⁻¹) to being bent around smaller cylinders, the smallest of which has a radius of curvature of R≈0.29 cm, which corresponds to the furthest right data point on the graph (3.4 cm⁻¹). 135

Figure 5.14. SEM images of the AZO coated MD PA6 fibers from Figure 5.12, after being strained. The samples were not sputter coated prior to imaging. As a result, non-conductive areas appear dark in the image, revealing the location of cracks in the AZO. The formation of cracks upon straining begin to form, then propagate radially around the fiber, at which point the polymer underneath the fracture can continue to stretch until other cracks are created as a result of localized stress in previously uncracked regions. For all strained samples imaged, there appeared fibers with significantly fewer cracks than a neighboring fiber, the difference is likely due to local variability in tensile forces imparted on the individual fibers by the nonwoven fiber network. 136

Figure 5.15. (a) An all fiber pressure sensor was fabricated using AZO coated nylon-6 nonwoven mats as electrodes. An electrically insulating polypropylene mat is placed between the electrodes, and the three are stitched together using insulating thread. An insulating nonwoven polypropylene layer with hole cut in the center (inset), allows the electrodes to be sewn together without electrical contact, but also permits contact when pressure is applied; (b) current response, $R = I_{on}/I_{off}$ under applied force as described in text; (c) average R values (from 4 data sets) versus applied force (example data set in inset). R increases exponentially with applied force up to ~ 50 g over ~1 cm². 137

Figure 6.1. (a) The overall 2-wire probe device with the quick-flange connection and electrical feed-through gasket can be seen at right while a sample being held by alligator clips can be seen in image left; (b) an image of a nylon-6 nonwoven substrate in the probe after 200 cycles of ZnO ALD; (c) front and (d) back images of nylon-6 substrate with woven gold electrodes used for a 4-wire measurement. 165

Figure 6.2. Representative plots of in situ conductance data taken showing the various aspects of the recorded data; this data was gathered during 200 ZnO ALD cycles were deposited on bare nonwoven polypropylene at 150°C. (a) A linear plot of the data shows the significance in behavior of, (i) the nucleation/coalescence period, (ii) the initial conductance uptake rate and then the transition to lower conductance uptake per cycle at high cycles, (iii) the steady state rate; (b) A logarithmic plot of conductance for the period immediately before and after the onset of measurable conductance. In the span of < 10 cycles the conductance of the coated sample increases 6 orders of magnitude; on this scale the nuances in rate of change shown in (a) are lost; (c) an example of conductance change within two ALD cycles. The DEZ dose causes conductance to decrease which continues until the introduction of the water

dose which causes an abrupt increase in conductance followed by a slow drop throughout the water purge step. 166

Figure 6.3. Conductance is plotted for three ZnO ALD cycles during deposition on a nylon-6 nonwoven, as measured (a) using the 2-wire probe under 0.5 volt bias; (b) using the 4-wire probe with 1 mA bias; and (c) using the 4-wire with 20 mA bias. The same trend can be seen in data gathered from both probes, suggesting that band bending at the ZnO surface, rather than changes in contact resistance are the cause of the observed oscillations during ZnO ALD. It can also be seen in 6.3(b) and 6.3(c) that with the 4-wire measurement, under 1 mA current there is more noise in the measurement than when using a 20 mA current; the 2-wire test under 0.5V bias produces inbetween 6-11 mA in the cycles shown in 6.3(a). (d) Current-Voltage curves taken on nylon-6 fibers coated with 225 cycles of ZnO ALD at 150°C; the 2-wire measurement was taken between the center electrodes of the 4-wire probe so that the curves represent measurements over the same distance. This plot shows that non-negligible contact resistance is present in the 2-wire measurement (taken using the 4-wire probe) on the nylon-6 sample with woven Au-wire electrodes. 167

Figure 6.4. An Arrhenius plot of the thermal activation of the conductance of a 100 cycle ZnO ALD coating deposited on bare quartz fibers. In situ, post-deposition conductance measurements were taken as a function of temperature, between 53°C and 350°C while the sample was kept under vacuum. For ZnO, as with any semi-conductor, thermally activated carriers cause a samples' conductivity to increase as temperature is increased, since more carriers have sufficient energy to be promoted to the conduction band. The conductivity thermal activation energy (E_a) of the plotted ZnO sample is $E_a \sim 0.42$ eV 168

Figure 6.5. ZnO ALD deposited on bare quartz fibers at 150°C; the current was measured and the conductance is plotted for samples (a) together and (b-d) individually, for samples measured under applied bias voltages of 0.05V, 0.5V and 5V; the first well defined DEZ/H₂O cycle is labeled for each sample. The use of higher voltage seems to require fewer cycles before the onset of measurable conductance occurs. (e-g) Steady state behavior for the same samples from (b-d), showing ZnO cycles #46-48 for each of the tests. 169

Figure 6.6. The onset of measurable conductance is plotted for ZnO deposition at 150°C on quartz fibers, nylon-6 fibers, and polypropylene fibers, both together (a), and individually (b-d). Figure (a) shows the extent of the difference for the substrates before conductance onset is reached, while Figures (b-d) highlight the conductance trends observed for each substrate once measurable signal is detected. In addition to differences in the number of cycles required before conductance can be measured, the dose/response characteristics appear different in the initial stages for all three substrates. For Figure 6.6(e-g), steady state conductance changes are plotted for ZnO cycles #147-149 on quartz fibers, nylon-6 and polypropylene substrates; note the differences in conductance as indicated on the y-axis scales. 170

Figure 6.7. (a) Conductance onset is shown for ZnO ALD on bare nylon-6 performed at different temperatures and plotted (a) together, and (b-d) individually for each temperature.

In Figure 6.7(a) it can be seen that the number of cycles required to reach measurable conductance is dependent on deposition temperature. Figure 6.7(b-d) shows the nature of increasing conductance for ZnO deposited on nylon-6 at 175°C, 150°C, and 100°C; deposition at 175°C and 150°C show similar dose/response trends but 100°C shows distinctly different behavior. (e-g) Steady state conductance curves are shown for the samples for three ZnO ALD cycles (#147-149). Note the differences in the y-axis scales of the plots. The largest conductance is observed for the 150°C sample, which is within the ZnO ALD window. The dose/response curves for the three samples also appear different, with the 100°C sample showing markedly different behavior. To the right of all three samples, plots of conductance change during and after the DEZ dose are shown. The inset of the 100°C sample shows a sizable bump in conductance, which corresponds in timing to the 2 second DEZ dose, as indicated, similar to the feature shown in Figure 6.5(g) for ZnO deposition on bare quartz when measured with a 5V applied bias..... 171

Figure 6.8. Conductance curves for ZnO depositions on bare quartz fibers, and quartz fibers coated with Al₂O₃ and TiO₂ coatings, plotted (a) together, and (b-e) individually for each surface coating. Conductance behavior of the nucleating ZnO coating is initially impacted by composition of the underlying metal-oxide coating, although this dependence is only an interfacial phenomenon; and (f-i) in under 50 ZnO ALD cycles, the conductance curves show similar dose/response behavior for all of the samples, which is not the case earlier in the deposition when conductance behavior is more influenced by interfacial characteristics. .. 173

Appendix Figure A.6.1. In situ conductance was measured during ALD of aluminum doped zinc oxide deposition on quartz fibers at 200°C; aluminum doping was achieved by depositing an Al₂O₃ ALD cycle from TMA and water after 19 cycles of ZnO ALD. The image on the left plots conductance for 200 Al-ZnO cycles (10 × [19 ZnO + 1 Al₂O₃] “super cycles”); the right image shows the first two super cycles and indicates the location of the TMA dopant dose. The dopant dose has a significant impact on conductance over the course of the next 10 ZnO cycles. 179

Appendix Figure A.6.2. In situ conductance measurements were taken of aluminum doped zinc oxide ALD deposited on quartz fibers using two different Al-doping recipes, based on work performed by Na et al.² The left figure shows deposition recipe which incorporates Al-doping by depositing an Al₂O₃ cycle following 19 ZnO cycles. The right figure shows a recipe which introduces the Al-dopant by dosing TMA after the 19th DEZ dose, rather than including a water dose in between, as was done in the left figure..... 180

Appendix Figure A.6.3. In addition to depositing Al-doped ZnO film, TiO₂ doped ZnO films were also deposited, using TiCl₄ and water as the TiO₂ precursor. (left) Using a 19 ZnO to 1 TiO₂ doping ratio, 200 ALD cycles were deposited on quartz fiber substrate in ALD2 at 200°C. (middle) A portion of the overall run is depicted, which include two TiCl₄ doses which cause a large drop in conductance, this can is clearly depicted in (right) which indicates precursor doses. 181

Appendix Figure A.6.4. (a) In situ conductance was measured for ZnO ALD on Al₂O₃ coated quartz fibers. After the ZnO deposition, the substrate was coated with 100 cycles of Al₂O₃ ALD, conductance was measured during the Al₂O₃ ALD, and is shown in (b). Since Al₂O₃ is an electrically insulating material, the current is attributed to the underlying ZnO layer, although curiously, the conductance continues to decrease in a linear rate for the remainder of the 100 Al₂O₃ cycles; an inset shows a magnified portion of the data part of the way through the 100 Al₂O₃ cycles, the duration of an Al₂O₃ cycle is indicated to give reference..... 182

Appendix Figure A.6.5. In situ conductance measurement of a nylon-6 nonwoven during ZnO deposition using “Dose and Hold” recipe where after dosing precursor into the ALD reactor, the gate to the pump is closed isolating the chamber to allow extended substrate-precursor interaction, after which the chamber is purged. (a) Onset of conductance for the sample, plotted logarithmically; (b) six dose and hold cycles after onset of measurable conductance has occurred, the conductance behavior resembles that from ZnO ALD plots; (c) a cycle during the ZnO dose and hold, with the portions of the conductance change labeled to show what step they correspond to, precursor dose, precursor hold, or nitrogen purge..... 183

Figure 7.1. (a) Mass gain as a function of ZnO ALD cycles on nylon-6 nanofibers and microfibers; (b) Mass gain as a function of hold time after precursor dose for substrates coated with 50 ZnO ‘dose and hold’ cycles, where normal ALD is indicated by a 0 second hold time. Longer hold times after precursor dosing may allow better surface coverage or precursor infiltration of the substrates. 196

Figure 7.2. (a) Mass gain as a function of AZO cycles for ALD on nylon-6 nanofiber and microfiber substrates; (b) the corresponding conductivity of the samples shown in 7.2(a), noting that the samples coated with < 80 AZO ALD cycles were not measurably conductive. The microfibers in 7.2(b) are machine direction oriented, so that any similarly AZO coated cross direction oriented samples would have lower conductivity than the microfibers plotted. 197

Figure 7.3. (a) As measured tensile data of Load (in Newtons) vs. Extension length, for nylon-6 nanofiber mats consisting of 100 nm or 200 nm fiber diameter electrospun nanofibers acquired from Elmarco and tested as-received. (b) Calculated tensile stress vs. strain data for uncoated nylon-6 nanofibers, as well as Allasso Industries nylon-6 Winged Fibers™. Using measured fiber mat thickness, the load can be converted into tensile stress, which provides a better comparison of the material performance rather than the sample specific performance; strain is found from known spacing between clamps performing the testing..... 198

Figure 7.4. (a) Representative Stress-Strain curves for 200 nm diameter electrospun nylon-6 nanofibers coated with different numbers of ZnO ALD cycles at 150°C. Samples with low or no ALD coating appear to behave similarly; however upon coating with 200 ZnO ALD cycles the stress-strain curve is significantly altered. The dashed lines indicate the maximum tensile stress for each sample; the strain value corresponding to the peak stress is referred to

as the strain at peak load. (b) The comparable ZnO ALD coated microfiber substrates for both MD and CD orientations. Unlike the nanofiber samples, the microfiber samples do not exhibit a trend upon ZnO ALD coating. 199

Figure 7.5. Tensile stress (a), and tensile strain (b) at peak load are plotted for nylon-6 nanofiber and microfiber samples as a function of the number of ZnO ALD coating cycles. A ZnO coating of 10 or 50 ZnO ALD cycles increases the tensile strength of nylon-6 nanofibers, while a 200 cycle coating causes a significant decrease; the tensile strain for these samples follows the same trend. ZnO coatings up to 200 cycles causes slight decreases in both tensile stress and strain performance for both nylon-6 microfiber samples. 200

Figure 7.6. Uncoated nonwoven nylon-6 substrates were subjected to heat treatment under vacuum to simulate the heating effects of ALD coating. The substrates were then tensile tested, and the tensile stress at peak load is plotted as a function of heat treatment temperature; unheated reference samples are plotted at a treatment temperature of 25°C. The heat treatment does not seem to impact the tensile stress at maximum load for either nanofiber sample or the cross direction microfibers. Machine direction microfibers appear to exhibit a slight increase in tensile performance upon heating for the samples tested. Trend lines are to guide the eye. 201

Appendix A1.1 Figure 1. Top-down SEM micrographs of anodic aluminum oxide samples treated with different thicknesses of ALD tungsten at 250,000X magnification (scale bars are 200 nm). The imaged AAO substrates have approximately 250 nm diameter pores. Image (a) is an uncoated substrate. Image (b), (c), and (d) were collected after 25 cycles of Al₂O₃ and 25, 45, and 100 cycles of W respectively at 200°C. These images show pore shrinkage due to increasing ALD coating thicknesses. Samples coated with higher cycle numbers show increasingly rounded edges and softer features in the nanometer scale due to the conformality of the coatings. 222

Appendix A1.1 Figure 2. Tungsten film thickness versus ALD cycle number on AAO and silicon substrates. Samples are pre-treated with 25 cycles of Al₂O₃ and processed at 200°C. Film thickness on the AAO were extracted from top-down SEM images of AAO pores shown in Figure 1. 223

Appendix A1.1 Figure 3. Cross-sectional view of AAO pores with: (a) 45 cycles; and (b) 100 cycles of W ALD after breaking the coated AAO. The AAO templates are pre-treated with 25 cycles of Al₂O₃ and processed at 200°C. In each image, an inner tube of tungsten is surrounded by an outer AAO substrate shell, and the W thickness increases with ALD cycle number. The arrow in image (a) points to the outer side-wall of a W tube where the AAO shell was removed. 224

Appendix A1.1 Figure 4. Photograph showing nonwoven nylon-6 fiber mats after coating with 100 cycles of W ALD at 140°C. The sample on the left is not treated with Al₂O₃, resulting in poor tungsten nucleation on the fibers, whereas the sample on the right shows proper W nucleation as a result of pre-treatment with 25 cycles of Al₂O₃ at 140°C. 225

Appendix A1.1 Figure 5. Micrographs of nylon-6 fibers (Allasso, Winged FibersTM) coated with 25 cycles of Al₂O₃ followed by 100 cycles of W at 160°C. The dark contrast is from the tungsten coating, which grows conformally around the fiber wings. The Al₂O₃ deposition is not visible at these magnifications. A cross-sectional SEM image of a PA-6 fibril is shown in (d), reproduced with permission from Allasso Industries Inc..... 226

Appendix A1.1 Figure 6. Effect of SiH₄ and WF₆ exposure on substrate mass gain after 25 Al₂O₃ cycles and 100 W ALD cycles at 145°C. The data points show mass uptake on the nylon fiber mat for: (open triangles) increasing silane exposure with fixed WF₆ exposure (= ~2×10⁵ L); and (closed squares) increasing WF₆ with fixed silane exposure (= ~4.5×10⁵ L). The pressure change during silane and WF₆ doses was 0.5 and 0.2 Torr, respectively. For films with 20% or more mass loading, the maximum error of the mean for fractional mass increase was ±5%, as shown by the error bars. The lines are a guide for the eye. 227

Appendix A1.1 Figure 7. Fiber mat effective conductivity as a function of SiH₄ and WF₆ exposure for 25 cycles of Al₂O₃ and 100 cycles of W deposition at 145°C. The data symbols correspond to the samples shown in Figure 6. The conductivity is approximately 1000 S/cm, independent of exposure conditions when sufficient coating thickness is present. The data points show effective conductivity on the nylon fiber mat for: (open triangles) increasing silane exposure with fixed WF₆ exposure (= ~2×10⁵ L); and (closed squares) increasing WF₆ with fixed silane exposure (= ~4.5×10⁵ L). The lines are a guide for the eye. Each data point represents an average of 7 measurements for each sample. The standard error of the mean is smaller than the size of the data points. 228

Appendix A1.1 Figure 8. Effect of varying silane dose times and short silane doses combined with varying hold times on W mass uptake on nylon-6 fiber mats. All samples were coated with 25 Al₂O₃ and 100 W cycles at 145°C. For the “hold” sequence, the silane dose time is set at 10 seconds after which the reactor is closed for a set hold time between 20 and 120 seconds. The remainder of the ALD cycle proceeded unchanged. We also compare runs done with different silane dose times without the hold step (triangle symbols, data from Figure 6). With the 10 second silane exposure, the hold step does not enhance W mass uptake on the fiber mat substrates. The error bars represent an uncertainty of ±5% in the mass loading analysis..... 229

Appendix A1.1 Figure 9. Change in conductivity for conducting layers deposited on fiber substrates when the fiber mats are bent around increasingly smaller cylinders. The conductivity of ZnO on polypropylene fibers is approximately 20 S/cm as prepared, but it decreases substantially upon bending. Similar experiments for the W-coated nylon studied here shows ~90% conductivity retention upon bending. Data from ZnO coated polypropylene is from reference 20. Tungsten-coated samples were prepared with 25 Al₂O₃ and 100 W cycles at 145°C. Each data point represents the mean of two conductivity values collected from each sample, and the error bars show typical variation. 230

Appendix A1.1 Figure A.1. (a) The maximum force achieved during the tensile test is plotted for each of the three types of tested substrates. (b) The tensile strain at maximum load is plotted for the three types of substrates. Error bars indicate one standard deviation..... 233

Appendix A1.1 Figure A.2. SEM images of (a) as-deposited, and (b) tensile tested tungsten ALD coated nylon-6 fibers. The as-deposited tungsten coated fibers show limited cracking from normal lab handling. The tensile tested tungsten coated nylon-6 shows much more significant cracking, as well as patches of delaminated coating which appear as dark spots in the image. 234

Appendix A1.2 Figure 1. A schematic of the 4-probe (a) line features and (b) experimental apparatus used to measure the resistivity of fiber systems. In this design, the outer electrode spacing is 1.9 cm and the inner probe spacing, $s = 0.5$ cm. The probe pads are fabricated by e-beam deposition of 200 nm of Au with a 10 nm Ti adhesion layer onto a glass slide. Another glass slide is used to apply a uniform compression onto the fiber substrate. Plots of current-voltage (c) for silver coated nylon nonwoven fiber mat and (d) ALD ZnO coated paper with a 2-probe apparatus and the 4-probe apparatus introduced in this work. For the 4-probe method, current was applied across the outer probes and voltage was measured across the two inner probes. For the 2-probe method, voltage was applied and current was measured across the two inner probes..... 264

Appendix A1.2 Figure 2. Plots of (a) conductance vs. coating mass; and (b) effective conductivity vs. coating mass for the silver coated nylon nonwoven fiber mat. The 4-probe measurements were conducted with a loading weight of 1700 g. Error bars reflect one standard deviation of the measured values. (c) Plot of conductance measured through silver-coated fiber mats as a function of applied loading mass. Increasing the loading mass compresses the fiber mats and generally increases conductance. The numbers on the right refer to the number of coated mats stacked during the measurement. Stacking multiple mats increases the amount of silver available for conductance. (d) Effective conductivity values obtained from the data in panel (c) after normalizing using equation (3). A somewhat larger value of saturated effective conductivity is obtained with one fiber mat which contained the fewest total number of fiber/fiber contact points..... 265

Appendix A1.2 Figure 3. SEM images of woven cotton (a) before ALD processing; and (b) after 480 ALD cycles of ZnO grown at 115°C. Plots of (c) conductance vs. loading mass; and (d) effective conductivity vs. loading mass for woven cotton fiber with 240-600 ALD cycles of ZnO coating grown at 115°C. The number of ZnO ALD cycles used for each sample is indicated. Prior to the ALD ZnO, 50 cycles of aluminum oxide was deposited at a temperature of 60°C..... 266

Appendix A1.2 Figure 4. SEM images of cotton paper (a) prior to ALD processing; and (b) after 480 ALD cycles of ZnO grown at 115°C; Plots of (c) conductance; and (d) conductivity vs. loading mass for cotton paper after ZnO ALD at 115°C. The number of ZnO ALD cycles is indicated on the right. Similar to the woven cotton in Figure 3, 50 cycles of aluminum oxide was deposited at 60°C prior to the ZnO ALD. 267

Appendix A1.2 Figure 5. Values of (a) conductance; and (b) conductivity of ZnO coated woven cotton fiber and cotton paper as a function of ZnO ALD cycles measured with 1000 g loading mass. The conductance values are not expected to be the same on the two substrates. However, normalization of the data using equation (3) produces an effective conductivity value that is approximately independent of substrate and extent of film coating..... 268

Appendix A1.2 Figure 6. (a) SEM image of polypropylene fiber with 480 ALD cycles of ZnO grown at 115°C before mass loading. Plot of (b) conductivity vs. loading weight for nonwoven polypropylene fiber mats with 50 cycles of ALD aluminum oxide followed by 180 to 600 cycles of ALD ZnO. The values do not show a consistent result in this case due to non-cohesive ALD film deposition on the polypropylene fibers. (c) SEM image of polypropylene fiber with 480 ALD cycles of ZnO grown at 115°C after loading with 2000 g, showing film cracking..... 269

Appendix A1.2 Figure 7. (a) SEM image; and (b) effective conductivity vs. loading mass obtained from quartz fibers coated with 200 cycles of ALD W at 200°C. A consistent effective conductivity of 1150 S cm⁻¹ is observed. (c) Picture of an all fiber-based metal–insulator–metal (MIM) capacitor fabricated with tungsten-coated quartz fiber (metal contacts) and polypropylene (insulator). A plot of (d) capacitance density vs. frequency evaluation of the MIM capacitor exposed to various chemical solutions..... 270

CHAPTER 1. Introduction

Atomic layer deposition (ALD) is coating method that utilizes alternating self-limiting vapor phase reactant chemistries to construct films in a layer by layer fashion with sub-nanometer level thickness control. As a result of the vapor phase reactants and self-terminating reaction chemistry, highly conformal films can be deposited on complex and very high aspect ratio features.¹ A variety of ALD chemistries have been demonstrated to date, including pure metals, metal oxides, metal nitrides, metal sulfides, and other binary compounds, in addition to a variety of ternary and quaternary compounds.² ALD finds application in the semiconductor industry for deposition of high quality dielectric oxides for applications such as trench capacitors in DRAM and high-k gate oxides in MOSFETs.³ Intel currently uses ALD to deposit HfO_2 gate oxide layers, due ALD's demonstrated ability to deposit very thin (2-3nm), high quality, pinhole free films in agreement with manufacturing requirements for their 45nm node chip design.⁴

Recently, ALD has been increasingly applied to a wider variety of substrates, including aerogels, graphene, carbon nanotubes, as well as polymer films and fibers.^{1,3,5-9} Deposition on these surfaces bring a variety of complications not typically present for deposition on silicon, including high aspect ratio coating considerations like dosing quantity and time, as well as differing levels of substrate-precursor reaction varying from inert carbon materials to very reactive polymers.⁶⁻⁹ The growing sub-division of ALD study on non-traditional substrates, still has much to be investigated, including even the use of fairly common precursor chemistries. For this work, application of transparent conducting oxides

on flexible polymer substrates is chosen as the topic of investigation, since it presents a new set of yet unmet challenges, with interesting potential applications for future research and manufacturing.

In this regard, the primarily materials of interest are zinc oxide films deposited by atomic layer deposition, which can be readily deposited using diethyl zinc (DEZ) and water, over a temperature range from 60°C to above 200°C. For applications as a transparent conducting oxide, high conductivity is desirable, and so deposition conditions are investigated with the goal of maximizing the conductivity of the ZnO films.

The zinc oxide ALD process is well studied for deposition on silicon and other planar substrates,¹⁰⁻¹⁵ but little work exists for deposition on other substrates, although recently the topic has come under more investigation.¹⁶⁻²¹ In addition, molecular layer deposition (MLD), a variant of ALD where molecules are deposited during a cycle rather than atoms, has incorporated DEZ as a co-reactant with the goal of developing a hybrid organic-inorganic deposition process that possesses ZnO-like conductivity, while incorporating the flexibility of organic molecules.²²⁻²⁴

Zinc oxide is an n-type semiconductor with a bandgap of ~3.3eV which makes it appealing for use in UV capture or emission in applications such as photovoltaics, UV lighting, and UV sensors. When exposed to various chemical species such as oxygen, water or ethanol vapor, a depletion layer forms at the ZnO/gas interface, enabling ZnO to be used for gas sensing.²⁵⁻²⁷

Intrinsic zinc oxide is a n-type semiconductor that owes its conductivity to a combination of native defects such as interstitial zinc atoms, oxygen vacancies, and hydrogen

doping, although the specifics of its origin is still under debate.^{28–30} Intrinsic ZnO can be natively doped through tuning of parameters impacting the amount of interstitial zinc or oxygen vacancies, for example by post-growth annealing.^{31,32}

The electrical conductivity of a ZnO film or crystal can vary significantly depending on the stoichiometry, impurities, and defect density, all of which are dependent on the conditions and method used to deposit or grown the ZnO. For example in one report,³¹ high purity, low defect, single crystal ZnO grown from melt solution had a bulk electrical conductivity of ~12 S/cm, while ZnO ALD films can have an electrical conductivity of ~150 S/cm for undoped as-deposited ZnO films on SiO₂.²⁰ Defects in the ZnO crystal also impact both the color and transparency of the ZnO; post-growth annealing of ZnO single crystals in an oxygen rich environment has been shown to increase transparency and reduce color, while annealing in a zinc rich environment reduces transparency and turns the ZnO crystal redish-brown.^{31,32} In addition to producing a color shift in the ZnO, annealing in an oxygen or zinc atmosphere, also caused conductivity to decrease, or increase, respectively.³¹

Highly conductive p-type ZnO films are not formed easily, which has limited the application for ZnO based materials for use in L.E.D.'s and solar cells.³³ Native defects cannot be used to dope ZnO p-type, which is thought to be due to the low formation enthalpy of donor defects, interstitial zinc, oxygen vacancies, compared to the high formation enthalpy of native acceptor defects, interstitial oxygen and zinc vacancies.²⁹ A recent report suggests that defect-defect interaction between oxygen vacancies and interstitial zinc maybe the cause of the n-type conductivity observed in many ZnO films.³⁰

Extrinsic doping is readily achieved in ZnO, primarily through n-type donors. ZnO films get additional electrons injected into the conduction band from shallow donor levels when, for example, an aluminum replaces a zinc atom.²⁹ By extrinsically doping ZnO, a defect level is formed which alters band behavior, producing different thermally dependent variation of the electrical conductivity for doped and undoped ZnO. Undoped semiconductors have carrier concentrations controlled by thermal excitation, so increasing temperature always leads to higher conductivity, and cooling leads to lower conductivity. Because dopant atoms ionize at low temperatures compared to that required for thermal excitation of carriers, doped semiconductors have a constant carrier density over a range of temperatures. Above temperatures when dopant atoms can ionize and contribute carriers to conduction, carrier concentration remains constant until thermally generated carriers begin to be promoted in sufficiently large amounts that they begin to dominate conduction, shifting behavior to that of an intrinsic semiconductor.

Zinc oxide is readily deposited by atomic layer deposition with sub-nanometer control, at low temperatures ($< 200^{\circ}\text{C}$).^{10,15,16,20,34} Doping ALD films can be readily achieved using standard delta doping by systematically alternating in dopant cycles, or if precursor chemistry allows, pre-mixing the primary metal precursor with that of the dopant metal precursor.³⁵ A variety of dopants have been investigated, the most common of which is aluminum,^{10,16,36-40} but others include gallium^{16,41}, hafnium,⁴² titanium,⁴³ indium,^{41,44,45} fluorine,⁴⁶ and phosphorous.⁴⁷ Post deposition annealing of ZnO ALD films has been performed using arsenic,⁴⁸ in order to create p-type ZnO. By aluminum doping ZnO (AZO)¹⁰ the conductivity of deposited films can be increased by an order of magnitude over undoped

films,¹⁶ producing a material that has conductivity close to that of indium tin oxide (ITO) films, the current benchmark for transparent conducting oxides. ITO is a very commonly used transparent conducting oxide that has applications in electronic displays and solar cell devices due to its high conductivity and transparency, but indium is not widely abundant in the earth's crust.⁴⁹ The production of indium metal from mined ore is inefficient, leading ITO to be expensive, and projected growth in displays (e.g. televisions, smart phones) and solar cells makes the availability and cost of using indium a concern, which has led to increasing interest in alternative materials with comparable performance characteristics.^{33,49}

In this work, zinc oxide will be deposited by ALD on insulating nonwoven polymer mats to produce conductive nonwovens which are then electrically and mechanically characterized. The conductivity of ZnO deposited on nonwoven substrates is also studied by in situ measurement, and it is used to study nucleation and coalescence of the ZnO ALD film as it is being deposited on substrates of different chemistries like metal oxides and polymers. Furthermore, a technique is demonstrated to pattern nonwovens by ZnO ALD, which could be used for example, to apply conductive metal or metal oxide electrodes onto a nonwoven by ALD.

References

1. Kucheyev, S. O. *et al.* Atomic layer deposition of ZnO on ultralow-density nanoporous silica aerogel monoliths. *Appl. Phys. Lett.* **86**, (2005).
2. Miikkulainen, V., Leskela, M., Ritala, M. & Puurunen, R. L. Crystallinity of inorganic films grown by atomic layer deposition: Overview and general trends. *J. Appl. Phys.* **113**, 021301 (2013).
3. George, S. M. Atomic Layer Deposition: An Overview. *Chem. Rev.* **110**, 111–131 (2010).
4. Guziewicz, E. *et al.* ALD grown zinc oxide with controllable electrical properties. *Semicond. Sci. Technol.* **27**, 074011 (2012).
5. Devine, C. K., Oldham, C. J., Jur, J. S., Gong, B. & Parsons, G. N. Fiber Containment for Improved Laboratory Handling and Uniform Nanocoating of Milligram Quantities of Carbon Nanotubes by Atomic Layer Deposition. *Langmuir* **27**, 14497–14507 (2011).
6. Spagnola, J. C. *et al.* Surface and sub-surface reactions during low temperature aluminium oxide atomic layer deposition on fiber-forming polymers. *J. Mater. Chem.* **20**, 4213–4222 (2010).
7. Gong, B. & Parsons, G. N. Quantitative in situ infrared analysis of reactions between trimethylaluminum and polymers during Al₂O₃ atomic layer deposition. *J. Mater. Chem.* **22**, 15672 (2012).

8. Farmer, D. B. & Gordon, R. G. Atomic Layer Deposition on Suspended Single-Walled Carbon Nanotubes via Gas-Phase Noncovalent Functionalization. *Nano Lett.* **6**, 699–703 (2006).
9. Wilson, C. A., Grubbs, R. K. & George, S. M. Nucleation and growth during Al₂O₃ atomic layer deposition on polymers. *Chem. Mater.* **17**, 5625–5634 (2005).
10. Lujala, V., Skarp, J., Tammenmaa, M. & Suntola, T. Atomic layer epitaxy growth of doped zinc oxide thin films from organometals. *Appl. Surf. Sci.* **82-83**, 34–40 (1994).
11. Yamada, A., Sang, B. S. & Konagai, M. Atomic layer deposition of ZnO transparent conducting oxides. *Appl. Surf. Sci.* **112**, 216–222 (1997).
12. Elam, J. W., Routkevitch, D. & George, S. M. Properties of ZnO/Al₂O₃ alloy films grown using atomic layer deposition techniques. *J. Electrochem. Soc.* **150**, G339–G347 (2003).
13. Elam, J. W. & George, S. M. Growth of ZnO/Al₂O₃ alloy films using atomic layer deposition techniques. *Chem. Mater.* **15**, 1020–1028 (2003).
14. Elam, J. W., Sechrist, Z. A. & George, S. M. ZnO/Al₂O₃ nanolaminates fabricated by atomic layer deposition: growth and surface roughness measurements. *Thin Solid Films* **414**, 43–55 (2002).
15. Guziewicz, E. *et al.* Extremely low temperature growth of ZnO by atomic layer deposition. *J. Appl. Phys.* **103**, 6 (2008).
16. Ott, A. W. & Chang, R. P. H. Atomic layer-controlled growth of transparent conducting ZnO on plastic substrates. *Mater. Chem. Phys.* **58**, 132–138 (1999).

17. Gong, B. *et al.* Sequential Vapor Infiltration of Metal Oxides into Sacrificial Polyester Fibers: Shape Replication and Controlled Porosity of Microporous/Mesoporous Oxide Monoliths. *Chem. Mater.* **23**, 3476–3485 (2011).
18. Oldham, C. J. *et al.* Encapsulation and Chemical Resistance of Electrospun Nylon Nanofibers Coated Using Integrated Atomic and Molecular Layer Deposition. *J. Electrochem. Soc.* **158**, D549–D556 (2011).
19. McClure, C. D., Oldham, C. J., Walls, H. J. & Parsons, G. N. Large effect of titanium precursor on surface reactivity and mechanical strength of electrospun nanofibers coated with TiO₂ by atomic layer deposition. *J. Vac. Sci. Technol. Vac. Surfaces Films* **31**, 061506 (2013).
20. Sweet, W. J., Jur, J. S. & Parsons, G. N. Bi-layer Al₂O₃/ZnO atomic layer deposition for controllable conductive coatings on polypropylene nonwoven fiber mats. *J. Appl. Phys.* **113**, 194303 (2013).
21. Jur, J. S., Sweet, W. J., Oldham, C. J. & Parsons, G. N. Atomic Layer Deposition of Conductive Coatings on Cotton, Paper, and Synthetic Fibers: Conductivity Analysis and Functional Chemical Sensing Using ‘All-Fiber’ Capacitors. *Adv. Funct. Mater.* **21**, 1993–2002 (2011).
22. Peng, Q., Gong, B., VanGundy, R. M. & Parsons, G. N. ‘Zincone’ Zinc Oxide–Organic Hybrid Polymer Thin Films Formed by Molecular Layer Deposition. *Chem. Mater.* **21**, 820–830 (2009).

23. Yoon, B., Lee, B. H. & George, S. M. Highly Conductive and Transparent Hybrid Organic–Inorganic Zinc Oxide Thin Films Using Atomic and Molecular Layer Deposition. *J. Phys. Chem. C* **116**, 24784–24791 (2012).
24. Tynell, T. & Karppinen, M. ZnO: Hydroquinone superlattice structures fabricated by atomic/molecular layer deposition. *Thin Solid Films* **551**, 23–26 (2014).
25. Cho, S. *et al.* Ethanol sensors based on ZnO nanotubes with controllable wall thickness via atomic layer deposition, an O₂ plasma process and an annealing process. *Sensors Actuators B Chem.* **162**, 300–306 (2012).
26. Takahashi, Y., Kanamori, M., Kondoh, A., Minoura, H. & Ohya, Y. Photoconductivity of Ultrathin Zinc Oxide Films. *Jpn. J. Appl. Phys.* **33**, 6611–6615 (1994).
27. Pearton, S. J., Norton, D. P., Ip, K., Heo, Y. W. & Steiner, T. Recent advances in processing of ZnO. *J. Vac. Sci. Technol. B* **22**, 932–948 (2004).
28. Min, Y.-S., An, C.-J., Kim, S.-K., Song, J.-W. & Hwang, C.-S. Growth and Characterization of Conducting ZnO Thin Films by Atomic Layer Deposition. *Bull. Korean Chem. Soc.* **31**, 2503–2508 (2010).
29. Zhang, S., Wei, S.-H. & Zunger, A. Intrinsic n-type versus p-type doping asymmetry and the defect physics of ZnO. *Phys. Rev. B* **63**, (2001).
30. Kim, Y.-S. & Park, C. Rich Variety of Defects in ZnO via an Attractive Interaction between O Vacancies and Zn Interstitials: Origin of n-Type Doping. *Phys. Rev. Lett.* **102**, (2009).
31. Schulz, D., Ganschow, S., Klimm, D. & Struve, K. Inductively heated Bridgman method for the growth of zinc oxide single crystals. *J. Cryst. Growth* **310**, 1832–1835 (2008).

32. Mikami, M., Eto, T., Wang, J., Masa, Y. & Isshiki, M. Growth of zinc oxide by chemical vapor transport. *J. Cryst. Growth* **276**, 389–392 (2005).
33. Moezzi, A., McDonagh, A. M. & Cortie, M. B. Zinc oxide particles: Synthesis, properties and applications. *Chem. Eng. J.* **185–186**, 1–22 (2012).
34. Luka, G. *et al.* Transparent and conductive undoped zinc oxide thin films grown by atomic layer deposition. *Phys. Status Solidi* **207**, 1568–1571 (2010).
35. Illiberi, A., Scherpenborg, R., Wu, Y., Roozeboom, F. & Poodt, P. Spatial Atmospheric Atomic Layer Deposition of Al(x)-ZnO(1-x)-O. *Acs Appl. Mater. Interfaces* **5**, 13124–13128 (2013).
36. Wu, Y. *et al.* Enhanced Doping Efficiency of Al-Doped ZnO by Atomic Layer Deposition Using Dimethylaluminum Isopropoxide as an Alternative Aluminum Precursor. *Chem. Mater.* **25**, 4619–4622 (2013).
37. Na, J. S., Scarel, G. & Parsons, G. N. In Situ Analysis of Dopant Incorporation, Activation, and Film Growth during Thin Film ZnO and ZnO:Al Atomic Layer Deposition. *J. Phys. Chem. C* **114**, 383–388 (2010).
38. Na, J.-S., Peng, Q., Scarel, G. & Parsons, G. N. Role of Gas Doping Sequence in Surface Reactions and Dopant Incorporation during Atomic Layer Deposition of Al-Doped ZnO. *Chem. Mater.* **21**, 5585–5593 (2009).
39. Baji, Z. *et al.* Temperature dependent in situ doping of ALD ZnO. *J. Therm. Anal. Calorim.* **105**, 93–99 (2011).

40. Genevée, P., Donsanti, F., Renou, G. & Lincot, D. Study of the aluminum doping of zinc oxide films prepared by atomic layer deposition at low temperature. *Appl. Surf. Sci.* **264**, 464–469 (2013).
41. Yen, K.-Y. *et al.* Characteristics of GaN-based LEDs using Ga-doped or In-doped ZnO transparent conductive layers grown by atomic layer deposition. *J. Cryst. Growth* **387**, 91–95 (2014).
42. Ahn, C. H., Kim, J. H. & Cho, H. K. Tunable Electrical and Optical Properties in Composition Controlled Hf:ZnO Thin Films Grown by Atomic Layer Deposition. *J. Electrochem. Soc.* **159**, H384 (2012).
43. Lee, D.-J. *et al.* Atomic layer deposition of Ti-doped ZnO films with enhanced electron mobility. *J. Mater. Chem. C* **1**, 4761 (2013).
44. Lee, D.-J. *et al.* Ultrasoft, High Electron Mobility Amorphous In–Zn–O Films Grown by Atomic Layer Deposition. *J. Phys. Chem. C* **118**, 408–415 (2014).
45. Illiberi, A., Scherpenborg, R., Theelen, M., Poodt, P. & Roozeboom, F. On the environmental stability of ZnO thin films by spatial atomic layer deposition. *J. Vac. Sci. Technol. Vac. Surfaces Films* **31**, 061504 (2013).
46. Choi, Y.-J. & Park, H.-H. A simple approach to the fabrication of fluorine-doped zinc oxide thin films by atomic layer deposition at low temperatures and an investigation into the growth mode. *J. Mater. Chem. C* **2**, 98 (2014).
47. Tynell, T., Okazaki, R., Terasaki, I., Yamauchi, H. & Karppinen, M. Electron doping of ALD-grown ZnO thin films through Al and P substitutions. *J. Mater. Sci.* **48**, 2806–2811 (2012).

48. Snigurenko, D. *et al.* XPS study of arsenic doped ZnO grown by Atomic Layer Deposition. *J. Alloys Compd.* **582**, 594–597 (2014).
49. Tolcin, A. *Commodity Statistics and Information, Non-fuel Minerals: Indium.* 74–75 (U.S. Geological Survey, 2012). at
<<http://minerals.usgs.gov/minerals/pubs/commodity/indium/mcs-2012-indiu.pdf>>

CHAPTER 2. Experimental Tools

2.1 Atomic Layer Deposition

Atomic layer deposition was performed in one of three homebuilt hot walled ALD reactors, all of which operate under similar deposition conditions. The primary reactor, which accounts for ~90% of the deposited samples in this work, has been described previously,¹ while the other similarly designed reactors have been described before elsewhere as well.²⁻⁴ All depositions were performed using nitrogen carrier gas that was filtered, dried, and supplied at ~150 sccm, corresponding to a reactor pressure of ~1.0 Torr. Depositions were performed over the temperature range from 50°C to 200°C. Typical deposition recipes for ZnO were DEZ/N₂/H₂O/N₂ = 2s/40s/2s/40s, where a 2.0s DEZ dose produced a pressure change of $\Delta P=0.07$ Torr. A typical Al₂O₃ dose had a recipe of TMA/N₂/H₂O/N₂ = 1.2s/30s/1.5s/30s, which produced a TMA pressure change of $\Delta P=0.05$ Torr. All recipes were constructed to have >2x the water dose of the metal oxide precursor, to ensure complete reaction of the metal organics. Furthermore, precursor doses and purge times were investigated at various deposition temperatures, to ensure appropriately saturating doses were provided, and that sufficiently long purge times were used to ensure ALD was being achieved. Non-saturating precursor doses produce lower growth per cycle and lead to non-uniform film growth, while insufficient purging increases the likelihood of precursors reacting in the gas phase and causing undesired chemical vapor deposition. Saturation curves were produced as a function of precursor dose time for each reactor, and this was used to verify similar deposition was occurring in all three reactors.

2.2 Ellipsometry

To determine the film thickness for the deposited ALD coating layer, as well as for the substrate thermal oxide layer, or spun-cast polymer film, spectroscopic ellipsometry (Alpha S.E., J.A. Woollam) was performed prior to, and after deposition, a minimum of four times per sample. At least two monitor wafers were used for each ALD run, one in the front and one in the rear of the reactor, to indicate if similar ALD was occurring across the length of the deposition zone.

2.3 Four point probe

Sheet resistance was measured for films deposited on electrically insulating thermal oxide silicon wafers, using a 4-point probe (Jandel multi-height probe with RM3-AR test unit), a minimum of four times per sample. Since the thermally oxidized silicon did not produce a measurable sheet resistance within the range of the 4-point probe, which has an upper limit of $10^7 \Omega/\text{square}$, we attribute any sheet resistance measured on the deposited film to be that of the ALD film, and assume the underlying substrate to be completely insulating.

2.4 Four Electrode Probe

In this work, a four-electrode probe described in previous work² was used to measure the resistance of the conductive coating on the nonwoven samples; the same mathematical analysis was performed in order to determine conductivity values discussed in this work. Additional analysis of the impact of fiber-fiber resistance on the effective conductivity of conductive nonwoven fiber mats will be discussed in this work.

Resistance measurements of the coated nonwovens were taken using a four-electrode probe attached to a Keithley 2400 Sourcemeter operating in sensing mode. The contact resistance between the electrodes and alligator clips connected to the Sourcemeter was measured prior to each use, and was found to be ≤ 15 Ohms using a multimeter. The resistances of the polymer substrates are too high to be detected within the sensitivity limit of the Keithley, therefore the resistance measured on the ZnO coated nonwovens is attributed only to the ZnO coating.

Only a portion of the ZnO coating actually contributes to a given resistance measurement, and that is the amount of coating between the probe's inner electrodes, which is where the voltage is measured. If we assume linear mass density of the sample, then the amount of sample between the center electrodes can be determined. We can determine the amount of nylon-6 between the center electrodes, using 1) the length of the sample perpendicular to the electrodes (e.g. 3.2 cm), and 2) the known center electrode spacing of 0.5 cm, we can estimate $(0.5 \text{ cm}/3.2 \text{ cm}=0.156)$ 15.6 % of the initial uncoated fiber mat mass $0.156 \times 25 \text{ mg} = 3.9 \text{ mg}$ is between the electrodes. With the calculated mass gain for a given sample, e.g. 45% mass gain for 300 cycles of ZnO at 150°C, we can estimate a ZnO coating mass of $m_{\text{coating}} = 0.0039\text{g} \times 0.45 = 1.76 \times 10^{-3} \text{ g}$ of ZnO coating is in-between the center electrodes, and thus contributing to the measured resistance.

Resistance, a measurable, extrinsic material property, is used to calculate a materials resistivity (the reciprocal of conductivity). Resistivity is an intrinsic property of a material, and is defined as:

$$\rho(\text{Ohm}\cdot\text{cm}) = \text{Resistance (Ohms)} \times \text{Cross Sectional Area (cm}^2\text{)} / \text{Length (cm)} \quad (2.1)$$

which holds regardless of the shape or length of the sample being tested, since the samples' resistance decreases proportional to increasing cross sectional area, and resistance increase proportional to sample length. Therefore, using the measured length and resistance of the samples, if we can calculate the cross section area through which current flows, resistivity (or conductivity) can be determined.

As derived previously,² by using 1) the coating density (ZnO ~ 5.71 g/cm³), 2) the length between the measuring (sensing) electrodes, and 3) the calculated contributing ZnO mass, we can determine the cross sectional area of the ZnO coating on the nonwoven is: $1.76 \times 10^{-3} \text{g} / (5.71 \text{g/cm}^3 \cdot 0.5 \text{cm}) = 6.16 \times 10^{-4} \text{cm}^2$. Since the length over which the resistance is being measured is known from the probes geometry (distance between the center sensing electrodes), we can then calculate the conductivity of the sample, by inverting equation 2.1, such that, $\sigma \text{ (S/cm)} = \rho^{-1} \text{ (Ohm}\cdot\text{cm)}^{-1} = \text{Length} / (\text{Area} \times \text{Resistance})$. Using the measured resistance of the sample (e.g. $R = 33 \text{ Ohms}$), the effective conductivity can be calculated by the equation:²

$$\sigma_{\text{eff}} \text{ (S} \cdot \text{cm}^{-1}\text{)} = \frac{L \cdot \rho}{m_{\text{coating}}} \cdot s \cdot \frac{1}{R} \quad (2.2)$$

which produces an effective conductivity value for this example sample of 24.6 S/cm, when using a ZnO density of $\rho = 5.71 \text{ g/cm}^3$, the sample length $L=0.5 \text{ cm}$ of the sample contributing to resistance measurement, and an electrode spacing $s = 0.5 \text{ cm}$.

The first group of terms in equation 2.2, $(L \times \rho / m_{\text{coating}})$ are the inverse of the cross sectional area of the conductive film. The spacing s , is a fixed value based on the probes construction; while a different value of L could be used in this calculation, as long as the ratio of contributing sample mass is adjusted accordingly, the change in these terms will cancel to produce the same effective conductivity.

This calculation is complicated if the substrate is not sufficiently electrically insulating, but the bare polymers used here are not conductive enough to produce a measurable conductance within the detection limits of the device (e.g. current \ll 1 nanoAmps in a field of 20 Volts).

2.5 Optical Imaging

Optical images were collected using a high resolution digital SLR camera with macro-filter attachments for some substrate images. For some of these images, the images' contrast was enhanced using GIMP 2.8 Graphics Software, and is noted in the captions of any enhanced figures.

High magnification optical images were taken using a Jenoptik optical microscope with a ProgRes CT5 digital microscope camera attachment. Microscope images were analyzed using ProgRes CapturePro 2.6 software package.

2.6 Scanning Electron Microscope

For some samples, a FEI Phenom scanning electron microscope (SEM) operating at a 5 kV accelerating voltage was used to image the substrates. For bare polymer substrates, a 5

nm Au/Pd coating was sputtered on the samples prior to imaging. For other samples, (e.g. in the case of AZO coated nylon) the samples did not require sputtering prior to imaging. As a result, such samples, such as the AZO coated nylon-6 substrates imaged after tensile testing, show a strong contrast between the AZO coating which appears bright, and the insulating nylon-6 polymer underneath, which appears dark.

Other samples were imaged in a Hitachi S3200N variable pressure scanning electron microscope with an Oxford Energy Dispersive X-ray Spectrometer (EDS) attachment, at the NCSU Analytical Instrument Facility with the assistance of Chuck Mooney. Samples prepared for analysis with this tool did not require a conductive coating to be applied since the tool can image non-conductive substrates. As a result, the contrast present in these images does not reflect a difference in localized conductivity of the substrate, as with the Phenom SEM images.

2.7 Transmission Electron Microscope

Some samples were analyzed by Transmission Electron Microscopy (TEM). The fiber samples were embedded in a low viscosity epoxy resin (Ladd Research Industries) and allowed to cure over-night at room temperature. The blocks were then cut to a thickness of 90nm using a Lecia Ultracut diamond knife microtome. The samples were then floated on 300 mesh grids and allowed to dry. Images were taken at the NCSU Analytical Instrument Facility with the assistance of Toby Tung and Roberto Garcia, using either a JEOL 2000FX S/TEM or a Hitachi HF-2000 FETEM, with cold field emission electron sources and accelerating voltages of 200kV.

2.8 Ultra Violet – Visible Light Spectrophotometer

UV-Vis transmission spectra were taken using an Evolution 300 Thermo Scientific UV-Vis spectrophotometer. Double side polished sintered quartz disc substrates (1 inch diameter) were used for the UV-Vis measurement because they have > 99.6% transmission in the 190 nm – 1100 nm wavelength range of the spectrophotometer. Prior to use, the quartz discs were rinsed with acetone, ethanol, and then de-ionized water to clean the surface, and then dried with nitrogen. The ALD coatings (e.g. 400 cycles of ZnO at 150°C) were then deposited onto two quartz discs; the discs were propped up during deposition to ensure uniform coverage on the front and back of the substrates. After deposition, one quartz disc was analyzed to obtain the UV-Vis transmission of the as-deposited ZnO ALD film. The other ZnO coated quartz disc was then subject to annealing in air at 800°C for 3 hours. After cooling the annealing furnace, the annealed ZnO coated quartz disc was removed and analyzed for UV-Vis transmission.

2.9 X-Ray Diffraction

X-ray diffraction (XRD) was performed at the NCSU Analytical Instrument Facility using a Rigaku SmartLab X-ray diffractometer with a CuK α X-ray source, with the assistance of Dr. Do Han Kim.

2.10 Tensile Testing

Tensile testing was primarily performed on nonwoven substrates that were cut into 12 mm x 60 mm strips for tensile testing. The testing was performed using an Instron 5943

Tensile Tester, using a 1 kN load cell, and a cross head speed of 10 mm/min. To determine the tensile strength of materials, data was gathered by testing the samples until failure to determine maximum load and extension measurements.

For other samples, the objective was to determine the impact of tensile strain on the conductivity of the coating. The conductivity of these samples was measured prior to tensile testing using the 4-electrode probe setup described earlier. Then these samples were strained a fixed amount (2%, 5%, 10%, 20%, or 50%) and these samples were then tested again for conductivity. The conductivity measurements and tensile straining of these samples were typically performed the same day the samples were deposited.

Four samples were tested where the conductance of the sample was measured as the tensile testing was performed, and these tests were carried out at the College of Textiles Physical Testing Lab using a MTS Q-Test/5 Universal Testing Machine. For these tests, a Keithley 2400 Sourcemeter was used to measure the current between two electrodes attached to a nonwoven sample with a conductive ALD coating. For these tests, 25 mm x 152 mm substrates were used rather than the typical 12 mm x 60 mm sample size. The Keithley 2400 Sourcemeter was set to collect current data as the tensile test was run. The samples were tested until failure, as indicated by a 50% reduction in load compared to the measured peak load. Even at mechanical failure however, samples registered non-zero current indicating that conductive pathways still remained through the sample.

2.11 References

1. Spagnola, J. C. *et al.* Surface and sub-surface reactions during low temperature aluminium oxide atomic layer deposition on fiber-forming polymers. *J. Mater. Chem.* **20**, 4213–4222 (2010).
2. Jur, J. S., Sweet, W. J., Oldham, C. J. & Parsons, G. N. Atomic Layer Deposition of Conductive Coatings on Cotton, Paper, and Synthetic Fibers: Conductivity Analysis and Functional Chemical Sensing Using ‘All-Fiber’ Capacitors. *Adv. Funct. Mater.* **21**, 1993–2002 (2011).
3. Oldham, C. J. *et al.* Encapsulation and Chemical Resistance of Electrospun Nylon Nanofibers Coated Using Integrated Atomic and Molecular Layer Deposition. *J. Electrochem. Soc.* **158**, D549–D556 (2011).
4. McClure, C. D., Oldham, C. J., Walls, H. J. & Parsons, G. N. Large effect of titanium precursor on surface reactivity and mechanical strength of electrospun nanofibers coated with TiO₂ by atomic layer deposition. *J. Vac. Sci. Technol. Vac. Surfaces Films* **31**, 061506 (2013).

CHAPTER 3 is a reprint of an article published in the *Journal of Applied Physics*, **113**, 194303 (2013), DOI: 10.1063/1.4804960, by Sweet, W.J., Jur, J.S., Parsons, G.N.

**CHAPTER 3. Bi-layer Al₂O₃/ZnO Atomic Layer Deposition for Controllable
Conductive Coatings on Polypropylene Nonwoven Fiber Mats**

William J. Sweet III,¹ Jesse S. Jur,² and Gregory N. Parsons^{1*}

¹*Department of Chemical and Biomolecular Engineering, North Carolina State University,
Raleigh North Carolina 27695, United States*

²*Department of Textile Engineering, Chemistry and Science, North Carolina State
University, Raleigh North Carolina 27695, United States*

3.1 Abstract

Electrically conductive zinc oxide coatings are applied to polypropylene nonwoven fiber mats by atomic layer deposition (ALD) at 50-155°C. A low temperature (50°C) aluminum oxide ALD base layer on the polypropylene limits diffusion of diethyl zinc into the polypropylene, resulting in ZnO layers with properties similar to those on planar silicon. Effective conductivity of 63 S/cm is achieved for ZnO on Al₂O₃ coated polypropylene fibers, and the fibers remain conductive for months after coating. Without the Al₂O₃ precoating, the effective conductivity was much smaller, consistent with precursor diffusion into the polymer and sub-surface ZnO nucleation. Mechanical robustness tests showed that conductive samples bent around a 6 mm radius maintained up to 40% of the pre-bending conductivity. Links between electrical conductivity and mechanical performance will help inform materials choice for flexible and porous electronics including textile-based sensors and antennas.

3.2 Introduction

Conductive fibers and mat materials are currently used in applications such as chemical and photo sensors, energy conversion and storage, biomedical, electromagnetic shielding, and communication devices.¹⁻⁵ For these uses, conductive fiber materials are made by directly spinning or extruding conductive fibrous materials, post-spinning treatment of conductive fiber precursors, mixing conductive additives into the source polymer, or by adding a conductive coating to the fibers.^{2,3,5-7} A large amount of conductive filler is often required to achieve good conductivity for polymer-particle mixtures, complicating production and impacting the mechanical performance of the polymer.^{6,8} While spinning conductive polymer fibers by techniques such as electrospinning are gaining interest, coating fibers with conductive material can be done by many techniques utilizing any fiber types and production methods. Although coated fibers can be highly conductive, bulky coatings are stiff and can add significant weight, and coating conformality is often limited.²

For this work we explored atomic layer deposition (ALD) to coat nonwoven polypropylene fiber mats with nanoscale zinc oxide to produce conductive coatings. Atomic layer deposition applies vapor phase co-reactants independently (either spatially or temporally) utilizing alternating self-limiting reactant chemistries to deposit a film coating layer by layer. The self-limiting process allows excellent conformality on three-dimensional non-planar substrate surfaces. Nonwoven mats consist of randomly oriented fibers of synthetic or natural polymers and present an interesting example of a 3D structure amenable to surface modification by ALD. Nonwovens can be made from many polymers, and offer

control of fiber diameter and geometry, as well as web density, and can be produced at high volume and low cost, all of which make nonwovens a versatile substrate choice.⁸ Nonwoven production methods include meltblown, spunbond, and electrospinning techniques, and the mats are often bound together by physical, chemical, or mechanical means.⁸ Polypropylene, for example, is a widely used nonwoven which offers a chemically inert substrate that could be used for sensing applications that involve corrosive species. We conjectured that a thin conductive film by ALD could add conductivity to nonwoven polypropylene without adding appreciable weight or significantly impacting mechanical flexibility, and therefore the ALD process could be advantageous over other known techniques to produce conductive fibers and fabrics. We chose zinc oxide as a coating material because it is a popular semi-transparent conductor that offers, for example, chemical and light sensitivity for sensor applications, and can be easily doped to increase conductivity.⁹ Also, zinc oxide can be readily deposited by ALD at temperatures compatible with polymers such as polypropylene, which can melt at temperatures as low as 165°C.⁸

The surface reactions during initial stages of atomic layer deposition on polymers depend strongly on the structure of the polymer substrate and the vapor phase reactants. Species can diffuse into polymers, and then react with functional groups in the polymer backbone, contaminates, or with un-removed precursor species; the extent of sub-surface growth depends on the detailed process and process conditions, especially temperature. Many studies have investigated Al₂O₃ deposition using trimethyl aluminum (TMA) and H₂O on inert polymers including polyethylene,¹⁰ polytetrafluoroethylene,¹¹ and

polypropylene.^{10,12-14} At low process temperature ($\sim 60^\circ\text{C}$) the TMA and water diffusion are limited, promoting a conformal coating primarily on the outer polymer surface.^{13,14}

Problems with sub-surface diffusion and reaction can be avoided by careful process design. For example, by applying a thin blocking layer under conditions that minimizes sub-surface reaction, a second layer can be added with a desired functionality. In our case, we coat the fibers with a thin Al_2O_3 base layer at low temperature, followed by a conductive ZnO layer at higher temperature. The entire process proceeds below the maximum process temperature for the polymer, 165°C .⁸ We then examine the resulting fiber mat conductivity as a function of ZnO ALD conditions and show initial results of how the fiber mat conductivity is affected by mechanical manipulation.

3.3 Experimental

Polypropylene (C_3H_6)_n is a non-polar, semi-crystalline thermoplastic that has high chemical resistance to many common solvents and acids, and has low water absorption.^{8,13} Polypropylene has a glass transition temperature of -10°C , and melts at $165\text{-}176^\circ\text{C}$.^{8,13} The nonwoven polypropylene used for this work was prepared on a pilot-scale melt-blowing line at the Nonwovens Cooperative Research Center at North Carolina State University. The raw polypropylene was from Sunoco Chemicals Polymer Division (product CP360H, $M_n=58.5$ kDa). The finished mat had a basis weight of roughly 40 g/m^2 and was used as received. The mat was approximately 0.3 mm thick, with fiber diameters between $1\text{-}5\ \mu\text{m}$, and a specific surface area of $1.6\text{ m}^2/\text{g}$ determined by Brunauer-Emmett-Teller (BET) surface analysis. The net effective surface area per unit sample size is then estimated as $(40\text{ g/m}^2) \times (1.6\text{ m}^2/\text{g}) =$

64, meaning that the surface area available to be coated, is 64 times larger than the lateral surface of a sample.

Polypropylene samples were cut from the melt-blown nonwoven, into 2.0 cm × 3.0 cm rectangles for deposition, giving them a lateral surface area of 6.0 cm² per sample and a net effective surface area of 384 cm² per sample (6.0 cm² × 64 = 384 cm²). Polypropylene samples were weighed using an analytical scale, before and after ALD. Three pieces of silicon were also coated simultaneously in each run; two 1.0 cm² pieces with native oxide present were used for ellipsometry measurements. A 2.5 cm × 2.5 cm piece of silicon with 150 nm thermal oxide was also coated and was used for the 4-point probe conductivity measurements. Because the resistivity of the oxide is very large, greater than the 10⁷ Ω/square sensitivity limit of the four point probe, the measured conductivity corresponds to that of the deposited film.

After measuring the starting mass of the fiber substrates, pieces to be coated were placed in a wire mesh sample holder along with the silicon, and then placed in the deposition chamber. The reactor was sealed and evacuated, and the temperature was allowed to equilibrate for at least 20 minutes. Deposition was performed in a custom built 1.5 inch diameter hot walled flow tube reactor described in previous work.¹⁴ Nitrogen gas (National Welders, 99.999% pure) was filter dried (Aeronex Gatekeeper) and used as a carrier gas with an approximately 150 sccm (standard cubic centimeters per minute) flow rate. The system was pumped by a rotary mechanical pump with a background pressure of 1×10⁻³ Torr and a leak rate of <1×10⁻³ Torr/min. Deposition was performed at a pressure of ~1.0 Torr as measured by a convectron gauge (Granville-Philips). Trimethyl aluminum (98% purity,

STREM Chemicals), diethyl zinc (95% purity, STREM Chemicals) and water (UV-deionized) were used as reactants. A typical precursor dose for Al₂O₃ was TMA/N₂/H₂O/N₂ = 1.2/30/1.5/30s and for ZnO was DEZ/N₂/H₂O/N₂ = 2/40/2/40s. A metering valve was used to regulate precursor dose; pressure reached $\Delta P \approx 0.10$ Torr for TMA, $\Delta P \approx 0.10$ Torr for DEZ, and $\Delta P \approx 0.20$ Torr for water during a dose. Depositions were performed between 50°C and 155°C. For bilayers of ZnO on Al₂O₃, the temperature of the reactor was slowly raised after Al₂O₃ deposition (at $\sim 3^\circ\text{C min}^{-1}$) to the temperature for ZnO deposition, and was then allowed to equilibrate for at least 20 additional minutes. Most ZnO on Al₂O₃ bilayer coatings were performed without breaking vacuum, unless otherwise noted.

Recently, Jur *et al.*² demonstrated a method to evaluate conductivity of a coated nonwoven, and that same method was used here. Specifically, we used a 4 electrode analyzer with a Keithley 2400 Sourcemeter, applying a known current through outer electrodes and measuring voltage between the inner pair. Samples were tested between eight and ten times each using a compression loading of between 10 and 2000 grams. The amount of ZnO present on the fibers is determined from the mass change upon coating, and we used a bulk density of 5.71 g/cm³ to estimate the effective conductivity for ZnO.² This analysis assumes linear electric field along the sample between the outer electrode pair and a uniform distribution of conductive material along the fiber mat. Each sample was 3.0 × 2.0 cm in size to maintain sample-to-sample consistency. We also measured resistivity of films deposited on oxidized silicon wafers using a 4-point probe (Jandel multi-height probe with RM3-AR test unit), a minimum of four times per sample. Film thickness on these samples was also measured using spectroscopic ellipsometry (Alpha S.E., J.A. Woollam).

Cross-sectional transmission electron microscopy (TEM) was used to evaluate the growth of zinc oxide ALD on polypropylene and aluminum oxide coated polypropylene. The samples were embedded in a low viscosity epoxy resin (Ladd Research Industries) and allowed to cure overnight at room temperature. The blocks were then cut to a thickness of 70nm using a Lecia Ultracut diamond knife microtome. The samples were then floated on 300 mesh grids, and allowed to dry. The TEM images were obtained using a Hitachi HF-2000 system using a cold field emission electron source, with an accelerating voltage of 200 kV. Due to differences in mechanical properties of the fiber, thin film coating, and epoxy, sheering can occur during the microtome process, resulting in void formation and film cracking.

Quartz crystal microbalance is very useful to measure mass gain during ALD on polymer films,^{10,13,14} but is not easily amenable for use with fibrous media. Therefore in this work the mass gain is directly determined on the nonwoven polypropylene fibers by comparing mass before and after ALD. The mass gain was measured using a Fisher Scientific Accu-124 Series analytical lab scale with a sensitivity limit of ± 0.1 mg. Figure 1 shows the percent mass gain for Al_2O_3 on polypropylene fibers as a function of ALD cycles. Based on previous analysis, we expect the Al_2O_3 film thickness to scale approximately linearly with number of ALD cycles when the deposition is performed at temperatures $\leq 60^\circ\text{C}$. The trend is approximately linear with number of cycles, consistent with well-defined ALD on this surface at low temperature.

The Al_2O_3 on polypropylene test series shown in Figure 3.1 was used to estimate aluminum oxide mass for samples deposited without vacuum break, for example, a 200 cycle

Al₂O₃ ALD coating produces a 9% increase in weight over the uncoated polypropylene mat. Percent mass gain was determined by using $MG\% = 100(M_{PAZ} - M_{PA})/M_P$ where M_P is the initial mass of the polypropylene, M_{PA} is mass of the fiber mat with only Al₂O₃ coating, and M_{PAZ} is the mass of the polypropylene fiber mat after coating with Al₂O₃ and ZnO. For consistency, samples were weighed immediately (within 5 minutes) after being removed from the reactor. Some samples were re-weighed after long exposures to lab air, and no appreciable change was observed. For a typical polypropylene fiber sample $M_P = 24-26$ mg, and after coating with 200 cycles of Al₂O₃ at 50°C, $M_{PA} = 27-29$ mg. After 100 cycles of ZnO, M_{PAZ} increased to ~ 30-32 mg. Using this analysis, we can directly determine the amount of ZnO deposited on polypropylene fibers, with and without Al₂O₃ pretreatment. To fabricate samples with ZnO/Al₂O₃ bilayers, the substrates were coated sequentially without removing samples from the reactor. To test this analysis, some of the samples were removed from the reactor and weighed after Al₂O₃ deposition, then replaced for ZnO deposition. The mass of these samples was indistinguishable from similar samples produced with continuous deposition.

The change in conductivity upon mechanical bending was measured for some of the samples by bending them around cylinders with diameters between 9.0 and 1.2 cm. To secure the fiber sample to the cylinder, the sample was placed flat onto a piece of paper that was attached by adhesive tape to the cylinder. When the cylinder was rolled over the sample, the sample was held between the paper and the cylinder, bending the sample along the cylinder circumference. The sample was then unrolled and the conductivity was re-measured. The process started by rolling over the largest cylinder followed by progressively smaller

cylinders. Therefore, any change or mechanical damage imparted during one rolling test remained present during the subsequent tests of that sample.

3.4 Results and Discussion

3.4.1 Mass Uptake Analysis of Zinc Oxide on Polypropylene Fibers

3.4.1.1 Influence of Deposition Temperature

We deposited zinc oxide on planar silicon and on polypropylene nonwoven fibers at temperatures between 50°C and 155°C. We also studied ZnO deposited on silicon and on polypropylene pretreated with 200 cycles of TMA/H₂O at 50°C. These four sample types are referred to as: ZnO/Si, ZnO/PP, ZnO/Al₂O₃/Si and ZnO/Al₂O₃/PP. Figure 3.2(a) shows the fractional mass gain, defined using the equation given above, versus deposition temperature for ZnO ALD on untreated polypropylene fiber mats, and mats pretreated with 200 cycles of Al₂O₃ ALD at 50°C. The ZnO mass increased significantly with increasing deposition temperature on the untreated fibers, but the mass change was smaller and nearly independent of temperature for samples with the Al₂O₃ pretreatment. Figure 3.2(b) shows the thickness of the ZnO film on silicon and on Al₂O₃/Si as measured by ellipsometry. Both sample sets show the same ZnO thickness over the temperature range studied. The decrease in growth rate at T<100°C is consistent with the expected temperature window for ZnO ALD,¹⁵ where lower temperatures produces less deposition per cycle, resulting in thinner films. The different trend in mass uptake for the PP and Al₂O₃/PP is consistent with diethylzinc diffusion into the untreated PP, whereas the low temperature Al₂O₃ pretreatment creates a

barrier to prevent diethylzinc diffusion. Other results regarding precursor diffusion are presented and discussed below.

3.4.1.2 Influence of Al₂O₃ Base Layer Thickness on ZnO Deposition Behavior

We also explored the impact of the Al₂O₃ layer thickness on growth and nucleation of ZnO ALD on PP. Figure 3.3 shows the percent mass gain after ZnO ALD (at 155°C) on polypropylene fibers with 0, 50, 100 or 200 Al₂O₃ ALD cycles (at 50°C). If we consider first the growth on the untreated polypropylene, we find that initially there is little growth, then after ~ 50 cycles the mass increases rapidly followed by a linear increase. This is similar to the trend previously described for Al₂O₃ ALD on polypropylene.¹² The other traces in Figure 3.3 show that adding a low temperature alumina coating before ZnO ALD reduces the initial ZnO mass uptake, but does not affect the linear rate of mass uptake observed after coalescence. Polypropylene first coated with 200 TMA/H₂O cycles at 50°C allows linear ZnO growth after only about 5-10 DEZ/H₂O cycles at 155°C. This suggests that 200 cycles of Al₂O₃ ALD produces a film sufficiently thick to prevent DEZ from penetrating the polypropylene fibers at 155°C.

Transmission electron microscopy (TEM) was used to examine ZnO deposition on polypropylene fibers with and without Al₂O₃ pretreatment. Figure 3.4(a) shows a TEM cross sectional image of polypropylene fiber coated with 300 cycles of ZnO ALD at 110°C. Figure 3.4(b) shows a polypropylene fiber first coated with 150 cycles of Al₂O₃ at 50°C followed by 300 cycles of ZnO ALD at 110°C. The higher contrast regions in the TEM images correspond to deposited ZnO. After ZnO ALD on untreated polypropylene, Figure 3.4(a)

shows the ZnO extending more than 100 nm into the fiber, with subsurface nucleation and granule growth towards the fiber edge. This agrees with the mechanism proposed by Wilson *et al.*, for Al₂O₃ ALD on polyethylene¹⁰ and TEM images shown by Jur *et al.* after Al₂O₃ ALD at 90°C on polypropylene.¹³ Figure 3.4(b) shows a uniform bilayer ZnO/Al₂O₃ coating with abrupt Al₂O₃/polypropylene and ZnO/Al₂O₃ interfaces. The abrupt Al₂O₃/PP interface is also consistent with uniform Al₂O₃ with minimal sub-surface growth on PP when substrate temperature was kept below 90°C.¹³ The Al₂O₃ layer in Figure 3.4(b) appears to be ~23 nm thick, which is thicker than the 15 nm expected for Al₂O₃ growth on silicon under these conditions. Because the fibers are aligned randomly in the sample, i.e. not perpendicular with the microtome cut, the apparent thickness measured in TEM can be larger than the physical film thickness.

3.4.1.3 Impact of Diethyl Zinc Dose Time on Mass Gain of Fibers

During ALD, diffusion of precursors into and through complex geometries can lead to precursor or reactant depletion, problems with reactant purging, and other effects that influence film growth.¹⁶ Therefore, it is important to examine the role of reactant dose time on ALD film growth on polymers. The impact of DEZ dose time at 155°C on the mass gain of 200 ZnO ALD cycles on untreated and Al₂O₃ pre-treated polypropylene fibers is shown in Figure 3.5(a). For these studies the water exposure time was 2 seconds, and the purge times (after DEZ and after H₂O exposure) were both 40 seconds. After 200 DEZ/H₂O cycles on uncoated polypropylene, the percent mass gain is very large (>100% for 1 second dose time) and continues to increase even up to 3 seconds dose times. The mass increase on the Al₂O₃

pre-treated fibers is substantially less. For the alumina treated fibers, mass uptake increases with dose time from 0 to 0.2 seconds, followed by saturation. Figure 3.5(b) shows similar trend for ZnO film thickness on silicon or Al₂O₃ treated silicon. Based on this analysis, we use a DEZ dose time of 2.0 s per cycle to achieve saturated growth on all the substrates studied here. The data shown in Figures 3.2-3.5 are all consistent with DEZ diffusion into the polypropylene fibers when the fibers are not pretreated with a sufficient alumina encapsulation layer.

We find that the ZnO ALD on the untreated and pretreated polypropylene changes the color of the polypropylene from white to a brown color, and it is especially visible on the untreated substrates after a large number of cycles (i.e. >300 cycles at 155°C). By peeling the nonwoven layers apart into multiple layers, as described in Hyde *et al.*¹² we visually confirm that the ZnO related color change penetrates uniformly throughout the nonwoven mat.

3.4.2 Conductivity of Zinc Oxide on Polypropylene Fibers

3.4.2.1 Influence of Deposition Temperature

Previous reports show ALD zinc oxide changes crystal orientation as deposition temperature changes, and this has been shown to influence the resulting zinc oxide conductivity.^{15,17} Figure 3.6 shows the conductivity of ZnO on silicon and alumina-coated silicon, as well as the effective conductivity² of ZnO deposited on untreated and alumina pretreated polypropylene nonwoven fiber mats, as a function of ZnO deposition temperature. The thermal oxidized silicon and polypropylene substrates are both highly insulating, so the measured conductivity was due to current flow through the ZnO coating. A highly

conductive substrate would dominate the current flow, not allowing the conductivity of the film to be characterized. For the effective conductivity analysis, the density of ZnO is assumed to be the bulk density value: $\rho = 5.71 \text{ g/cm}^3$. The reported effective conductivity is related linearly to the density; if the actual density differs from the bulk value by $\pm 10\%$, it will produce a $\pm 10\%$ error in effective conductivity, which is within our uncertainty level. Similar to previous reports, the conductivity of zinc oxide increases with deposition temperature. On the oxidized silicon substrate the ZnO conductivity reaches 160 S/cm at 155°C, consistent with previous reports of ALD ZnO formed under similar conditions.¹⁷ The effective conductivity of the ZnO on untreated polypropylene is very small, consistent with subsurface ZnO mass that does not contribute to conductivity. The effective conductivity of the ZnO on the alumina pretreated polypropylene is within a factor of ~2-3 of that on planar substrates.

3.4.2.2 Influence of Precursor Dose Influence of Deposition Temperature

We also measured conductivity versus DEZ dose time for ZnO deposited on silicon and polypropylene, with and without the alumina pretreatment. Results are presented in Figure 3.7. Analogous to the mass uptake saturation data in Figure 3.5, it takes longer exposure times to saturate the conductivity for films deposited on untreated polypropylene compared to silicon. For short exposure times, less mass is deposited per cycle so more cycles are needed to achieve film coalescence. Film coalescence is further impeded on the polypropylene because of subsurface precursor diffusion and particle growth. Any isolated ZnO particles formed below the surface contribute to the total mass change, but do not

increase current flow, leading to the smaller effective conductivity on polypropylene, as shown in Figure 3.7(a). The alumina pretreatment reduces the exposure time needed for conductivity saturation on both silicon and polypropylene. The Al_2O_3 layer promotes ZnO film coalescence and continuous (conductive) film growth.

For high exposures, the conductivity saturates at ~ 100 S/cm for ZnO on silicon, ~ 150 S/cm for ZnO on alumina-coated silicon, < 0.1 S/cm on uncoated polypropylene and ~ 40 S/cm for ZnO on alumina-coated polypropylene fibers. Again, the effective conductivity on the Al_2O_3 /polypropylene is a factor of ~ 3 less than on the Al_2O_3 /Si substrates. The increased resistance through the fiber matrix compared to the continuous film is ascribed to fiber-fiber resistance effects. The random arrangement of the coated fibers in the nonwoven matrix will lead to current flow between touching fibers, introducing an additional resistance that is not present in the planar thin film on silicon. The much larger surface area on the fibers may also introduce additional surface scattering effects which will also decrease the apparent conductivity.

3.4.2.3 Influence of the Number of Zinc Oxide Cycles

Figure 3.8 shows the effective conductivity of the ZnO plotted versus number of ZnO ALD cycles for coatings on (a) PP and Al_2O_3 /PP, and (b) Si and Al_2O_3 /Si substrates. The ZnO on the Al_2O_3 /PP fibers initially increases then stabilizes at ~ 55 S/cm after 200 ZnO cycles, consistent with nuclei coalescence followed by uniform film growth. For ZnO on untreated PP fibers, the effective conductivity continues to increase even after 700 cycles and its magnitude remains much less (~ 2 S/cm) than on the pretreated polymer. For ZnO on

silicon, the conductivity also increases then saturates at ~ 150 S/cm. The values are generally larger when the silicon substrate is pretreated with Al_2O_3 . Similar to the results shown in Figures 3.6 and 3.7, the ZnO conductivity on alumina pretreated polypropylene is close (within a factor of ~ 2 -3) to that measured on the silicon substrates.

The results in Figure 3.8 show a primary result of this work. That is, that careful preparation of nonwoven polymer fiber mats, in this case by pre-coating the fibers with Al_2O_3 at low temperature, allows conductive materials to be readily coated onto the fibers, and the material conductivity on the fiber mats can be similar to that achieved on planar substrates.

For the ZnO on the $\text{Al}_2\text{O}_3/\text{Si}$ substrate, one data point shows higher conductivity for 200 ZnO ALD cycles, followed by a decrease then saturation at ~ 150 S/cm for thicker ZnO layers. This trend, along with the observed higher conductivity for ZnO on alumina versus ZnO on SiO_2 , is consistent with surface band-bending at the ZnO/ Al_2O_3 interface. Surface OH generally leads to surface depletion layers on hydroxylated ZnO, but making contact with ALD Al_2O_3 can decrease interface charge and reduce the depletion layer potential.^{18,19} The decrease in surface charge depletion will tend to increase the measured lateral conductivity. Due to the influence of the underlying Al_2O_3 on the near-surface ZnO, an increase in conductivity is expected for samples where the ZnO film thickness is less than the accumulation layer thickness, which is ~ 10 -30 nm for ZnO films deposited at low temperature.^{2,9,19} This is consistent with the peak in conductivity near 200 ZnO cycles for the ZnO on Al_2O_3 coated silicon in Figure 3.8(b). Previous studies of in-situ conductance during ZnO ALD show that conductance oscillates with the reactant exposure.⁹ This was ascribed to

stable bulk conductivity combined with a modulated surface conductivity, where surface conductivity oscillations resulted from changes in surface band bending and charge for the different surface terminations present during the ALD sequence.

The conductivity of very thin films or narrow features is often less than the bulk material conductivity because of charge scattering by surface roughness and grain boundaries.²⁰ Results in Figure 3.8(a) shows that for ZnO deposited at 155°C, the conductivity of ZnO/Al₂O₃/PP decreases for thicknesses less than 200 ZnO cycles (corresponding to ~360 Å on Si), which is on the order of the ~20 nm mean free path of electrons in ZnO measured using time-resolved optical absorption.²¹ Figure 3.8(b) shows the same trend for ZnO on Si where 300 - 400 ZnO cycles (540-720 Å) is required to reach full conductivity. Figure 3.9 compares conductivity of ZnO/Al₂O₃/PP for ZnO deposited at 155°C and 110°C. The thickness required to saturate the conductivity is nearly the same at the lower temperature. The smaller conductivity for the data set deposited at 110°C, agrees with the temperature dependence of ZnO conductivity shown in Figure 3.6.

3.4.3 The Influence of Mechanical Bending on Conductivity

To study the mechanical flexibility of coated fibrous substrates, we measured the effective conductivity of fiber samples before and after bending around cylinders of various diameters. The samples were ZnO/Al₂O₃ bilayers on polypropylene nonwovens with various thicknesses of ALD ZnO. Like the samples discussed above, the Al₂O₃ was deposited at 50°C. The ZnO deposition was done at 155 °C. Figure 3.10(a) shows an image of a sample being bent around a cylinder with 1.13 cm radius, and Figure 3.10(b) shows a schematic of

the sample bending. For this experiment, we first measured the starting fiber mat conductivity (lying flat in our probe apparatus). We then rolled and unrolled the fiber mat once under the cylinder and measured the effective conductivity again (with the sample lying flat). This was repeated using cylinders with progressively smaller bending radii, using the same sample again. Therefore, any damage incurred during one rolling step remained present during subsequent testing of that sample. Figure 3.11 shows the measured conductivity plotted versus inverse bending radius, where the extent of bending increases along positive x-axis. For each ZnO thickness, two or more samples were measured, and the points in Figure 3.11 represent average values with error bars corresponding to one standard deviation. Conductivity decreased upon bending, consistent with a relatively brittle $\text{Al}_2\text{O}_3/\text{ZnO}$ coating on the polymer fiber. We note that all samples tested maintained a measureable conductivity even after bending at the smallest radius (6 mm). Inorganic coatings on polymers, including ALD ZnO on polytetrafluoroethylene, have been shown to enhance the polymer tensile strength.¹¹ Once cracks begin to form, they readily spread across the plane of the film. Therefore, it is reasonable to expect the strain force applied during bending to decrease the conductivity as is shown in Figure 3.11. One advantage for conductive coatings on fibers relative to coating on planar films is that while cracking does occur on individual fibers, the large number of conductive pathways mitigates the problems associated with cracking, i.e., large conductivity loss requires many cracks on fibers, whereas one crack on a film can significantly degrade charge flow. Overall, the data shows that good conductive coatings can be produced using several different ALD materials on polymer

fibers, and the results provide a starting reference point to characterize conductivity of other coatings under mechanical stress.

3.5 Conclusions

The results shown here demonstrate that a low temperature (50°C) Al₂O₃ ALD coating applied to polypropylene prior to ZnO deposition can reduce the temperature dependent DEZ precursor infiltration and reduce the precursor dose required for saturated ZnO ALD film growth. This allowed for higher density ZnO to be deposited on top of the Al₂O₃ coated polypropylene. By depositing ZnO at temperatures above 125°C, effective conductivity as high as 63 S/cm was achieved on fibers, and > 200 S/cm on silicon. ZnO on alumina had higher conductivity than ZnO deposited on SiO₂, and this is ascribed to charge accumulation and surface band bending effects at the ZnO/Al₂O₃ interface. The ZnO/Al₂O₃/PP samples remained conductive for long periods (up to 16 months to date) after deposition.

The conductivity of the ZnO on polypropylene decreased systematically upon mechanical bending. Even after bending around a 6 mm radius, the samples maintained between 20-40% of their original conductivity. The aluminum oxide pretreatment generally improved the conductivity of ZnO coatings on polypropylene, but the relatively thick Al₂O₃ layer also increased the fiber brittleness. While this work establishes that ZnO conductivity on polymer fibers can be similar to that on planar substrates, further work using other more flexible encapsulation coatings and other conductive layers could lead to highly conductive fiber coatings that are robust under mechanical stress.

3.6 Acknowledgments

We acknowledge the North Carolina State University Nonwovens Cooperative Research Center (NCRC) Project 09-118 for support for W.J.S.

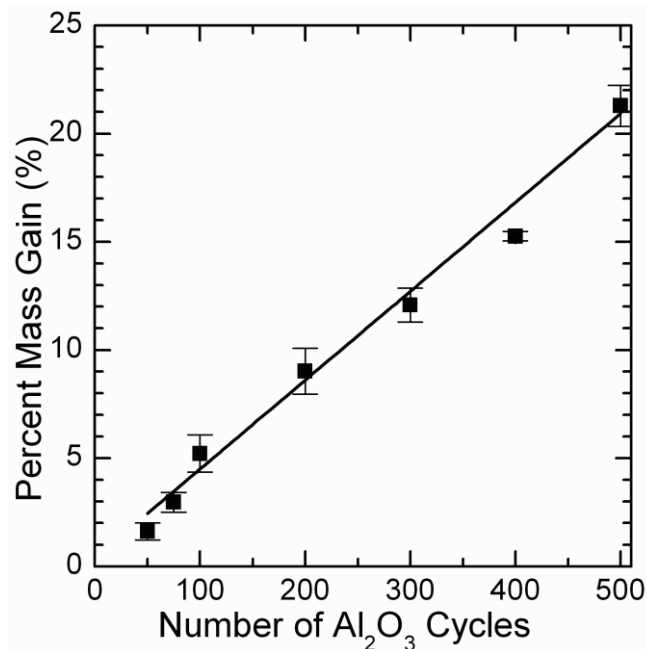


Figure 3.1. Percent mass gain for Al₂O₃ ALD deposition on polypropylene nonwoven fiber mats (at 50°C) as a function of Al₂O₃ cycle number. Mass gain was measurable at 50 Al₂O₃ cycles, and increased as more cycles were applied. This data provides a reference mass to determine the mass gain after ZnO ALD onto Al₂O₃-coated fibers. A linear trend is fitted to the data with an R-squared value of 0.99; it is noted that non-linear growth maybe occurring at low cycle numbers, although this was not investigated further due to sensitivity limitations of the measurement technique.

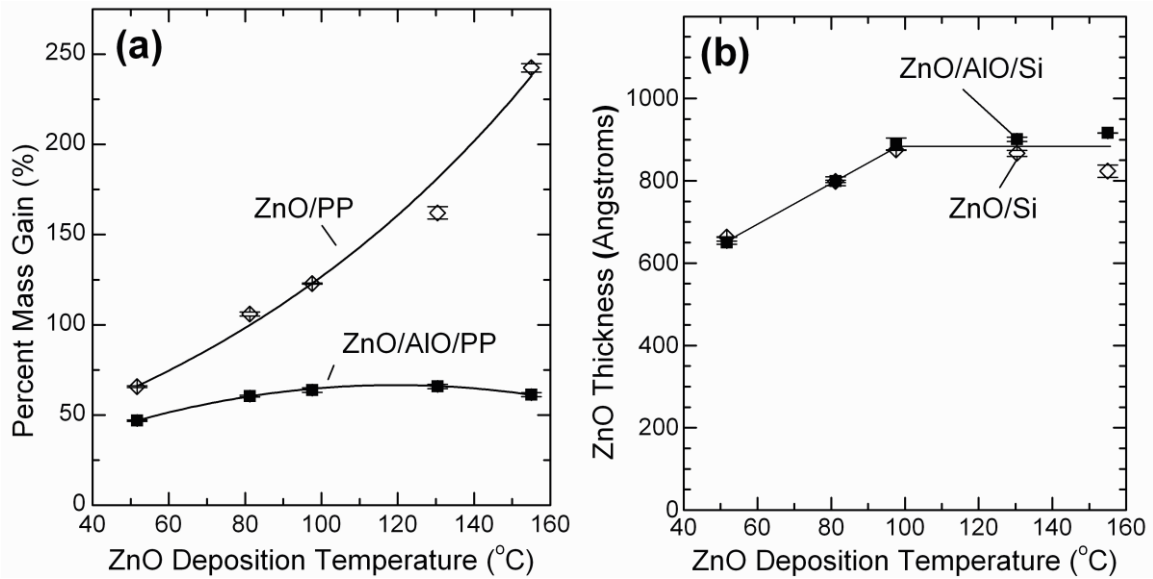


Figure 3.2. (a) The percent mass gain of 500 ZnO ALD cycles (at 155°C) is plotted as a function of deposition temperature for: 1) deposition on virgin polypropylene (\diamond); 2) deposition on polypropylene first coated with 200 Al_2O_3 ALD cycles at 50°C (\blacksquare). The samples are labeled ZnO/PP and ZnO/AlO/PP respectively; (b) The corresponding film thickness for ZnO growth on silicon corresponding to the deposition on polypropylene fibers from Fig. 3.2(a), and are signified by labels ZnO/Si or ZnO/AlO/Si.

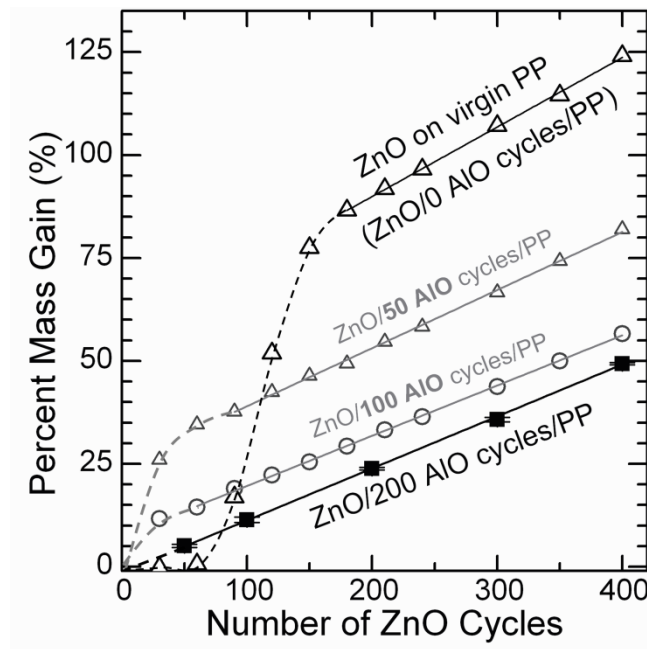


Figure 3.3. ZnO mass gain (%) plotted as a function of ZnO cycle number for ZnO ALD on 1) virgin polypropylene (Δ); 2) polypropylene coated with 50 (Δ), 100 (\circ), and 200 (\blacksquare) Al_2O_3 ALD cycles (at 50°C) prior to ZnO deposition. By first coating the polypropylene with Al_2O_3 , the ZnO nucleates more quickly on the Al_2O_3 coating than on virgin polypropylene, reducing the cycles before linear mass gain is achieved.

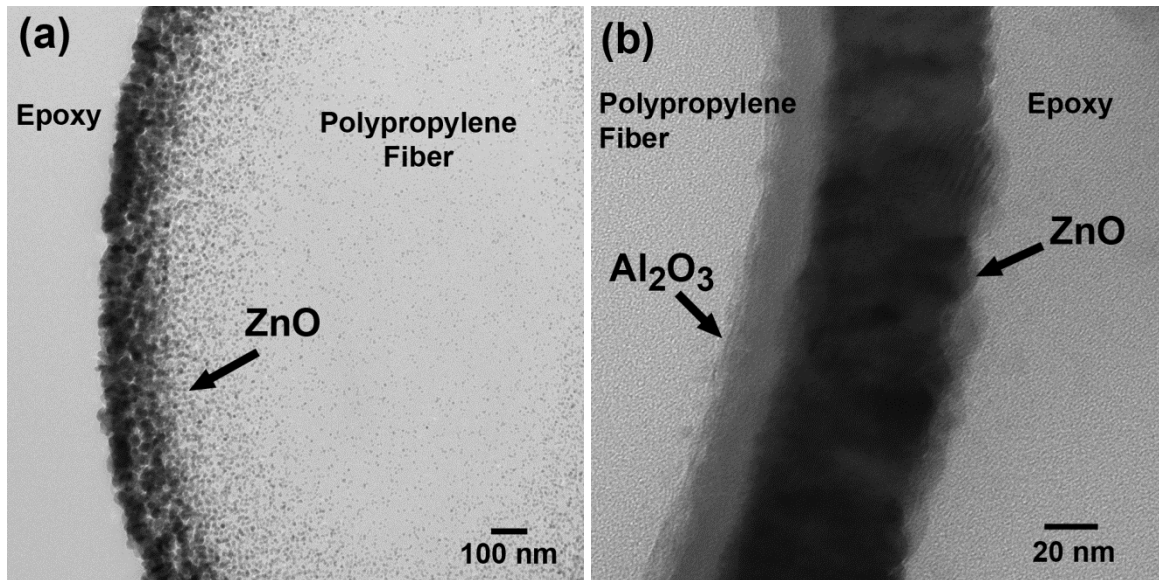


Figure 3.4. TEM images of polypropylene after 300 cycles of ZnO ALD at 110°C for (a) untreated polypropylene and (b) polypropylene pre-treated with 150 cycles of Al₂O₃ ALD at 50°C. The untreated polypropylene fiber shows small granular formation towards the center, growing larger towards the edge of the fiber. For the pre-treated fiber (b), two distinct layers can be seen, the Al₂O₃ pretreatment and the ZnO coating.

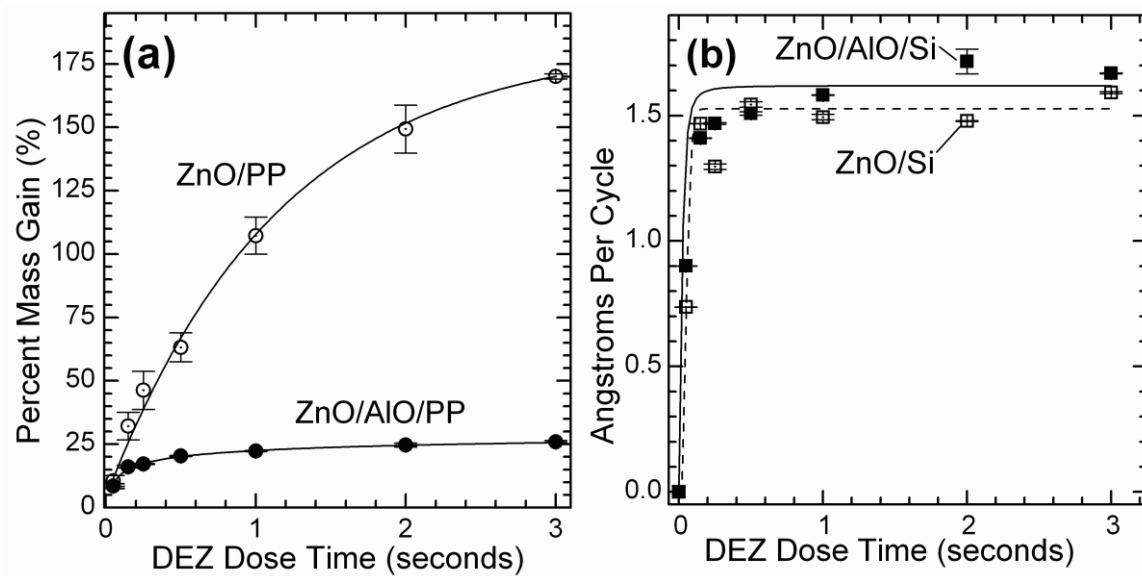


Figure 3.5. (a) Percent mass gain of ZnO ALD at 155°C is plotted as a function of DEZ dose time for 1) 200 ZnO cycles on untreated polypropylene (ZnO/PP ○); and 2) 200 ZnO cycles on polypropylene pre-coated with 200 Al₂O₃ cycles at 50°C (ZnO/AlO/PP ●). (b) Film growth on simultaneously deposited silicon substrates shows ZnO deposition on bare Si, and Al₂O₃ coated Si, is achieved quickly. Similar to the silicon substrates, Al₂O₃ coated polypropylene shows saturation is achieved with short precursor doses.

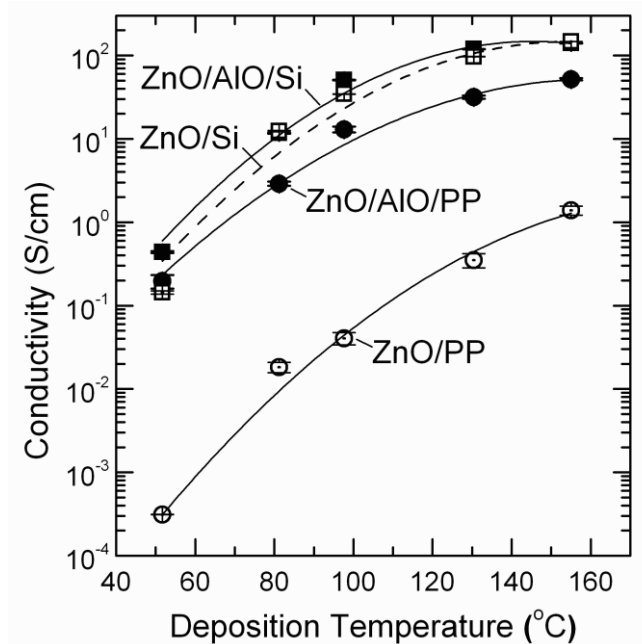


Figure 3.6. Conductivity of polypropylene after a 300 cycle ZnO ALD coating deposited at various temperatures on 1) virgin polypropylene (○), and 2) polypropylene with a 200 cycle Al₂O₃ ALD barrier layer deposited at 50°C (●), and corresponding silicon samples (□, ■) respectively. The Al₂O₃ barrier results in ZnO with higher conductivity; presumably because higher quality ZnO is deposited on the Al₂O₃ barrier layer. Fig. 3.4 shows higher density ZnO is deposited on top of the Al₂O₃ barrier coated polypropylene. Higher temperature ZnO ALD leads to higher conductivity, most likely due to a shift in preferred crystalline orientation of the deposited ZnO.

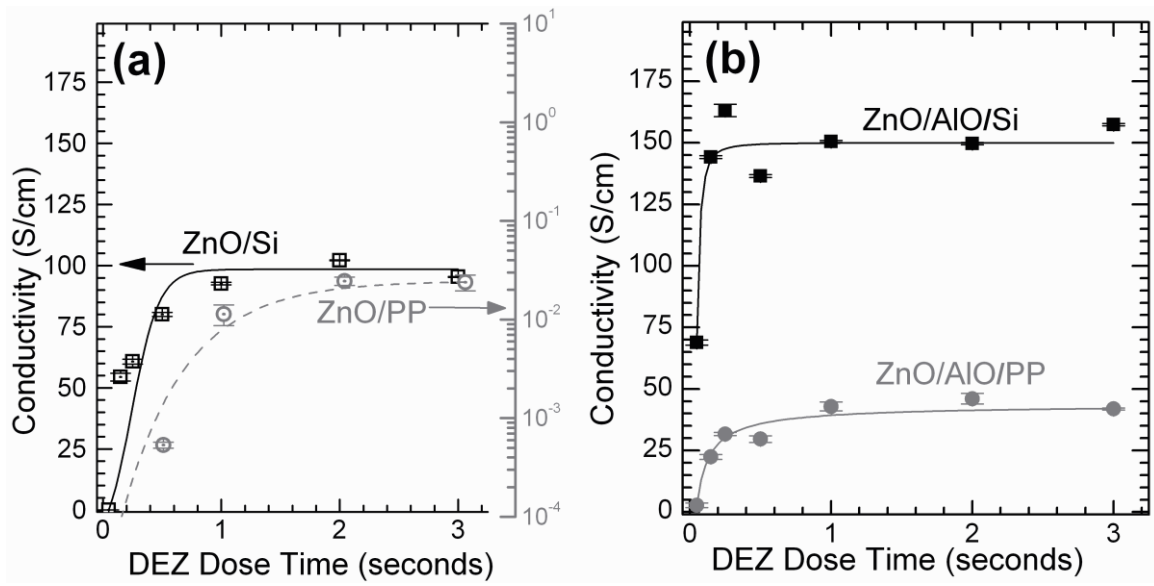


Figure 3.7. (a) Conductivity of ZnO deposited at 155°C on 1) thermal oxide silicon; and 2) virgin polypropylene, as a function of DEZ dose time. The conductivity of ZnO on silicon plateaus with a 1 second dose. Conductivity of ZnO on virgin PP increases with dose times up to 3 seconds. (b) Conductivity of ZnO deposited at 155°C on 1) Al₂O₃ coated thermal oxide silicon; and 2) ZnO on PP first treated with 200 Al₂O₃ cycles at 50°C; both samples show saturation with a 1 second dose. This shows that Al₂O₃ is eliminating some of the non-ideality of ZnO ALD on PP that is shown in (a).

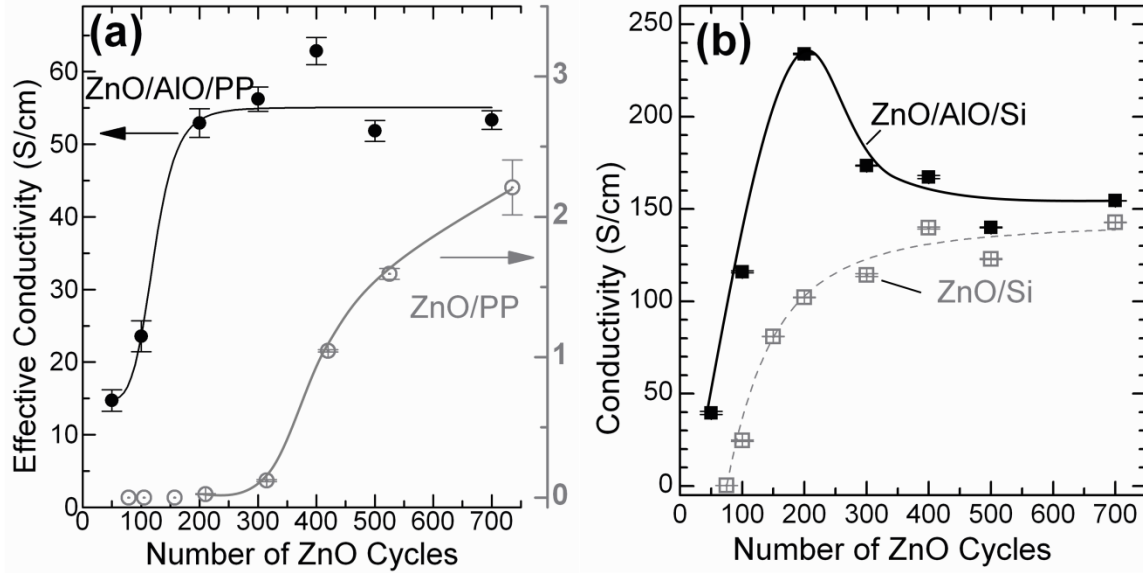


Figure 3.8. (a) Conductivity as a function of ZnO cycle number for 1) ZnO on virgin polypropylene at 155°C (○); and 2) ZnO (at 155°C) on polypropylene first coated with a 200 cycle Al₂O₃ barrier (●). (b) Conductivity as a function of zinc oxide ALD cycles for 1) zinc oxide deposited on a 150 nm thermal oxide silicon (□), and 2) zinc oxide deposited on 200 Al₂O₃ ALD cycles on top of a 150 nm thermal oxide silicon wafer (■). Conductivity of ZnO deposited on Al₂O₃ is noticeably higher than ZnO without the Al₂O₃ layer. A peak exists at 200 ZnO cycles (~360 Å of ZnO), after which conductivity decreases towards a bulk value of ~150 S/cm, in line with the value for ZnO deposited directly on thermal oxide.

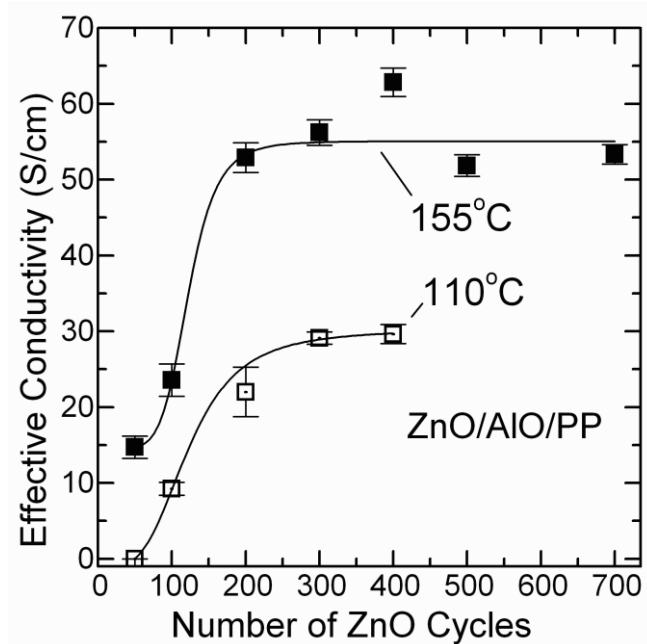


Figure 3.9. Conductivity is plotted as a function of the number of ZnO ALD cycles, for ZnO/AIO/PP samples deposited at two different temperatures. As demonstrated in Fig. 3.6, conductivity is higher for ZnO samples deposited at higher temperatures. This shows that conductivity exhibits similar behavior as a function of ZnO thickness, for two different deposition temperatures. Both samples show low conductivity for < 200 ZnO cycles, and then exhibit “plateau” like behavior for thicker ZnO depositions.

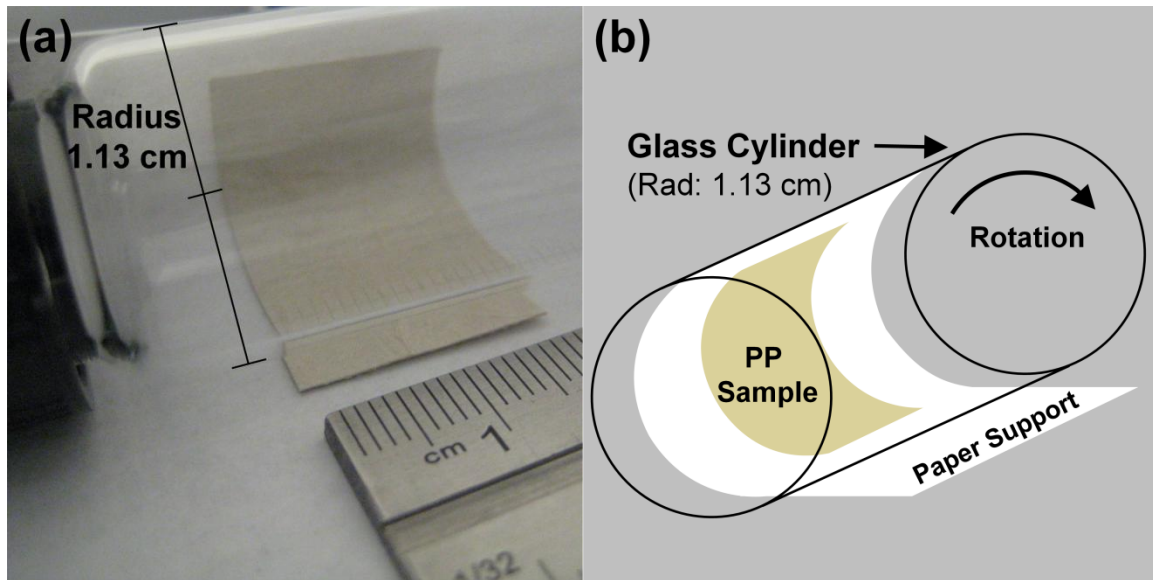


Figure 3.10. (a) A picture and (b) a schematic of a ZnO coated polypropylene sample as it is being bent around a glass cylinder with 1.13cm radius. As the cylinder is rolled over the sample, the sample becomes sandwiched between the cylinder wall and the paper support adhered to the cylinder. This causes the sample to roll up the side as the cylinder is rotated forward; the cylinder is then rolled in reverse, the sample is removed and the conductivity is measured.

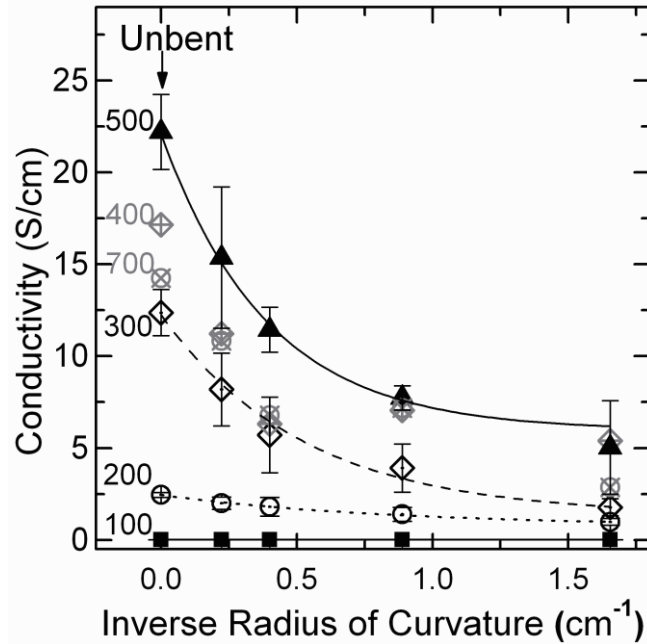


Figure 3.11. The conductivity of ZnO/Al₂O₃ coated polypropylene samples (from Fig. 3.8(a)) as function of the inverse of the diameter of bending. The samples were tested prior to bending (“unbent”), as well as after bending around cylinders of decreasing diameters. Trend lines were fit for samples with 100, 200, 300, and 500 ZnO cycles (deposited at 155°C on 200 cycle Al₂O₃ coated polypropylene). Data is shown for other samples, but was not fit, in order to reduce clutter in the figure. Because the samples sat in ambient for up to 16 months before testing, the unbent conductivity is lower than initially measured from Fig. 3.8(a).

3.7 References

- ¹ Y.Z. Long, M.M. Li, C. Gu, M. Wan, J.L. Duvail, Z. Liu, and Z. Fan, *Prog. Polym. Sci.* **36**, 1415 (2011).
- ² J.S. Jur, W.J. Sweet, C.J. Oldham, and G.N. Parsons, *Adv. Funct. Mater.* **21**, 1993 (2011).
- ³ M.R. Abidian, D.H. Kim, and D.C. Martin, *Adv. Mater.* **18**, 405 (2006).
- ⁴ A. Rida, L. Yang, R. Vyas, and M.M. Tentzeris, *IEEE Antennas Propag. Mag.* **51**, 13 (2009).
- ⁵ H. Okuzaki and M. Ishihara, *Macromol. Rapid Commun.* **24**, 261 (2003).
- ⁶ W. Thongruang, R.J. Spontak, and C.M. Balik, *Polymer* **43**, 2279 (2002).
- ⁷ C. Burger, B.S. Hsiao, and B. Chu, *Annu. Rev. Mater. Res.* **36**, 333 (2006).
- ⁸ S.J. Russell and Textile Institute, *Handbook of Nonwovens* (CRC Press; Woodhead Pub. Ltd., Boca Raton, Fla.; Cambridge, 2007).
- ⁹ J.S. Na, G. Scarel, and G.N. Parsons, *J. Phys. Chem. C* **114**, 383 (2010).
- ¹⁰ C.A. Wilson, R.K. Grubbs, and S.M. George, *Chem. Mater.* **17**, 5625 (2005).
- ¹¹ S.M. Lee, V. Ischenko, E. Pippel, A. Masic, O. Moutanabbir, P. Fratzl, and M. Knez, *Adv. Funct. Mater.* **21**, 3047 (2011).
- ¹² G.K. Hyde, G. Scarel, J.C. Spagnola, Q. Peng, K. Lee, B. Gong, K.G. Roberts, K.M. Roth, C.A. Hanson, C.K. Devine, S.M. Stewart, D. Hojo, J.S. Na, J.S. Jur, and G.N. Parsons, *Langmuir* **26**, 2550 (2010).
- ¹³ J.S. Jur, J.C. Spagnola, K. Lee, B. Gong, Q. Peng, and G.N. Parsons, *Langmuir* **26**, 8239 (2010).

- ¹⁴ J.C. Spagnola, B. Gong, S.A. Arvidson, J.S. Jur, S.A. Khan, and G.N. Parsons, *J. Mater. Chem.* **20**, 4213 (2010).
- ¹⁵ A. Yamada, B.S. Sang, and M. Konagai, *Appl. Surf. Sci.* **112**, 216 (1997).
- ¹⁶ J. Musschoot, J. Dendooven, D. Deduytsche, J. Haemers, G. Buyle, and C. Detavernier, *Surf. Coatings Technol.* **206**, 4511 (2012).
- ¹⁷ G. Luka, T. Krajewski, L. Wachnicki, B. Witkowski, E. Lusakowska, W. Paszkowicz, E. Guziewicz, and M. Godlewski, *Phys. Status Solidi A* **207**, 1568 (2010).
- ¹⁸ J.P. Richters, T. Voss, D.S. Kim, R. Scholz, and M. Zacharias, *Nanotechnology* **19**, 4 (2008).
- ¹⁹ W.C. Sun, Y.C. Yeh, C.T. Ko, H. He, and M.J. Chen, *Nanoscale Res. Lett.* **6**, 1 (2011).
- ²⁰ S.M. Rossnagel and T.S. Kuan, *J. Vac. Sci. Technol. B* **22**, 240 (2004).
- ²¹ J.B. Baxter and C.A. Schmuttenmaer, *J. Phys. Chem. B* **110**, 25229 (2006).

CHAPTER 4 is a reprint of an article published in *ACS Applied Materials and Interfaces*, **6**, 9280 (2014). DOI: 10.1021/am501582p, by Sweet, W.J., Oldham, C.J., Parsons, G.N.

CHAPTER 4. Atomic Layer Deposition of Metal Oxide Patterns on Nonwoven Fiber Mats using Localized Physical Compression

William J. Sweet III, Christopher J. Oldham, and Gregory N. Parsons

Department of Chemical and Biomolecular Engineering, North Carolina State University,

Raleigh North Carolina 27695, United States

Keywords: patterning, atomic layer deposition, nonwoven, zinc oxide, flexible electronics

4.1 Abstract

Patterning is an essential part of many industrial processes from printing to semiconductor manufacturing. In this work we demonstrate a new method to pattern and selectively coat nonwoven textiles by atomic layer deposition (ALD) using compressive mask patterning. A physical mask combined with mechanical compression allows lateral definition and fidelity of the ALD coating to be controlled. We produce features of several sizes on different nonwoven fiber materials, and demonstrate the ability to limit diffusion effects to within $< 200 \mu\text{m}$ of the pattern edge. Lateral and vertical penetration of reactive growth species into nonwoven mats is investigated by plan-view and cross-sectional imaging. Vertical growth is also analyzed by imaging coating depth into fiber mat stacks. We develop a full quantitative transport model that describes well the effect of fiber structure and mechanical compression on the extent of coating under the physical mask. This method could be implemented for high-volume patterning for applications including flexible electronics.

4.2 Introduction

Patterning of thin films is a primary process in manufacturing of integrated circuits for electronic memory, logic, displays and other systems.^{1,2} There is growing interest in additive patterning processes where film patterns are formed directly on a substrate using substrate-selective reactions, chemical blocking layers, or surface-localized balancing of deposition/etch rates.³ Shadow mask patterning is an early example of an additive process that takes advantage of line-of-sight species adsorption and reaction in thin film sputtering or other physical deposition processes.⁴ Using shadow masks with more conformal deposition methods, including chemical vapor deposition (CVD), plasma CVD, and especially atomic layer deposition (ALD), precursor diffusion leads to film growth under the edge of the mask, making it difficult to generate well-defined patterns. For example, Langston et al.² found that for shadow-mask patterning during ALD onto planar silicon, the gap between the substrate and mask must be held near ~10 nm to achieve reliable patterning. Other studies of ALD growth profiles in pores or narrow slits^{5,6} give insight into species diffusion and growth mechanisms during thermal or plasma-enhanced ALD.

Flexible, breathable or stretchable substrate materials, including fibrous textiles and nonwoven fiber mats, have been explored as supports for unique integrated electronic device systems.^{7,8} Fibrous substrates are readily available at low cost, and they are also interesting as substrate materials, in part, because of their physical dimension and aspect ratio (i.e. small diameter and long length). Under bending stress, the fiber shape helps to balance the mechanical forces encountered by thin conformal coatings, including forces that direct stress

toward the coating/fiber interface. Weaving and surface printing technologies are well developed for fibrous media, and studies have applied these approaches to integrate metal wires and other electronic elements.⁷ However, electronic weaving or printing requires or produces relatively large wires which add bulk and noticeably degrade the texture or ‘feel’ of the fabric. There is growing interest in electronic “decals” that are affixed to finished products, but those also add bulk and diminish breathability.

Recently, researchers have explored vapor-phase atomic layer deposition and related methods to produce conformal metal and semiconductor thin film coatings on textiles and nonwoven fiber mats.⁸⁻¹³ Atomic layer deposition enables conformal nano-scale metal coatings on fibers, for example, so that each fiber within a textile or nonwoven mat receives the same film layer thickness.¹¹⁻¹³ Nonwovens are interesting because they are made at very low cost and high rate, and are used in many commercial, consumer and engineered devices, ranging from personal hygiene products to high performance filtration devices and charge storage batteries. Coated fiber mats may provide a unique capacity for integrating electronic insulators, semiconductors and metallic conducting layers onto nonwovens.¹¹⁻¹³ Because the coating is very thin (less than 100 nm)¹¹⁻¹³ the coating can be remain intact and stay conductive, for example, without significantly affecting the fiber weight, flexibility, breathability or tactile texture. However, results to date for metal ALD on fabrics are limited to coatings that cover the entire substrate surface. Electronic device integration into textiles is emerging, and is interesting for large-area applications, such as temperature, gas or liquid sensors, or for antennas or other communication elements. Patterning will be important for active layers, contacts, passivation or other functional regions. Cost and simplicity will be

critical, and because of the large substrate area, very large device feature sizes (0.1 – 1 mm or even larger) could be sufficient or even preferred. Early device applications could include integrated antennas and patterned electrodes or wiring in fiber-based electronics. Mask patterning is simpler and less costly than lithography. Large feature sizes could be sufficient for these uses, and approaches to minimize lateral species transport may enable smaller feature definition.

In this work, we demonstrate that compressive diffusion mask patterning applied to a porous fibrous mat substrate is a functional method to create metal oxide thin film patterns, with pattern control in both lateral and vertical directions on the substrate. To generate the pattern a metal patterned mask is placed on top of a fiber mat, and the fibers beneath the covered regions are mechanically compressed, effectively restricting lateral precursor transport. The exposed area remains more open, allowing precursors and reactants to diffuse and deposit on surfaces throughout the region. In some instances, by controlling the time per ALD cycle that reactant species can diffuse vertically into the patterned zone, we also achieve a vertical pattern in the deposited film coating. In addition, we show that the characteristic structure and arrangement of the fibers in the fabric affect species diffusion and transport, and thereby affect the pattern integrity and resolution.

4.3 Experimental

4.3.1 Fiber Substrate Materials

Images of nonwoven fiber mats and woven fiber fabrics used in this study are shown in Figure 4.1. Nonwoven melt-blown polypropylene (PP) was acquired from the Nonwovens

Institute at the North Carolina State University with a basis weight of $\sim 39 \text{ g/m}^2$ and an as-received mat thickness of $\sim 0.3 \text{ mm}$ (uncompressed).¹⁴ Fibers within the mats had a circular cross-section with diameter in the 1-5 micron range. Samples were cut from the as-received nonwoven rolls into $\sim 2 \text{ cm} \times 3 \text{ cm}$ pieces.¹² In addition, hydro-entangled nylon-6 (PA6) nonwoven Winged FibersTM mats were acquired from Allasso Industries. The mats were approximately 0.4 mm thick (uncompressed) with a weight of $\sim 66 \text{ g/m}^2$. Individual fibers were 5-10 microns in diameter. The individual fibers had a lobed cross section¹³ to increase the overall surface area.

To understand the extent of film growth on the fiber mats, we also analyze the total surface area of the fibers per unit area of fiber mat. This ‘surface area enhancement factor’, f_{SA} is a unitless value corresponding to the total fiber surface area per unit projected area of the fiber mat sample. The value for f_{SA} is determined by measuring the specific surface area of a nonwoven (m^2/g) using Brunauer–Emmett–Teller (BET) surface area analysis, followed by multiplying surface area by the sample basis weight (g/m^2) measured with a laboratory scale. For the polypropylene, we find: $f_{SA} = 1.6 \text{ m}^2/\text{g} \times 39 \text{ g/m}^2 = 62$, whereas for the nylon-6, $f_{SA} = 2.5 \text{ m}^2/\text{g} \times 66 \text{ g/m}^2 = 166$.

Another important factor in the fiber materials is the overall void fraction, ε , i.e. the ratio of the net fiber mat density ρ_m and the polymer density ρ_p , where the fiber mat density is estimated from the fiber mat thickness t_m (which changes upon compression) and basis weight m_m :

$$\rho_m = m_m / t_m \quad (4.1)$$

$$\varepsilon = 1 - \rho_m / \rho_p = 1 - m_m / (\rho_p \cdot t_m) \quad (4.2)$$

Using $\rho_p = 0.99 \text{ g/cm}^3$ for polypropylene and 1.084 g/cm^3 for nylon-6, we obtain $\varepsilon = 77\%$ for partially compressed nylon-6, 53% for fully compressed nylon-6, 84% for partially compressed polypropylene and 57% for fully compressed polypropylene.

During nonwovens fabrication, spun fibers are collected on a belt moving in the ‘machine direction’ (MD), perpendicular to the ‘cross direction’ (CD). Fiber orientation is generally random, but depending on the belt speed and fiber spinning output, the fibers in the nonwoven can take on a preferential orientation in the MD. Fiber imaging and analysis software in the Nonwovens Institute was used to determine the preferential orientation of the mats used for this study. The nylon mats showed some orientation in the machine direction, with 12% greater orientation in the machine direction and 10% less orientation in the cross direction than would be expected from a uniform distribution. By comparison, the melt-blown polypropylene is $\sim 6\%$ preferentially oriented in the machine direction. Results for ALD on the nylon-6 show different extent of reactant diffusion in the MD and CD, as expected for partially aligned fibers. The diffusion appears uniform in direction for the polypropylene, consistent with a random fiber orientation. In this work, a “MD sample” has fibers oriented *perpendicular* to feature being patterned, whereas a “CD sample” has fibers oriented *parallel* to the feature direction.

Woven nylon fabric with a plain weave structure ($\sim 125 \text{ g/m}^2$) was acquired from the NC State University College of Textiles. The weave consisted of fiber strands or yarns ~ 250 microns in diameter, made up of many twisted fibers, each ~ 15 microns in diameter. The fabric weave, comprised of perpendicular warp and weft yarns, orients the fibers and creates

a spatial variation in fiber density across the substrate. The yarn size, density and type of weave strongly influence fluid and particle transport through the fabric.

4.3.2 Atomic Layer Deposition and Fiber Imaging

Atomic layer deposition of ZnO was performed in a homemade tubular hot-wall reactor described previously.¹⁴ During processing, nitrogen carrier gas (99.999% N₂, National Welders) was filter dried (Aeronex Gatekeeper) and directed to flow continuously into the reactor at a flow rate of 150 standard cubic centimeters per minute (sccm). Pressure during deposition was typically ~ 1.0 Torr, and temperature was fixed between 125°C and 155°C. Zinc oxide deposition was performed using diethyl zinc (DEZ 95%, Strem Chemical) and water (UV-deionized, DI). The precursor and reactant dose times during ZnO ALD were typically fixed at DEZ/N₂/H₂O/N₂ = 2/40/2/40 seconds, respectively. The reactor pressure increased $\Delta P \approx 0.07$ Torr during precursor exposure and $\Delta P \approx 0.28$ Torr during the water exposure step.

For 400 ALD cycles at 125°C-155°C, the ZnO ALD on the polypropylene and nylon-6 led to a distinct color change,¹² as shown for ZnO on polypropylene in Figure 4.2. Films deposited on glass slides and quartz fibers also show similar coloration. The composition pattern was confirmed for several samples using Energy Dispersive X-ray Spectroscopy (EDS) of coated and uncoated regions. We find that 100 cycles of ZnO is not visibly distinct from uncoated nylon-6, whereas 200 cycles shows clear color change. When measuring the extent of coating, we maintain at least 400 ALD cycles, and visible imaging can therefore be used to compare patterns made under different processing conditions.

Optical images were collected using a high resolution digital SLR camera with macro-filter attachments for close up shots of the substrates. For some of these inset images, contrast was enhanced using GIMP 2.8 Graphics Software, as noted in the respective figure captions. High magnification optical images were taken using a Jenoptik optical microscope with a ProgRes CT5 digital microscope camera attachment. Microscope images were analyzed using ProgRes CapturePro 2.6 software package. For diffusion length measurements, for each data point at least two different samples were measured, in at least four different locations, for no less than eight measurements per data point. The measurements were taken from the same locations for all samples, in order to maintain consistency.

4.3.3 Pattern Deposition and Processing

Patterning was performed by compressing the nonwoven or woven fiber samples between a pair of aluminum metal masking plates as shown schematically in Figure 4.3. The open areas on masking plates, which permitted precursors to diffuse into the fiber mats, could be on one or both of the plates, depending on the desired pattern.

The extent of compression was controlled by screws that held the plates together. The screws were finger-tightened and the plate separation was measured using a digital caliper; additional tightening was performed as required using a hex wrench. Two different values of compression were studied. The fibers were either “fully” compressed, where the plate spacing at 0.13 ± 0.02 mm for the nylon-6 nonwoven, and 0.09 ± 0.02 mm for polypropylene nonwoven. For the “partially” compressed samples the screws were tightened to provide a

spacing of 0.25 ± 0.02 mm for polypropylene nonwoven and 0.27 ± 0.02 mm for the nylon-6 nonwoven samples. Unless otherwise stated, we used “fully” compressed samples for the studies described here.

4.4 Results

Figure 4.4(a) shows a sample mask with 10 mm wide slits, with lengths of 1.6 mm, 3.2 mm, 6.4 mm, and 12.7 mm, spaced at least 5 mm apart and 5 mm from the edge. Figure 4.4(b) shows the resulting pattern of ALD ZnO deposited using 400 cycles at 155°C on the top and bottom sides of a MD nylon-6 substrate. The mask effectively limits precursor access only to the uncovered regions. The edges of the mat are also exposed, allowing visible growth around the sample border.

To verify the color change is due to the coating of ZnO ALD on the nonwoven, elemental analysis was performed by elemental dispersion X-ray spectroscopy (EDS) analysis on a ZnO patterned polypropylene substrate. Figure 4.5(a) shows an SEM image of the ZnO patterned polypropylene substrate along with EDS scans that were taken, the locations of which are indicated on the SEM image with corresponding numbers.

Inside the patterned region, the EDS results in Figure 4.5(a,I) show strong Zn and a relatively weak C signals, consistent with the patterned ZnO coating on polymer. In the transition region, which is the area that is compressed and located near the pattern opening, there is still a strong zinc peak, but also a more significant carbon peak. In the uncoated region, the compressed area beyond where the DEZ could diffuse, EDS shows only carbon, with zinc below the detection limit. The zinc signals correspond well with the visible

coloration of the sample, so the optical color can be used to identify the distance that the ZnO coating has progressed from the feature edge.

The red-brown color of our as-deposited ZnO is ascribed to oxygen vacancy or other related gap states in the films deposited at low temperature.^{15,16} To confirm this, quartz discs were coated with 400 cycles of ZnO ALD at 155°C for UV-Vis analysis, and results for as-deposited and annealed (3h at 800°C in air) films are shown in Figure 4.5(b). Upon anneal the ZnO band gap increases from 3.10 to 3.19 eV, consistent with defect oxidation. Previous research¹⁶ has shown as-grown ZnO single crystals with zinc rich stoichiometry are colored, and become visibly transparent upon high temperature anneal in air due to defect oxidation. We also find that white nonwoven quartz fiber mats coated with 400 ZnO ALD cycles at 155°C appear red-brown, and become more white colored upon 800°C anneal (inset, Fig. 4.5b), again consistent with oxidation. The red-brown color on the fibers is therefore a good visible marker for extent of ZnO ALD.

To determine the extent of precursor diffusion, we use optical microscopy as shown in Figure 4.6. The growth extension under the mask is the distance between the mask edge (which is clearly visible in reflection mode) and the edge of the coating coloration (which is clearly visible in transmission mode).

The bottom panels in Figure 4.6 show an arrow, set by eye that corresponds to the measured distance for lateral growth under the mask. Using the magnification scale, we see that the ZnO coats approximately 1.25 mm into the polypropylene and 0.95 mm into the nylon-6 for these samples. The extent of diffusion into the open regions between fibers is expected to depend on precursor dose time, the number of ALD cycles, deposition

temperature, the compression force, and the structure of the fiber mat (i.e. nonwoven vs. woven). Generally we observe diffusion laterally under the covering mask, but for thicker fiber mat samples, we also observe a vertical diffusion pattern. How dose time, compression and other factors affect the growth pattern will likely depend on substrate chemistry, so we investigate polypropylene and nylon-6 polymer fibers. Results of the patterning studies are shown in Figures 4.7 through 4.12. We note that while saturated precursor exposure is expected to produce conformal coatings on the fibers, the coating near the growth transition region will likely not be fully conformal. Near the edge of the film growth region, diminished precursor exposure will prevent full surface saturation which is necessary for conformal coverage.

4.4.1 Influence of Precursor Dose Time on Pattern Definition

The effect of DEZ dose time per cycle on precursor diffusion length, and subsequently pattern resolution, is shown in Figure 4.7 for machine direction cut nylon-6. For these studies, the fibers were “fully” compressed. The shortest dose time of 0.25 seconds per cycle produces a light color, consistent with sub-saturated ALD, whereas dose times of 0.5 seconds and longer lead to darker coating. For dose times exceeding 2 seconds, the coloration extends beyond the masked area, consistent with diffusion into the void space between compressed fibers.

In addition to monitoring lateral film deposition profiles, we can look at growth vertically within relatively thick fiber mats, where only one side of the mat is exposed to

precursor. Figure 4.8 for example, shows a pattern created when 10 fiber mats are stacked and compressed in a pattern before coating in the ALD reaction chamber.

Figure 4.8(a) shows photographs: (i) prior to; and (ii) after coating with 400 ZnO ALD cycles, where the sample was cut to reveal the vertical penetration pattern. Figure 4.8(b) also shows: (i) a schematic sample cross section; and (ii-iv) a series of nylon-6 nonwoven stacks deposited using different DEZ dose times from 0.5 to 2 seconds. The images (a, ii) and (b, iv) in Figure 4.8 correspond to different perspectives of the same sample, showing minimal lateral growth under the mask, but significant growth vertically into the fiber mat stack. The consistent color of the coated region in Figure 4.8(b) (images iii and iv) indicates uniform film thickness in the growth zone. The images also show the extent of vertical growth increases with increasing dose time per cycle. Samples can be readily deconstructed layer by layer, to view vertical penetration depth of the precursor; Figure 4.8(c) shows the top and bottom three pieces of a ten piece nylon-6 stack.

4.4.2 Number of ZnO ALD Cycles

Growth initiation during ALD is sensitive to the starting surface, especially for deposition on polymer materials.^{12,14,17-19} Polypropylene is chemically inert, so ALD nucleation proceeds via sub-surface precursor diffusion. Nylon-6 has amide groups that are more chemically reactive. We measured mass change of polypropylene fiber mats versus number of ZnO ALD cycles and found that nucleation requires ~60-90 cycles at 155°C. After ~60 cycles, mass increases rapidly then slows to steady growth.¹² On nylon-6 fibers, ZnO mass uptake shows a similar growth incubation period, followed by steady growth.

Ellipsometry analysis of film thickness versus cycle number on planar spun cast nylon films further confirms this nucleation trend.

Figure 4.9 shows images after 400 and 800 ALD cycles for patterned ZnO on (a) nylon-6; and (b) polypropylene substrates. The nylon-6 samples show similar patterns for 400 and 800 cycles of ZnO. The 800 cycle sample appears darker, consistent with a thicker coating layer. The polypropylene substrates, however, show a notably larger growth area after 800 ALD cycles compared to 400 cycles. This may be due to the trends in subsurface vs. surface growth for ALD on polypropylene. During the early ALD cycles, before an encapsulating coating is formed, precursor can diffuse into the fibers depleting the gas phase concentration. Subsurface diffusion is blocked after full layer coating, allowing the precursor to reach further into the compressed region as the number of ALD cycles increases.

4.4.3 Deposition Temperature

The deposition temperature is also expected to affect the pattern shape and fidelity. Higher temperatures lead to thermal expansion, followed by melting (at $\sim 165^{\circ}\text{C}$ for polypropylene¹² and $\sim 215^{\circ}\text{C}$ for nylon-6¹³). For conductive coatings, higher deposition temperatures are preferred for higher conductance. Figure 4.10 shows 400 cycles of ZnO deposited at 125°C and 155°C on MD nylon-6 and polypropylene nonwovens.

On nylon-6, growth under the pattern edge is independent of temperature, whereas on polypropylene the coating is darker (i.e. thicker) and more confined near the feature edge at higher temperature. The more confined growth at higher temperature is ascribed to softening or partial melting of the polypropylene, which will tend to block precursor transport. For

further analysis, the deposition temperature was maintained at 125°C on polypropylene and 155°C for nylon-6 substrates.

4.4.4 Extent of Substrate Compression

The extent of fiber compression will influence the distance the precursor travels under the masked region during the dose time. The precursor diffusion coefficient is set by the gas species present in the open spaces (i.e. DEZ in N₂), so we expect any change in precursor travel distance to reflect a change in tortuosity. Figure 4.11 shows ZnO ALD (400 cycles, 2s DEZ dose/cycle at 155°C on MD nylon-6) patterns on fully and partially compressed nylon-6.

As expected, the more fully compressed samples show more confined coating for all mats studied. The images for nylon in Figure 4.11 show the coating is more extended in the machine direction (i.e. along the aligned fibers). For the quantitative analysis discussed below, coating length in the MD and CD are measured and tabulated separately. As noted above, the PP mats have more random fiber alignment, so the extent of coating is independent of direction.

4.4.5 Nonwoven versus Woven Fiber Substrates

To explore the effect of substrate fiber geometry on pattern resolution, we patterned ALD ZnO at 155°C on nonwoven and woven nylon and results are shown in Figure 4.12.

The images show a much better defined pattern on the nonwoven compared to the woven fibers. The smaller average fiber diameter and random fiber orientation in the nonwoven helps limit lateral reactant transport, thereby enabling better pattern definition.

4.4.6 Coating Distance Under the Mask vs. DEZ Dose

Using the optical microscopy images, we quantified the lateral coating distance under the mask edge as a function of the DEZ dose time on polypropylene and nylon-6 nonwovens under full and partial compression, and the resulting data points are plotted in Figure 4.13. The error bars represent one standard deviation and are shown only for the sample with the largest deviation.

As expected, the fiber compression limits the extent of growth under the mask and therefore improves pattern uniformity. We note that if the precursor is not fully consumed during the exposure time, the substrate will continue to be exposed while the precursor moves back out during the purge cycle step. This means that the actual DEZ exposure time may be somewhat larger than the measured DEZ exposure time, especially for the longer exposures. We note that a full model of growth vs cycle number must consider nucleation delay which is present in ZnO ALD on polymers. However, since we find nucleation proceeds similarly on polypropylene and nylon-6, and the data we use for the extent of growth uses a fixed and relatively large number (400) of ALD cycles, the model effectively normalizes the effect of the nucleation delay.

4.5 Modeling Reaction-Diffusion for ALD in a Nonwoven

A key aspect for patterning coatings is to understand the mechanisms associated with pattern generation and fidelity. Compressing the fiber mat will reduce reactant transport under the mask edge, but other factors including fiber alignment and ALD process conditions are also found to be important. To understand the interrelations between these parameters,

we develop a simple transport model to describe the extent of reactant transport, and analyze how the transport scales as the fiber mats are compressed. We thereby model the extent of growth laterally in the covered or compressed fiber region between the metal masking plates as a function of fiber type, orientation and extent of compression.

The problem geometry is simplified as a 1D semi-infinite media with continuum flow. For some conditions, the Knudsen number is sufficiently large that Knudsen transport could also be considered, but we choose to use continuum molecular diffusion to capture a broad range of process and sample conditions. Specifically, we build on a time dependent reaction-diffusion model described by Yanguas-Gil and Elam²⁰ for ALD in high aspect ratio materials, but we redefine parameters and introduce terms to better describe ALD in fiber mats. In particular, we redefine specific surface area, \bar{s} , in terms of the fiber mats' surface enhancement factor, and we establish an effective diffusion coefficient, D_{eff} to account for the void volume and diffusion tortuosity.

Using conservation of mass and assuming equimolar counter diffusion, then one dimensional unsteady state mass transport follows:

$$\frac{\partial C}{\partial t} = -\frac{\partial}{\partial z}(J_{DEZ}) - r \quad (4.3)$$

where C is the concentration of DEZ molecules, r is the rate of DEZ loss through chemical reaction, and J_{DEZ} is the precursor flux given by Fick's first law, $J_{DEZ} = -D dC/dz$, where D is the diffusion coefficient. The rate of DEZ loss through reaction is determined by the precursor flux to the reactive sites on the wall (J_{wall}), the available surface area (normalized per unit volume) \bar{s} , and the surface reaction probability, taken to be first order with respect

to available sites (first order irreversible Langmuir adsorption, $\beta = \beta_0 \cdot \theta$). Equation 4.3 then becomes²⁰

$$\frac{\partial C}{\partial t} = D \frac{\partial^2 C}{\partial z^2} - \beta_0 \cdot \theta \cdot J_{wall} \cdot \bar{S} \quad (4.4)$$

where β_0 is the initial reaction probability on an un-reacted surface, θ is the fraction of available reaction sites, and \bar{S} is the specific surface area (area per unit volume).

For nonwoven substrates, the value for $\bar{S} = f_{SA}/t_m$ where f_{SA} is the surface area enhancement factor (defined above) and t_m is the thickness of the fiber mat (which decreases upon compression). The values for \bar{S} are $\sim 2,500 \text{ cm}^{-1}$ for partially compressed polypropylene, $\sim 6,800 \text{ cm}^{-1}$ for fully compressed polypropylene, $\sim 6,200 \text{ cm}^{-1}$ for partially compressed nylon-6, to $\sim 12,800 \text{ cm}^{-1}$ for fully compressed nylon. By contrast, in a cylindrical pore, $\bar{S} = 2/R$ where R is the pore radius, so this range of \bar{S} values (2,000-10,000 cm^{-1}) would be found in pores with $R = 2\text{-}10$ microns.

The kinetic theory of gases gives $J_{wall} = \frac{1}{4} C \cdot \bar{v}$ where \bar{v} is the mean thermal speed of the diffusing particles. The rate equation for site consumption during film deposition is given by²⁰

$$\frac{d\theta}{dt} = -\frac{1}{4} \bar{v} \cdot C(z,t) \cdot \beta_0 \cdot \theta(z,t) \cdot S_0 \quad (4.5)$$

where S_0 is the average area of a reaction site.

For growth on a planar surface, $S_0 \approx 20\text{\AA}^2$, which corresponds to ~ 5 adsorbed molecules nm^{-2} .²¹ However, on a polymer surface, subsurface precursor diffusion and reaction can be significant.^{12-14,19,22} Analysis of the extent of reaction between trimethyl

aluminum and various polymers¹⁹ shows an effective adsorption site density (i.e. the effective “number of monolayers” adsorbed per ALD cycle) can be 1000× or more larger than S_0 . Therefore, significant sub-surface reaction could help limit precursor transport and improve pattern fidelity, although the deposition would not yield a purely metal oxide coating. While studies of DEZ reactions on polymers are not as extensive,^{12,18,22} results show that compared to TMA, DEZ leads to much less sub-surface reaction on polyester fibers.²² For this work using DEZ, therefore, we maintain the value $S_0 \approx 20\text{\AA}^2$.

During the precursor dose time, we set the precursor concentration at the edge of the feature to be constant and vertically uniform. That is, we work under conditions where the vertical transport in the exposed fiber region is fast relative to lateral transport in the covered fibers between the metal plates. The boundary condition at the inlet ($z=0$) is then, $C(0,t)=C_0$ during the dose time. The value for C_0 was estimated from the measured pressure change upon DEZ dosing, $\Delta P \sim 0.07$ Torr which corresponds to $C_0 \approx 1.6 \times 10^{15}$ molecules cm^{-3} . Far away from the inlet, $C(\infty,t)=0$. At $t=0$, $C(z,0)=0$, and the surface is fully available for deposition: $\theta(z,0)=1$.

The value for β_0 is the probability for reaction between the precursor and available surface site upon collision. For rapid reaction, $\beta_0 = 1$, and a sharp growth boundary will form, while $\beta_0 < 0.01$ results in a more tapered growth edge profile, but the average coating distance from the edge will not be affected. We use $\beta_0 = 0.01$, but find that under the conditions studied, the outcome is not strongly sensitive to β_0 between 1 and $\sim 10^{-3}$.

Equations 4.4 and 4.5 are solved using MATLAB® for various dose times to determine the expected adsorbed DEZ coverage (i.e. extent of ZnO coating) as a function of

normalized distance from the feature edge (z/L). As noted above, the ZnO coating is visible after >100 ALD cycles. After 400 ALD cycles, therefore, the coating edge will appear where the surface coverage per cycle θ is ≥ 0.25 . When β_0 is set between 0.01 and 1 the coating thickness vs. lateral distance into the fiber mat changes abruptly. Therefore, θ between 0.25 and 0.75 produce only a small change (< 3%) in the expected visible coating distance. For all samples, we set θ ‘critical’, $\theta_c = 0.5$ in the model to identify the visible coating distance.

Equation 4.4 also requires input for the diffusion coefficient for DEZ in N_2 : D_{DEZ} . This value can be approximated using the value for O_2 diffusion through N_2 ,²³ adjusted from standard conditions by $D_1 \cdot P_1 \cdot T_1^{-3/2} = D_2 \cdot P_2 \cdot T_2^{-3/2}$. At 155°C at 1 Torr, this yields $D_{DEZ} \sim 270$ cm^2/s . However, this value for gaseous diffusion needs to be adjusted for diffusion through a porous network²⁴

$$D_{eff} = \frac{D_{DEZ} \cdot \varepsilon}{\tau^2} \quad (4.6)$$

The effective diffusion coefficient, D_{eff} , is less than D_{DEZ} due to the volume void fraction (ε) and the tortuosity within the matrix, τ . The tortuosity is defined as the actual transport path length relative to the linear distance traveled, and is generally greater than one:

$$\tau = L_{tran} / L_{lin} \quad (4.7)$$

To calculate the model curves for visible coating distance versus DEZ exposure time, we use parameters defined above for each sample set, i.e. f_{SA} , S_0 , t_m , and ε , and set $\beta_0=0.01$ and $\theta_c=0.5$, and left the tortuosity, τ as an adjustable parameter. The resulting model curve fits are plotted with the experimental data in Figure 4.13. The tortuosity, and corresponding D_{eff} values are presented in Table 4.1.

Table 4.1. The effective diffusion coefficients and calculated tortuosity values for the model curves plotted in Figure 4.13.

		Nylon-6		Polypropylene	
		Tortuosity τ	D_{eff} (cm ² /s)	Tortuosity τ	D_{eff} (cm ² /s)
Partial Compression	MD	2.6	30	4.3	11
	CD	3.7	15		
Full Compression	MD	3.3	13	3.8	9.5
	CD	4.7	6.5		

The effective diffusion coefficients and the tortuosity values calculated under both partial and full compression for both Machine Direction and Cross Direction PA6, as well as PP.

For the nylon-6 samples, consistent with expected results, transport is more favorable along the machine direction where fibers are aligned with the precursor diffusion. Moreover, for all samples, we see the effective diffusivity decreases upon compression. However, the tortuosity increases upon compression in the nylon-6, but appears to decrease upon compression in the polypropylene. We interpret these results as follows. In the nylon-6, where fiber alignment is not uniform, compression increases tortuosity and decreases void fraction, leading to a net decrease in D_{eff} and an overall decrease in visible coating distance under the mask. Compared to the nylon-6, the tortuosity is larger in the more random polypropylene. Upon compression the tortuosity in the nylon-6 increases. In polypropylene

the apparent decrease in τ is relatively small, and we believe the decrease in travel distance (i.e. the decrease in D_{eff} in Table 1) upon compression is due primarily to a decrease in void fraction (i.e. the small change in τ in compressed polypropylene is not quantitatively significant). It is reasonable that a more random network with smaller fibers (1-5 microns for polypropylene vs. 5-10 microns for nylon-6) will produce a relatively large tortuosity, with relatively small change in tortuosity upon compression.

Overall, the quantitative model describes well the observed trends in pattern extension under the coating mask: larger compression and more random fiber orientation improves the pattern fidelity. The model also suggests that increasing the density of reactive sites in the polymer (i.e. choosing a functionalized polymer and using precursors with more propensity for subsurface diffusion and reaction) will also improve fidelity, but will produce a precursor/polymer fiber mixture rather than a uniform thin film fiber coating.

4.6 Conclusions

A method to pattern and selectively deposit ALD thin film layers on fiber mats was demonstrated using a mask with applied physical compressive force. Patterned ZnO ALD coatings were formed on nylon-6 and polypropylene nonwovens, and we showed how substrate properties such as fiber diameter and orientation, polymer chemistry and structure (woven vs. nonwoven) play a key a role in determining the extent of reactant transport into the covered fiber matrix. Both lateral and vertical penetration of reactive growth species into nonwoven mats was observed, and lateral species transport was modeled to quantitatively

analyze the effect of fiber structure and mechanical compression on the extent of coating under the physical mask.

We find that the extent of reactant transport is affected by the amount and direction of fiber alignment within the fiber substrate, and the degree of physical compression applied. By fitting the experimental results for coating distance versus precursor exposure time to a quantitative diffusion model, we find that the mechanisms by which physical compression affects species transport depends on the structure of the starting fiber matrix. For small random fibers, compression predominantly decreases the void volume, whereas for larger and more aligned fibers, compression tends to decrease void volume and increase transport path tortuosity. The quantitative model fits the observed trends in pattern fidelity and provides a valuable tool to estimate the extent of precursor diffusion and transport in fiber matrices during coating by atomic layer deposition.

4.7 Acknowledgments

We acknowledge the Nonwovens Institute at North Carolina State University (NWI) Project 09-118 for support for W.J.S. We acknowledge Amy Minton for help performing the fiber orientation analysis at the Nonwovens Institute Microscopy and Imaging Lab, Richard Lamy and Christopher Sanford at the NCSU Precision Instrument Machine Shop for help fabricating the patterning masks, and Chuck Mooney at the NC State Analytical Instrument Facility for his assistance with SEM and EDS analysis.

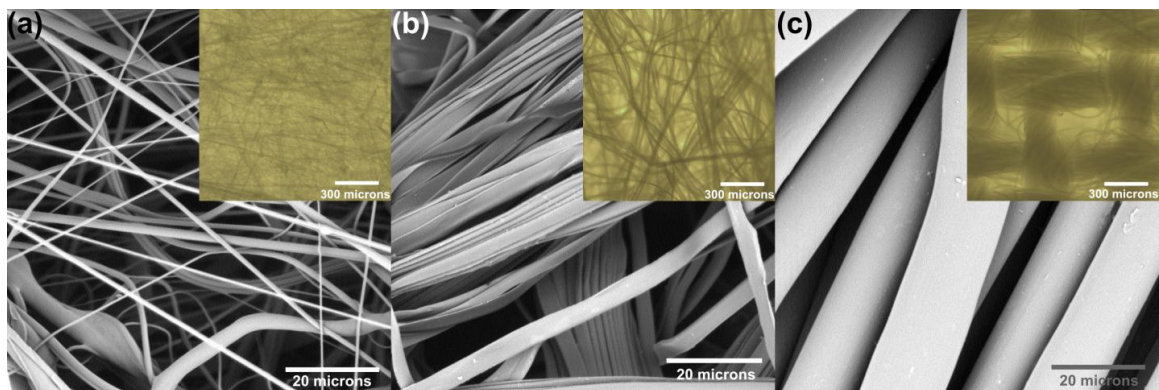


Figure 4.1. Scanning electron microscope images of (a) polypropylene nonwoven, (b) nylon-6 nonwoven, and (c) nylon woven mats used in this study; all SEM scale bars are 20 microns. Insets are low magnification optical microscopy images of the respective substrates to show context for the SEM images, the scale bars for the inset images are 300 microns. Optical images are of the fibers as received; a 5 nm Au/Pd coating was sputtered onto the substrates prior to the SEM images.

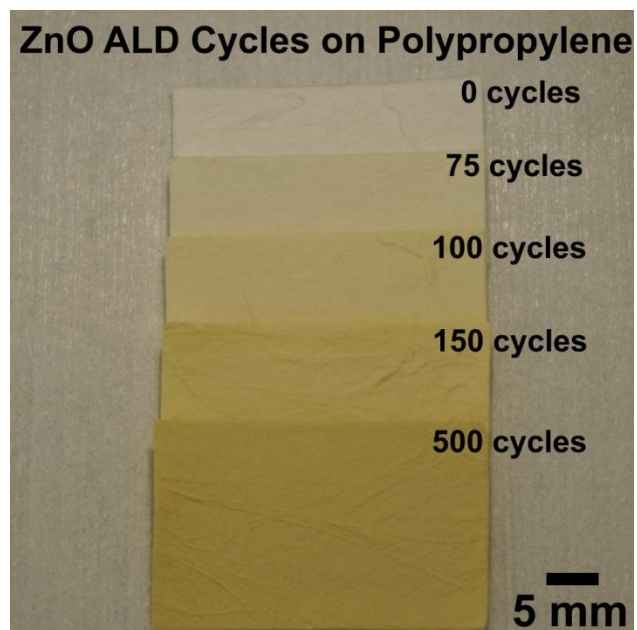


Figure 4.2. ZnO ALD on nonwoven polypropylene deposited at 155°C, with different numbers of ALD cycles. The color change reflects the thickness of the ALD coating.

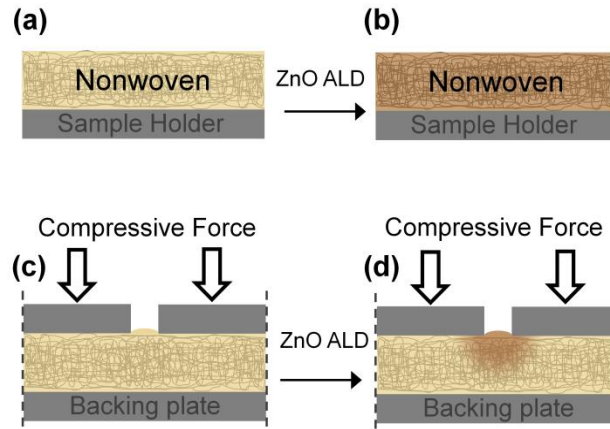


Figure 4.3. Schematic cross-section showing ALD coating on a nonwoven mat (a,b) without a mask; and (c,d) with a compression mask in place. The mask limits lateral diffusion of the precursors within the nonwoven, producing a pattern that is restricted to exposed portions of the mask. This example shows a solid backing plate. The solid plate allows the extent of growth in the vertical direction to also be controlled by adjusting the precursor dose time per cycle.

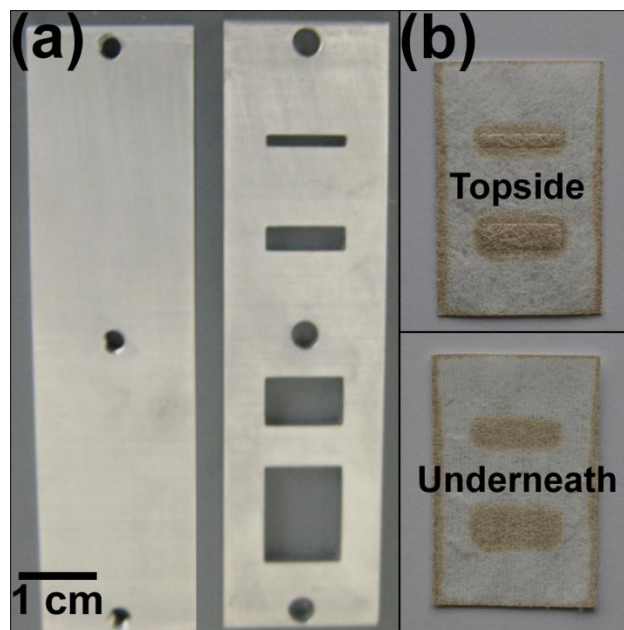


Figure 4.4. (a) Aluminum solid back plate and pattern mask with mask with slits 10 mm wide and lengths of 1.6 mm, 3.2 mm, 6.4 mm, and 12.7 mm, spaced at least 5 mm apart and 5 mm from the edge. (b) Both sides of a nylon-6 nonwoven patterned with 400 cycles of ALD ZnO at 155°C show a pattern, demonstrating that the precursors vertically permeate through the nonwoven to also produce a pattern on the side that was covered by the solid metal back plate. The patterned color of the oxide is visible, with some coating also on the edge of the samples.

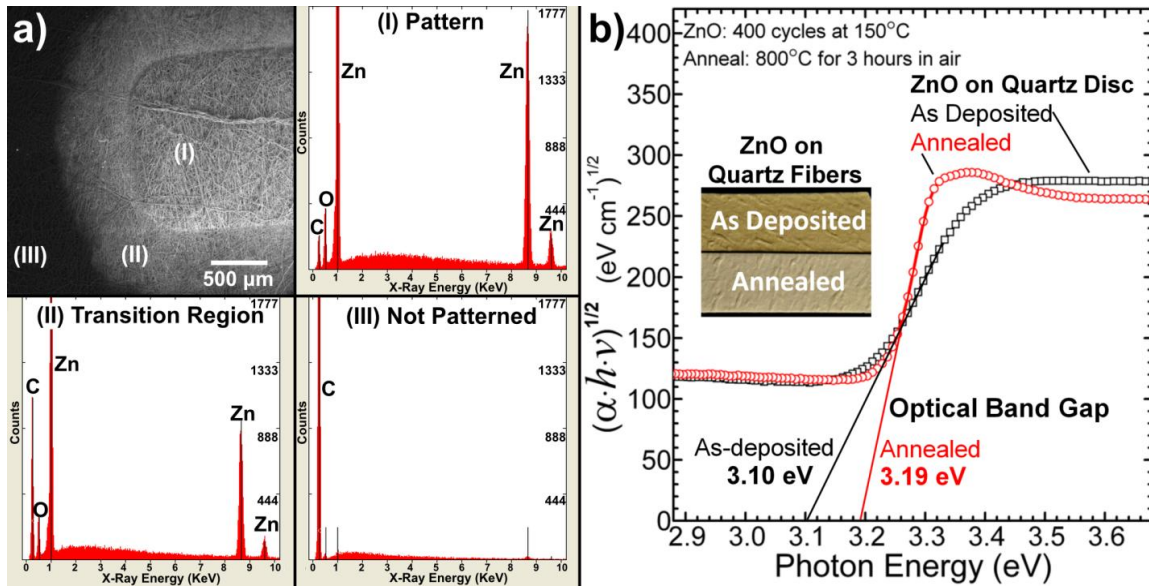


Figure 4.5. (a) An SEM image and EDS scans of a ZnO patterned feature on a polypropylene nonwoven. The numbers on the image correspond to locations where the EDS scans were taken. (I) The patterned region is not covered by the mask; (II) the compressed region near the opening where DEZ diffuses during dosing; (III) compressed region beyond where DEZ diffuses. The zinc signal is strongest relative to carbon in the patterned feature, location (I). Carbon signal is strongest in the region that is not patterned, and no zinc signal is detected. (b) Optical absorption data vs. photon energy for ZnO (400 cycles at 155°C) on quartz disks, for as-deposited and after annealing at 800°C in air for 3 hours. Inset shows the same films deposited on quartz fibers. The visible color on the as-deposited fibers is ascribed to ZnO with oxygen vacancy or other related defects.

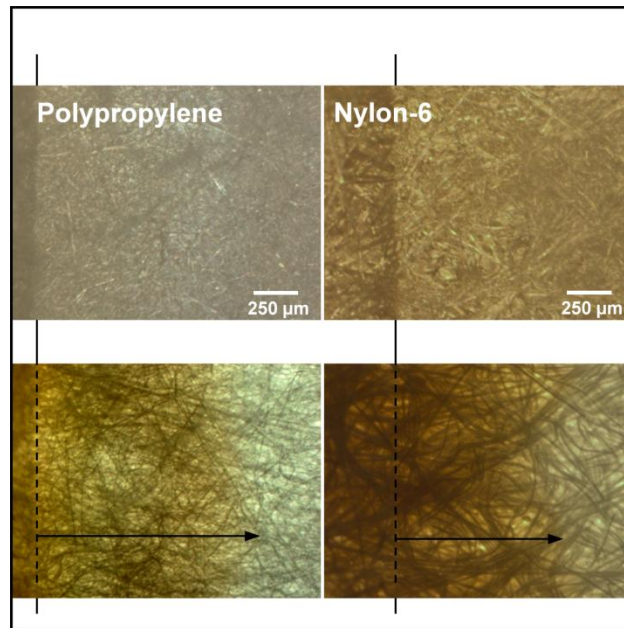


Figure 4.6. Optical microcopy in reflection (top images) and transmission mode (bottom) of patterned ZnO ALD on polypropylene and nylon-6 nonwoven fiber mats. The pattern edge is readily visible in reflection, and the average extent of coating under the pattern is observed transmission.

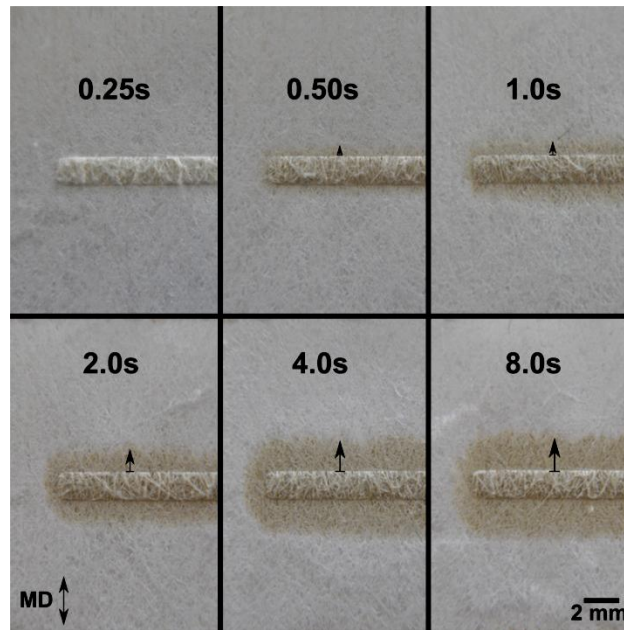


Figure 4.7. Machine direction cut nylon-6 was patterned with 400 cycles of ZnO ALD using various DEZ dose times. Short dose times produce a feature that is well defined with minimal diffusion distance beyond the boundary of the compressive mask. Longer dose times result in longer diffusion lengths. This process was repeated for cross direction cut nylon-6 and polypropylene substrates; the results of which are compared and discussed in later sections of this work.

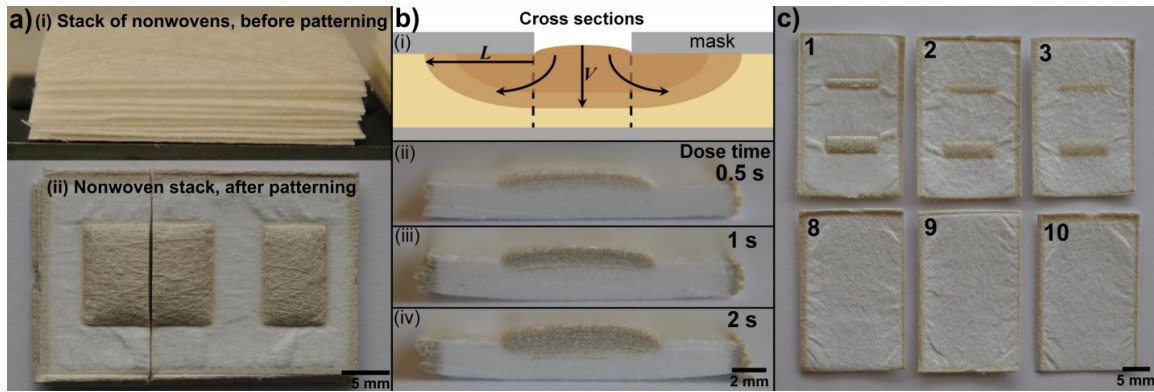


Figure 4.8. Patterned layers made by compression of porous substrates. 4.8(a) shows a stack of 10 nonwoven nylon-6 mats stacked (a,i) before and (a,ii) after compression and patterning. 4.8(b) shows (b,i) a cross section schematic of precursor diffusing through a sample, where L and V indicate lateral and vertical diffusion, respectively; and (b,ii-iv) stacks patterned with increasing DEZ dose times. For longer exposure times per ALD cycle, the coating penetrates completely in the vertical direction while maintaining the lateral pattern through the stack. 4.8(c) shows the top three and bottom three layers of a 10 nylon-6 mat tall stack patterned with a 2 second dose time, the numbers signify the position within the stack. The top-most sample (1) is coated uniformly, but the bottom-sample (10) shows minimal coating. ALD can achieve patterned growth with controlling depth on a fiber substrate.

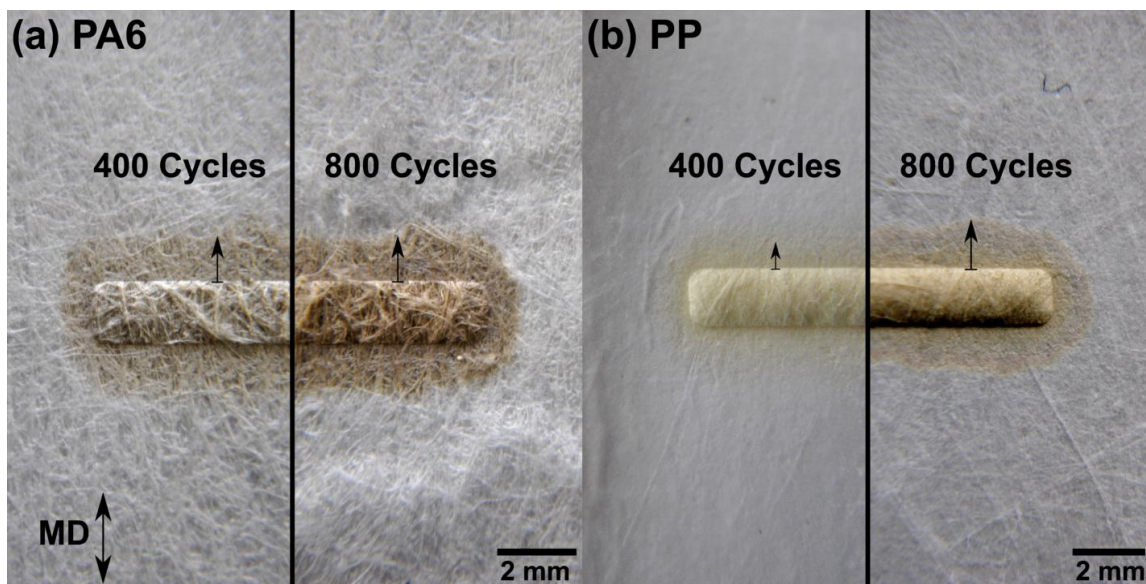


Figure 4.9. ZnO ALD on (a) nylon-6 nonwoven fiber mats cut in the machine direction, and (b) polypropylene nonwoven mats. For deposition on nylon, the extent of diffusion under the masked area is the same for 400 vs 800 ALD cycles, whereas for the polypropylene substrate the 800 cycle deposition is more spread out than the 400 cycle sample. For more deposition cycles, precursor diffusion into the polypropylene polymer may extend growth further under the mask region. The images were digitally enhanced to increase contrast by 50%.

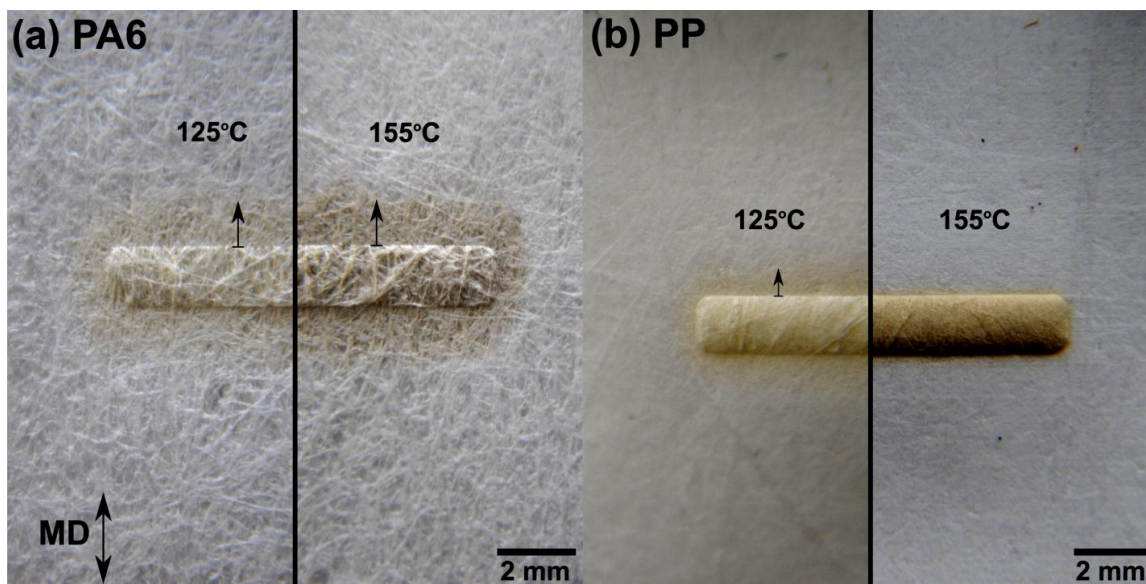


Figure 4.10. Nonwoven nylon-6 and polypropylene were patterned at 125°C and 155°C to determine the impact of deposition temperature on the pattern. (a) Nylon-6 shows a darker color pattern is created when deposited at higher temperature, but the diffusion length, as indicated by the arrows, remains the same. (b) Polypropylene also shows a darker feature when coated at higher temperature, however, the sample also shows significantly lower extent of diffusion of the coating at higher temperatures. Deposition on polypropylene at 155°C while under compression may cause the polypropylene to deform, fusing fibers and increasing tortuosity of diffusing precursor molecules. The contrast of the images was increased 50% to make the coated region more apparent.

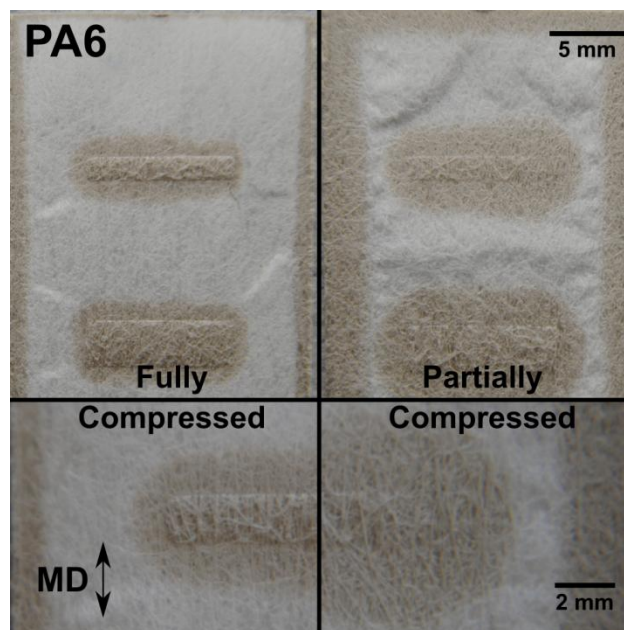


Figure 4.11. ZnO patterns on nonwoven nylon-6 after coating with 400 cycles at 155°C. The extent of deposition under the exposed mask depends on the amount of compression used. In this case, ‘full compression’ indicates masking blocks are fully tightened with self tightening screws using a hexagonal wrench, and ‘partial compression’ are tightened to finger tight; for consistency, digital calipers were used to measured height of the combined mask and nonwoven samples to verify tightening was consistent throughout a data set.

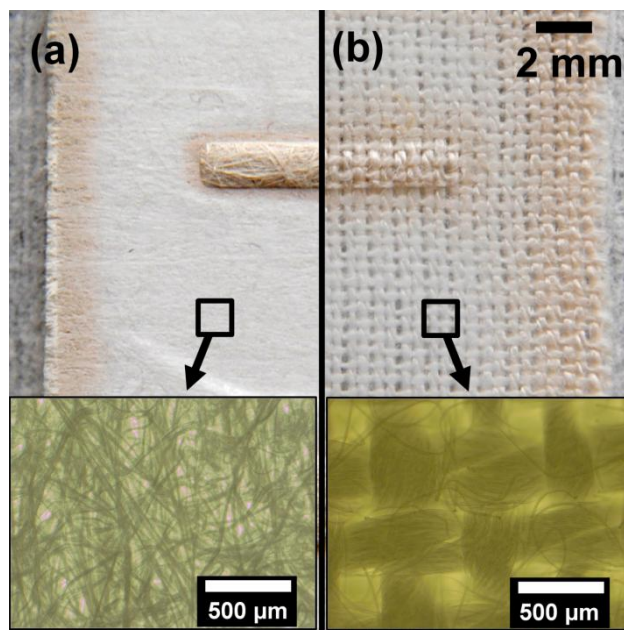


Figure 4.12. Optical images of (a) nonwoven nylon; and (b) woven nylon fiber substrates after pattern-coating with ZnO ALD. Optical microscopy images from each sample show the physical structure of each material. The random orientation of the fibers in the nonwoven compared to the oriented fibers in the woven yarns restricts lateral reactant transport to achieve better feature definition. The images were digitally enhanced to increase contrast by 40%.

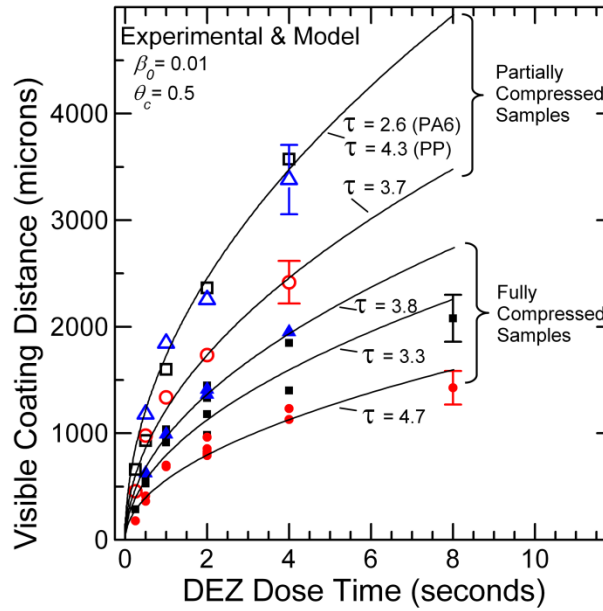


Figure 4.13. Data from experimental measurements of visible diffusion length for different substrates deposited using various DEZ dose times are shown; polypropylene (blue triangles) and nylon cut in the machine direction (black squares) and cross direction (red circles). Samples were patterned while under both full compression (solid symbols) and partial compression (hollow symbols). Distance measurements were taken using an optical microscope, four micrographs were taken per sample and the maximum and minimum diffusion distances were measured for each. The average distance is plotted, and the error bars shown are for the highest standard deviation sample for each of the data sets. The curves shown are derived from the solutions to equation 4.4 and 4.5, which are solved using $\beta_0=0.01$, $\theta_C =0.5$, each substrates physical parameters (\bar{s} , T), but allowing the effective diffusion coefficient (D_{eff}) to vary to fit the data. The tortuosity can then be found for each substrate using equation 4.6.

APPENDIX

4.8 Appendix – Supplemental Items Not Published

These figures include interesting and important findings that were removed from the during drafting of the published article; they are included here since they may provide useful information for any further work on the topic.

Impact of Precursor Dose on Saturation and Surface Coverage

Figure A.4.1(a) shows the growth per cycle for ZnO ALD on silicon at 155°C as a function of DEZ dose time where the deposition recipe is DEZ/purge/H₂O/purge = X/40s/2/s/40s. Using these conditions, we measured growth rate on planar silicon as a function of DEZ exposure time and found ALD saturation for DEZ exposure times >0.5 seconds per cycle, with some increase in growth/cycle for exposure >1 sec/cycle (i.e. ‘soft saturation’).

Coverage profiles were simulated using equations 4.4 and 4.5; using a reaction probability of $\beta_0=0.01$, coverage profiles are plotted in Figure A.4.1(b) for DEZ dose times of 0.25, 0.5, 1, 2, 4, and 8 seconds, as a function of normalized distance (z/L). The coverage profiles utilize the model previously described, with an infinite DEZ source at $x=0$ corresponding to a partial pressure of 0.07 Torr. The simulation accounts for dose times of up to 8 seconds of exposure time, however, exposure of the fibers surface underneath the patterning mask maybe different. The fibers may experience exposures up to twice that of a silicon monitor wafer, since DEZ must enter and exit through the same portion of the mask, rather than flow-over, as with planar silicon.

In addition, the reversal of the precursor gradient at the mask/substrate interface may not immediately cause the reversal of diffusing DEZ molecules, which may continue to move producing a ‘stretching’ effect with long dose times. If DEZ molecules continue to ‘stretch’ compared to the DEZ dose time, this effect would be more pronounced at long dose times, requiring x-error bars to account for the trend versus expected behavior based on flow-over saturating coverage profile from silicon.

Impact of Extent of Compression on Pattern Resolution

In the nonwoven production process, spun nylon-6 (PA-6) fibers are collected on a collection belt moving in the “machine direction”, MD. Preferential orientation toward the machine direction in the nylon samples is observed, the difference is clearly visible upon comparison of Figure A.4.2(a) and A.4.2(b). The process for PP mats however, produces a more random fiber alignment where orientation effects are less significant. During the subsequent ALD coating, precursor transport will be favored along open channels parallel to aligned fibers. Therefore, for the PA-6, we expect more coating under the mask in the machine direction, whereas it should be mostly isotropic for the PP. The images in Figure A.4.2 (c) show anisotropic coating, consistent with this expectation. For the quantitative analysis discussed below, coating length in the MD and CD are measured and tabulated separately.

Unique Applications

ALD patterning nonwovens is an enabling technology, and offers applicability in electronic textiles, sensors, design, and anti-counterfeiting applications. A requirement for

use in such applications is the ability to pattern complex designs. Figure A.4.3 shows an optical image of North Carolina State University logo patterned onto nonwoven polypropylene using a one second DEZ dose time, inset images were taken with an SEM. Smaller fibers and shorter dose times can be used to improve pattern resolution. The size of the patterning mask is only limited to the ability to pattern the masking material, and as shown in this work, the resulting ALD pattern is influenced by precursor dose time, deposition conditions, and substrate chemistry and structure. The pattern used to make the sample in Figure A.4.3 was produced using the smallest available drill bit in the NCSU machine shop to produce the N and C letters which is 1/16", so use of other techniques such as a 3D printed patterning mask could achieve much better line width and therefore be capable of achieving much more complicated patterns.

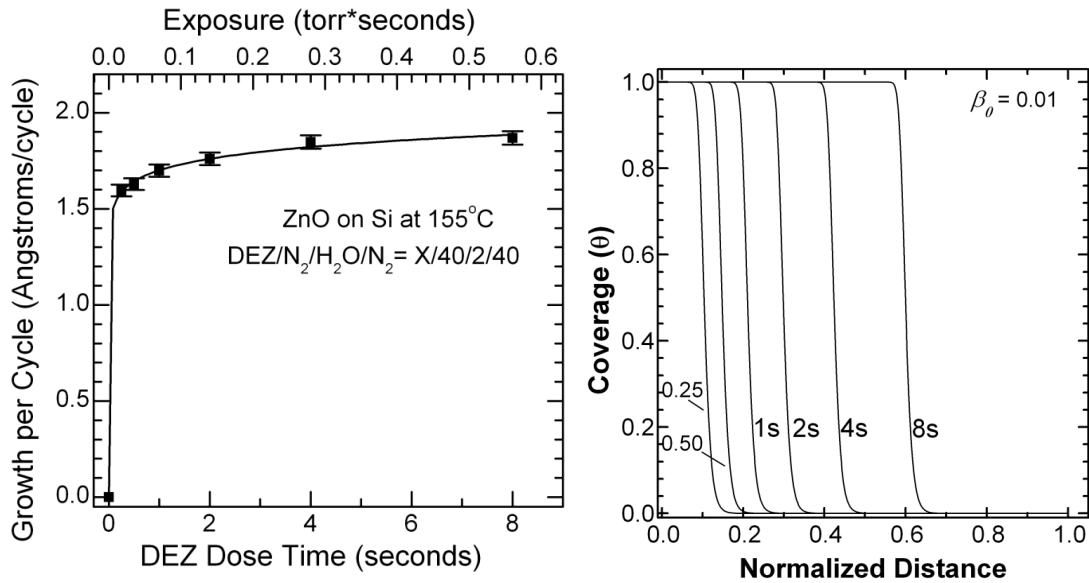
Improvements in pattern resolution may be further attained by depositing ALD coatings at higher pressures. Because the diffusion coefficient changes inversely proportional with pressure, increasing the deposition pressure from ~1 Torr to ~760 Torr for atmospheric ALD, will greatly decrease the amount that DEZ diffuses under the patterning mask.

Use of this technique for application of metal ALD for patterning flexible nonwovens antennas or circuits could provide a fundamental mechanical advantage over devices created with printing or line of sight deposition methods. Specifically, printed metal lines for an antenna will result in a thin metal film carrying the current, which upon significant bending could lead to fracturing, resulting in additional resistances and performance failure in the device. Line of sight deposition will produce features that fail during bending, as the coated portions of fibers lose contact and rearrange. However, ALD coatings of metals such as

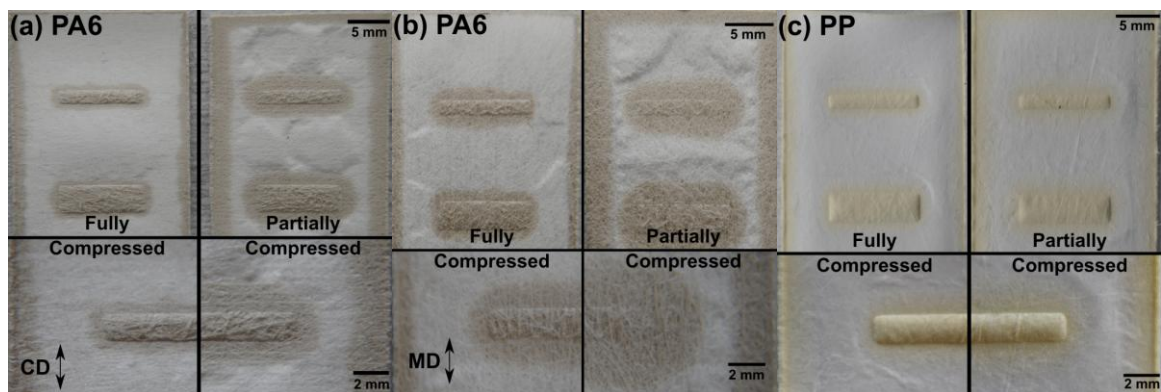
tungsten¹³ conformally coat fibers while avoid binding adjacent fibers. As a metal coated ALD nonwoven feature is bent, fibers will rearrange due to differentials in compressive and tensile forces, as this occurs, some fibers will lose contact with one another, while others make new contacts, allowing current to be maintained without significant degradation. Tungsten coated metal fibers were recently shown to maintain high conductivity even after bending around a 6 mm radius cylinder,¹³ enforcing the prospect of ALD coated nonwovens as a realistic approach towards patterning designs for use in circuits or antennas.

Although the color changing effects of ZnO coatings on the nylon and polypropylene nonwovens used in this work make demonstrating the process easy, clearly the technique is not limited to these chemistries. Nor is the application of compressive forces exclusive to the way in which it has been demonstrate here as applied by screws; any sufficiently heavy weight could be used to produce compression, provided it didn't block access of the precursor to the exposed portions of the patterning mask. Similarly, any sufficiently flat substrate should provide the ability to produce the required compression to produce a coating pattern. As an example of diversity of applicable masks as well as for other applications, nonwoven polypropylene was coated with Al₂O₃, a process that is known to produce a hydrophobic to hydrophilic transition on polypropylene. Figure A.4.4(a.b) shows nonwoven polypropylene inside the patterning mask, as well as what the substrate looks like when placed in water; the 200 cycle Al₂O₃ coating was applied to the substrate at 60°C, and did not produce a visible color change in the coated regions. Clearly the portions of pattern that were covered, maintain polypropylenes natural hydrophobicity, while Al₂O₃ coated portions are wetted by water. A discrepancy in pattern definition can be seen in the patterned sample upon

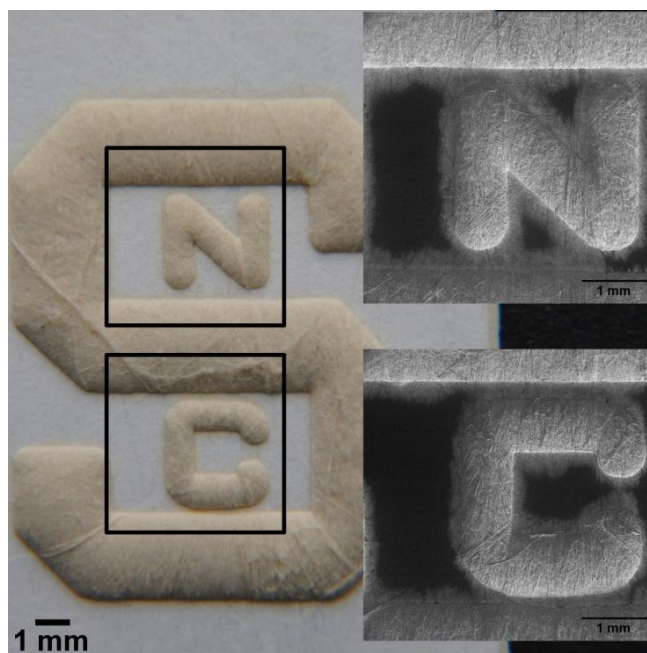
wetting, which is likely due to non-uniform application of compressive force during Al_2O_3 deposition. The compressive force for this substrate was applied by screws and nuts; better pattern uniformity could be achieved by using a more uniform compressive force, but the process is clearly capable of being implemented with readily available materials. Figure A.4.4(c) shows a larger set of three samples being patterned using diamond shaped metal mask the compressive force was applied by screws and nuts as well. Figure A.4.4(d) shows the ZnO patterned polypropylene corresponding to the indicated area of the mask in A.4.4(c). The ability to scale in size is only limited to the ability to uniformly compress the substrate with the patterning mask. In this case, sufficient compression is achieved using rudimentary methods to apply the ZnO pattern shown, but more compression, better force distribution, and careful selection of substrate choice could allow the ability to produce large scale designs with high feature fidelity. For implementation in large scale, a cylindrical roll with patterned stencil could be produced; with precursor gases originating from the cylinders' center, and passing through alternating chemistry zones by method like that of spatial ALD, a roll to roll method for patterning ALD production could be created.



Appendix Figure A.4.1. (a) Growth per cycle for ZnO ALD on silicon, as a function of DEZ dose time, for 400 ZnO cycles deposited at 155°C where a cycle is DEZ/purge/H₂O/purge = X/40s/2s/40s. The observed pressure change during a DEZ dose is ~0.07 Torr, and during an H₂O dose is ~0.28 torr. (b) Coverage profile curves as a function of normalized distance (z/L) for various dose times, using an initial reaction probability of $\beta_0=0.01$; lower initial reaction probabilities produce less abrupt changes in the coverage profile. The coverage curves shown here are related to the experimentally data plot of coating distance vs. dose time, by θ_c the critical coverage value, which is the amount of coverage required to produce a visible coating, which we estimate to be $0.25 \leq \theta_c \leq 0.5$.

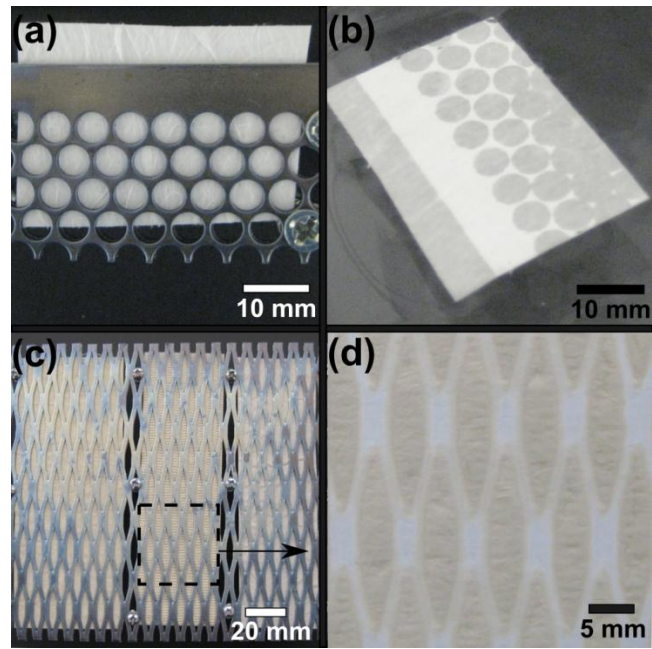


Appendix Figure A.4.2. ZnO patterns in nonwoven nylon and polypropylene after coating with 400 cycles at 155°C on nylon, and 125°C on polypropylene. For both substrate materials, the extent of deposition under the exposed mask depends on the amount of compression used. In this case, ‘full compression’ indicates masking blocks are fully tightened using self tightening screws using an hexagonal wrench, and ‘partial compression’ are tightened to finger tight; for consistency, digital calipers were used to measured height of the combined mask and nonwoven samples to verify tightening was consistent throughout a data set.



Appendix Figure A. 4.3. The NCSU logo patterned on a polypropylene nonwoven mat using ZnO ALD. The insets show SEM images, where the ZnO coating appears lightly colored and the uncoated polypropylene appears dark. The sample was coated with 400 cycles of ZnO at 155°C using dose times of DEZ/purge/H₂O/purge = 1s/40s/1s/40s. This demonstrates the ability to pattern complex designs using ALD and compressive masking. Shorter dose times, smaller diameter fibers and higher compression could be used to increase the resolution of patterned features.

Appendix Figure A.4.4. Patterning is easily performed using Al_2O_3 and ZnO ALD, and can be achieved using anything that can compress the substrate. (a) Perforated aluminum plates are used to compress a polypropylene mat, and is held together using nuts and bolts. 200 cycles of aluminum oxide ALD are deposited at 60°C on the substrate. No color change is observed but the aluminum coating changes the surface energy of the polypropylene to produce a transition from hydrophobic to hydrophilic. (b) The Al_2O_3 patterned substrate is floated on water; the sample selectively wets where the Al_2O_3 coating was deposited, but remains hydrophobic where the substrate was covered by the mask. Uniformity of the compressive force is the key to obtaining well defined pattern replication. The force distribution of the screws is not uniform, resulting in variable pattern quality; a large weight could be used instead of screws to apply force, as long as it permitted sufficient transport of the precursors during ALD. (c) Large scale patterning can be achieved with the technique, and is only limited to the ability to apply sufficient compressive force, the uniformity of which determines pattern quality; (d) the pattern created from ZnO ALD onto polypropylene the location of which is indicated in Figure A.4.4(c).



4.9 References

- (1) Campbell, S. A. *Fabrication Engineering at the Micro and Nanoscale*, 3rd ed; Oxford University Press: New York, 2008.
- (2) Langston, M. C.; Usui, T.; Prinz, F. B. Mechanical Masking of Films Deposited by Atomic Layer Deposition. *J. Vac. Sci. Technol., A* **2012**, *30*, 01A153.
- (3) Kudas, T. T.; Hampden-Smith, M. J. *The Chemistry of Metal CVD*. 1st ed.; VCH: Weinheim, 1994.
- (4) Dolan, G. J. Offset Masks for Lift-Off Photoprocessing. *Appl. Phys. Lett.* **1977**, *31*, 337.
- (5) Dendooven, J.; Deduytsche, D.; Musschoot, J.; Vanmeirhaeghe, R. L.; Detavernier, C. Modeling the Conformality of Atomic Layer Deposition: The Effect of Sticking Probability. *J. Electrochem. Soc.* **2009**, *156*, P63.
- (6) Musschoot, J.; Dendooven, J.; Deduytsche, D.; Haemers, J.; Buyle, G.; Detavernier, C. Conformality of Thermal and Plasma Enhanced Atomic Layer Deposition on a Non-Woven Fibrous Substrate. *Surf. Coat. Technol.* **2012**, *206*, 4511–4517.
- (7) Cherenack, K.; van Pieterse, L. Smart Textiles: Challenges and Opportunities. *J. Appl. Phys.* **2012**, *112*, 091301.
- (8) Wei, Q.; Yu, L.; Wu, N.; Hong, S. Preparation and Characterization of Copper Nanocomposite Textiles. *J. Ind. Text.* **2008**, *37*, 275–283.

- (9) Mackus, A. J. M.; Garcia-Alonso, D.; Knoop, H. C. M.; Bol, A. A.; Kessels, W. M. M. Room-Temperature Atomic Layer Deposition of Platinum. *Chem. Mater.* **2013**, *25*, 1769–1774.
- (10) Parsons, G. N.; Atanasov, S. E.; Dandley, E. C.; Devine, C. K.; Gong, B.; Jur, J. S.; Lee, K.; Oldham, C. J.; Peng, Q.; Spagnola, J. C.; Williams, P. S. Mechanisms and Reactions During Atomic Layer Deposition on Polymers. *Coord. Chem. Rev.* **2013**, *257*, 3323–3331.
- (11) Jur, J. S.; Sweet, W. J.; Oldham, C. J.; Parsons, G. N. Atomic Layer Deposition of Conductive Coatings on Cotton, Paper, and Synthetic Fibers: Conductivity Analysis and Functional Chemical Sensing Using ‘All-Fiber’ Capacitors. *Adv. Funct. Mater.* **2011**, *21*, 1993–2002.
- (12) Sweet, W. J.; Jur, J. S.; Parsons, G. N. Bi-Layer Al₂O₃/ZnO Atomic Layer Deposition for Controllable Conductive Coatings on Polypropylene Nonwoven Fiber Mats. *J. Appl. Phys.* **2013**, *113*, 194303.
- (13) Kalanyan, B.; Oldham, C. J.; Sweet, W. J.; Parsons, G. N. Highly Conductive and Flexible Nylon-6 Nonwoven Fiber Mats Formed using Tungsten Atomic Layer Deposition. *ACS Appl. Mater. Interfaces* **2013**, *5*, 5253–5259.
- (14) Spagnola, J. C.; Gong, B.; Arvidson, S. A.; Jur, J. S.; Khan, S. A.; Parsons, G. N. Surface and Sub-Surface Reactions During Low Temperature Aluminium Oxide Atomic Layer Deposition On Fiber-Forming Polymers. *J. Mater. Chem.* **2010**, *20*, 4213.
- (15) Guziewicz, E.; Godlewski, M.; Wachnicki, L.; Krajewski, T. A.; Luka, G.; Gieraltowska, S.; Jakiela, R.; Stonert, A.; Lisowski, W.; Krawczyk, M.; Sobczak, J. W.;

Jablonski, A. ALD Grown Zinc Oxide with Controllable Electrical Properties. *Semicond. Sci. Technol.* **2012**, *27*, 074011.

(16) Mikami, M.; Eto, T.; Wang, J.; Masa, Y.; Isshiki, M. Growth of Zinc Oxide by Chemical Vapor Transport. *J. Cryst. Growth* **2005**, *276*, 389–392.

(17) Wilson, C. A.; Grubbs, R. K.; George, S. M. Nucleation and Growth during Al₂O₃ Atomic Layer Deposition on Polymers. *Chem. Mater.* **2005**, *17*, 5625–5634.

(18) Oldham, C. J.; Gong, B.; Spagnola, J. C.; Jur, J. S.; Senecal, K. J.; Godfrey, T. A.; Parsons, G. N. Encapsulation and Chemical Resistance of Electrospun Nylon Nanofibers Coated Using Integrated Atomic and Molecular Layer Deposition. *J. Electrochem. Soc.* **2011**, *158*, D549.

(19) Gong, B.; Parsons, G. N. Quantitative In Situ Infrared Analysis of Reactions Between Trimethylaluminum and Polymers During Al₂O₃ Atomic Layer Deposition. *J. Mater. Chem.* **2012**, *22*, 15672.

(20) Yanguas-Gil, A.; Elam, J. W. Self-Limited Reaction-Diffusion in Nanostructured Substrates: Surface Coverage Dynamics and Analytic Approximations to ALD Saturation Times. *Chem. Vap. Deposition* **2012**, *18*, 46–52.

(21) Puurunen, R. L. Surface Chemistry of Atomic Layer Deposition: A Case Study for the Trimethylaluminum/Water Process. *J. Appl. Phys.* **2005**, *97*, 52.

(22) Gong, B.; Peng, Q.; Jur, J. S.; Devine, C. K.; Lee, K.; Parsons, G. N. Sequential Vapor Infiltration of Metal Oxides into Sacrificial Polyester Fibers: Shape Replication and Controlled Porosity of Microporous/Mesoporous Oxide Monoliths. *Chem. Mater.* **2011**, *23*, 3476–3485.

- (23) Welty, J. R.; Wicks, C. E.; Wilson, R. E.; Rorrer, G. *Fundamentals of Momentum, Heat, and Mass Transfer*, 4th ed; Wiley: New York, NY, 2001.
- (24) Epstein, N. On Tortuosity and the Tortuosity Factor in Flow and Diffusion through Porous Media. *Chem. Eng. Sci.* **1989**, *44*, 777–779.

CHAPTER 5 is a reprint of a manuscript submitted for publication.

CHAPTER 5. The Conductivity and Touch-Sensor Application for ALD ZnO and Al:ZnO on Nylon Nonwoven Fiber Mats

William J. Sweet III, Christopher J. Oldham, and Gregory N. Parsons*

Department of Chemical and Biomolecular Engineering, North Carolina State University,

Raleigh North Carolina 27695, United States

5.1 Abstract

Flexible electronics and wearable technology represent a novel and growing market for next generation devices. In this work, we deposit conductive zinc oxide films by atomic layer deposition onto nylon-6 nonwoven fiber mats and spun-cast films, and quantify the impact that deposition temperature, coating thickness, and aluminum doping have on the conductivity of the coated substrates. We produce aluminum doped zinc oxide (AZO) coated fibers with conductivity of 230 S/cm, which is $\sim 6\times$ more conductive than ZnO coated fibers. Furthermore, we demonstrate AZO coated fibers maintain 62% of their conductivity after being bent around a 3mm radius cylinder. As an example application, we fabricate an ‘all-fiber’ pressure sensor using AZO coated nylon-6 electrodes. The sensor signal scales exponentially under small applied force ($< 5 \text{ g/cm}^2$), yielding a $\sim 10^6\times$ current change under 200 g/cm^2 . This lightweight, flexible and breathable touch/force sensor could function, for example, as an electronically active nonwoven for personal or engineered system analysis and diagnostics.

5.2 Introduction

Conductive oxides have found a wide array of applications in solar cells, electronic displays and lighting, as well as in UV and chemical sensors.¹⁻⁴ Zinc oxide is low cost and can be readily doped with other earth-abundant materials to form an n-type transparent conductor with $\sigma > 1000$ S/cm.^{1,4} Zinc oxide is easily deposited by atomic layer deposition (ALD) at low temperatures ($< 200^\circ\text{C}$) using diethyl zinc DEZ and water,¹⁻⁵ and adding cycles of trimethylaluminum (TMA), trimethylgallium (TMG) or trimethylindium to the ALD sequence leads to Al-doped ZnO (AZO)^{1,4}, Ga-doped ZnO (GZO),^{4,6} or In-doped ZnO,^{6,7} respectively. The typical temperature range for ALD ZnO is $100\text{-}180^\circ\text{C}$,^{2,5} but deposition at higher temperatures maybe appealing to increase conductivity.³ For conductive coatings on polymer fibers, nonwoven fiber mats are highly versatile because they can be produced in high volume at low cost, in many polymer chemistries, and offer control over fiber geometry, fiber diameter ($10\ \mu\text{m}$ to $<100\ \text{nm}$), web density, and specific surface area.⁸ Polyamide-6 is an attractive example nonwoven substrate, in part, because it does not begin to melt until $\sim 215^\circ\text{C}$.⁹

Previous reports demonstrate ZnO ALD on various polymer fibers substrates including nylon-6,^{10,11} cotton,¹² paper,¹² polypropylene,^{5,12,13} polyethylene terephthalate,¹³ polybutylene terephthalate,¹⁴ polylactic acid,¹⁵ and polyacrylonitrile.¹⁶ Most reports focus on performance of the deposited samples, rather than understanding how properties are affected by process conditions. In this work, we examine the effect of substrate preparation and ALD processing conditions on deposition and conductivity of ZnO and Al-doped ZnO coatings on

nylon-6 nonwoven fiber mats. We also investigate the mechanical performance through tensile strain and bend testing Al-doped ZnO coated substrates and characterize the failure method of the ceramic/polymer interface under these deforming forces. Furthermore, we build, calibrate, and demonstrate an all-fiber pressure sensor using AZO coated nylon-6 nonwoven electrodes, and demonstrate change in current, $\Delta I > 10^6$ for 200 g load.

5.3 Experimental

Preparation of Fibers and Films

Spunbond nylon-6 hydroentangled nonwoven fabric was provided by Allasso Industries. The Allasso-PA6 had a basis weight of $\sim 75\text{g/m}^2$, average fiber diameters of 1-10 microns, and multi-lobal winged fiberTM cross section. The nylon nonwoven mat was approximately 0.3 mm thick and had a specific surface area of $\sim 2.5\text{ m}^2/\text{g}$ as determined using the Brunauer-Emmett-Teller (BET) surface analysis technique.

Figure 5.1 shows optical and scanning electron micrograph images of the nylon-6 substrate. Figure 5.1 also includes a histogram with the orientation distribution of fibers relative to the cross direction, which is a common metric for analyzing the anisotropic nature of the fiber orientation within the nonwoven.

Nonwoven materials are formed continuously by extruding or spinning onto a moving belt, yielding flat mats with randomly oriented fibers. The belt moves in the machine direction (MD), and the direction along the mat width is the cross direction (CD). At high production speeds, fibers can become more preferentially ordered into the machine direction, as determined from fiber orientation distribution analysis. Fiber orientation distribution was

measured from 0° - 180° (relative to the cross direction at 0°), and the data is plotted in Figure 5.1(d). The fraction at 0° corresponds to CD fibers and that at 90° are MD fibers. A fully uniform orientation shows ~5% in each column.

Nylon-6 fiber samples were cut into either 3.2 cm x 1.2 cm or 6.0 cm x 1.2 cm rectangles. Nylon samples were weighed before and after ALD using a Fisher Scientific Accu-124 Series analytical lab scale, which has a ± 0.1 mg sensitivity limit. We measured the fractional mass gain after ALD using $\%MG = (m_2 - m_1)/m_1$, where m_1 is nylon mass prior to deposition and m_2 is the mass of the sample after ALD coating. A typical sample would weigh between 24-27 mg prior to deposition. After 300 ALD cycles, the mass increases by 18-20 mg (45% mass gain). The mass of the ZnO is then used in the effective conductivity analysis.

To compare growth on fibers with films on planar substrates, nylon-6 planar films were prepared on 1x1 inch pieces of silicon. After dissolving the Allasso nylon-6 nonwoven in formic acid (Fluka Analytical, 98% purity, 2% H₂O) at 60°C for two hours, a solution of 3wt% nylon-6 in formic acid was spun at 6000 rpm for 1 minute, and then annealed on a hot plate for 1 minute at 90°C . The ALD then proceeded under the same conditions as for the fibers. Spectroscopic ellipsometry was used to measure the thickness of the films before and after deposition, multiple measurements were averaged for the data shown. Control experiments showed no change in polymer film thickness by ellipsometry during heating at deposition conditions.

Atomic Layer Deposition Reactor and Process

In addition to the nylon-6 fibers and films, three pieces of silicon, (one with a 150 nm thermal oxide), were simultaneously coated in each run. The thermal oxide silicon sample was ~2.5 cm x 2.5 cm, and was used for four-point probe conductivity analysis.

After preparation, all samples were placed in a wire mesh sample holder along with the silicon, and then placed in the deposition chamber and allowed to equilibrate for at least 20 minutes at the deposition temperature. This anneal removed excess water from hygroscopic nylon-6, which can contain up to 3 wt.% water. Deposition was performed in a custom built hot wall reactor described in previous work.¹⁷ Nitrogen gas (National Welders, 99.999% pure) was filter dried by an Aeronex Gatekeeper and used as a carrier gas flowing at 150 standard cubic centimeters per minute (sccm). The system was pumped by a rotary mechanical pump with a background pressure of 1×10^{-3} Torr and a leak rate of $\sim 1 \times 10^{-3}$ Torr/min. Deposition was performed at a pressure of 1 Torr as measured by a convectron gauge (Granville-Philips). Trimethyl aluminum (98% purity, STREM Chemicals), diethyl zinc (95% purity, STREM Chemicals) and water (UV-deionized) were used as reactants. A typical ZnO deposition run had precursor doses of $\text{DEZ}/\text{N}_2/\text{H}_2\text{O}/\text{N}_2 = 2.0/40/2.0/40\text{s}$ and was performed between 80°C and 200°C. Aluminum doping was used to produce the AZO samples, and was performed by introducing an Al_2O_3 cycle after 19 ZnO cycles. A typical dopant cycle is $\text{TMA}/\text{N}_2/\text{H}_2\text{O}/\text{N}_2 = 2.0/40/2.0/40\text{s}$. A metering valve was used to regulate precursor dose. The pressure change was $\sim \Delta P = 0.1$ Torr during the TMA dose, $\sim \Delta P = 0.07$ Torr for DEZ, and $\sim \Delta P = 0.28$ Torr for water.

Conductivity Analysis

Using four-electrode probe described previously¹² we determine the effective conductivity of the deposited coating on the fiber mat, σ_{eff} , using:

$$\sigma_{\text{eff}} (S \cdot \text{cm}^{-1}) = \frac{L \cdot \rho}{m_{\text{coating}}} \cdot s \cdot \frac{1}{R} \quad (5.1)$$

where we use the bulk ZnO density, $\rho = 5.71 \text{ g/cm}^3$, the electrode length $L=0.5 \text{ cm}$ and separation $s = 0.5 \text{ cm}$, the mass of ZnO between the inner electrodes $m_{\text{coating}} = 1.76 \times 10^{-3} \text{ g}$ (determined from the mass change upon coating), and the measured resistance, R . Typical applied current is 0.1 μA -1 mA, which typically produces a voltage of $\sim 20 \text{ mV}$ in a conductive sample. The nylon-6 fibers without a conductive coating have $R > 2 \times 10^8 \Omega$, which is the upper limit for resistance using this probe. A 300 cycle ZnO coating yields $R=33\Omega$ which gives $\sigma_{\text{eff}} = 24.6 \text{ S/cm}$. For fiber mats with preferred fiber orientation (i.e. in the machine direction or cross direction), measurements are collected with samples oriented in each direction.

For comparison, sheet resistance was measured for films deposited on electrically insulating thermal oxide silicon wafers using a 4-point probe (Jandel multi-height probe with RM3-AR test unit), a minimum of four times per sample. The thickness of spun-cast nylon and planar ZnO films was determined using spectroscopic ellipsometry (Alpha S.E., J.A. Woollam), and was performed multiple times on each sample. Imaging was performed using a FEI Phenom scanning electron microscope (SEM) operating at a 5 kV accelerating voltage. For bare nylon-6 substrates, a 5 nm Au/Pd coating was sputtered on the samples prior to imaging. X-ray diffraction (XRD) was performed at the NCSU Analytical Instrument

Facility using a Rigaku SmartLab X-ray diffractometer with a CuK α X-ray source. Fiber orientation analysis was performed in the NCSU College of Textiles, using an optical microscope equipped with orientation analysis software. Data was gathered from five replicates for the substrate material, the average values are plotted in Figure 5.1(d).

5.4 Results and Discussion

Nucleation and Growth of Zinc Oxide on Polyamide-6

Figure 5.2(a) shows ZnO thickness on silicon and planar spun-cast nylon-6 film (measured by ellipsometry) versus cycle number at T=150°C. Growth is linear at 1.7 Å/cycle, and extrapolation of the data on silicon shows a ~6 cycle nucleation delay. On planar nylon-6, the growth rate is similar, and the delay is ~71 cycles. Figure 5.2(b) contains the net mass gain of the ZnO/nylon-6 nonwoven versus DEZ dose time and ALD cycle number. The delay in mass gain is ~60 cycles, although mass gain during ALD on polymers does not scale linearly at low cycle number.^{5,17} The amide group in nylon-6 will react with trimethyl aluminum¹⁷ and diethyl zinc,¹⁰ although it is less reactive with DEZ.¹⁸ The high surface area of the nylon-6 “winged” fibers results in a larger mass gain than would be expected for ALD on the same mass of cylindrical fibers of comparable diameter.

Figure 5.3 shows the saturation behavior, as determined from mass gain, for deposition on silicon and nylon fiber, as a function of DEZ dose time. Deposition was 300 cycles using DEZ/N₂/H₂O/N₂ = x/40/x/40s. A 0.5 s DEZ dose was sufficient for saturation on silicon, whereas a larger dose was needed on the higher surface area fibers. Figure 5.4

plots ZnO film thickness on silicon and mass gain on nylon fibers as a function of deposition temperature. Results follow expected trends.^{2,3,5}

Figure 5.5 shows cross sectional transmission electron micrographs of nylon-6 fibers coated with 300 cycles of ZnO at 100°C and 190°C. Figures 5.5(a) and 5.5(b) show that the lobed fiber structure of the Allasso Winged FibersTM form trenches between them which increases the surface area of the nonwoven compared to a circular fiber of similar diameter. ALD forms a conformal ZnO coating along the fiber lobes, and the coating/polymer interface is abrupt. From the TEM images, the ZnO thickness appears to be ~68 nm for the 100°C sample, and ~41 nm for the 190°C, which correspond reasonably well to 50 and 38 nm for 100 and 190°C samples, respectively, as measured by ellipsometry. We note that cross sectional TEM can distort the thickness measurement for coatings on fibers, in part because the fiber axis is not necessarily oriented perpendicular to the microtome cut.

To investigate the effect of deposition temperature on crystal structure, Figure 5.6 shows XRD scans for samples with 300 cycles of ZnO deposited at 100°C, 125°C, 150°C and 200°C on (a) thermal oxide silicon, and (b) nylon-6 nonwovens. Results from a control nylon fiber sample without ZnO coating is also shown. Peaks at 33° and 62° in Figure 5.6(a) are due to the underlying Si(100) substrate. The dominant ZnO crystal orientation for films deposited at 100°C on silicon is (100), with a strong (002) peak and a small (110), consistent with hexagonal ZnO. At deposition temperatures $\geq 125^\circ\text{C}$, the (002) peak is dominant, and for depositions at 150°C and 200°C, a (101) peak forms and the (100) peak weakens in intensity. Nylon-6 has a higher surface area than silicon, and therefore the resulting XRD scans have stronger signal intensity.

On fibers, the (100) and (101) peaks appear stronger, with deposition at 100°C showing a (100) strongest peak, and films deposited $\geq 125^\circ\text{C}$ show strongest (101) peaks, while all temperatures show a less intense (002) peak than on silicon, possibly resulting from the conformal growth of the film, or from some difference in nucleation orientation on the polymer fibers.

Previous reports^{1,3,19-21} of ZnO conductivity show conductivity tends to increase with deposition temperature up to 200°C, and an accompanying transition in crystallinity. In addition to crystallinity fraction, conductivity can also be affected by film roughness, average crystal size, and the Zn:O ratio.^{3,22,23} The most conductive films deposited at temperatures near 200°C have high carrier concentrations but low electron mobility.^{19,22,24,25}

Impact of Fiber Orientation on Zinc Oxide Conductivity

Figure 5.7 plots the conductivity as a function of DEZ dose time for samples coated with 300 cycles of ZnO ALD on thermal oxide silicon, spuncast nylon-6 film, and nylon nonwoven fibers oriented in the machine and the cross direction. Generally, the conductivity is small for the smallest dose times, corresponding to sub-saturated growth, and it increases and saturates at longer dose times. On planar SiO₂ substrates, the ZnO conductivity saturates is ~ 135 S/cm, and on a spuncast PA-6 film we measure $\sigma = \sim 105$ S/cm which is reasonably close to that on planar substrates. On fiber mats, the conductivity is reduced by 3 \times and 5 \times for mats with fibers preferentially oriented in the machine direction and cross directly, respectively. Fibers oriented in the machine direction run in parallel with the current flow in

the measurement system. For the cross direction, fiber alignment perpendicular to current flow adds extra resistance because current must move more between fibers.

Aluminum Doping of ZnO on Fibers

ALD zinc oxide can be readily doped by using alternating cycles of a dopant such as trimethylaluminum.²⁶ We deposited Al-doped ZnO (AZO) using 1 Al₂O₃ ALD cycle after each 19 ZnO ALD cycles. The coating conductivity was investigated as a function of ALD cycle number for both ZnO and AZO as shown in Figure 5.8. For AZO on silicon at 150°C, the conductivity approaches 6×10^2 S/cm for 1000 cycles which is close to $5 - 12 \times 10^2$ S/cm reported previously.^{1,25,27} The conductivity versus thickness on the fibers follows the same trends as on planar substrates, but the conductivity is $\sim 3-5 \times$ less, depending on the fiber alignment.

The effect of deposition temperature on σ_{eff} of ZnO and AZO on various substrates is shown in Figure 5.9. The conductivity of AZO is relatively constant above $\sim 130^\circ\text{C}$ for deposition on silicon and on fibers. For ZnO, the conductivity decreases on fibers for $T = 190^\circ\text{C}$, which is approaching the PA-6 melting temperature of 215°C . This decrease is not observed for AZO at $T > 190^\circ\text{C}$, possibly because the TMA may react at the ZnO/polymer interface to stabilize the material. For further analysis, we maintained deposition temperature $< 190^\circ\text{C}$.

The conductivity of ZnO and AZO coated fibers and films was measured for an extended period of time to investigate how the conductivity of the materials changed upon extended exposure to the labs ambient conditions. The initial conductivity measurements

were taken a few minutes after the samples were taken out of the ALD reactor, and then measurements were taken intermittently for up to 10,000 hours, in between measurements the samples were stored exposed to lab air in covered vessels. On fibers and planar silicon, the AZO conductivity stayed constant ($\pm 5\%$) over the measurement period. A small decrease in ZnO conductivity was also observed, likely due to reaction with ambient oxygen.

Mechanical Properties of AZO Coated Nylon-6 Nonwovens

Mechanical performance of ALD coatings applied to polymers is of interest for applications in flexible electronics, packaging and encapsulation, and electronic textiles. Recent reports show ALD coatings can enhance or degrade mechanical performance, depending on properties of the substrate and the coating.^{11,28-30} For some applications, conductive fibers may have a mechanical advantage over planar films because fibers offer a multiplicity of parallel conduction pathways, so that many fractures are needed before failure.^{29,30}

To investigate durability of AZO on fibers, we exposed coated fibers to various amounts of tensile strain and measured σ_{eff} after strain release. Results are plotted in Figure 5.11. While the conductivity is larger for deposition at higher temperature, growth temperature between 115°C and 200 °C does not greatly impact the change in conductivity upon tensile strain. Recently Sun et al³⁰ showed with nano-indentation that the critical strain required to induce crack formation increased with deposition temperature between 60°C and 120°C for Al₂O₃ ALD deposited on spun-cast PA6 films. Our results suggest that this propensity for crack propagation with increasing temperature does not extend to ZnO ALD

films on fibers. Figure 5.11(b) shows conductivity versus tensile strain for different thickness AZO coatings formed at 200°C. The thicker films show larger conductivity, but as in Figure 5.11(a) the conductivity change upon tensile strain is nearly the same for all samples. Jen et al²⁹ found for Al₂O₃ on heat stabilized polyethylene naphthalate sheets, decreasing the coating thickness from 80 nm to 5 nm made them more robust, capable of withstanding ~1.9% larger tensile strain before cracking. Our results do not show a marked change in strain resistance as ZnO films decrease in thickness from ~ 61 to 12 nm. Results in Figure 5.12 show the effect of fiber orientation relative to applied stress. As expected, applying stress parallel to the fiber direction (along the machine direction) degraded conductivity more than for similar stress applied perpendicular to the fiber alignment (cross direction). Stress along the cross direction tended to reorient the fibers, with less cracking and related damage. Because the conductivity follows many pathways in a conductive fiber mat, applying mild stress (< 20%) does not cause catastrophic conductivity loss. The materials studied here do not exhibit elastic behavior, so re-straining a previously strained sample is expected to add strain to the coating.

The Impact of Fiber Orientation on Conductivity Retention upon Flexing

In addition to tensile stress response, we measured conductivity change upon fiber mat flexing around a radius between 4.50 and 0.29 cm in the cross direction (fibers parallel to the bending axis) or the machine direction (fibers perpendicular to bending axis). Figure 5.13 shows the conductivity of AZO coated MD and CD nylon-6 as a function of the inverse bending radius. All samples show decreased conductivity upon bending, but the extent of

loss depends on fiber alignment relative to the bending. Samples measured in the cross direction start with somewhat smaller σ_{eff} but the conductivity loss is 38%, versus 53% for fibers measured and bent in the machine direction. We note that the AZO-coated fibers have higher conductivity than similar fibers coated with undoped ZnO, and the AZO-coated nylon-6 fibers retain their conductivity better than ZnO-coated samples under the same measurement conditions.⁵

We also used SEM to examine crack formation upon straining AZO-coated PA6 fibers (Figure 5.14). Before straining (i.e. after routine sample handling), no cracks are seen in the AZO coating. Upon 5% strain, cracks are visible, although large portions of the fiber remain uncracked. Arrows in Figure 5.14 highlight partial fractures in the AZO after 5% strain. After 10% strain, cracking increases, including both partial and fully separated cracks. After 20%, most cracks appear separated. We also note that along an individual fiber, the crack spacing appears to be uniform, indicating uniform applied stress. Furthermore, each set of fibers imaged (up to 20% strain) showed some fibers that remained unfractured.

As a possible application for conductive coatings on fibers, Figure 5.15(a) shows an all-fiber pressure sensor using AZO coated nylon-6 nonwoven. Gold wire contact electrodes were threaded through two nylon nonwoven substrates, followed by coating with 400 cycles of AZO at 150°C. The AZO electrodes were then stacked with an insulating nonwoven polypropylene spacer between them, then the three materials were stitched together with insulating cotton thread. A small hole cut in the PP spacer (inset in Fig. 5.15a) allows the conducting electrodes to make contact under applied pressure. The current response, $R = I_{\text{on}}/I_{\text{off}}$, where I_{on} and I_{off} are the current (bias voltage = 1V, contact area $\sim 1\text{cm}^2$) with and

without mass applied, respectively, is plotted for different applied mass in Figures 5.15(b) and (c). Figure 5.15(b) shows R under light, medium and heavy applied finger pressing force. The R value is repeatable and returns to ~ 1 (i.e. $I=I_{\text{off}}$) after each touch. Figure 5.15(c) shows similar measurements using known mass applied over $\sim 1\text{cm}^2$. The R value increases exponentially between 0 and ~ 50 g, then saturates at $R\approx 10^6$ for ~ 200 g, or ~ 10 mA compared to 10 nA with no applied mass. This exponential change in signal with applied force could be useful, for example, for lightweight, flexible and breathable touch or force sensor electrodes integrated into textiles or advanced electronically active nonwoven materials for personal or engineered system analysis and diagnostics.

5.5 Conclusion

In this work we have investigated ZnO deposition on nylon-6 nonwoven fibers and spun-cast films, and examined the impact of deposition conditions on ZnO ALD film growth behavior and as well as the conductivity of the deposited ZnO on silicon, spun-cast nylon-6 films, and nylon-6 nonwoven fibers. As a function of ALD cycle number, we found the conductivity of ZnO coatings on films and fibers increases as a function of cycle number until reaching saturation conductivity on all substrates by 600 ZnO ALD cycles. It was also determined that the effective conductivity measured for ZnO coated nylon-6 was dependent on the dominant orientation of the fibers in the nonwoven mat; the more conductive fiber orientation produced samples that had an effective conductivity $\sim 2.5\times$ than the less conductive orientation. Aluminum doping of the ZnO films produced a $\sim 4\times$ increase in conductivity of films deposited on silicon and $\sim 6\times$ on fibers, and thin film AZO coatings did

not show the same dramatic drop off in conductivity exhibited by undoped ZnO coatings for thicknesses of ≤ 200 cycles. Both Al-doped and undoped ZnO films exhibited lower conductivity for substrates deposited $\leq 120^{\circ}\text{C}$, while higher temperatures up to 190°C produced increasing conductivity for ZnO and AZO on silicon, as well as AZO on nylon-6, while it resulted in lower conductivity undoped ZnO coated nylon-6 fibers. AZO coated nylon-6 fibers were shown to better maintain their conductivity after being exposed to ambient conditions, with samples maintaining between 91-98% of their initially measured conductivity after $>10,000$ hours ambient exposure, while ZnO coated nylon-6 fibers maintained only 58-62% of their initially measured conductivity over the same period.

AZO coated nylon-6 nonwovens were subjected to tensile straining and bending and the conductivity was measured afterwards to determine the impact of such mechanical deformation to the conductivity of the coated substrate. The AZO coated substrates proved to be mechanically robust, maintaining up to 14% of their conductivity after having been stretched 20%, or maintaining up to 62% of their conductivity after having been bent around a 3mm radius cylinder. SEMs of the stretched samples suggest fibers in close proximity can be subjected to very different forces, as evidence by significant cracking damage in one fiber while the adjacent fiber is hardly affected. The conductivity durability of the tested material arises in part due to the multitude of pathways that exist in a conductive nonwoven, which is what makes them particularly robust compared to planar thin films, which are subject to critical failure upon the formation of a crack. As demonstrated through the fabrication of an all-fiber pressure sensor, AZO coated nonwovens can be sufficiently conductive to serve as electrodes for flexible devices. Through the systematic study of the electrical and mechanical

properties of ZnO ALD thin films deposited on an industrially important thermoplastic that is both sufficiently reactive and thermally stable, we have incorporated conductivity into a strong, flexible and light weight material that could be used to enable new applications for use in next generation materials, flexible electronics, wearable technology and e-textiles.

5.6 Acknowledgements

We acknowledge the Nonwovens Institute at North Carolina State University (NWI) Project 09-118 for support for W.J.S. We acknowledge Amy Minton for help performing the fiber orientation analysis at the Nonwovens Institute Microscopy and Fiber Imaging Lab, as well as Roberto Garcia and Toby Tung at the NC State Analytical Instrument Facility for their assistance with TEM imaging and analysis.

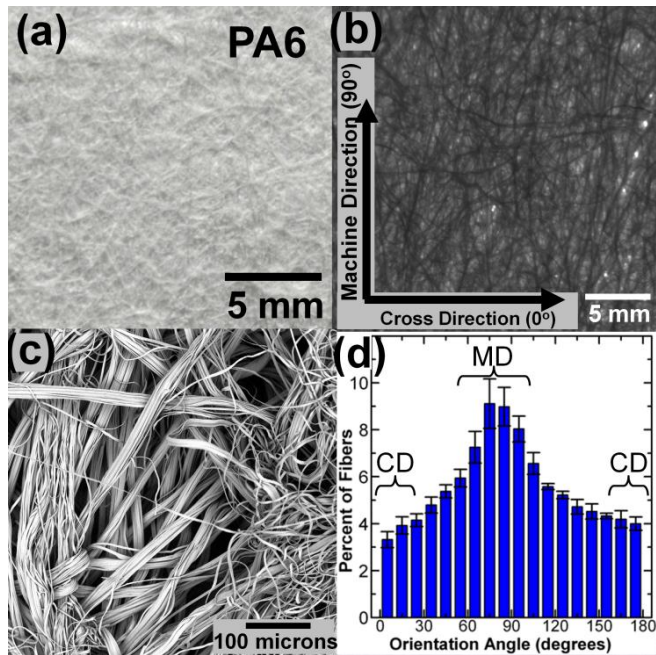


Figure 5.1. The nylon-6 nonwoven substrate used in this work, as shown in (a) picture, (b) optical microscopy image, (c) scanning electron micrograph. The orientation distribution of fibers that comprise the nonwoven is shown in (d), which plots the percentage of fibers aligned relative to the cross direction; in this histogram the ‘machine direction’ orientation is in the center.

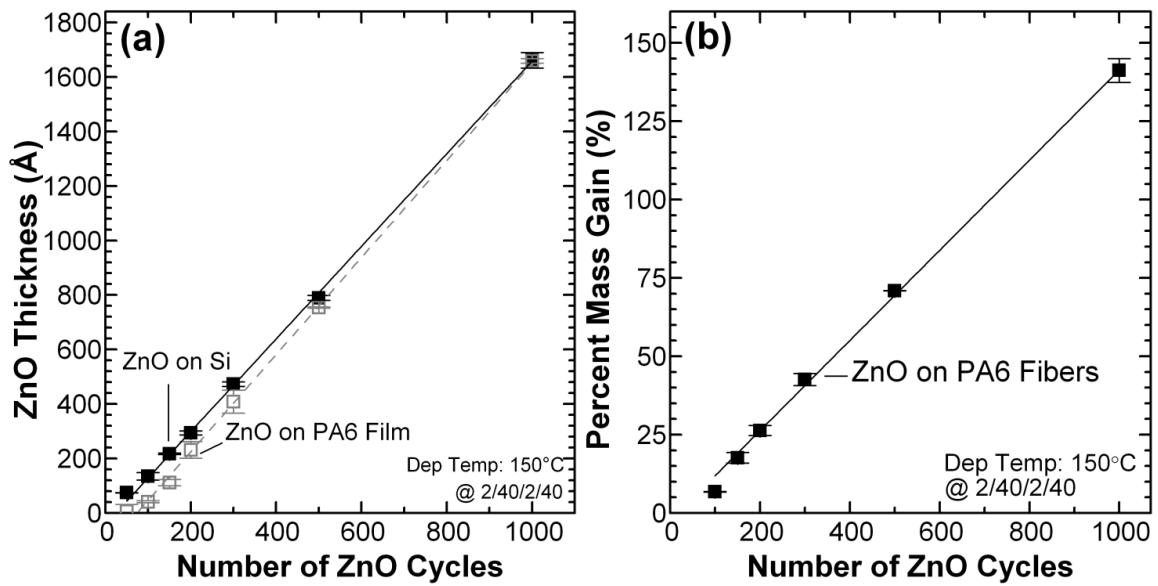


Figure 5.2. (a) Zinc oxide film thickness is plotted as a function of cycle number for deposition on silicon and spuncast nylon-6 films. ZnO films appear to grow well on native silicon, exhibiting ~1.7 Angstroms/cycle growth, whereas deposition on nylon-6 film appears to initially inhibit ZnO deposition. (b) The mass gain measured after ZnO deposition on nylon-6 fibers is plotted as a function of cycle number.

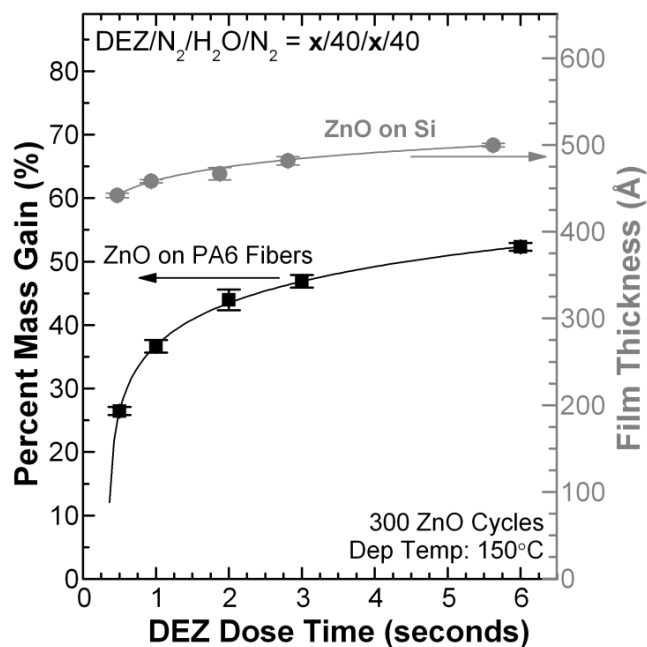


Figure 5.3. Mass gain for 300 cycles of ZnO deposited at 150°C, as a function of DEZ/H₂O dose time for deposition on Allasso Winged Fiber™ nylon-6 nonwoven (black squares); ZnO film thickness on silicon (grey circles) is plotted for reference. Saturation is easily achieved on silicon, where a 0.5 second dose is sufficient to achieve ~90% of the film thickness of a 6 second dose, whereas the PA6 fibers require a 2 second dose to meet this requirement. The nylon-6 is a higher surface area material and therefore requires more precursor to reach saturation.

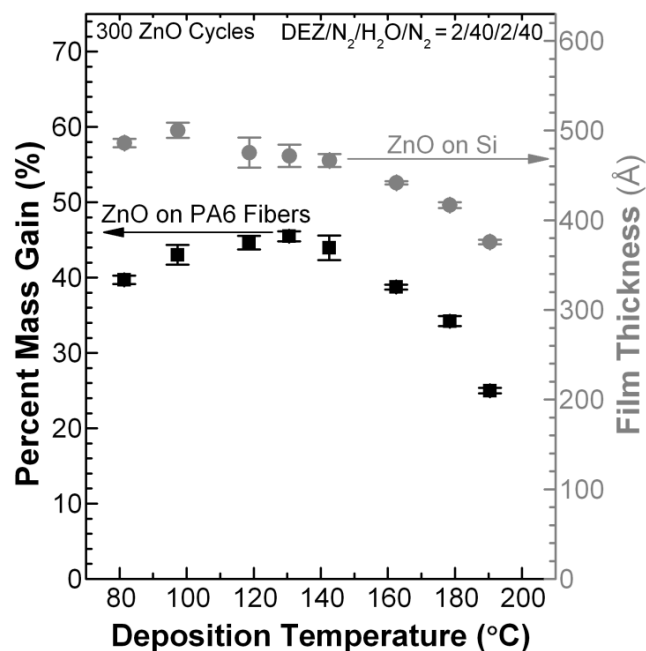


Figure 5.4. The mass gain of ZnO coated nylon nonwoven samples is plotted as a function of deposition temperature. ALD on polymers is a function of both the coating chemistry (such as properties of the ALD window) as well as properties of the polymer. Thermal expansion of the polymer as a function of temperature may influence the deposited coating by effecting diffusion. The limiting characteristic such as reactivity or diffusivity may shift over the deposition window. At higher temperatures, reactivity of the coating may decrease diffusion into the polymer, which may explain the observed lower mass gain at higher deposition temperatures.

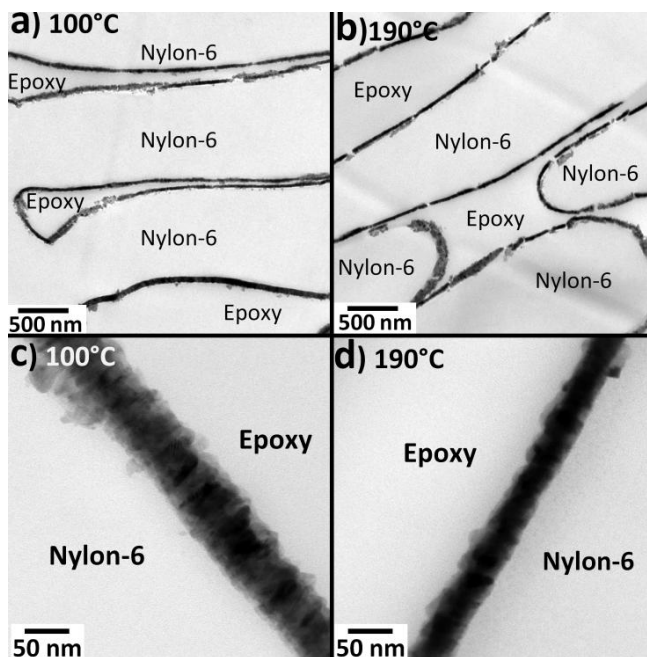


Figure 5.5. TEM images of 300 cycles of ZnO ALD deposited on nylon-6 fibers at (a,c) 100°C and (b,d) 190°C. The lobe structure of the Winged Fibers™ can be seen in the low magnification images. The high magnification images show abrupt ZnO/nylon-6 interfaces for both 100°C and 190°C deposition with no significant diffusion region or subsurface nucleation.

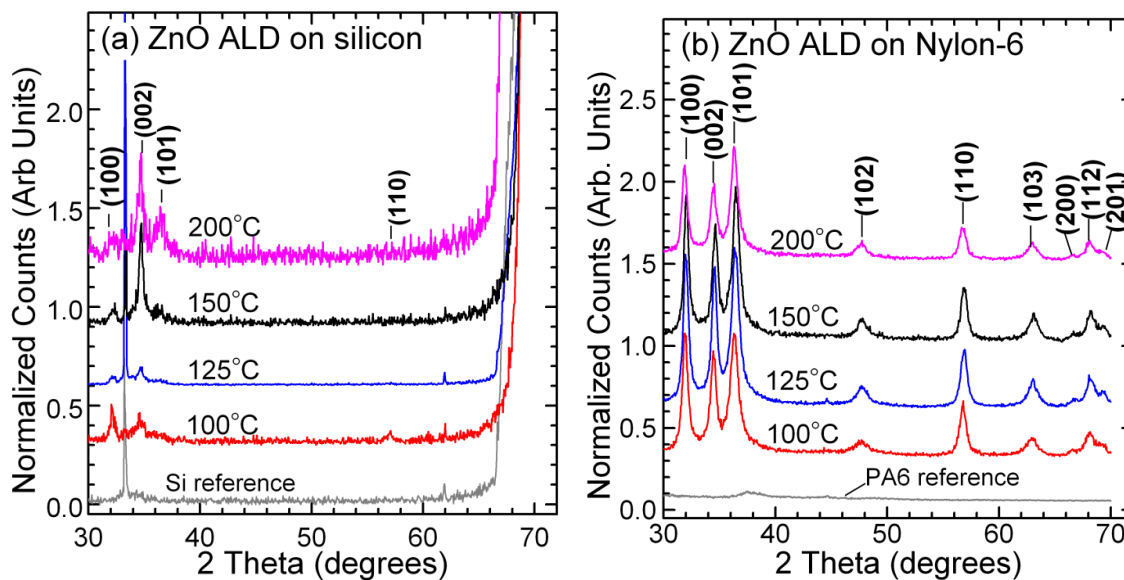


Figure 5.6. XRD scans of 300 ZnO ALD cycles deposited at various temperatures on (a) thermal oxide silicon, and (b) nylon-6 fibers. In the nylon-6 fiber XRD, higher surface area material leads to more clearly defined peaks, but most of the same features are visible in the silicon XRD as well. A scan of the silicon substrate that was used is shown for reference, as is an uncoated piece of nylon-6 fibers. The XRD scans are normalized to the highest peak value. Peak identification was determined by the use of ICDD (PDF 2009) 00-036-1451 and 00-054-2323 material data files.

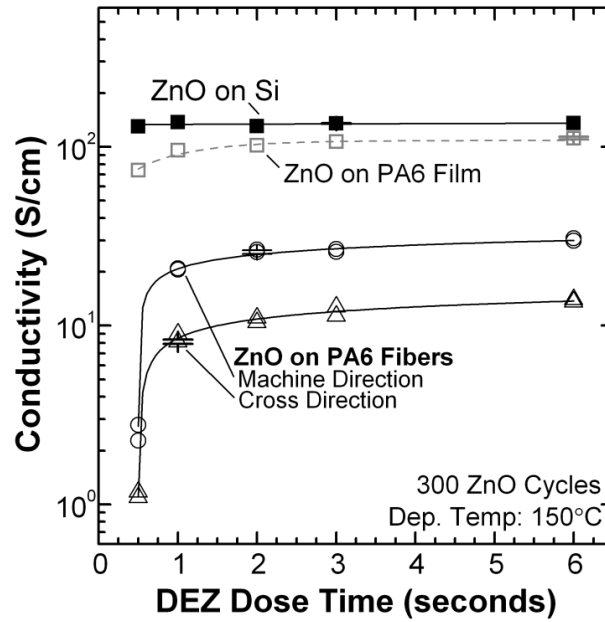


Figure 5.7. Conductivity of 300 cycle ZnO ALD coated substrates as a function of DEZ dose time on thermal oxide silicon (black squares), spuncast nylon-6 film (hollow squares), nonwoven fibers oriented in the machine direction (hollow circle) and the cross direction (hollow triangles). Machine direction fibers preferentially aligned perpendicular to the measurement electrodes, whereas cross direction fibers are preferentially oriented paralell to the measurement electrodes. As a result, cross direction fibers have higher inter-fiber transfer of current, which introduces additional fiber-fiber resistances, resulting in lower effective conductivity for the same ZnO coating.

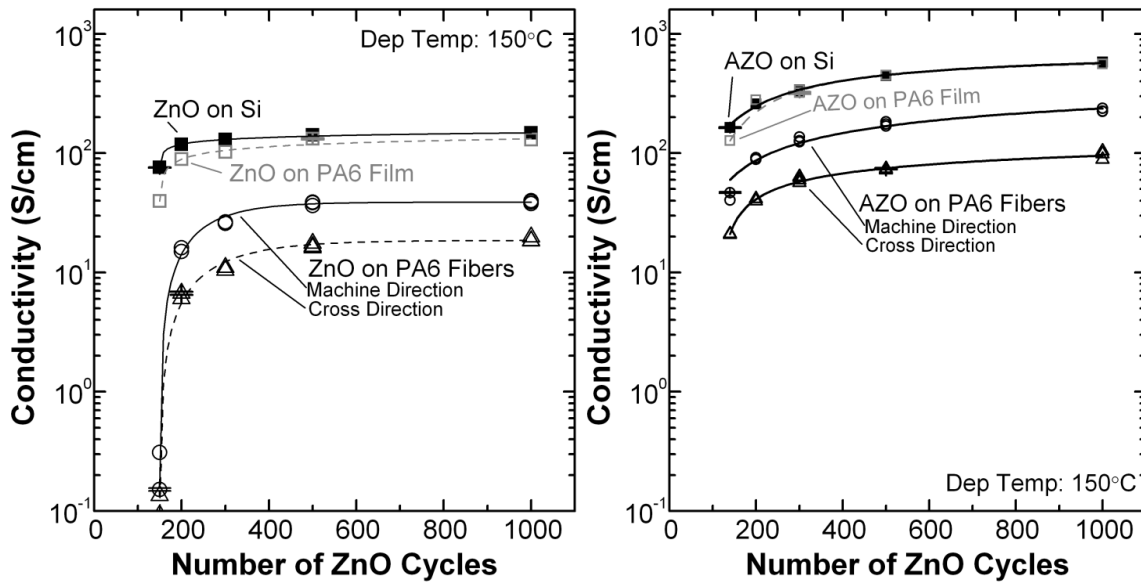


Figure 5.8. Conductivity of various planar and fibrous substrates, plotted as a function of ALD cycle number, for (a) ZnO ALD and (b) AZO ALD coatings. ZnO conductivity is dependent on film thickness for thin films (< 400 ALD cycles); only moderately so for films on silicon for spuncast PA6 films, but the conductivity of coated fibers shows a strong dependence. The conductivity of AZO films appear dependent on film thickness for all substrates, over the range of thicknesses investigated. Interestingly, thinner AZO coatings on fibers do not exhibit a decrease in conductivity to the same extent as the ZnO coated fibers in (a). Both ZnO and AZO films were deposited at 150°C. The AZO film was deposited using a 19:1 ZnO:Al₂O₃ doping ratio.

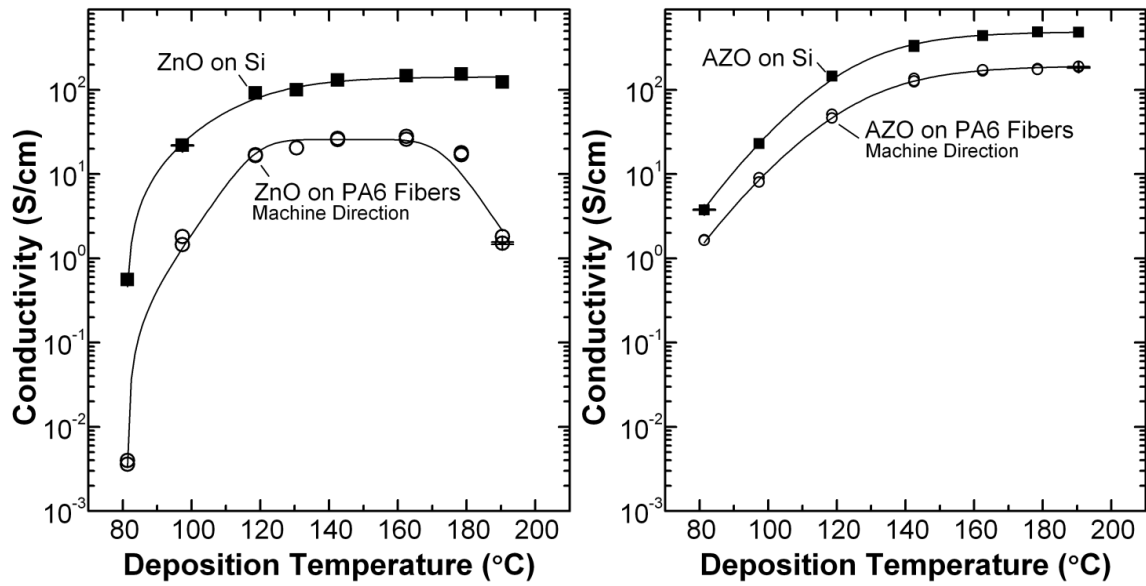


Figure 5.9. Conductivity of (a) ZnO and (b) AZO coatings, deposited on MD nylon-6 and thermal oxide silicon as a function of deposition temperature. The samples were coated with 300 cycles of ZnO or AZO, using recipes of two second precursor doses (ZnO: DEZ, H₂O and AZO: DEZ, H₂O, TMA) and 40 second N₂ purges inbetween. The laminate structure for AZO was 19 ZnO – 1 Al₂O₃.

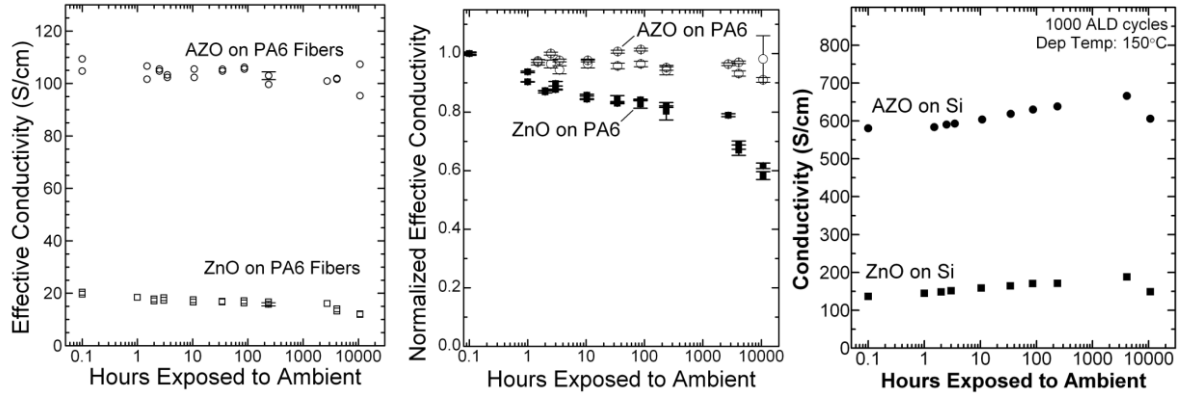


Figure 5.10. (left) The conductivity of ZnO and AZO coated cross direction nylon-6 fibers was measured intermittently, and is plotted on a log scale as a function of time since being exposed to ambient lab conditions upon removal from the ALD reactor at $t=0$ hours. **(middle)** The conductivity data for the ZnO and AZO samples from (a) was normalized to the initial measurement after deposition (taken 0.1 hours after removal); **(right)** Conductivity of the corresponding ZnO and AZO films deposited on thermal oxide silicon.

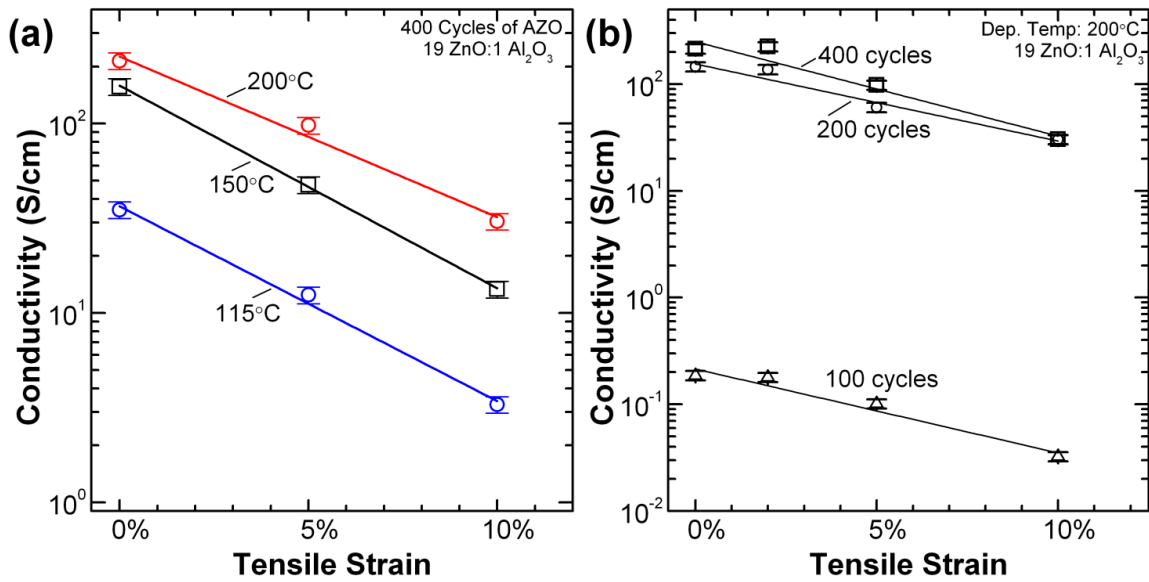


Figure 5.11. Conductivity after mechanical strain is applied for MD PA6 coated with (a) 400 cycles of AZO deposited at 115°C, 150°C, and 200°C; (b) 100, 200, 400 cycles of AZO deposited at 200°C. The as-deposited conductivity (at 0% strain) of the AZO coated fibers in (a) increases with deposition temperature, but their decrease in conductivity upon straining appears to follow the same trend. Similarly, increasing the AZO coating thickness increases the as-deposited conductivity of the fibers as shown in (b), but the trend upon straining appears to remain the same.

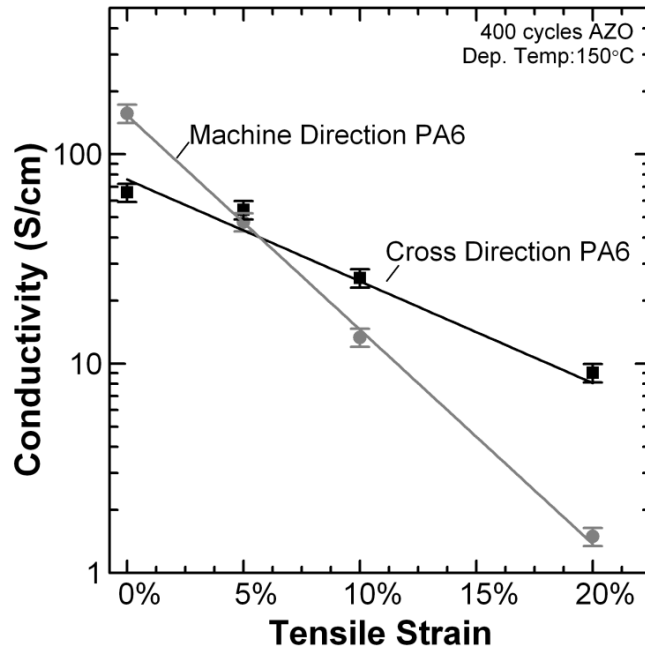


Figure 5.12. Nylon-6 nonwoven substrates with preferential fiber orientation in the machine direction and the cross direction were coated with AZO and subject to tensile testing. A fixed mechanical strain was applied using a universal tensile tester, and the conductivity of the samples was measured afterwards. Machine direction oriented fibers align parallel to the deformation force, whereas cross direction fibers align perpendicular to the deformation force. The coating applied was 400 cycles of AZO ALD at 150°C using a 19:1 ZnO:Al₂O₃ doping ratio.

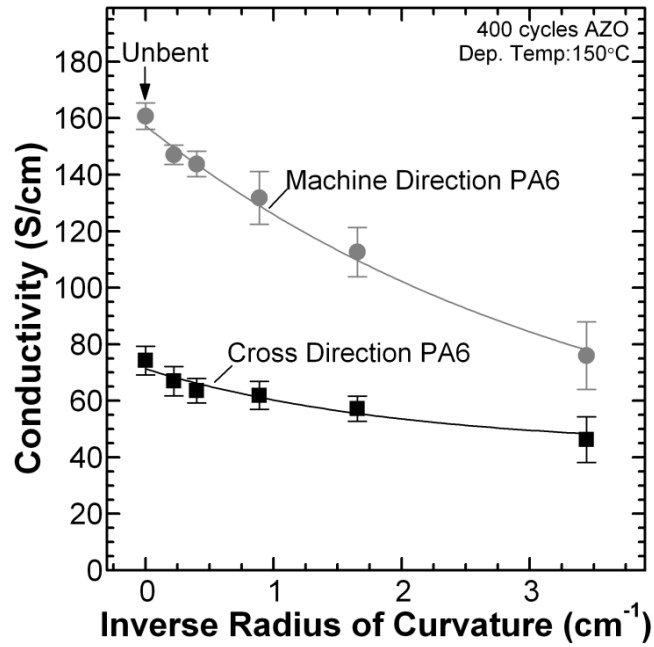


Figure 5.13. Conductivity for AZO coated machine and cross direction nylon is plotted as a function of the inverse radius of curvature, to show how the conductivity of the two substrates orientations changes from initially as-deposited (unbent, 0 cm^{-1}) to being bent around smaller cylinders, the smallest of which has a radius of curvature of $R \approx 0.29 \text{ cm}$, which corresponds to the furthest right data point on the graph (3.4 cm^{-1}).

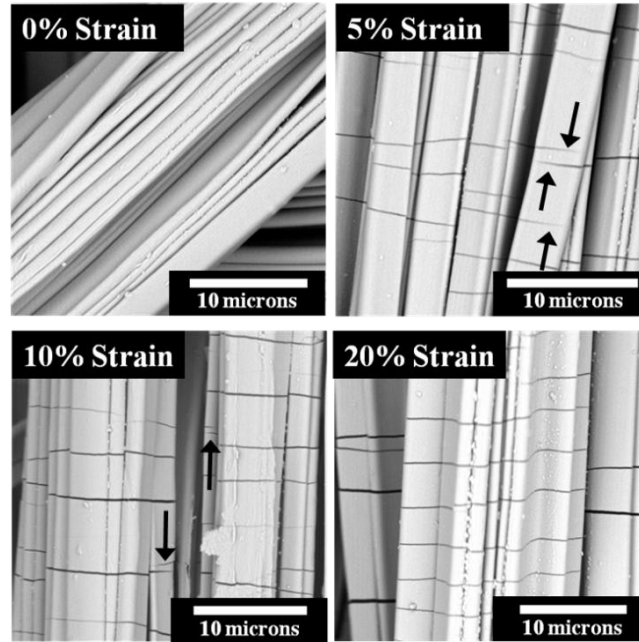


Figure 5.14. SEM images of the AZO coated MD PA6 fibers from Figure 5.12, after being strained. The samples were not sputter coated prior to imaging. As a result, non-conductive areas appear dark in the image, revealing the location of cracks in the AZO. The formation of cracks upon straining begin to form, then propagate radially around the fiber, at which point the polymer underneath the fracture can continue to stretch until other cracks are created as a result of localized stress in previously uncracked regions. For all strained samples imaged, there appeared fibers with significantly fewer cracks than a neighboring fiber, the difference is likely due to local variability in tensile forces imparted on the individual fibers by the nonwoven fiber network.

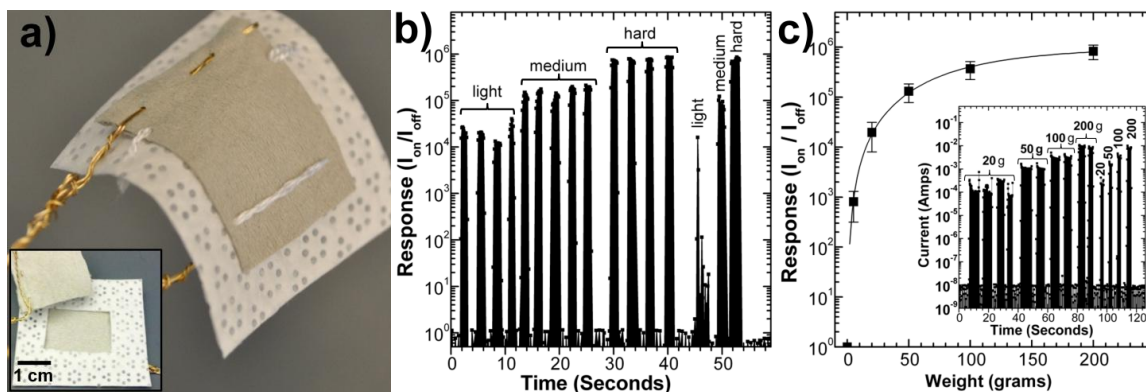


Figure 5.15. (a) An all fiber pressure sensor was fabricated using AZO coated nylon-6 nonwoven mats as electrodes. An electrically insulating polypropylene mat is placed between the electrodes, and the three are stitched together using insulating thread. An insulating nonwoven polypropylene layer with a hole cut in the center (inset), allows the electrodes to be sewn together without electrical contact, but also permits contact when pressure is applied; (b) current response, $R = I_{on}/I_{off}$ under applied force as described in text; (c) average R values (from 4 data sets) versus applied force (example data set in inset). R increases exponentially with applied force up to ~ 50 g over ~ 1 cm².

5.7 References

1. Lujala, V., Skarp, J., Tammenmaa, M. & Suntola, T. Atomic layer epitaxy growth of doped zinc oxide thin films from organometals. *Applied Surface Science* **82-83**, 34–40 (1994).
2. Guziewicz, E. *et al.* Extremely low temperature growth of ZnO by atomic layer deposition. *Journal of Applied Physics* **103**, 6 (2008).
3. Luka, G. *et al.* Transparent and conductive undoped zinc oxide thin films grown by atomic layer deposition. *Physica Status Solidi A* **207**, 1568–1571 (2010).
4. Ott, A. W. & Chang, R. P. H. Atomic layer-controlled growth of transparent conducting ZnO on plastic substrates. *Materials Chemistry and Physics* **58**, 132–138 (1999).
5. Sweet, W. J., Jur, J. S. & Parsons, G. N. Bi-layer Al₂O₃/ZnO atomic layer deposition for controllable conductive coatings on polypropylene nonwoven fiber mats. *Journal of Applied Physics* **113**, 194303 (2013).
6. Yen, K.-Y. *et al.* Characteristics of GaN-based LEDs using Ga-doped or In-doped ZnO transparent conductive layers grown by atomic layer deposition. *Journal of Crystal Growth* **387**, 91–95 (2014).
7. Illiberi, A., Scherpenborg, R., Theelen, M., Poodt, P. & Roozeboom, F. On the environmental stability of ZnO thin films by spatial atomic layer deposition. *Journal of Vacuum Science & Technology A: Vacuum, Surfaces, and Films* **31**, 061504 (2013).
8. Russell, S. J. & Textile Institute. *Handbook of nonwovens*. (CRC Press; Woodhead Pub. Ltd., 2007).

9. Kalanyan, B., Oldham, C. J., Sweet, W. J. & Parsons, G. N. Highly Conductive and Flexible Nylon-6 Nonwoven Fiber Mats Formed using Tungsten Atomic Layer Deposition. *ACS Applied Materials & Interfaces* **5**, 5253–5259 (2013).
10. Oldham, C. J. *et al.* Encapsulation and Chemical Resistance of Electrospun Nylon Nanofibers Coated Using Integrated Atomic and Molecular Layer Deposition. *J. Electrochem. Soc.* **158**, D549–D556 (2011).
11. McClure, C. D., Oldham, C. J., Walls, H. J. & Parsons, G. N. Large effect of titanium precursor on surface reactivity and mechanical strength of electrospun nanofibers coated with TiO₂ by atomic layer deposition. *Journal of Vacuum Science & Technology A: Vacuum, Surfaces, and Films* **31**, 061506 (2013).
12. Jur, J. S., Sweet, W. J., Oldham, C. J. & Parsons, G. N. Atomic Layer Deposition of Conductive Coatings on Cotton, Paper, and Synthetic Fibers: Conductivity Analysis and Functional Chemical Sensing Using ‘All-Fiber’ Capacitors. *Adv. Funct. Mater.* **21**, 1993–2002 (2011).
13. Roy, A. K., Deduytsche, D. & Detavernier, C. Wetting transitions of polymers via thermal and plasma enhanced atomic layer depositions. *Journal of Vacuum Science & Technology A* **31**, 01A147 (2012).
14. Gong, B., Peng, Q., Na, J.-S. & Parsons, G. N. Highly active photocatalytic ZnO nanocrystalline rods supported on polymer fiber mats: Synthesis using atomic layer deposition and hydrothermal crystal growth. *Appl. Catal. A-Gen.* **407**, 211–216 (2011).

15. Gong, B., Spagnola, J. C., Arvidson, S. A., Khan, S. A. & Parsons, G. N. Directed inorganic modification of bi-component polymer fibers by selective vapor reaction and atomic layer deposition. *Polymer* **53**, 4631–4636 (2012).
16. Cho, S. *et al.* Ethanol sensors based on ZnO nanotubes with controllable wall thickness via atomic layer deposition, an O₂ plasma process and an annealing process. *Sensors and Actuators B: Chemical* **162**, 300–306 (2012).
17. Spagnola, J. C. *et al.* Surface and sub-surface reactions during low temperature aluminium oxide atomic layer deposition on fiber-forming polymers. *J. Mater. Chem.* **20**, 4213–4222 (2010).
18. Gong, B. *et al.* Sequential Vapor Infiltration of Metal Oxides into Sacrificial Polyester Fibers: Shape Replication and Controlled Porosity of Microporous/Mesoporous Oxide Monoliths. *Chem. Mat.* **23**, 3476–3485 (2011).
19. Baji, Z. *et al.* Temperature dependent in situ doping of ALD ZnO. *Journal of Thermal Analysis and Calorimetry* **105**, 93–99 (2011).
20. Min, Y.-S., An, C.-J., Kim, S.-K., Song, J.-W. & Hwang, C.-S. Growth and Characterization of Conducting ZnO Thin Films by Atomic Layer Deposition. *Bulletin of the Korean Chemical Society* **31**, 2503–2508 (2010).
21. Yamada, A., Sang, B. S. & Konagai, M. Atomic layer deposition of ZnO transparent conducting oxides. *Applied Surface Science* **112**, 216–222 (1997).
22. Guziewicz, E. *et al.* ALD grown zinc oxide with controllable electrical properties. *Semiconductor Science and Technology* **27**, 074011 (2012).

23. Elam, J. W., Sechrist, Z. A. & George, S. M. ZnO/Al₂O₃ nanolaminates fabricated by atomic layer deposition: growth and surface roughness measurements. *Thin Solid Films* **414**, 43–55 (2002).
24. Luka, G. *et al.* ZnO films grown by atomic layer deposition for organic electronics. *Semiconductor Science and Technology* **27**, 074006 (2012).
25. Luka, G. *et al.* Aluminum-doped zinc oxide films grown by atomic layer deposition for transparent electrode applications. *Journal of Materials Science-Materials in Electronics* **22**, 1810–1815 (2011).
26. Na, J.-S., Peng, Q., Scarel, G. & Parsons, G. N. Role of Gas Doping Sequence in Surface Reactions and Dopant Incorporation during Atomic Layer Deposition of Al-Doped ZnO. *Chem. Mat.* **21**, 5585–5593 (2009).
27. Elam, J. W., Routkevitch, D. & George, S. M. Properties of ZnO/Al₂O₃ alloy films grown using atomic layer deposition techniques. *J. Electrochem. Soc.* **150**, G339–G347 (2003).
28. Lee, S.-M. *et al.* Greatly Increased Toughness of Infiltrated Spider Silk. *Science* **324**, 488–492 (2009).
29. Jen, S.-H., Bertrand, J. A. & George, S. M. Critical tensile and compressive strains for cracking of Al₂O₃ films grown by atomic layer deposition. *J. Appl. Phys.* **109**, (2011).
30. Sun, Y. *et al.* Influence of Subsurface Hybrid Material Growth on the Mechanical Properties of Atomic Layer Deposited Thin Films on Polymers. *Chemical Vapor Deposition* **19**, 134–141 (2013).

CHAPTER 6 is a manuscript in preparation to be submitted.

CHAPTER 6. In Situ Nucleation Analysis during Zinc Oxide Atomic Layer Deposition on Polymers using Real-time Conductance Measurement

6.1 Introduction

In situ monitoring of film growth is critical for industrial semiconductor manufacturing in order to maximize reactor up-time, as well as for fundamental investigations into film deposition by academic and industrial researchers. Quartz crystal microbalances are commonly used to measure film deposition rates for a variety of deposition techniques, including Atomic Layer Deposition (ALD) in which it is widely used to study mass uptake for deposition on metal oxide or polymer films.¹⁻⁴ A technique not widely used to study film growth during ALD processes is in situ conductance monitoring, although the technique can give useful information on the character of interfacial chemistry and physics, and importantly, give insight into the coalescence of the deposited film. This work will demonstrate the adoption of a simple in situ 2-wire and 4-wire conductance test, investigate the nature of ZnO ALD on polymer and quartz fiber substrates, and explore the impact that various pre-deposited metal oxide ALD base layers have on the subsequent nucleation and growth of ZnO ALD films.

Previous works have utilized in situ conductance analysis to study ALD processes of ZnO^{1,2,5,6}, SnO₂,³ and tungsten.⁵ However, most work to date has demonstrated steady state fluctuations in conductance, while only a few have shown conductance onset associated with film coalescence.^{1,2} To our knowledge, none have shown a systematic investigation of the

ability to study film nucleation or coalescence using this technique. In this work, we will demonstrate a simple but effective method to monitor the deposition of conductive films, through the use of zinc oxide atomic layer deposition as a representative process. Furthermore, we will analyze the consistency, influencing parameters, and the potential pitfalls of this approach. Utilizing high surface area polymeric and ceramic fiber substrates, we will look into the impact of substrate choice, as well as the influence of deposition temperature, and compare film growth on bare SiO₂ to that of Al₂O₃ and TiO₂ ALD coated SiO₂.

6.2 Experimental

Atomic Layer Deposition Reactor and Process

The substrate material used consisted of nylon-6, polypropylene and quartz fiber mats. The polypropylene nonwoven substrates were melt blown and received from the Nonwovens Institute at North Carolina State University. The polypropylene nonwoven mats had a 40 g/m² basis weight and 1.6 m²/g specific surface area, and were used as received. The nylon-6 nonwovens were produced by Allasso Industries and consisted of hydro-entangled spunbond nylon-6 nonwoven Winged FibersTM, with a 75 g/m² basis weight and 2.5 m²/g specific surface area, and they were used as received. Quartz fiber mats were purchased from Millipore and had an 85 g/m² basis weight; these substrates were rinsed in hot ethanol and then dried, prior to use.

Depositions were performed in a custom built hot walled ALD reactor. The reactor chamber consists of a stainless steel tube 36" in length with a 1.5" diameter that is heated by

Thermo Scientific Lindberg Blue M Mini-Mite tube furnace; depositions were performed at between 60°C and 200°C.

Depositions were performed under vacuum which is maintained by a rotary mechanical pump with a background pressure of 1×10^{-3} Torr. Filtered dried nitrogen (99.999%, National Welders) was flowed through the reactor at ~125 sccm (standard cubic centimeters per minute) which produced a deposition pressure of ~900 mTorr. Precursors were used at room temperature and the nitrogen feed lines were kept at ~60°C. Diethyl zinc (DEZ, 95%, Strem Chemical) and trimethyl aluminum (TMA, 98%, Strem Chemical), titanium tetrachloride (TiCl_4 , 99% Strem Chemical) and UV de-ionized water (DI water) were used for ZnO, Al_2O_3 and TiCl_4 - TiO_2 deposition. Some samples were pre-coated with a TiO_2 coating using titanium tetraisopropoxide (TTIP, Strem Chemical) and water, which were performed on a similar reactor; after deposition these samples were placed in the in situ conductance probe, and ZnO deposition was performed in the primary reactor.

Prior to in situ conductance measurements of our ZnO films, 100 cycles of ZnO ALD were deposited to condition the chamber before the probe was placed in the reactor. Once the probe was placed in the reactor, the system was allowed to equilibrate for 30 minutes at deposition conditions, prior to the start of the in situ conductance measurement. An initialization period of 120 seconds was recorded before the first DEZ dose, to record the state of the probe prior to being exposed to precursors; the 120 second initialization time was included in all the data plotted. A typical ZnO dose consists of $\text{DEZ}/\text{N}_2/\text{H}_2\text{O}/\text{N}_2 = 2\text{s}/40\text{s}/2\text{s}/40\text{s}$, with a resulting pressure change during dosing of $\Delta P \approx 0.07$ Torr, and $\Delta P \approx 0.28$ Torr for water, depositing ~ 1.7 Å/cycle on silicon at 150°C. A typical Al_2O_3 cycle

consists of TMA/N₂/H₂O/N₂ = 2s/40s/2s/40s, with a pressure change during TMA dosing of $\Delta P \approx 0.07$ Torr, and $\Delta P \approx 0.28$ Torr for water, depositing ~ 1.1 Å/cycle at 150°C on silicon. A typical TiCl₄ TiO₂ cycle was TiCl₄/N₂/H₂O/N₂ = 1/40s/1/40s, and $\Delta P \approx 0.05$ Torr, and $\Delta P \approx 0.28$ Torr for water, which at 150°C produced 0.5 Å/cycle on silicon. The TiO₂ coatings from TTIP utilized a bubbler which was charged with N₂ for two seconds prior to dosing, and used a recipe of 2s/0.5s/40s/0.1s/40s = N₂ charge/TTIP Dose/N₂ purge/H₂O/N₂ purge, which produces a $\Delta P \approx 0.2$ Torr of dilute TTIP in N₂ during dosing, and a $\Delta P \approx 0.28$ Torr for water, which at 105°C produced 0.25 Å/cycle on silicon. Prior to TTIP TiO₂ coating, a 150 cycle TTIP TiO₂ condition run was performed. When required, base layer coatings of Al₂O₃ or TiO₂-TiCl₄ were deposited in situ prior to ZnO ALD, after which the reactor was allowed to equilibrate for 30 minutes prior to ZnO deposition.

The two wire probe used to hold the nonwoven substrate consisted of a two wire copper wire electrical feed-through vacuum gasket attachment, which was attached using vacuum screws to ~ 15 " of 12-gauge copper wire with alligator clips soldered to the end. The probe length was sufficient to place the sample being measured in the middle of the furnace heating the reactor, the same location the temperature measurements were taken to calibrate the furnace. The four wire probe consists of a similar four-wire electrical feed through gasket attachment, which is connected to four ~ 15 " 12-gauge copper wires. The ends of the copper wire were looped back onto themselves, to which entwined 22-gauge gold-plated copper wire was wrapped, and then sewn through the substrate to be measured. The copper wires for both probes were self supporting such that the substrate being measured could be placed in the center of the reactor without touching the walls. Upon placing the probe in the reactor,

resistance measurements were taken to ensure that the wires holding the sample were not touching the reactor walls thereby shorting the measurement; further detail is provided in the following method section.

In Situ Conductance Measurement Method

For this work, a set of 2-wire and 4-wire probes were made to hold nonwoven substrate. The 2-wire probe was used for the majority of data gathering, and was made using alligator clips that were soldered to copper wires which were attached to a gasket with electrical feed through. A similar construction was used for the 4-wire probe, but due to the size constraints of the reactor geometry, probe contacts were woven into substrates using conductive gold-plated copper wires, which were then attached to the copper wires in the 4-wire electrical feed through gasket. Figure 6.1 shows the overall probe set up for the 2-wire probe, a close up image of a substrate in the 2-wire probe, and the front and back images of the woven electrodes used for the 4-wire substrate tests.

Before attaching a substrate to be measured, a resistance test was performed on the empty probe, to ensure no short was present between the copper wires holding the sample. An applied bias of 15-30V was found to be sufficient to reveal the presence of a low conductivity ZnO short, which would eventually form on the ceramic insulators that electrically separate the copper feed-through wires from the stainless steel gasket body. If a low conductivity ZnO short was present, a 15-30V bias was sufficient to produce 10^{-10} – 10^{-9} Amps (non-zero) of current. To reduce the likelihood of this issue, the probe was cleaned every day before use, and when a short was detected. The best method for removing the ZnO

was to detach the copper wire-clamps used to hold the samples, and subject the body of the probe to a dilute acid wash, and then recondition the probe with Al₂O₃ and ZnO ALD.

Using the 2-wire probe, the substrates for deposition were then placed in between the alligator clips, which were placed with 5 mm of separation. The wires holding the samples were aligned vertically and horizontally as required to prevent them from touching the reactor walls once inside. The substrate was placed in the reactor chamber, and after being evacuated, filter dried nitrogen was flown over the substrate. To ensure the substrate was not touching the walls, a resistance test was performed using applied voltage of 0.5V to ensure no short with the walls was being created; a non-shortening sample would have a net-zero average resistance measurement. The sample was then allowed to equilibrate to the deposition temperature for 30 minutes prior to deposition.

An example of a representative data set is shown in Figure 6.2, which plots the deposition of 200 ZnO cycles deposited on bare polypropylene at 150°C. The three figure set shows a linear plot of the conductance data, a logarithmic plot of conductance immediately before the onset of measureable conductance, and the steady state conductance change during two ZnO cycles.

The shape the conductance curve on a linear plot, such as the one shown in Figure 6.2(a), is substrate dependent, as growth characteristics impact the shape of the curve. For example, in Figure 6.2(a), the transition can be seen to occur from nucleation and coalescence in part (i), to rapid increase in conductance in part (ii) where ZnO growth is transient and subsurface film growth may still be occurring, to region (iii) which is the beginning of steady state ALD growth rate which remains linear for the duration of the deposition, as observed

for runs up to 400 cycles, twice as long as the deposition shown in 6.2(a)). Other reports have shown mass uptake on bare polypropylene under similar deposition conditions reaches linear, ALD growth, after about 200 ZnO ALD cycles.⁷ By contrast, nylon-6 has a similar length nucleation/coalescence phase (i), but a short variable rate growth phase (ii), reaching steady state phase (iii) growth more quickly than the polypropylene samples in Figure 6.2(a). Deposition on quartz fibers exhibits very short nucleation/coalescence and variable rate growth regimes, quickly reaching steady state growth, making it a highly repeatable standard test substrate for the depositions performed to evaluate in situ conductance monitoring as a method.

Similarly, characteristics differences between the substrates impact parameters for the data as shown in Figure 6.2(b) and 6.2(c). For example, in the data plotted in Figure 6.2(b) it can be seen that for the first ~5 ZnO cycles after the onset of measurable conductance, after the water dose the conductance stays constant throughout the purge step, whereas in the last few cycles of Figure 6.2(b) as well as in Figure 6.2(c), it can be seen that conductance decreases throughout the purge step. This transition is unique to deposition on bare polypropylene substrates. We suspect this transition maybe a function of polypropylenes' hydrophobic nature, rather than the hydrophilic nylon-6 and quartz fiber surfaces. Figures 6.2(b) and 6.2(c) are representative of how most data is compared in this work since it lends insight into differences in nucleation/coalescence and steady state behavior, although figures like Figure 6.2(a) can provide insight into overall growth behavior.

A Keithley 2400 Soucemeter was used to apply bias voltage or current during the tests, and LabTracer software package was used to record the measurement data. For long

depositions of >100 cycles like the one shown in Figure 6.2, a 250 millisecond delay was used after each measurement, which allowed the software program controlling the measurement to last the duration of the deposition, but also stay underneath the data collection limit of 100k data points per test. For shorter depositions, a 100 millisecond delay was used, to give a more detailed dataset. It was determined that for long runs, (e.g. 200 ZnO cycles with a 250ms data delay) that a small time distortion (< 1.0%) arose between the time as reported by the Keithley and the actual time, causing the Keithley to report shorter than expected timescales. The distorted effects of the time reporting can be seen in Figure 6.2(c) which reports the end of the 199th ZnO cycle to have occurred 16,684 seconds into the measurement, when in fact the end of that cycle occurred 16,834 seconds into the measurement. The difference between reported time and actual time was ~2.3% for measurements taken with a 100 millisecond delay. Because the delay appears uniform over the length of the measurement, it can easily be accounted for while analyzing the data.

The Keithley was used to apply the bias voltage or bias current for both 2-wire and 4-wire measurements. Depositions with the 2-probe device were measured using an applied bias, typically 0.5 volts, and then the resulting current was measured. For a 4-wire measurement, a current was applied between the outer electrodes, while the inner electrodes measured a voltage; this 4-wire design allows for the separation of contact resistance from sample resistance producing a more accurate resistance value. Figure 6.3(a) shows measurements from the 2-wire and 4-wire probes for three ZnO cycles during deposition at 150°C on bare nylon-6, while Figure 6.3(b) shows current-voltage curves for the 2-wire and

4-wire tests (performed with the four wire probe) after 225 cycles of ZnO were applied to bare nylon-6 at 150°C.

During a typical ZnO ALD cycle, oscillations in current were observed, which correspond to a decrease in current during a DEZ dose, and an increase in current during water dose. Similar oscillations have been observed previously during ZnO deposition using a 2-probe device.^{1,2} Such oscillation effects were previously ascribed band bending at the ZnO surface, caused by electron withdraw by DEZ and electron donation by water.¹ To exclude the potential that the aforementioned observed phenomenon was due to fluctuations in contact resistance during precursor dosing, 4-wire measurements were taken. Such a 4-wire test applies a current across the sample and measures a voltage in-between. By separating the circuit applying current from the circuit measuring the voltage, it is possible to separate the contact resistance from the measured resistance of the sample, for a better measurement of the sample itself. This removes the possibility that fluctuating contact resistance is the cause for observed oscillations in conductance during an ALD cycle. The 2-wire probe provided easy set up for measurement because it utilizes alligator clips to make contact with the sample, compared to the 4-wire apparatus which requires the electrodes to be woven into the substrate to be measured. A larger reactor design would allow for the construction of a 4-wire apparatus that utilizes alligator clips to hold the sample, but while utilizing a 1.5” diameter flow tube reactor for this work, the 2-wire probe was found to be more feasible and was deemed sufficient for use in all the measurements discussed hereafter.

In order to demonstrate the thermal activation of carriers present in the ALD ZnO films deposited on quartz fibers, conductance was measured over a range of reactor

temperatures in post-deposition temperature tests. Plotting the conductance and measurement temperature on an Arrhenius plot will reveal the conductivity thermal activation energy for thermally promoted carriers as the slope of the curve for $\ln(\text{conductance})$ vs. $1000/T(\text{K})$, which can be used to solve $\text{Slope} = E_a / (1000 \times k_b)$.

Thermal activation data of ZnO coated quartz fibers coated with 100 cycles of ZnO at 150°C is plotted in Figure 6.4. The measurement was taken in situ without breaking vacuum after depositing the 100 cycle ZnO coating onto bare quartz fibers. As the samples are heated from 52°C to 350°C the conductance increases slightly up to ~150°C before decreasing rapidly between 150°C-215°C, followed by a rapid increase in conductance between 215°C-350°C. We ascribe this behavior to thermal excitation of carriers within the as-deposited, defect rich ZnO film between 52°C and 150°C, followed by the annealing out of intrinsically doping native defects in the ZnO film as the temperature is raised from 150°C to 215°C, followed by further thermal excitation of carriers in the annealed ZnO semiconductor from 215°C to 350°C. The slope of the measurements taken between 215°C and 350°C corresponds to a conductivity thermal activation energy of $E_a \sim 0.42\text{eV}$.

For two probe measurements, using an applied bias rather than applied current was determined to be best, since a fixed bias voltage allows current to increase during measurement and maintains response throughout the length of the deposition, whereas using a fixed current bias eventually leads to lower measured voltages as the film thickness increases, leading to lower signal-to-noise ratios as film thickness increases.

Deposition of ZnO films at 150°C was performed on bare quartz fiber substrates and measured using an applied voltage bias of 0.05, 0.5, and 5 Volts, to determine the impact on

detection sensitivity. Figure 6.5(a) depicts the onset of measurable conductance for samples measured under 0.05V, 0.5V and 5V, and Figure 6.5(b) plots three ZnO cycles for the same samples once the processes has reached steady state change.

In Figure 6.5(a) it can be seen that the measurement taken under 5 volt bias registers the onset of conductance before the measurements taken at 0.5V or 0.05V. However, after ~15 cycles all three measurements converge on the same conductance trend line. In previous work, Na et. al. used a similar 2-wire in situ measurement technique on silicon and detected the onset of conductance for ZnO films grown on silicon at under 20 ZnO cycles, although film nucleation and coalescence is not significantly addressed in their prior work.¹ Figure 6.5(e-g) shows cycles #46-48 for all three measurements. The decrease in current response during the DEZ dose and purge steps appears to be highest for the measurement taken under 0.05V, and lowest for measurement under 5V. Since conductance is plotted, the data is directly comparable since $I / V = 1 / R$, the higher voltage should produce proportionally higher current, therefore any differences may be attributed to slight differences between the various quartz fiber substrates used.

A clearly distinguishable feature of the measurement taken under 5V is the current response after the water dose, which produces a larger increase in current than either the 0.5V or 0.05V measurements. For the first ~25 ZnO ALD cycles during the test shown in Figure 6.5(d), the conductance curve for the 5V measurement appears very similar to that of the 0.5V or 0.05V measurement, i.e. the large peak in conductance during the water dose shown in Figure 5(g) is not present throughout the entire deposition, but rather develops as the ZnO coating gets thicker. The high 5V bias produces much larger currents than in the

other measurements, which maybe the cause of the large spike seen in Figure 6.5(g). For example, in Figure 6.5(g) the water dose is followed by an increase in current from 23mA to 75mA in a few tenths of a second. We suspect that such large current flow may be causing localized heating through the conductive film, which in turn could influence precursor sorption.

For the depositions typical in our study, we found a 0.5V measurement bias provided sufficient sensitivity to nucleation and film coalescence, and avoided producing currents so high they distorted the measurement, such as the 5V measurement shown in Figure 6.5(g). Alternatively, by sweeping voltage from 5V to 0.5V over the course of the measurement would allow low cycle number sensitivity, while avoiding distorting high end currents.

Another notable feature present in the 5V measurement is the presence of a small peak after the DEZ dose is introduced. We attribute this to the ending of the 2-second DEZ dose, and thus the decrease in DEZ flux to the substrate being measured; this feature is present in other conductance graphs and will be discussed in a later section.

6.3 Results and Discussion

Conductance measurements were used to study nucleation of ZnO ALD films on quartz, nylon-6, and polypropylene nonwoven substrates. As shown in Figure 6.5, nucleation of ZnO occurs quickly on quartz fibers, taking between 9 and 12 ZnO ALD cycles for samples to have measurable conductance, which indicates the ZnO coating has coalesced sufficiently to allow for electron transport through the ZnO. The quartz fibers are analogous to deposition on planar silicon, since they offer SiO₂ surfaces for precursor nucleation, and

do not show significant infiltration, thermal expansion or degradation under our deposition conditions, aspects that complicate deposition on polymers. The significant difference between ZnO nucleation on quartz fibers and polymer fibers can be seen in Figure 6.6(a); by contrast both the polypropylene and the nylon-6 nonwoven substrates take about 81 cycles before onset of measurable conductance occurs.

As mentioned earlier, the infiltration effects present in polymers, like the polypropylene sample shown in Figure 6.2(a), do not manifest during deposition on quartz fiber substrates, which is apparent when comparing the substrates plotted in Figure 6.6(a). Interestingly, the polypropylene and nylon-6 substrates appear to take the same number of ZnO cycles before becoming conductive enough to be measured. This is a surprising difference since polypropylene is chemically inert, and nylon-6 contains an amide group which has shown to be very reactive to other ALD precursors such as trimethyl aluminum.^{4,8,9}

Another interesting difference is the shape of the dose/response curves for the various substrates during the first few cycles after the onset of measurable conductance. Figure 6.6(b) shows ZnO growth on quartz initially resembles the same trend as is observed during steady state, with the one significant exception. During the first four cycles after conductance is measurable for ZnO on quartz fibers, during the post DEZ dose nitrogen purge, conductance appears to increase throughout the duration of the purge. This behavior is only observed in coatings on quartz during the first ~17 ZnO ALD cycles, and this may indicate it is related to absolute film growth rather than due to growth on quartz specifically.

It can be seen in Figure 6.6(a) that ZnO deposition on polypropylene and nylon-6 undergo different growth behavior after the onset of measurable conductance, as highlighted by the divergence of the respective curves after the first few measurable cycles. The growth behavior for polypropylene was discussed in Figure 6.2(a), and although not evident as plotted in Figure 6.6(a), nylon-6 undergoes considerably faster transition to steady state deposition compared to polypropylene. The nylon-6 conductance curve in Figure 6.6(a) shows conductance increasing a few orders of magnitude in the ~3 cycles after conductance is first measured, but then transitions to a slower growth rate for the next ~30 cycles, at which point it then transitions to a lower growth rate. Even on quartz fibers, it can be seen in Figure 6.6(a) that once conductance becomes measurable, there is a rapid increase over a few orders of magnitude, but after ~5 cycles the increase in conductance per cycle starts to mitigate; as the fluctuations decrease in magnitude towards a steady state value, the curve appears to thin, (e.g. ~1800-6000s) until it approaches steady state growth, $t > 7000s$.

Figure 6.6(e-g) shows cycles #147-149 for all three substrates, and it can be seen that all three appear to exhibit the similar behavior. Nylon-6 shows the largest change in conductance in response to water doses, but this to be expected as it is the highest specific surface area material of the three. For polypropylene as depicted in Figure 6.6(g), the conductance decreases after the water dose at a linear rate compared to the logarithmic loss exhibited for growth on quartz or nylon-6 nonwovens. As the only hydrophobic polymer, we ascribe this difference in behavior to the continued influence of the underlying hydrophobic polypropylene. Recall that, as was discussed with regards to growth modes in Figure 6.2(a), the steady state behavior for ZnO growth on polypropylene was not observed until towards

the end of the 200 cycle run. The dose/response curves for the ZnO on polypropylene in Figure 6.6(g), transitions to resemble that of the ZnO growth on quartz and nylon-6; Figure 6.2(c) shows two of the last cycles of the same sample in 6.5(g), after the water dose the conductance no longer decreases at a linear rate. It appears to take growth of ZnO on quartz fibers ~80 cycles, nylon-6 ~130 cycles, and polypropylene ~180 cycles, before they reach their respective steady state rates of change. This transition signifies that the dose/response curve for the conductance plot can signify at what point the underlying polymer character is fully encapsulated, as indicated by the transition in post-water dose physisorption behavior of ZnO coated polypropylene from hydrophobic to hydrophilic.

This approach could be used on polymers for in situ study of ZnO coatings as a function of deposition temperature, to indicate at what point encapsulation was achieved. Similarly, it could be used to determine if an Al₂O₃ ALD base layer coating, as we have shown can be used for encapsulation of polypropylene prior to ZnO ALD,⁷ was performing to task, depending on the dose/response curve of the ZnO ALD top layers.

The Impact of ZnO Deposition Temperature

The impact of deposition temperature was investigated for ZnO ALD on nylon-6 nonwovens, which is a good polymer choice when depositing ZnO films because it is thermally stable up to ~210°C, and reaches steady state ALD growth regime more quickly than similar depositions on polypropylene. Nylon-6 can be used to investigate ZnO ALD at temperatures well above the ZnO “ALD window” for the DEZ + water process, allowing for the characterization of the different temperature limited growth regimes that define the ALD

window. In addition, the thermal expansion and infiltration that occurs during ALD on polymers is potentially a very interesting topic that may be investigated by the in situ conductance method. However, if probing characteristics of the ZnO film growth was the goal, using quartz fiber substrates would be less complicated than using polymer fibers.

The conductivity of zinc oxide ALD deposited on silicon is dependent on deposition temperature as well as film thickness.¹ Generally, higher temperatures deposit more conductive ZnO films, with maximum conductivity values for films deposited 200°C to 250°C. Deposition at these temperatures on thermally sensitive substrates like polymers, maybe possible if an appropriate polymer can be identified. In addition to the thermal restrictions polymers impose on the deposition conditions, growth is often complicated by sub-surface growth, thermal expansion of the polymer, precursor infiltration/removal issues, and the growth dynamics between precursors and polymers, which are governed by the temperature dependent balance of precursor diffusion and reaction kinetics.^{4,10,11} The ZnO films analyzed in this work are sufficiently thin^{1,7} that both the conductivity (S/cm) and the conductance (S) are dependent on film thickness, the temperature at which the ZnO was deposited, and the measurement temperature. Therefore, analyzing in situ conductance for ZnO deposition on nylon-6 nonwovens as a function of deposition temperature imparts additional challenges to interpreting and understanding the measured data.

We deposited 200 cycles of ZnO on nylon-6 substrates at 100°C, 150°C, and 175°C as depicted in Figure 6.7, to probe the differences in film nucleation and growth, as well as conductance change, as a function of deposition temperature. Figure 6.7(a) plots the conductance of the ZnO coatings deposited on nylon-6 nonwovens at 100°C, 150°C and

175°C; a significant difference can be seen in the required number of ZnO cycles needed to produce a coating that has a measurable conductance.

The data plotted in Figure 6.7(a) shows the differences in time (ZnO cycles) required to deposit a film of sufficient thickness and conductivity that a measurable amount of current can be detected under a 0.5 Volt bias. These are the only plots that incorporate two variables for comparison, film thickness per cycle as a function of deposition temperature, and ZnO conductivity as a function of deposition temperature; lower temperature films are generally thicker but less conductive. The most intriguing observation may be the initially counter-intuitive result that the deposition that shows the earliest onset of measurable conductance is the lowest temperature deposition, 100°C on nylon-6. Comparing the conductivity of ZnO films deposited at different deposition temperatures, it has been shown that a ZnO film deposited on planar silicon 175°C would be much more conductive than a film deposited at 100°C for the same number of ZnO cycles, despite being ~10% thinner than the 100°C film, as was shown in Chapter 5.

However, CVD effects caused by incomplete purging in the low temperature sample maybe a significant contributing factor to the faster nucleation at lower temperatures, because precursor doses and the purge times are held constant between these samples.

Others have reported low temperature depositions by ALD, for example, using Al₂O₃ or ZnO ALD at temperatures below 40°C,^{12,13} although the authors utilized comparatively long purge times in their runs in order to provide sufficient purging of un-reacted precursors, even though, in some cases, the ‘extended purges’ were still short compared to the ones used here.¹³ As a comparison, Al₂O₃ ALD in a comparable viscous flow tube ALD reactor

operated under similar conditions, utilized a 180 second purge after the water dose to fully remove un-reacted precursors, while the authors found only a 5 second purge was required after the water dose for depositions at 177°C.¹²

The deposition at 100°C in Figure 6.7(a) not only nucleates faster than the depositions at 150°C and 175°C under the given deposition conditions, as is seen in Figure 6.7(d) it also exhibits a completely different trend after the onset of measureable conductance. By comparison, the depositions at 150°C and 175°C show similar dose/response behavior to ZnO deposition at 150°C on quartz fibers from Figure 6.6(b). Furthermore, the trend behavior of the steady state change for the sample deposited at 100°C shows characteristics not seen in the 150°C or 175°C runs, such as is shown in Figure 6.7(b), an increase in conductance as a function of time after the water dose, rather than the typical conductance spike at the start of the water dose, followed by a slow conductance decrease over the length of the purge. Rather, at 100°C, it can be seen that the spike/purge behavior is replaced with conductance saturation by the end of the water purge. The purge step after the DEZ dose appears to be insufficient for the 100°C sample, compared to the 150°C and 175°C samples, as is indicated by the conductance rate of change immediately before a subsequent water dose.

The shape of the dose/response conductance curves in Figure 6.7(e,f) show a noticeable difference to the 100°C in Figure 6.7(g); a slight “bump” in conductance can be seen during the purge step after the DEZ dose, similar to that seen on the ZnO deposition on quartz measured with 5V bias. This is attributed to the end of the DEZ dosing, and the close up figures to the right in Figure 6.7(e-g) show a magnified plot of the ‘bump feature’ with the

location and duration of the DEZ dose signified above the dose/response curve. Although the trend is most evident in the 100°C sample, a small feature is observed for all the depositions. In the higher temperature deposition the conductance fluctuation during a normal ALD cycle is significantly larger than the 100°C sample, making the ‘bump’ associated with the end of the DEZ dose only a small feature of the overall decreasing trend.

Nucleation of ZnO on Bare and Metal-Oxide Coated Quartz Fibers.

We have investigated the nucleation and growth behavior as a function of coating chemistry to determine the impact that pre-deposited ALD coatings have on the nucleation and growth of ZnO films. To do this, we deposit Al₂O₃ and TiO₂ coatings on quartz fibers prior to ZnO deposition, and compare the conductance behavior of ZnO films deposited on coated quartz to that on bare quartz. We compare the conductance of ZnO films deposited on TiO₂ films grown using two different precursors, titanium tetrachloride (TiCl₄-TiO₂) and water, and titanium tetraisopropoxide and water (TTIP-TiO₂). For the Al₂O₃ and TiO₂ base layer coatings, we deposit ~25Å of coating, which corresponds to 25 Al₂O₃ cycles, 50 TiCl₄-TiO₂ cycles, and 100 TTIP-TiO₂ cycles. The Al₂O₃ and TiCl₄-TiO₂ coatings were deposited on bare quartz fibers in situ prior to ZnO deposition, and TTIP-TiO₂ coatings were deposited on bare quartz in another reactor, then placed in the conductance probe and inserted into the primary reactor for ZnO deposition. Figure 6.8(a-e) plots the conductance of ZnO films deposited on ALD Al₂O₃ and ALD TiO₂ base layer coatings during the first 29 cycles of ZnO deposition. Figure 6.8(f-i) show the steady state conductance behavior of the deposited ZnO films on the various substrates, after 47 cycles of ZnO ALD, at which point the conductance

dose/response curves are very similar, having largely outgrown the effects of the underlying coating chemistry.

In Figure 6.8(a) it is evident that a different number of ZnO ALD cycles are required before the onset of measurable conductance is achieved for deposition on the various coating types. Furthermore, the conductance curves for ZnO deposited on Al₂O₃ and TTIP-TiO₂ coatings, as well as bare quartz exhibit similar growth trends after the first few ZnO cycles after the onset of measurable conductance. However, the ZnO conductance trend in Figure 6.8(e) for deposition on the TiCl₄-TiO₂ surface is distinctly different than the other three coatings. Nucleation on TiCl₄-TiO₂ takes a bit longer than nucleation on TTIP-TiO₂ and once nucleation occurs, the conductance increases more quickly than on TTIP-TiO₂. The early cycle ZnO growth on TiCl₄-TiO₂ in Figure 6.8(e) also appears fluctuate less in response to DEZ or H₂O dosing, than the three other substrate types.

Zinc oxide deposited on Al₂O₃ has been shown to exhibit increased conductivity for ZnO thin films (< 34 nm) thickness compared to ZnO deposited on SiO₂ surfaces.⁷ The ZnO film in Figure 6.8(c) deposited on 25Å Al₂O₃ ALD coated quartz, shows onset of measurable conductance much earlier than ZnO films deposited on other coatings. There does not appear to be a difference in the cycles required to produce a measurable conductance for ZnO deposition on bare or TTIP-TiO₂ coated quartz. After the first four cycles it appears as though the ZnO film deposited on TTIP-TiO₂ coated quartz is not increasing conductance as quickly as the ZnO deposited on bare quartz. Figure 6.8(f-i) shows similar conductance fluctuation behavior for the ZnO deposited on each substrate during the DEZ/H₂O doses.

We suspect that better nucleation and growth of the deposited ZnO ALD film, reduced charge trapping at the ZnO/Al₂O₃ interface, or differences in depletion layer effects may account for why the conductance is measured much more quickly for ZnO deposited on Al₂O₃ coated surfaces.^{7,14} Furthermore, the onset of measurable conductance for ZnO deposited on bare and TTIP-TiO₂ coated quartz takes the same number of cycles, after which, the conductance behaviors diverge. We suspect divergence in conductance change, maybe a result of different interfacial growth rates of the ZnO, or band bending effects caused by differences in interface quality or depletion layer formation.

We ascribe the behavior in Figure 6.8(e) for ZnO deposition on TiCl₄-TiO₂ coated quartz to be a result of DEZ/H₂O interaction with un-reacted TiCl₄ precursor molecules, byproducts, or contamination. The TiCl₄-TiO₂ coating was the only film deposited using a halogenated precursor, and ZnO is known to be readily etched by a variety of acids,¹⁵ so we suspect small amounts of HCl contamination may retard ZnO growth, or reduce the conductivity of ZnO that does deposit. Changes in the growth rate or the conductive properties of the deposited ZnO could account for the observed slower onset of measurable conductance, and the unique conductance dose/response curve observed for ZnO deposited on TiO₂ grown from TiCl₄ and water, that is not observed for ZnO deposited on TiO₂ surfaces grown with a metal organic precursor. After deposition of the ZnO film on the TiCl₄-TiO₂ coated quartz plotted in Figure 6.8(e), pitting was observed on the alligator clips holding the substrate, indicative of that the surface observed during initial ZnO ALD cycles was corrosive.

6.4 Conclusions

The ability to measure in situ conductance during deposition of conductive zinc oxide films by ALD onto nonwoven substrates was demonstrated. Both 2-wire and 4-wire in situ conductance measurements were taken during ZnO ALD, and both show a decrease in conductance during the DEZ precursor dose and an increase in conductance during the water dose. Measurable conductance was observed after as few as 10 cycles of ZnO ALD on bare quartz fiber substrates, although the conductance for ZnO ALD films deposited on nylon-6 and polypropylene was not measurable until after ~80 ZnO ALD cycles.

Regardless of how many cycles were required to produce a sufficiently conductive ZnO coating, such that the conductance could be measured, over the course of the next ~10 ZnO cycles the conductance of the ZnO coating increased up to six orders of magnitude, before slowing towards a more linear increase in conductance as a function of cycle number. Conductance measurements were performed for ZnO ALD films deposited on bare and metal oxide coated quartz fibers, and the conductance curves of the ZnO films were impacted by the metal oxide coating on which it was being deposited. ZnO deposited on aluminum oxide coated quartz fibers produced measurable conductance with fewer cycles than ZnO deposited on bare quartz. ZnO deposited on bare quartz showed similar nucleation behavior as ZnO deposited on a TiO₂ coating deposited with TTIP and water precursors, although ZnO deposited on a TiO₂ coating from TiCl₄ and water precursors had a longer nucleation delay before a measurable conductance was achieved, and afterwards, the conductance curve exhibited a completely unique dose/response behavior during a ZnO ALD cycle.

Importantly, regardless of the interface characteristics between the substrate and the ZnO ALD film being deposited, eventually all the measurements evolved into the same conductance behavior in response to DEZ and water doses. This demonstrates that although the interface properties initially dominant the onset of measureable conductance for the ZnO coating, the steady state behavior of ZnO ALD will eventually evolve as the film achieves sufficient thickness and is no longer impacted by the chemistry of the underlying substrate. The simplicity of the design and implementation of this in situ conductance measurement technique, combined with the demonstrated sensitivity and ability to studying coating-substrate interface characteristics, makes this technique a promising method for in situ characterization of conductive ALD films.

6.5 Acknowledgements

We acknowledge the Nonwovens Institute (NWI) at the North Carolina State University College of Textiles for support for W.J.S.

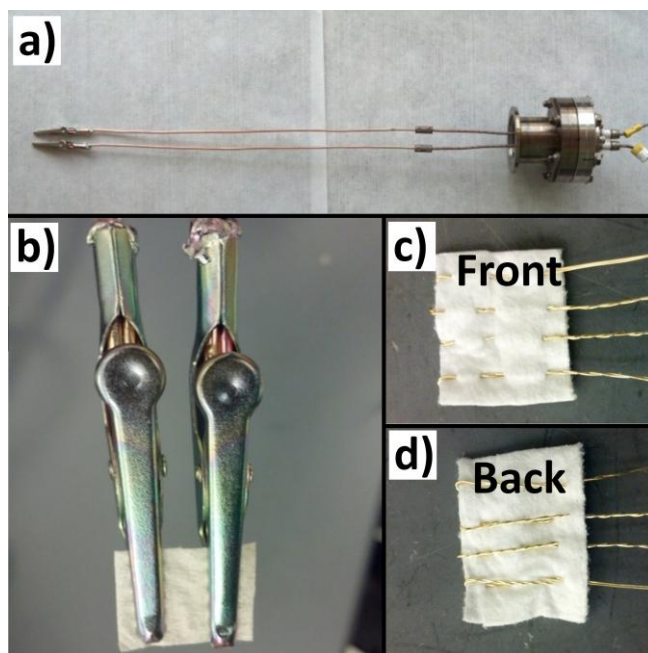


Figure 6.1. (a) The overall 2-wire probe device with the quick-flange connection and electrical feed-through gasket can be seen at right while a sample being held by alligator clips can be seen in image left; (b) an image of a nylon-6 nonwoven substrate in the probe after 200 cycles of ZnO ALD; (c) front and (d) back images of nylon-6 substrate with woven gold electrodes used for a 4-wire measurement.

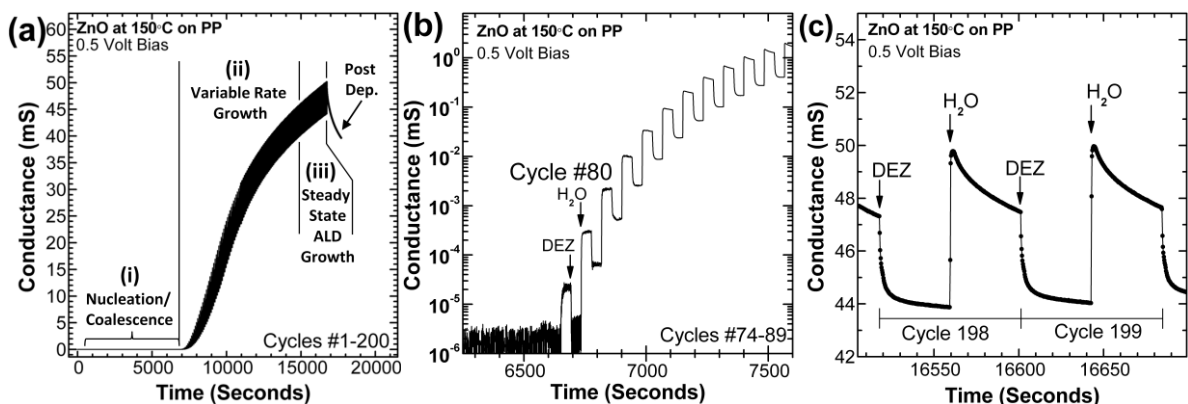


Figure 6.2. Representative plots of in situ conductance data taken showing the various aspects of the recorded data; this data was gathered as 200 ZnO ALD cycles were deposited on bare nonwoven polypropylene at 150°C. **(a)** A linear plot of the data shows the significance in behavior of, (i) the nucleation/coalescence period, (ii) the initial conductance uptake rate and then the transition to lower conductance uptake per cycle at high cycles, and (iii) the steady state rate; **(b)** A logarithmic plot of conductance for the period immediately before and after the onset of measurable conductance. In the span of < 10 cycles the conductance of the coated sample increases 6 orders of magnitude; on this scale the nuances in rate of change shown in (a) are lost; **(c)** an example of conductance change within two ALD cycles. The DEZ dose causes conductance to decrease which continues until the introduction of the water dose which causes an abrupt increase in conductance followed by a slow drop throughout the water purge step.

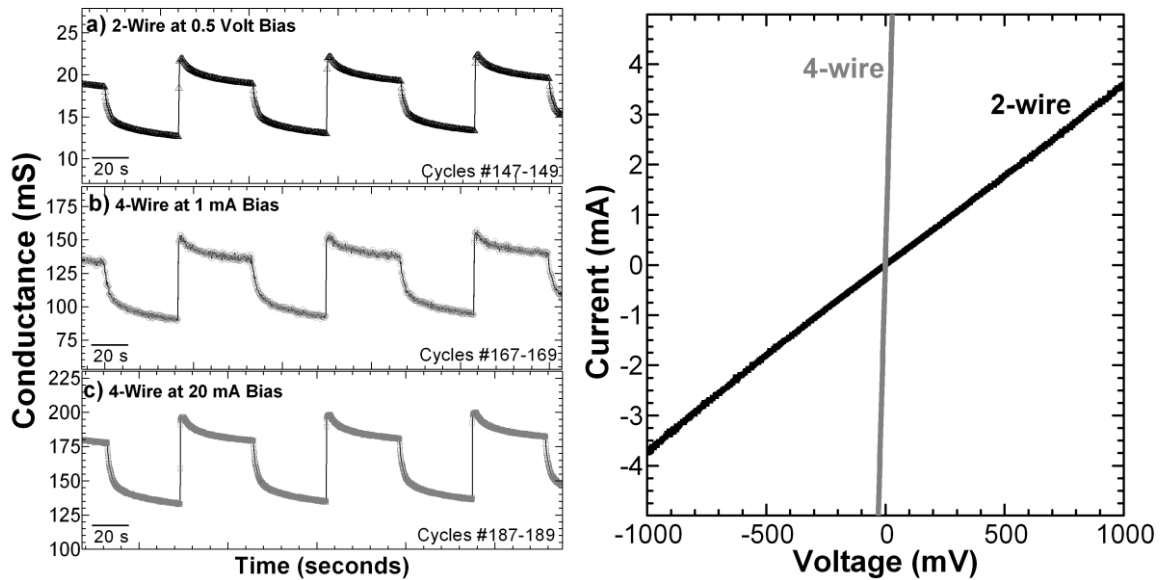


Figure 6.3. Conductance is plotted for three ZnO ALD cycles during deposition on a nylon-6 nonwoven, as measured (a) using the 2-wire probe under 0.5 volt bias; (b) using the 4-wire probe with 1 mA bias; and (c) using the 4-wire with 20 mA bias. The same trend can be seen in data gathered from both probes, suggesting that band bending at the ZnO surface, rather than changes in contact resistance are the cause of the observed oscillations during ZnO ALD. It can also be seen in 6.3(b) and 6.3(c) that with the 4-wire measurement, under 1 mA current there is more noise in the measurement than when using a 20 mA current; the 2-wire test under 0.5V bias produces inbetween 6-11 mA in the cycles shown in 6.3(a). (d) Current-Voltage curves taken on nylon-6 fibers coated with 225 cycles of ZnO ALD at 150°C; the 2-wire measurement was taken between the center electrodes of the 4-wire probe so that the curves represent measurements over the same distance. This plot shows that non-negligible contact resistance is present in the 2-wire measurement (taken using the 4-wire probe) on the nylon-6 sample with woven Au-wire electrodes.

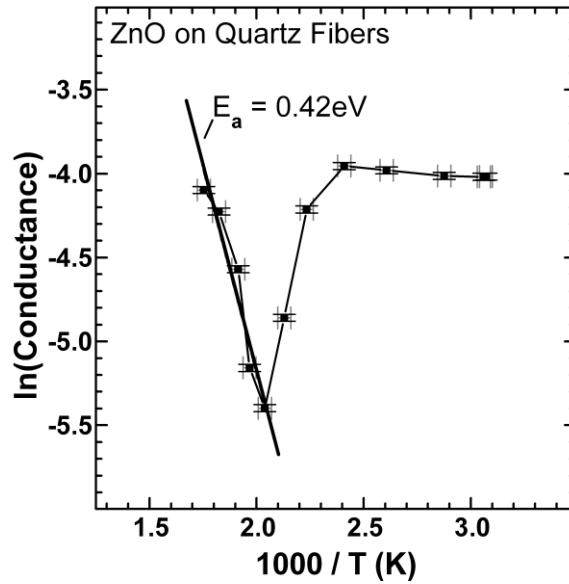


Figure 6.4. An Arrhenius plot of the thermal activation of the conductance of a 100 cycle ZnO ALD coating deposited on bare quartz fibers. In situ, post-deposition conductance measurements were taken as a function of temperature, between 53°C and 350°C while the sample was kept under vacuum. For ZnO, as with any semi-conductor, thermally activated carriers cause a samples' conductivity to increase as temperature is increased, since more carriers have sufficient energy to be promoted to the conduction band. The conductivity thermal activation energy (E_a) of the plotted ZnO sample is $E_a \sim 0.42\text{ eV}$

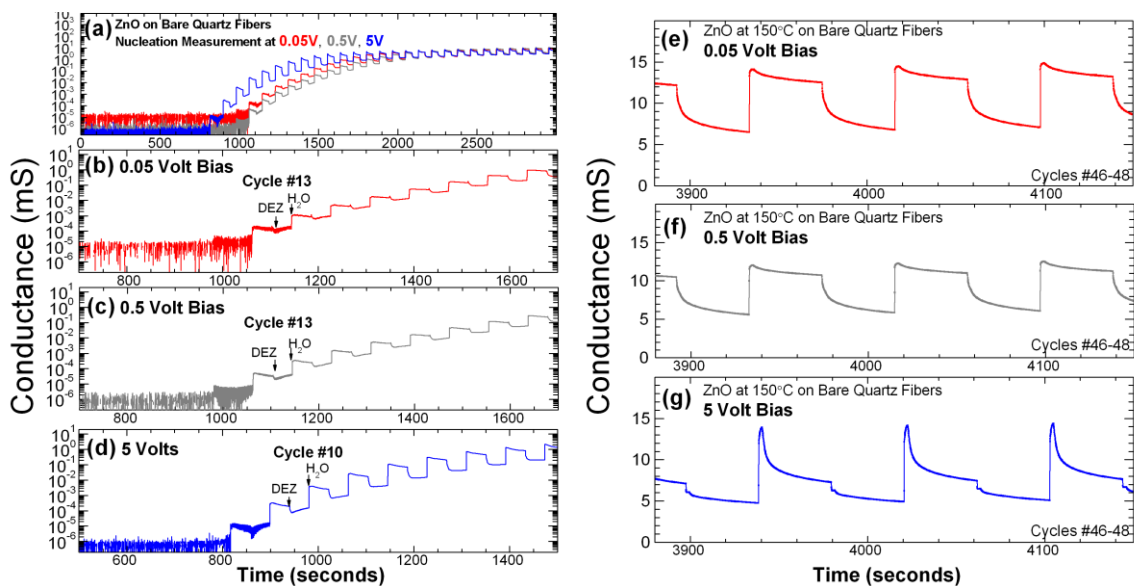


Figure 6.5. ZnO ALD deposited on bare quartz fibers at 150°C; the current was measured and the conductance is plotted for samples (a) together and (b-d) individually, for samples measured under applied bias voltages of 0.05V, 0.5V and 5V; the first well defined DEZ/H₂O cycle is labeled for each sample. The use of higher voltage seems to require fewer cycles before the onset of measurable conductance occurs. (e-g) Steady state behavior for the same samples from (b-d), showing ZnO cycles #46-48 for each of the tests.

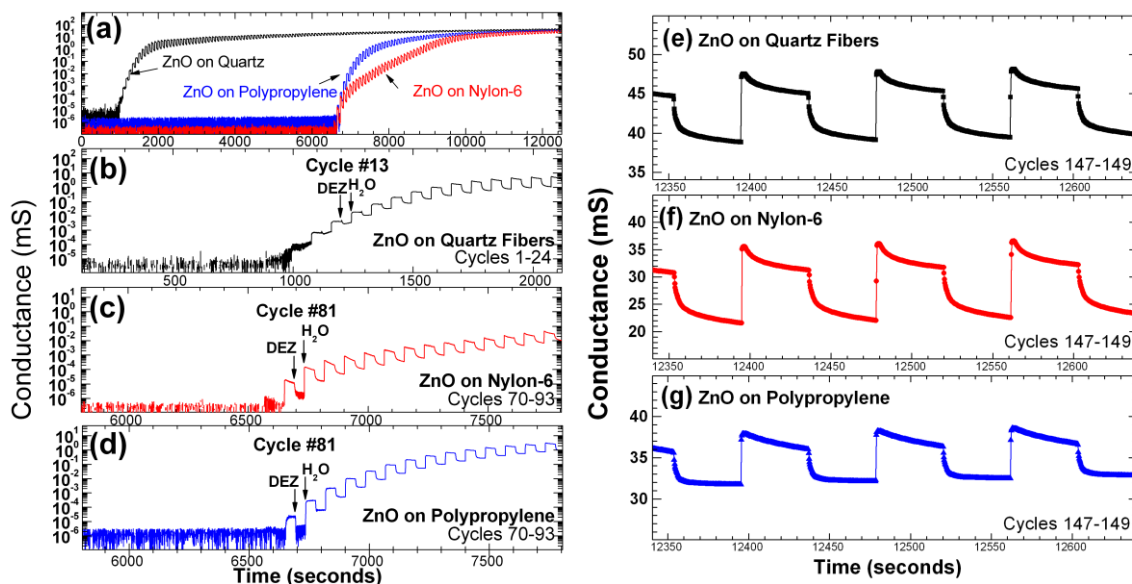
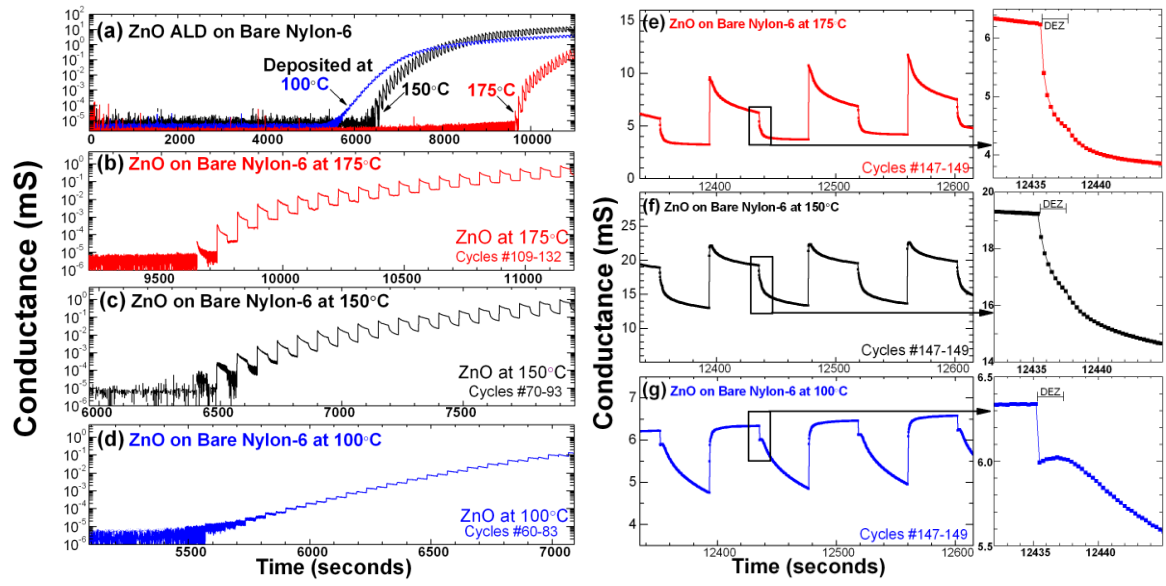


Figure 6.6. The onset of measurable conductance is plotted for ZnO deposition at 150°C on quartz fibers, nylon-6 fibers, and polypropylene fibers, both together (a), and individually (b-d). Figure (a) shows the extent of the difference for the substrates before conductance onset is reached, while Figures (b-d) highlight the conductance trends observed for each substrate once measurable signal is detected. In addition to differences in the number of cycles required before conductance can be measured, the dose/response characteristics appear different in the initial stages for all three substrates. For Figure 6.6(e-g), steady state conductance changes are plotted for ZnO cycles #147-149 on quartz fibers, nylon-6 and polypropylene substrates; note the differences in conductance as indicated on the y-axis scales.

Figure 6.7. (a) Conductance onset is shown for ZnO ALD on bare nylon-6 performed at different temperatures and plotted (a) together, and (b-d) individually for each temperature. In Figure 6.7(a) it can be seen that the number of cycles required to reach measurable conductance is dependent on deposition temperature. Figure 6.7(b-d) shows the nature of increasing conductance for ZnO deposited on nylon-6 at 175°C, 150°C, and 100°C; deposition at 175°C and 150°C show similar dose/response trends but 100°C shows distinctly different behavior. (e-g) Steady state conductance curves are shown for the samples for three ZnO ALD cycles (#147-149). Note the differences in the y-axis scales of the plots. The largest conductance is observed for the 150°C sample, which is within the ZnO ALD window. The dose/response curves for the three samples also appear different, with the 100°C sample showing markedly different behavior. To the right of all three samples, plots of conductance change during and after the DEZ dose are shown. The inset of the 100°C sample shows a sizable bump in conductance, which corresponds in timing to the 2 second DEZ dose, as indicated, similar to the feature shown in Figure 6.5(g) for ZnO deposition on bare quartz when measured with a 5V applied bias.



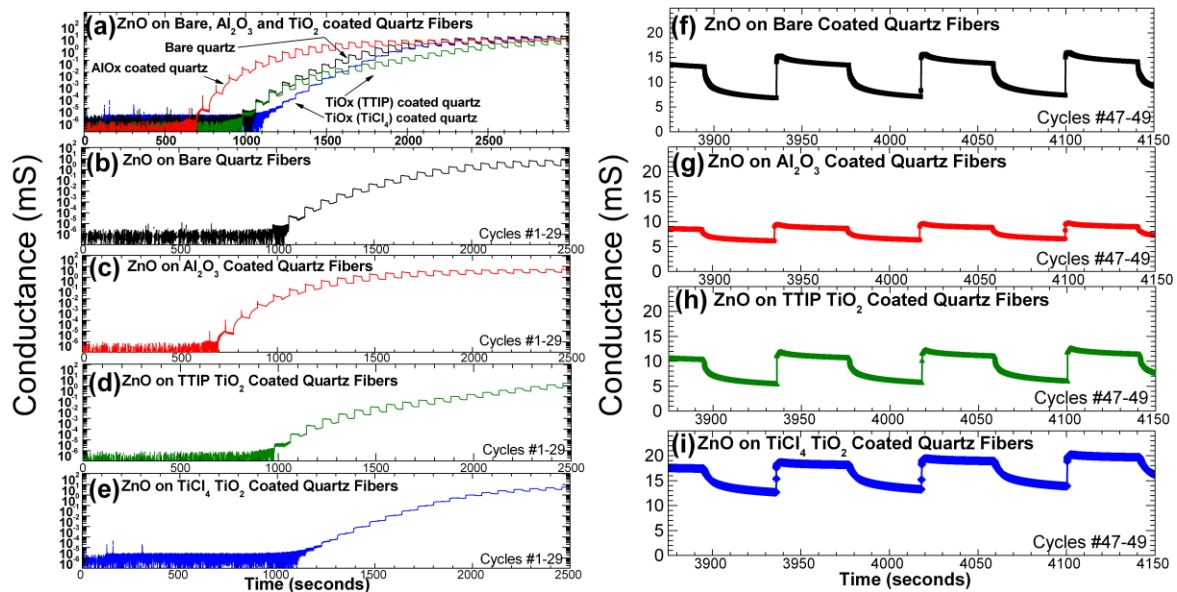


Figure 6.8. Conductance curves for ZnO depositions on bare quartz fibers, and quartz fibers coated with Al_2O_3 and TiO_2 coatings, plotted (a) together, and (b-e) individually for each surface coating. Conductance behavior of the nucleating ZnO coating is initially impacted by composition of the underlying metal-oxide coating, although this dependence is only an interfacial phenomenon; and (f-i) in under 50 ZnO ALD cycles, the conductance curves show similar dose/response behavior for all of the samples, which is not the case earlier in the deposition when conductance behavior is more influenced by interfacial characteristics.

APPENDIX

6.6 Appendix - Supplemental Items Not Published

The figures and discussion included below are supplemental information for the prior article, and were deemed important work for this thesis and are thus included here.

In situ conductance curves taken during ALD of aluminum doped zinc oxide are shown in Figure A.6.1. The AZO film consist of a 19 ZnO ALD cycles followed by 1 Al₂O₃ ALD cycle; the impact of the Al-doping cycle is clearly depicted in Figure A.6.1(b). In Figure A.6.1(a), it can be seen that over the course of the 200 total ALD cycles, the slope of the conductance curve continues to increase, meaning the Al doped ZnO has not reached a “steady state” of conductive film deposition, like was achieved for ZnO on quartz which reaches steady state change in about ~80 cycles. This means that the last 19:1 ZnO:Al ‘super cycle’ is more conductive than the proceeding super cycle, suggesting that ‘bulk conductivity’ is not reached within the 200 cycles studied. This trend agrees with earlier findings from this group that show conductivity of Al doped ZnO does not reach bulk value within the 1000 cycles plotted, whereas undoped ZnO reached bulk conductivity in only 400 cycles, as reported in Chapter 5. This might suggest that there is some longer range order to the Al dopant incorporation in conductivity.

The left image shown in Figure A.6.2 has a dopant cycle that is incorporated into the ZnO ALD as a normal Al₂O₃ cycle, and it can be seen that the TMA dose causes a decrease in conductance similar to DEZ doses, but has distinctly different purging features. The

following water dose produces an as-expected increase in conductance. The next seven ZnO cycles however produce an increase, decreasing, and then an increase in conductance.

In the right image shown in Figure A.6.2, the TMA dose follows directly after the DEZ preceding DEZ dose, which interestingly causes an increase in conductance, in contrast with the decrease produced by the other recipe. Another interesting feature is that after the TMA dose is complete, conductance continues to increase during the purge step, which has not been reported elsewhere. The following seven ZnO cycles show similar behavior as was observed for deposition using the first recipe, primarily the increase, decrease, then increase in conductance.

Although TiO_2 in its as-deposited state at these temperatures is not expected to be very conductive, reports have shown that Ti doping ZnO films can provide a significant increase to ZnO film conductivity.¹⁶ In this report, the authors use titanium tetraisopropoxide (TTIP) as the Ti-dopant precursor, rather than TiCl_4 . Both precursors are commonly used to deposit TiO_2 films, however TiCl_4 can be deposited by vapor draw precursor delivery, whereas TTIP typically requires a bubbler due to the lower vapor pressure, making TiCl_4 chemistry easily interchangeable on the system in use without requiring modification or addition of a bubbler delivery system. A potential byproduct of TiO_2 films deposited using TiCl_4 and water could be hydrochloric acid, which has the potential to destroy the crystal structure of the underlying ZnO film, reducing conductivity.

As can be seen in the left plot of Figure A.6.3, conductance for this ZnO film with TiCl_4 doping can be measured, and is shown for 200 cycles, using a 19 ZnO:1 TiO_2 doping ratio. The conductance for these samples is noticeably lower than either ZnO or Al-ZnO

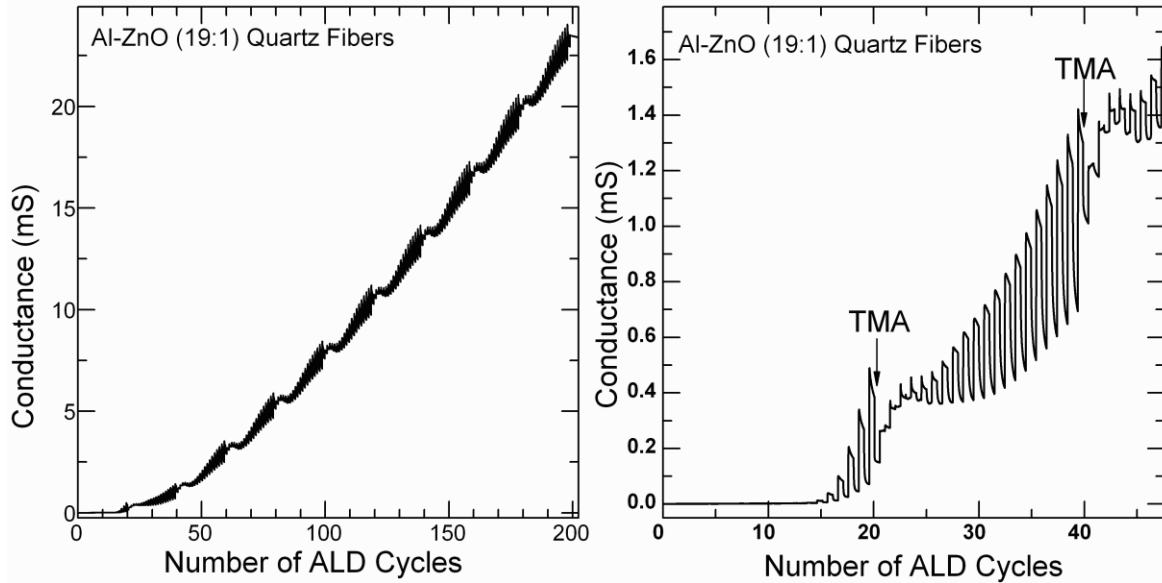
deposited on quartz fiber substrates. As depicted in the middle plot of Figure A.6.3, there is a large drop in conductance, which in the right plot of Figure A.6.3 is indicated to be due to the TiCl_4 dopant dose.

Al_2O_3 is electrically insulating, and so no signal is expected to be measured from the Al_2O_3 film itself. However the underlying ZnO film remains conductive and capable of producing current when the measurement bias is applied. The first few Al_2O_3 cycles deposited on top of the conductive ZnO film increase conductance of the substrate, most likely due to interface effects such as band bending, which has been observed for ZnO deposition on Al_2O_3 .⁷ After the initial interface effects, the conductance slowly drifts downward in a linear fashion. This may be caused by a few factors, including potential thermal instability during the TMA/water dosing, or the ZnO film slowly annealing which would likely decrease defect density and therefore maybe expected to decrease film conductivity and thus measured conductance. The inset of Figure A.6.4(b) shows the small, but regularly spaced fluctuation in conductance, halfway through the 100 cycle Al_2O_3 deposition. This may support the idea that thermal fluctuation during Al_2O_3 dosing, or perhaps the exothermic nature of the Al_2O_3 reaction itself, maybe causing slight variations in conductance over the course of the deposition.

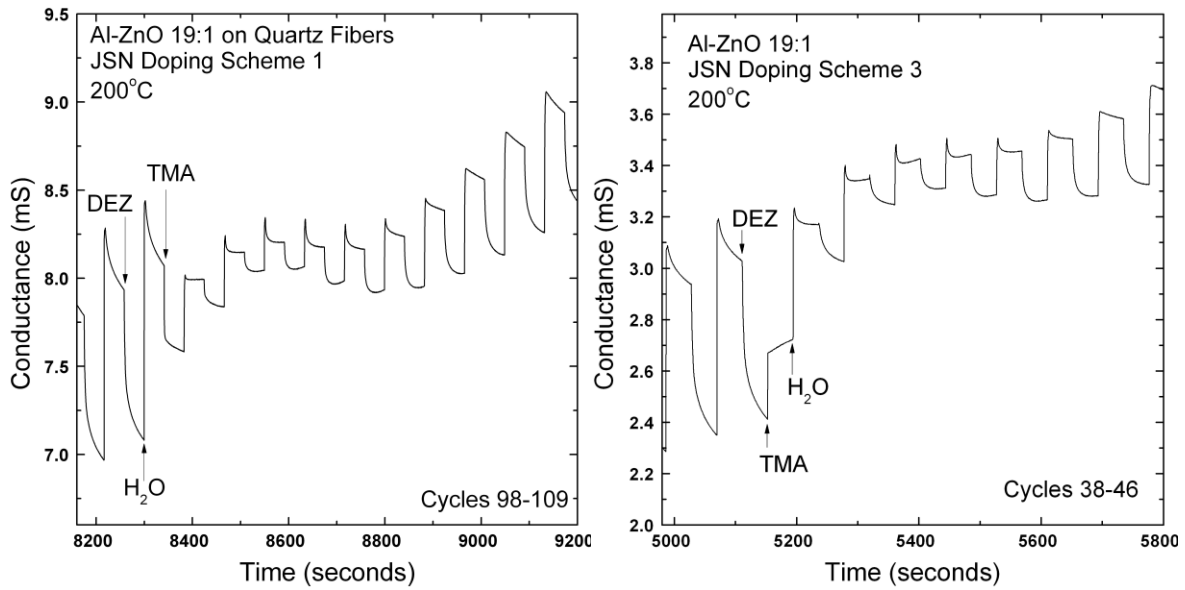
An attempt to measure the conductance of ZnO coatings applied using ‘dose and hold’ precursor dosing was made, to determine if insights into sub-surface nucleation and growth, or the vapor phase infiltration process could be gained by in situ conductance measurements. The results for ZnO ALD on a nylon-6 nonwoven using a ‘dose and hold’ recipe are plotted in Figure A.6.5, which shows (a) the logarithmically plotted onset of measurable

conductance, (b) conductance change during six ‘dose and hold’ ZnO cycles, and (c) an individual ‘dose and hold’ cycle shown in more details with the steps of the process labeled for reference.

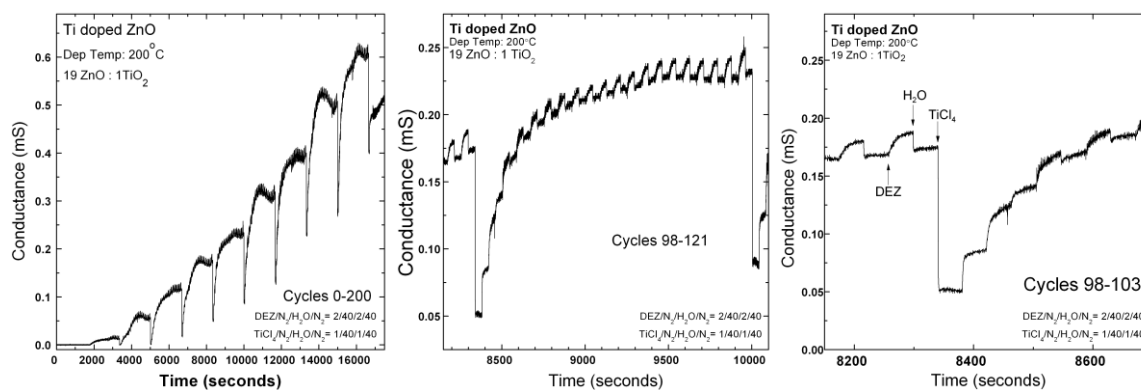
The same characteristics can be seen in Figure A.6.5 as in the typical conductance plot of a ZnO ALD cycle; as shown best in Figure A.6.5(c), upon dosing DEZ the conductance of the sample decreases, and upon water dosing, the conductance increases substantially. As mentioned earlier, ZnO ALD on nylon-6 forms a relatively abrupt interface, unlike ZnO ALD on polypropylene. Although the fundamental behavior in these plots does not seem to be substantially different than that shown in the normal ZnO ALD on nylon-6 plots, this process maybe worth trying with other substrates that produce sub-surface nucleation growth during ZnO ALD films.



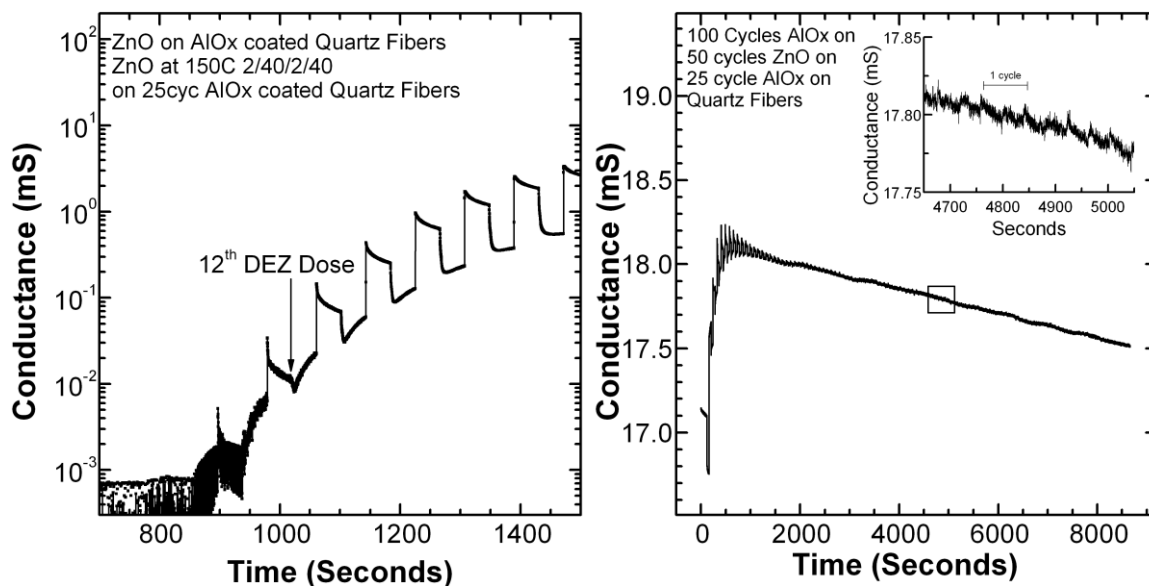
Appendix Figure A.6.1. In situ conductance was measured during ALD of aluminum doped zinc oxide deposition on quartz fibers at 200°C; aluminum doping was achieved by depositing an Al₂O₃ ALD cycle from TMA and water after 19 cycles of ZnO ALD. The image on the left plots conductance for 200 Al-ZnO cycles (10 × [19 ZnO + 1 Al₂O₃] “super cycles”); the right image shows the first two super cycles and indicates the location of the TMA dopant dose. The dopant dose has a significant impact on conductance over the course of the next 10 ZnO cycles.



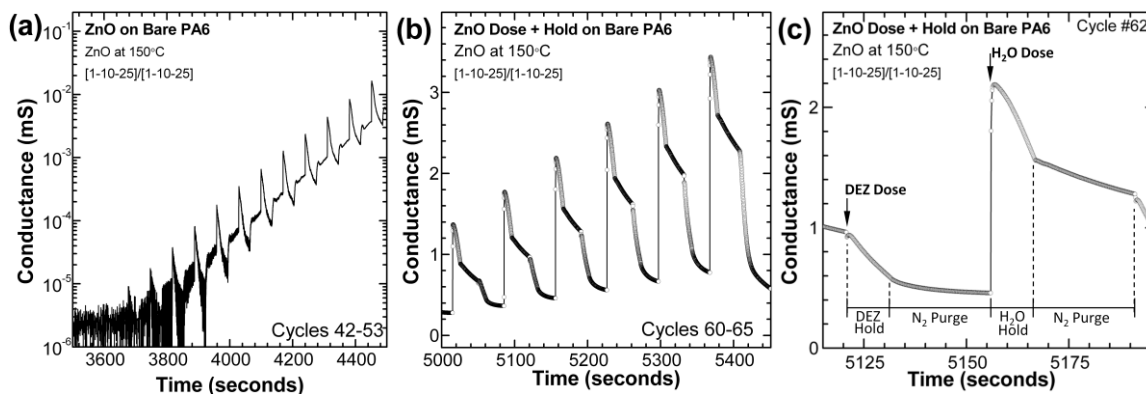
Appendix Figure A.6.2. In situ conductance measurements were taken of aluminum doped zinc oxide ALD deposited on quartz fibers using two different Al-doping recipes, based on work performed by Na et al.² The left figure shows deposition recipe which incorporates Al-doping by depositing an Al₂O₃ cycle following 19 ZnO cycles. The right figure shows a recipe which introduces the Al-dopant by dosing TMA after the 19th DEZ dose, rather than including a water dose in between, as was done in the left figure.



Appendix Figure A.6.3. In addition to depositing Al-doped ZnO film, TiO₂ doped ZnO films were also deposited, using TiCl₄ and water as the TiO₂ precursor. **(left)** Using a 19 ZnO to 1 TiO₂ doping ratio, 200 ALD cycles were deposited on quartz fiber substrate in ALD2 at 200°C. **(middle)** A portion of the overall run is depicted, which include two TiCl₄ doses which cause a large drop in conductance, this can be clearly depicted in **(right)** which indicates precursor doses.



Appendix Figure A.6.4. (a) In situ conductance was measured for ZnO ALD on Al₂O₃ coated quartz fibers. After the ZnO deposition, the substrate was coated with 100 cycles of Al₂O₃ ALD, conductance was measured during the Al₂O₃ ALD, and is shown in (b). Since Al₂O₃ is an electrically insulating material, the current is attributed to the underlying ZnO layer, although curiously, the conductance continues to decrease in a linear rate for the remainder of the 100 Al₂O₃ cycles; an inset shows a magnified portion of the data part of the way through the 100 Al₂O₃ cycles, the duration of an Al₂O₃ cycle is indicated to give reference.



Appendix Figure A.6.5. In situ conductance measurement of a nylon-6 nonwoven during ZnO deposition using “Dose and Hold” recipe where after dosing precursor into the ALD reactor, the gate to the pump is closed isolating the chamber to allow extended substrate-precursor interaction, after which the chamber is purged. **(a)** Onset of conductance for the sample, plotted logarithmically; **(b)** six dose and hold cycles after onset of measurable conductance has occurred, the conductance behavior resembles that from ZnO ALD plots; **(c)** a cycle during the ZnO dose and hold, with the portions of the conductance change labeled to show what step they correspond to: precursor dose, precursor hold, or nitrogen purge.

6.7 References

1. Na, J. S., Scarel, G. & Parsons, G. N. In Situ Analysis of Dopant Incorporation, Activation, and Film Growth during Thin Film ZnO and ZnO:Al Atomic Layer Deposition. *J. Phys. Chem. C* **114**, 383–388 (2010).
2. Na, J.-S., Peng, Q., Scarel, G. & Parsons, G. N. Role of Gas Doping Sequence in Surface Reactions and Dopant Incorporation during Atomic Layer Deposition of Al-Doped ZnO. *Chem. Mater.* **21**, 5585–5593 (2009).
3. Du, X. & George, S. M. Thickness dependence of sensor response for CO gas sensing by tin oxide films grown using atomic layer deposition. *Sensors Actuators B-Chem.* **135**, 152–160 (2008).
4. Spagnola, J. C. *et al.* Surface and sub-surface reactions during low temperature aluminium oxide atomic layer deposition on fiber-forming polymers. *J. Mater. Chem.* **20**, 4213–4222 (2010).
5. Schuisky, M., Elam, J. W. & George, S. M. In situ resistivity measurements during the atomic layer deposition of ZnO and W thin films. *Appl. Phys. Lett.* **81**, 180–182 (2002).
6. Ferguson, J. D., Weimer, A. W. & George, S. M. Surface chemistry and infrared absorbance changes during ZnO atomic layer deposition on ZrO₂ and BaTiO₃ particles. *J. Vac. Sci. Technol.* **23**, 118–125 (2005).
7. Sweet, W. J., Jur, J. S. & Parsons, G. N. Bi-layer Al₂O₃/ZnO atomic layer deposition for controllable conductive coatings on polypropylene nonwoven fiber mats. *J. Appl. Phys.* **113**, 194303 (2013).

8. Gong, B. & Parsons, G. N. Quantitative in situ infrared analysis of reactions between trimethylaluminum and polymers during Al₂O₃ atomic layer deposition. *J. Mater. Chem.* **22**, 15672 (2012).
9. Oldham, C. J. *et al.* Encapsulation and Chemical Resistance of Electrospun Nylon Nanofibers Coated Using Integrated Atomic and Molecular Layer Deposition. *J. Electrochem. Soc.* **158**, D549–D556 (2011).
10. Jur, J. S. *et al.* Temperature-Dependent Subsurface Growth during Atomic Layer Deposition on Polypropylene and Cellulose Fibers. *Langmuir* **26**, 8239–8244 (2010).
11. Sun, Y. *et al.* Influence of Subsurface Hybrid Material Growth on the Mechanical Properties of Atomic Layer Deposited Thin Films on Polymers. *Chem. Vap. Depos.* **19**, 134–141 (2013).
12. Groner, M. D., Fabreguette, F. H., Elam, J. W. & George, S. M. Low-temperature Al₂O₃ atomic layer deposition. *Chem. Mater.* **16**, 639–645 (2004).
13. Malm, J., Sahramo, E., Perälä, J., Sajavaara, T. & Karppinen, M. Low-temperature atomic layer deposition of ZnO thin films: Control of crystallinity and orientation. *Thin Solid Films* **519**, 5319–5322 (2011).
14. Richters, J. P., Voss, T., Kim, D. S., Scholz, R. & Zacharias, M. Enhanced surface-excitonic emission in ZnO/Al₂O₃ core-shell nanowires. *Nanotechnology* **19**, 4 (2008).
15. Pearton, S. J., Norton, D. P., Ip, K., Heo, Y. W. & Steiner, T. Recent advances in processing of ZnO. *J. Vac. Sci. Technol. B* **22**, 932–948 (2004).
16. Lee, D.J. *et al.* Atomic layer deposition of Ti-doped ZnO films with enhanced electron mobility. *J. Mater. Chem. C* **1**, 4761 (2013).

CHAPTER 7 is a manuscript in preparation to be submitted.

CHAPTER 7. Atomic Layer Deposition on of Zinc Oxide on Nylon-6 Nanofibers and Microfibers: A Comparison of Conductivity and Tensile Properties

7.1 Introduction

Nylon-6 is a mechanically and thermally robust polymer that is widely used in the nonwoven industry. Many applications that utilize nonwoven fiber mat material would benefit from the availability of higher surface area substrates, such as uses for filtration or disposable wipes. Nanofibers offer high surface area compared to standard microfibers because they have a higher surface area to volume ratio due to their smaller fiber diameter. Commercial viability, cost, and scalable production volume remain obstacles to wider industrial adoption, although many solutions are under development.

As a result, recent work in the nonwovens industry has lead to the development of high surface area microfiber substrates that can be produced by traditional microfiber spinning techniques. One example produced by Allasso Industries, utilizes Winged FibersTM which have a multi-lobel design that resembles cooling fins on a heat sink.

Surface functionalization of nanofibers is of interest to nanofiber manufacturers since it offers the potential to expand their applicability into new markets. Atomic layer deposition is a surface functionalization process that utilizes vapor phase precursors that are capable of coating high surface area materials through the use of self-limiting precursor chemistry.

Work towards surface functionalization of nylon-6 nanofibers has previously been reported using low temperature Al₂O₃, ZnO, TiO₂ ALD, as well as MLD coatings.^{1,2} Thus

far, work has been focused towards characterizing the mechanical strength or chemical resistance imparted by the ALD/MLD coatings on nylon-6 nanofibers. In this work, we will deposit zinc oxide coatings on nylon-6 nanofibers and winged microfibers, comparing their mass-uptake as a function of coating thickness and precursor exposure. We will also test the tensile strength of the ZnO coated nano and microfibers, and show how the conductivity of Al-doped zinc oxide coatings on nano and micro fibers compare to those on planar silicon.

7.2 Experimental

Atomic layer deposition was performed in one of three similarly constructed home built hot walled ALD reactors, described in more detail elsewhere.²⁻⁴ Deposition was performed under vacuum which was maintained using a rotary mechanical pump. Filter dried nitrogen was allowed to flow at ~140 sccm (standard cubic centimeters per minute) to maintain ~1 Torr pressure in the chamber during deposition. Diethyl zinc (DEZ, 95% STREM Chemical) and trimethyl aluminum (TMA, 98% STREM Chemical) and deionized water (DI, H₂O) were used as reactants. A typical precursor dose of DEZ/N₂/H₂O/N₂ = 2s/40s/2s/40s and produced $\Delta P \sim 0.07$ Torr during DEZ dose, and $\Delta P \sim 0.28$ Torr during the water dose. Aluminum doping was performed by introducing an Al₂O₃ ALD cycle after 19 ZnO ALD cycles; a typical Al₂O₃ cycle had precursor doses of TMA/N₂/H₂O/N₂ = 2s/75s/2s/75s and produced $\Delta P \sim 0.05$ Torr during TMA dose, and $\Delta P \sim 0.28$ Torr during the water dose. The fiber samples were weighed prior to deposition using a Accu-124 Fischer Scientific lab scale, placed in the ALD reactor in a mesh wire sample holder with native

silicon and thermal oxide silicon monitor wafers, and allowed to equilibrate for at least 20 minutes prior to deposition. Depositions were performed between 50°C and 200°C.

Electrospun nylon-6 nonwoven nanofibers were provided by Elmarco, and the primary samples used for this study were reported to be ~100 nm and ~ 200 nm diameter fibers, although the accuracy of these estimates has not been independently verified. The average mat thicknesses were determined to be 0.17 mm for the 100 nm substrates, and 0.44 mm for the 200 nm substrates. Spunbond hydro-entangled Winged Fiber™ nylon-6 nonwovens were provided by Allasso Industries, which we have reported on more extensively elsewhere.^{5,6} The fiber mat thickness was measured to be 0.39 mm.

7.3 Results and Discussion

Conductive ZnO and AZO Coated Nylon-6 Nano and Microfibers

Initial work on the nylon-6 nonwoven nanofibers was performed to characterize the substrates in response to ALD coatings. Initially the substrates were coated with between 50 and 200 cycles of ZnO ALD cycles using reactor ALD2, and the mass gain for both the nano and microfiber samples is plotted in Figure 7.1(a). Additionally, a “Dose and Hold” coating recipe was used, where after introducing the precursor into the reactor chamber, the gate valve to the pump was closed, isolating the precursor and substrate for an extended period of time. This is shown in Figure 7.1(b) for 50 ZnO cycles, as a function of ‘hold time’ where normal ALD coating is plotted on $x = 0$, as indicated by the labeling.

Linear mass uptake is not sufficient to prove self-limiting ALD chemistry is occurring, although with ALD coatings, mass uptake typically is linear with respect to cycle

number. To fully demonstrate that ALD was occurring, rather than pulsed-CVD for example, precursor saturation curves would need to be shown, indicating that mass gain with respect to dose times and purge times, was saturating. Due to the scarcity of the material and limited time allocated for the initial study, a sufficiently thorough precursor dose and purge time optimization study was not possible. However, to indicate whether or not the available surface area was being coated with the provided precursor during ALD, a ‘dose and hold’ recipe, typically used for high surface area materials,⁷ was used to see what effect it had and the results are plotted in Figure 7.1(b). After introducing the hold step, the mass gain for the nanofibers increased from ~18% for 50 ZnO cycles, to ~85% for 50 cycles using a 30 second hold. Importantly, this dosing recipe used a dose-then-close format, indicating that normal N₂ flow occurred throughout the 2 second dose, only after which did the gate to the vacuum pump close. Therefore, it is important to point out that the mass gain produced by introducing the hold step may have saturated after 30 seconds not because the substrate saturated with precursor, but due to precursor depletion. In response to the increase in surface area of the substrates being coated, the typical precursor dose was doubled, and the purge time increased from 40 to 75 seconds so that the typical ZnO dose used for the study was DEZ/N₂/H₂O/N₂ = 4s/75s/4s/75s.

Aluminum doped zinc oxide films (AZO) were deposited because they provide a more conductive coating and are easily deposited by ALD in a well studied process. After 19 cycles of ZnO ALD, an Al₂O₃ ALD cycle was deposited using trimethyl aluminum and water as precursors. Prior work has shown the conductivity of the AZO films to be substantially higher than that of undoped ZnO films,^{8,9} although trimethyl aluminum and nylon-6 react

significantly even at low temperatures,^{2,3,10} which has been reported to lead to degradation of the underlying fiber substrate.² Deposition of AZO films was found to keep the substrate sufficiently intact for post-deposition testing when 19 cycles of ZnO were deposited first, followed by the Al₂O₃ dopant dose. Utilizing the dopant dose first rather than last in the laminate structure was found to cause significant change to the underlying substrate, and so the laminate structure was kept as 19 ZnO then 1 Al₂O₃ for the entirety of the study. The mass gain curves for the AZO coating on the nano and microfiber substrates are plotted in Figure 7.2(a). The corresponding conductivity measurements for the samples in Figure 7.2(a), are plotted in 7.2(b), although the samples with < 80 AZO cycles were not measurably conductive.

As with the mass gain plotted in Figure 7.1(a), the mass gain shows a linear increase with respect to cycle number. The conductivity plot in Figure 7.2(b) generally shows a trend of increasing conductivity with ALD cycle number, for AZO coated nylon-6 nanofibers and microfibers, as well as AZO coated silicon. The error bars in Figure 7.2(b) indicate a $\pm 10\%$ standard deviation from the average. Samples were also coated with 300 cycles of AZO, although during conductivity measurement, the nylon-6 nanofiber substrate fractured completely in half, preventing the gathering of any sample data. It can be seen for the sample plotted in Figure 7.2(b) that the nylon-6 nanofibers were more conductive than the nylon-6 microfibers for all the samples. The microfibers in Figure 7.2(b) are machine direction oriented, and therefore represent the most conductive orientation of microfibers; cross direction cut microfibers would plot even lower relative to the AZO coated nanofibers.

To determine how the ALD coatings would impact the mechanical properties of the nanofiber substrates, tensile testing was performed on the ALD coated, heat treated, and as-received nanofiber and microfiber substrates.

To remove the potential impact of the Al-dopant on the mechanical properties during the test, ZnO ALD films were studied rather than AZO films. As has been reported, the Al-dopant we use in the AZO films, trimethyl aluminum, has been shown to be very detrimental to nylon-6 nanofibers,² although it is not the only precursor that can serve as an Al-dopant source,¹¹ so ZnO ALD coatings were used here to make the findings more applicable to future work, independent of the precursor used for Al-doping.

Tensile Testing ZnO coated Nylon-6 Nano and Microfibers

Figure 7.3(a) plots the raw force versus extension data, as it was collected from the universal tensile testing apparatus; measurements were performed on 100 nm and 200 nm diameter nanofiber substrate materials. The performance differences between the two nanofiber substrate materials is mostly due to the differences in nanofiber mat thickness, this is supported by the fact that when accounting for mat thickness in calculating tensile stress, the nanofiber stress-strain curves are almost identical, as seen in Figure 7.3(b). Included in Figure 7.3(b) are the stress-strain curves calculated from the measured force-extension curves of the nonwoven nylon-6 microfiber substrate, for samples cut oriented in the machine direction and cross direction. The nonwoven microfibers are anisotropic, and show preferential orientation in the Machine Direction (MD) compared to the Cross Direction (CD). To account for this property of the substrate, microfiber substrates were prepared and

tested with alignments in the machine direction, and the cross direction, where the machine direction oriented nonwoven has fibers preferentially oriented along the sample length, parallel to the tensile force during the test, while cross direction fibers are preferentially oriented perpendicular to the deforming force. As a result of this non-uniformity in fiber orientation distribution, machine direction oriented microfiber substrates can withstand higher maximum tensile stress, but exhibit that maximum stress at lower strain values than cross direction fibers, which can handle more strain but at lower maximum stress.

Figure 7.3(b) shows the microfiber samples can withstand higher tensile stress and higher tensile strain than both nylon-6 nanofiber samples. In addition, the shapes of the stress-strain curves are significantly different between the micro and nanofiber samples. The nanofiber substrates display abrupt failure after achieving maximum stress, similar to behavior exhibited by single fiber tensile testing. Both microfiber samples show a more gradual decrease after reaching maximum stress, compared to the nanofiber samples.

The ZnO ALD coated fibers display significantly different behavior than the as-received substrates; Figure 7.4(a) shows tensile tests performed on 200 nm nylon-6 nanofibers coated with 10, 50, or 200 cycles of ZnO ALD. Compared to uncoated reference nanofibers, the samples with 10 and 50 cycles of ZnO ALD can withstand higher tensile stress, and show similar tensile strain at maximum load, while the nanofibers coated with 200 cycles of ZnO ALD perform significantly differently with both lower maximum stress and lower strain at peak load, although greatly increased Young's Modulus; this behavior is more characteristic of a ceramic than a polymer.¹ A fully encapsulating ZnO ALD coating of 200

cycles ($2 \times 34 \text{ nm} \sim 68 \text{ nm}$), has a coating thickness that is approaching that of the fiber radius ($\sim 100 \text{ nm}$).

Figure 7.4(b) shows both MD and CD oriented nylon-6 microfibers samples, coated with the same ZnO ALD coatings. There appears to be an increase in maximum tensile stress for the MD microfibers for thin ZnO ALD coatings, although the effect is not as pronounced as on the nylon-6 nanofibers.

The mechanical enhancement/degradation effect of the ZnO ALD coating is better captured as plotted in Figure 7.5, which shows the tensile stress and tensile strain at max load for the sample set in Figure 7.4, as a function of ZnO ALD cycle number. The plotted data in Figure 7.5 can more clearly indicate whether or not there is a benefit to the tensile properties imparted by the ZnO ALD coating. Figure 7.5(a) plots the tensile stress at maximum load for the 100 nm and 200 nm diameter nylon-6 nanofibers and both orientations of the nylon-6 microfiber substrates, as a function of ZnO ALD cycle number.

Tensile stress at maximum load, for the microfiber substrates in Figure 7.5(a), appear on average to be slightly worse with coatings up 200 ZnO ALD cycles. The tensile strain at maximum load for the two microfiber substrates plotted in Figure 7.5(b) also appear slightly degraded when ZnO ALD coatings are applied.

In contrast, both the 100 nm and 200 nm nylon-6 nanofiber substrates appear to have significantly degraded tensile stress at maximum load for 200 cycle ZnO ALD coatings, although coatings of 10-50 ZnO ALD cycles appear unaffected by the coating, and maybe even made stronger as a result. The tensile strain for the coated nanofibers only decreases with ZnO ALD cycle number. Therefore, it appears that all the ZnO ALD coated nylon-6

fibers tested, seem to suffer a reduction in tensile strain at maximum load as a result of the ZnO ALD coating. However, for thin coatings of 10-50 ZnO ALD cycles, the nanofiber nylon-6 nonwovens appear to experience a small increase in tensile strength as a result of the ZnO ALD.

To better demonstrate whether or not the ZnO ALD coating is the reason for the change in tensile strength or tensile strain seen in Figure 7.4 and Figure 7.5, heat treatment of the as-received substrates was performed under vacuum, to emulate the deposition conditions of ALD. The effect of the heat treatment on the uncoated substrates is shown in Figure 7.6, which shows the average performance of a set of each substrate, subjected to heat treatment performed under vacuum in the ALD reactor prior to tensile testing.

The as-received substrate results are plotted at $T \sim 25^{\circ}\text{C}$ in Figure 7.6 to indicate what effect, if any, the heating had on the substrates. There does not appear to be a trend amongst the samples tested, most appear to be unaffected by the vacuum anneal. The impact of vacuum annealing the machine direction cut nylon-6 substrates is unclear, since the substrates heated to 50°C and 100°C appear to have higher tensile strength than the as-received substrate, and the error bars for the substrate heated to 150°C are too large to allow a conclusive determination, although the average of the measurements does appear roughly the same tensile stress at max load, as the as-received material.

7.4 Conclusions

Zinc oxide coatings were successfully applied to nylon-6 nanofiber substrates using atomic layer deposition, and the nanofibers showed enhanced mass uptake per ALD cycle

compared to microfiber nylon-6 nonwoven mats. Aluminum doped ZnO films were also deposited on the nylon-6 nanofiber and microfiber substrates, and thin AZO coatings of less than 300 ALD cycles could be deposited without causing the nanofibers to become too brittle to handle. The AZO coated nylon-6 nanofibers were more conductive than the comparable machine direction oriented microfibers with the same coating, for samples coated with between 80-200 AZO ALD cycles.

Tensile testing of nylon-6 nanofibers coated with 10-50 ZnO ALD cycles, appear to exhibit a slight increase in tensile strength, although when coated with 200 ZnO ALD cycles the nanofibers performed substantially worse than the uncoated fibers. The tensile strength of the nylon-6 microfibers was only marginally decreased as a result of the thickest ZnO ALD coating tested.

The tensile strain at maximum load for both the nanofibers and microfibers substrates was harmed for all thicknesses of ZnO ALD coatings tested. The decrease in tensile strain at maximum load is most evident for the 200 ZnO ALD coatings, which slightly decrease the performance of the microfibers, but caused the tensile strain at maximum load for the 200 nm nanofiber substrate to decrease from ~40% strain, to < 2% strain at maximum load; the stress/strain curve reveals a large increase in the Young's Modulus of the sample, characteristic of a ceramic material.

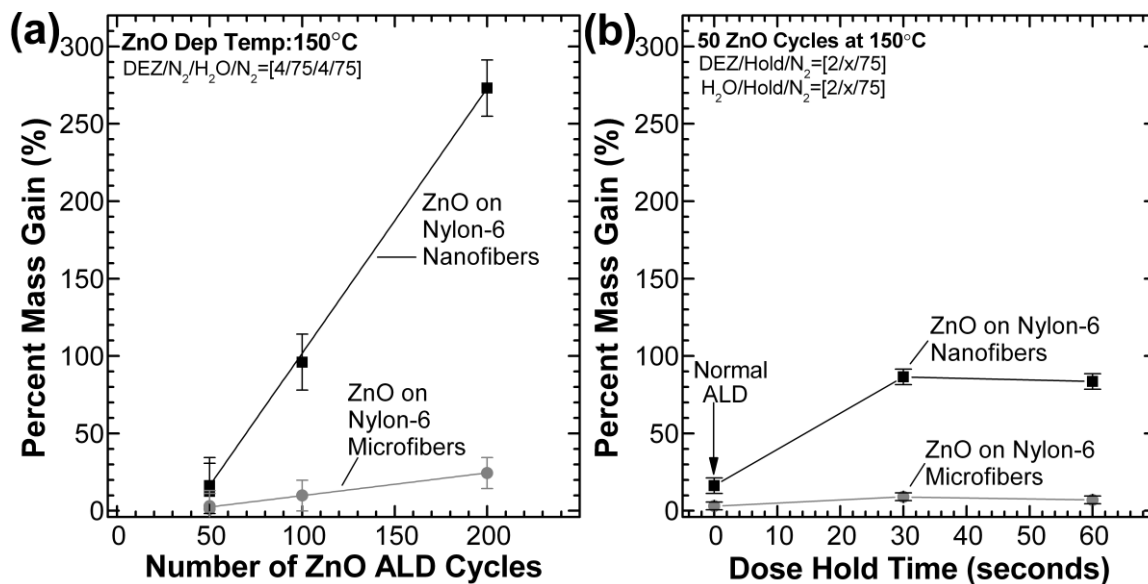


Figure 7.1. (a) Mass gain as a function of ZnO ALD cycles on nylon-6 nanofibers and microfibers; (b) Mass gain as a function of hold time after precursor dose for substrates coated with 50 ZnO ‘dose and hold’ cycles, where normal ALD is indicated by a 0 second hold time. Longer hold times after precursor dosing may allow better surface coverage or precursor infiltration of the substrates.

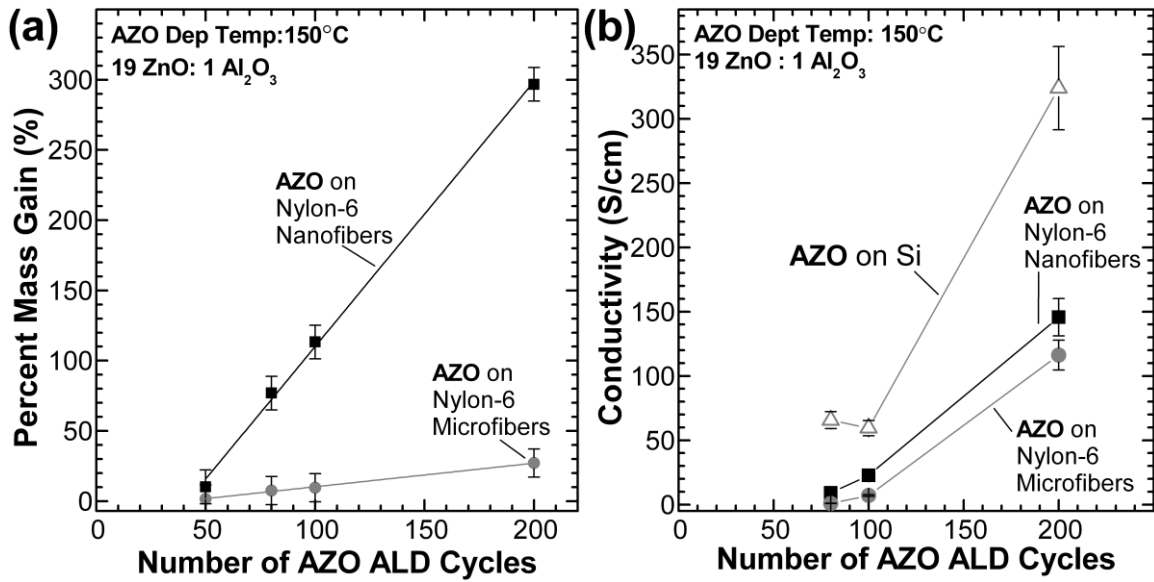


Figure 7.2. (a) Mass gain as a function of AZO cycles for ALD on nylon-6 nanofiber and microfiber substrates; (b) the corresponding conductivity of the samples shown in 7.2(a), noting that the samples coated with < 80 AZO ALD cycles were not measurably conductive. The microfibers in 7.2(b) are machine direction oriented, so that any similarly AZO coated cross direction oriented samples would have lower conductivity than the microfibers plotted.

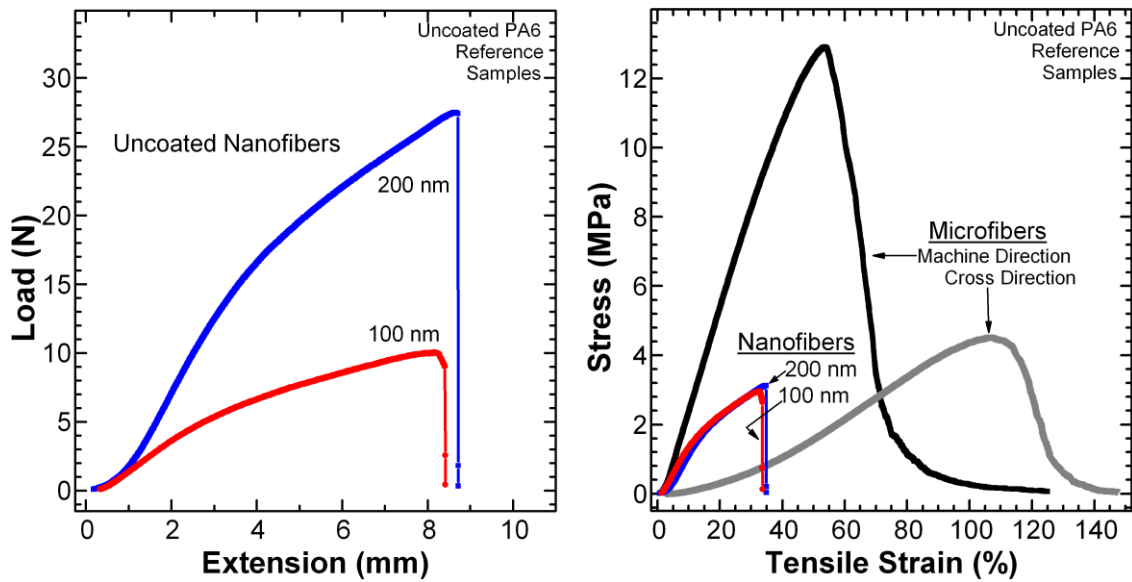


Figure 7.3. (a) As measured tensile data of Load (in Newtons) vs. Extension length, for nylon-6 nanofiber mats consisting of 100 nm or 200 nm fiber diameter electrospun nanofibers acquired from Elmarco and tested as-received. (b) Calculated tensile stress vs. strain data for uncoated nylon-6 nanofibers, as well as Alllasso Industries nylon-6 Winged Fibers™. Using measured fiber mat thickness, the load can be converted into tensile stress, which provides a better comparison of the material performance rather than the sample specific performance; strain is found using the known spacing between the clamps performing the test.

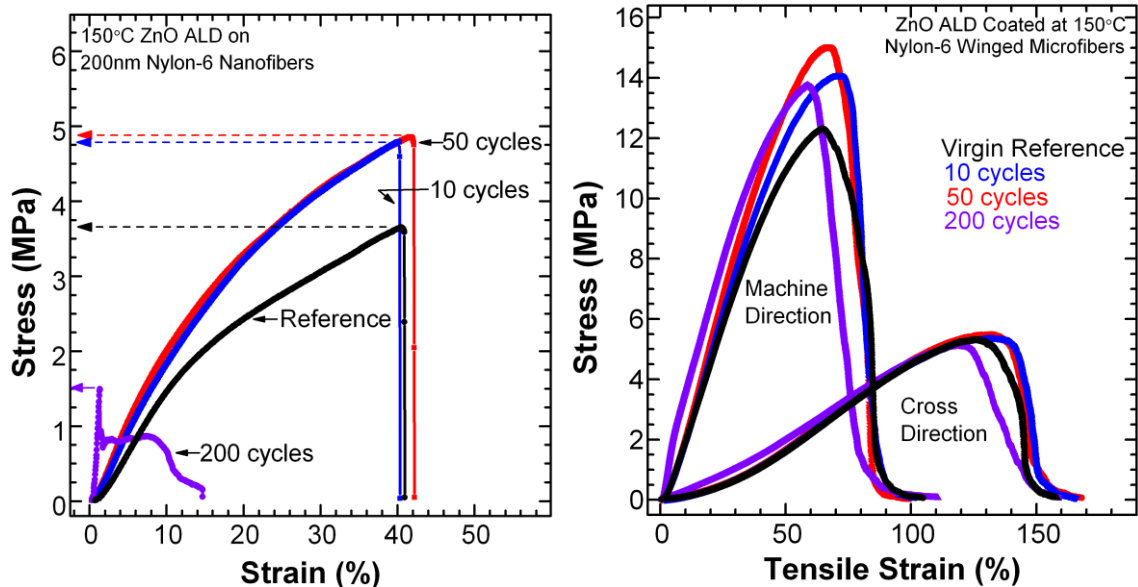


Figure 7.4. (a) Representative Stress-Strain curves for 200 nm diameter electrospun nylon-6 nanofibers coated with different numbers of ZnO ALD cycles at 150°C. Samples with low or no ALD coating appear to behave similarly; however upon coating with 200 ZnO ALD cycles the stress-strain curve is significantly altered. The dashed lines indicate the maximum tensile stress for each sample; the strain value corresponding to the peak stress is referred to as the strain at peak load. (b) The comparable ZnO ALD coated microfiber substrates for both MD and CD orientations. Unlike the nanofiber samples, the microfiber samples do not exhibit a trend upon ZnO ALD coating.

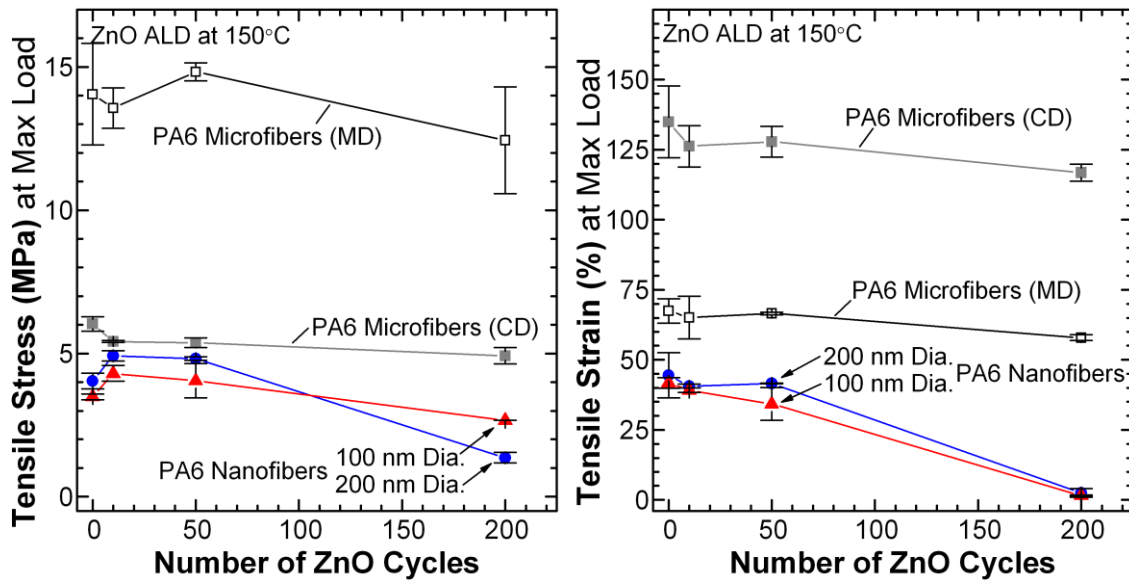


Figure 7.5. Tensile stress (a), and tensile strain (b) at peak load are plotted for nylon-6 nanofiber and microfiber samples as a function of the number of ZnO ALD coating cycles. A ZnO coating of 10 or 50 ZnO ALD cycles increases the tensile strength of nylon-6 nanofibers, while a 200 cycle coating causes a significant decrease; the tensile strain for these samples follows the same trend. ZnO coatings up to 200 cycles causes slight decreases in both tensile stress and strain performance for both nylon-6 microfiber samples.

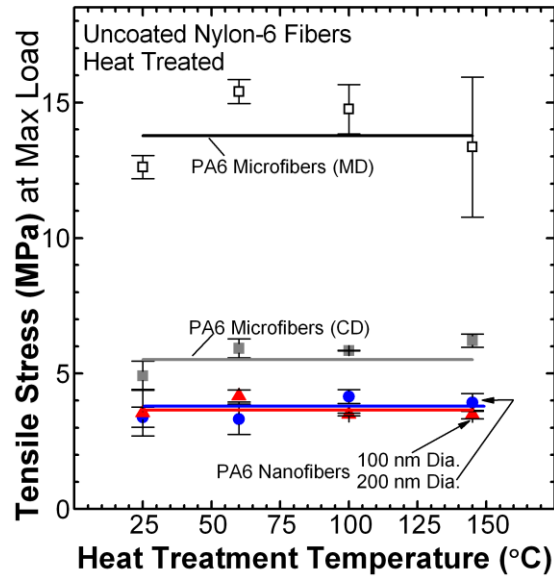


Figure 7.6. Uncoated nonwoven nylon-6 substrates were subjected to heat treatment under vacuum to simulate the heating effects of ALD coating. The substrates were then tensile tested, and the tensile stress at peak load is plotted as a function of heat treatment temperature; unheated reference samples are plotted at a treatment temperature of 25°C. The heat treatment does not seem to impact the tensile stress at maximum load for either nanofiber sample or the cross direction microfibers. Machine direction microfibers appear to exhibit a slight increase in tensile performance upon heating for the samples tested. Trend lines are to guide the eye.

7.5 References

1. McClure, C. D., Oldham, C. J., Walls, H. J. & Parsons, G. N. Large effect of titanium precursor on surface reactivity and mechanical strength of electrospun nanofibers coated with TiO₂ by atomic layer deposition. *J. Vac. Sci. Technol. Vac. Surfaces Films* **31**, 061506 (2013).
2. Oldham, C. J. *et al.* Encapsulation and Chemical Resistance of Electrospun Nylon Nanofibers Coated Using Integrated Atomic and Molecular Layer Deposition. *J. Electrochem. Soc.* **158**, D549–D556 (2011).
3. Spagnola, J. C. *et al.* Surface and sub-surface reactions during low temperature aluminium oxide atomic layer deposition on fiber-forming polymers. *J. Mater. Chem.* **20**, 4213–4222 (2010).
4. Jur, J. S. *et al.* Temperature-Dependent Subsurface Growth during Atomic Layer Deposition on Polypropylene and Cellulose Fibers. *Langmuir* **26**, 8239–8244 (2010).
5. Sweet, W. J., Jur, J. S. & Parsons, G. N. Bi-layer Al₂O₃/ZnO atomic layer deposition for controllable conductive coatings on polypropylene nonwoven fiber mats. *J. Appl. Phys.* **113**, 194303 (2013).
6. Kalanyan, B., Oldham, C. J., Sweet, W. J. & Parsons, G. N. Highly Conductive and Flexible Nylon-6 Nonwoven Fiber Mats Formed using Tungsten Atomic Layer Deposition. *Acs Appl. Mater. Interfaces* **5**, 5253–5259 (2013).

7. Devine, C. K., Oldham, C. J., Jur, J. S., Gong, B. & Parsons, G. N. Fiber Containment for Improved Laboratory Handling and Uniform Nanocoating of Milligram Quantities of Carbon Nanotubes by Atomic Layer Deposition. *Langmuir* **27**, 14497–14507 (2011).
8. Na, J. S., Scarel, G. & Parsons, G. N. In Situ Analysis of Dopant Incorporation, Activation, and Film Growth during Thin Film ZnO and ZnO:Al Atomic Layer Deposition. *J. Phys. Chem. C* **114**, 383–388 (2010).
9. Lujala, V., Skarp, J., Tammenmaa, M. & Suntola, T. Atomic layer epitaxy growth of doped zinc oxide thin films from organometals. *Appl. Surf. Sci.* **82-83**, 34–40 (1994).
10. Sun, Y. *et al.* Influence of Subsurface Hybrid Material Growth on the Mechanical Properties of Atomic Layer Deposited Thin Films on Polymers. *Chem. Vap. Depos.* **19**, 134–141 (2013).
11. Wu, Y. *et al.* Enhanced Doping Efficiency of Al-Doped ZnO by Atomic Layer Deposition Using Dimethylaluminum Isopropoxide as an Alternative Aluminum Precursor. *Chem. Mater.* **25**, 4619–4622 (2013).

APPENDIX

APPENDIX A1. Co-Authored Work

Appendix A1.1 is a reprint of a co-authored article published in *ACS Applied Materials and Interfaces*, 2013, 5, 5253–5259, DOI: 10.1021/am401095r.

Appendix A1.1 Highly Conductive and Flexible Nylon-6 Nonwoven Fiber Mats Formed using Tungsten Atomic Layer Deposition

*Berç Kalanyan, Christopher J. Oldham, William J. Sweet III and Gregory N. Parsons**

Department of Chemical and Biomolecular Engineering

North Carolina State University

Raleigh North Carolina 27695

*My contribution to this work included designing, implementing, and analyzing the experiments for tungsten ALD on nylon-6 fibers, including the results shown in Figure 4 and Figures 6 through 9, as well as Figures A.1 and A.2 of the appendix.

A1.1.1 Abstract

Low temperature vapor-phase tungsten atomic layer deposition (ALD) using WF_6 and dilute silane (SiH_4 , 2% in Ar) can yield highly conductive coatings on nylon-6 microfiber mats, producing flexible and supple nonwovens with conductivity of ~ 1000 S/cm. We find that an alumina nucleation layer, reactant exposure, and deposition temperature all influence the rate of W mass uptake on 3D fibers, and film growth rate is calibrated using high surface area anodic aluminum oxide. Transmission electron microscopy (TEM) reveals highly conformal tungsten coatings on nylon fibers with complex ‘winged’ cross-section. Using reactant gas ‘hold’ sequences during the ALD process, we conclude that reactant species can transport readily to reactive sites throughout the fiber mat, consistent with conformal uniform coverage observed by TEM. The conductivity of 1,000 S/cm for the W-coated nylon is much larger than found in other conductive nonwovens. We also find that the nylon mats maintain 90% of their conductivity after being flexed around cylinders with radii as small as 0.3 cm. Metal ALD coatings on nonwovens make possible the solvent-free functionalization of textiles for electronic applications.

A1.1.2 Introduction

Conductive fibers have applications in medicine, fluidics, catalysis, filtration, separation, energy storage, electromagnetic shielding,¹ smart textiles,² and chemical sensing.²⁻⁴ Natural and synthetic fibers are made electrically conductive using a variety of methods including incorporation of metal fillers into fibers,⁵ application of exterior conductive polymer coatings by in-solution polymerization⁶ or spray-coating,^{7,8} and core-shell fiber structures with conductive core or shell.⁹ Fibers that incorporate organic conductive coating or blends,^{6,10-12} result in fibers with conductivity values less than 2 S/cm. Composite nanofibers containing oriented multiwalled carbon nanotubes reach about 1 S/cm conductivity¹³ and Kevlar fibers coated with single-walled nanotubes result in 65 S/cm⁷. Metallic coatings on fibers are inherently more conductive. Successively Ni- and Au-plated Kevlar fibers can display electrical conductivity values of 6 S/cm¹⁴. Silicone fibers filled with Ag flakes⁵ reach 470 S/cm, while nylon fiber mats coated with Ag using a commercial electroless plating solution exceed ~1800 S/cm when loaded with ~17 wt.% Ag.⁴

Another method of imparting conductivity to materials with complex geometries, such as nonwoven fabrics, is by applying coatings using vapor deposition techniques. In a previous work, we showed the application of tungsten coatings on woven quartz fiber mats by atomic layer deposition (ALD) for chemical sensing applications.⁴ Here, we use the tungsten ALD process to coat nonwoven polyamide nylon-6 mats that have complex fibril cross-sections. The atomic layer deposition process allows for precise thickness control and film conformality on complex and high surface area substrates. Furthermore, WF_6 and TMA

employed in this study are common ALD precursors in the electronics industry. ALD processing is highly scalable and is more recently available in roll-to-roll configurations (e.g. Beneq WCS 500).

Tungsten ALD was first developed by adapting existing tungsten chemical vapor deposition (CVD) reactions.¹⁵ Specifically, ALD of tungsten was conceived as a conformal nucleation layer for tungsten plug contacts typically prepared by CVD^{16,17} for microelectronics applications. More recently, W ALD films were deposited on polymeric substrates^{18,19}, nanoparticles²⁰, and carbon nanotubes²¹. In this work we expose nylon-6 mats to sequential doses of tungsten hexafluoride (WF_6) and 2% silane (SiH_4) diluted in argon in a flow-tube reactor to deposit tungsten thin films. We characterize the resultant conductive fibers using transmission electron microscopy, mass gain analysis, and four-probe conductivity. The W-coated fibers show excellent electrical conductivity and film conformality. Using the W-ALD process we reach conductivity values of 1,000 S/cm which exceed most fabricated conductive fiber systems. The dry ALD process avoids common issues with substrate wetting and coating uniformity. We also show that W-coated nylon fiber mats maintain high conductivity upon bending around small cylinders. These features make W-ALD coated fibers attractive for flexible textile-based electronics or other related applications.

A1.1.3 Experimental

We deposited tungsten in a custom built hot-walled ALD reactor housed inside a walk-in fume hood. The main reactor chamber consists of a 24 inch long stainless-steel tube

with inside diameter of ~ 1.6 inches. Precursors are delivered into the reaction zone through 1/4-inch stainless steel tubes, heated to 70°C to preheat the process gas and prevent any precursor condensation. Pressure is monitored using a convection enhanced Pirani gauge installed downstream from the reaction zone, near the gas flow outlet. All gas flow rates are metered using needle valves and switched on and off by pneumatically actuated diaphragm valves. The reactor chamber was pumped by an Alcatel Pascal 2010SD rotary vane pump (9.7 L/min).

For aluminum oxide deposition we used 98% trimethyl aluminum (TMA) (Strem Chemicals) and reagent grade water (Ricca Chemicals) as precursors. The tungsten source was 99.9% tungsten hexafluoride (WF_6) from Sigma-Aldrich. The tungsten co-reactant was a dilute mixture (2% by weight) of silane in 99.999% Ar (Custom Gas Solutions, Durham NC). We used 99.999% pure N_2 as the carrier gas passed through an Entegris GateKeeper inert gas purifier to remove any residual water and oxygen from the nitrogen gas supply. Excess precursor and product gases are pumped out of the reactor using an Alcatel Pascal 2010SD (9.7 L/min) rotary vane pump filled with fluorocarbon oil (Fomblin 25/6 grade). Before reaching the pump, gases are scrubbed using two in-line filters (Visi-Trap by Mass-Vac Inc.).

Nylon-6 (polyamide-6, PA-6) samples used were hydro-entangled winged fibers, ~ 70 g/m^2 , from Allasso Industries Inc., Morrisville NC. Since nylon-6 melts at 215°C ²² we limit deposition to a maximum temperature of $\sim 200^{\circ}\text{C}$. The fiber mat basis weight is 70 g/m^2 , and the Brunauer Emmett Teller (BET) specific surface area was measured to be 2.5 m^2/g using a Quantachrome Autosorb-1. Anodic aluminum oxide (AAO) disk substrates were purchased from Whatman (Anopore Anodisc). The disks were 13 mm in diameter and 60 μm thick, and

the average pore diameter was 200 nm. Silicon wafers for process monitoring were purchased from WRS Materials (wafers manufactured by MEMC) and were used as received.

Before each tungsten deposition, the carrier gas pressure was adjusted to 2.0 Torr. P-type silicon (100) wafers were cleaved into 1 x 1 cm pieces and loaded into the chamber using a flat sample boat, positioned at the midpoint of the reaction zone (12" downstream from gas inlet). The fiber and AAO substrates were held in place between two pieces of fine stainless steel mesh. The silicon and fiber samples were placed in the reactor so that precursor gases flowed parallel to the samples (i.e. perpendicular to the sample normal), whereas the AAO samples were positioned upright in the reactor (gas flow parallel to the sample normal, i.e. 'flow-through' configuration) to help promote gas transport through the substrates.

After loading the samples, the reactor was pumped down to 80 mTorr followed by dry N₂ flow for 30 minutes at the operating pressure between of 2.0 Torr to allow the sample to reach the reaction temperature. Prior to tungsten deposition, all samples were coated with 25 cycles of Al₂O₃ in order to promote W nucleation.^{23,24} One ALD cycle for aluminum oxide consisted of the sequence TMA/N₂/H₂O/N₂ with times of 0.3/30/0.3/30 s respectively, producing 1.1-1.2 Å of growth per cycle. Film thickness was measured after deposition using spectroscopic ellipsometry (J.A. Woollam Co. alpha-SE) with the CompleteEASE data analysis software package. The Al₂O₃ optical constants were obtained by fitting ellipsometry data from a ~100 nm alumina film on silicon to a Cauchy model. The typical native silicon oxide thickness was measured to be ~1.7 nm and was included in the model.

Tungsten ALD films were deposited by dosing 2% SiH₄ and WF₆ precursor gases into the reactor in alternating pulses. The pulse sequence followed the WF₆/N₂/SiH₄/N₂ pattern with typical exposure times of 1/30/45/30 seconds. For some runs, we used a “hold” step where we closed all the valves in the reactor immediately after a precursor dose in order to expose the sample to precursor vapor for an extended period of time. We recently studied the effect of silane exposure and deposition temperature on W ALD using WF₆ and dilute silane.²⁵ Using silane and WF₆ exposures of $\sim 6 \times 10^5$ and $\sim 10^6$ Langmuirs, respectively, we find an ALD “temperature window” between 200°C and 300°C with a W growth rate of $\sim 6.0 \pm 0.5$ Å/cycle. At 150°C, a silane exposure of 6×10^5 L leads to saturated growth at ~ 4 Å/cycle. Using 2% silane in Ar, this exposure is attained for a 30 second exposure when the pressure change during the SiH₄/Ar dose is controlled at 1.0 Torr.²⁵ In this work, we investigate the role of silane and WF₆ dose on mass uptake and effective conductivity of the coated nylon fiber mats.

The gas exposure is estimated by the net pressure change multiplied by the dose time. When the WF₆ cycle produces $\Delta P = 0.2$ Torr, a 1 second gas pulse time corresponds to $0.2 \text{ Torr} \times 1 \text{ sec} = 2.0 \times 10^5$ L exposure. For the 2% silane in argon, the exposure times are longer, so for $\Delta P = 0.5$ Torr, a 30 second gas pulse time corresponds to $0.5 \text{ Torr} \times 0.02 \times 30 \text{ sec} = 3.0 \times 10^5$ L. These exposure values are rough estimates. The analysis neglects gauge sensitivity to non-inert gases, the contributions of reaction by-products to the measured pressure, as well as effects of gas flow dynamics (including pressure transients and any composition-dependent pumping speed). We use these estimates only to compare relative exposures under various run conditions.

Growth rate on fibers was determined by measuring the mass of the substrate before and immediately after deposition (Fisher Scientific Accu 124 mass balance). The percent mass gain is the difference between the mass before and after coating divided by the starting mass. All of our nylon samples were cut into uniform sizes from the same fabric stock.

Conductivity of tungsten-coated nylon-6 fiber mats was measured using a four-probe apparatus.⁴ Briefly, coated fiber substrates were contacted by four parallel gold contact pads with the outer electrode pair connected to a current source and the inner pair connected to a volt meter (Keithley 2605 source meter). Samples were then subjected to a normal compressive force of known magnitude to enhance contact between the individual fibers. Assuming that the conductive coating is uniform between the electrode contacts, the effective conductivity of the coating was determined by normalizing to the coating mass and coating material density (taken to be the coating material bulk density). For comparison, the resistivity of tungsten films on oxide-coated silicon was measured using a Jandel four-point probe with an RM3-AR head.

Transmission electron microscopy was performed on nylon-6 fiber samples prepared by microtome (Leica Ultracut 7 equipped with a diamond knife). The fibers were embedded in Spurr's epoxy (EMS) and cured using a standard curing schedule. The embedded fibers were cut at room temperature into 90–110 nm thick slices. Sections collected on 300 mesh sample holder were imaged using a cold field emission electron source with an accelerating voltage of 200 kV (Hitachi HF2000).

Porous AAO samples were imaged in an FEI XL30 scanning electron microscope system equipped with a field emission electron gun. Prior to imaging, bare AAO samples were coated with Au/Pd (80%/20%) for 2 minutes in a sputter coater. Tungsten ALD coated AAO samples did not require any sputtering due to the high conductivity of the thin films.

A1.1.4 Results and Discussion

W ALD Growth Rate Calibration on Anodic Aluminum Oxide

As a first step in characterizing tungsten deposition on nylon substrates, we deposited tungsten films on commercial anodic aluminum oxide substrates and examined film thickness by SEM and TEM. These substrates have an effective aspect ratio of $>300:1$, which is larger than that for the nonwoven nylon fibers mats. Although the effect of gas exposure and reactant ‘hold’ times were not explored for these structures, we used hold steps for TMA, H_2O , and WF_6 doses. The silane doses consisted of long exposure times (i.e. 120 seconds) without hold steps. After coating with 25 cycles of Al_2O_3 , we deposited 25, 45, or 100 cycles of W, all at $200^\circ C$. The Al_2O_3 recipe was TMA/ N_2 / H_2O / N_2 = 0.3(20)/60/0.3(20)/90 seconds, respectively. Similarly, the W ALD cycle followed SiH_4 / N_2 / WF_6 / N_2 = 120/90/1(60)/60 seconds. The pressure change in the reactor was 1.0 Torr during the 2% silane dose and the WF_6 dose.

Figure 1 shows a series of plan-view SEM images of the partially filled AAO pores after Al_2O_3 and W ALD.

Figure 1(a) shows an uncoated AAO substrate coated with a thin Pd/Au layer to facilitate electron imaging. The pores are not highly uniform, but the average diameter is

estimated to be 251 ± 14 nm. Image (b) was collected after 25 W ALD cycles. Average pore diameter is reduced to 212 ± 13 nm after the ALD coating. Edge definition is also lost to some extent, as features appear less sharp. After 45 W cycles, image (c) shows pore sizes further reduced to 186 ± 30 nm and edge features are rounded as would be expected from a conformal coating. Increasing the coating thickness to 100 cycles in image (d), the average pore diameter becomes 94 ± 17 nm. Some smaller pores appear to be closed completely and the top surface of the AAO is rounded. The change in pore size yields a growth rate of ~ 7.8 Å/cycle. Considering the nonuniform starting surface, this is reasonably similar to the ~ 6 Å/cycle we observed on planar Si(100) substrates coated separately under similar conditions.²⁵ Growth thickness versus cycle number for deposition on AAO (from TEM) and on silicon are shown in Figure 2.

In addition to a cross-section view of the W coating, the cracking also removed parts of the AAO walls to reveal the W formed along the inner pore walls (see for example the arrow in Figure 3(a)). The coating in image Figure 3(b) is $\sim 2\times$ thicker than in (a), consistent with the increased coating cycles. The W growth rate from these images is 6.6 Å/cycle. The results on AAO confirm that the W ALD process using dilute silane can produce good W ALD coatings on high aspect ratio structures.

W ALD Nucleation and Conformality on Nylon-6 Nonwovens

While the amide functional group in nylon-6 is reactive with trimethylaluminum, and to a lesser extent, with diethyl zinc^{26,27} the reactions for direct deposition of W from WF_6 and SiH_4 on nylon are not known. Tungsten ALD on various polymers including polyethylene,

polyvinyl chloride, polystyrene, polycarbonate, polypropylene, polymethylmethacrylate, Kapton[®] polyimide and polyethylene naphthalate has previously been reported,^{19,24} and results show that W ALD nucleates well when the polymer is pretreated with several cycles of ALD Al₂O₃. We find that a thin (25 cycle) Al₂O₃ pretreatment also helps promote W nucleation on nylon-6. Figure 4 shows two nylon-6 fiber samples after 100 W ALD cycles at 140°C, with and without 25 cycles of alumina pretreatment.

The sample without pretreatment shows no visible tungsten nucleation and is electrically resistive when measured with the four-probe apparatus. The pretreated sample shows a uniform tungsten coating and shows good overall conductivity (as discussed later on). Previous infrared analysis of TMA/H₂O on nylon fibers showed significant sub-surface precursor diffusion, reaction, and nucleation during ALD at 90°C, producing detectable nuclei more than 100 nm from the fiber surface.^{26,28} The alumina pretreatment used here was done at the same temperature as the W ALD (between ~140° and 200°C), so alumina is expected to be present on and below the surface of the nylon fiber.

Transmission electron micrographs from PA-6 samples with 25 cycles of alumina pretreatment and 100 cycles of W are shown in Figure 5.

The cross-sectional images show the high surface area “winged” structure of the fiber. The dark contrast in the images corresponds to the tungsten coating which is uniform and conformal on the fiber. The highest magnification image (panel c) shows a “wing” edge where the apparent layer thickness is ~75 nm. The actual film thickness is difficult to quantify for polymers after microtome sectioning. The microtome slice is in the range of ~100 nm, so it is possible that when the microtome cuts the relatively soft polymer, the hard

metal coating folds partly onto its side, distorting the thickness analysis. The metal film can be thought as a ribbon or a strip wrapped conformally around the fiber. When a cross-section is cut by mechanical shearing, the metal strip may twist, exposing its planar side to the electron beam, rather than its line edge. What appear to be film thickness non-uniformities, especially visible in panels (a) and (c) on the wing tips, are likely an artifact of TEM sample preparation.

Effect of WF_6 and SiH_4 Exposure on W ALD on Nylon Fibers

We explored the effect of temperature on mass uptake for W ALD on nylon. Using silane and WF_6 exposures of $\sim 4.5 \times 10^5$ and $\sim 2 \times 10^5$ Langmuirs, we see minimal growth at $T < 140^\circ C$, with more growth at higher temperatures up to $180^\circ C$. The amount of W deposited during the WF_6 exposure half-cycle is affected by the amount of silicon left on the growth surface during the previous silane half-cycle step.²⁹ Tungsten ALD can be achieved at near room temperature using very large silane and WF_6 exposure steps. For example, Wilson et al.²⁴ report good W ALD at $80^\circ C$ using repeated static Si_2H_6/WF_6 doses which produce large gas exposures. For some runs, we also observe anomalously low growth rates, especially at higher temperatures near $200^\circ C$. The decreased deposition on the polymer fiber is ascribed to reactor wall effects in our tubular hot-wall reactor system. Specifically, under the high silane exposures used here, the reaction between SiH_4 and the W surface is thermally activated, so silane may be consumed upstream on the walls before a sufficient amount reaches the high surface area fiber mat substrate. Studies of the dilute silane process²⁵ suggest that the silane depletion occurs even when the reactor walls are

pretreated with a thin (2-3 nm) layer of alumina. Pretreating the reactor wall with large silane doses before loading the substrate (and before depositing the alumina nucleation layer) appears to eliminate the unexpected low growth rates.²⁵ Although the mechanisms are not clear, these observations suggest that the thin alumina nucleation layer may permit some transport of silicon species.

Tungsten and silane exposure affect W growth on the nylon mats. Mass uptake saturation as a function of silane and WF₆ exposure is shown in Figure 6 for deposition at 145°C.

For varying WF₆ exposure, the silane pulse was fixed at $\sim 4.5 \times 10^5$ L, and for varying SiH₄ exposure, the WF₆ was fixed at $\sim 2 \times 10^5$ L. The mass uptake increases with both SiH₄ and WF₆ exposure, although the rate is more sensitive to the silane exposure in the range studied. Using the sample basis weight, measured fiber surface area, and expected W density, the mass uptake values are $\sim 2 \times$ smaller than expected for uniform $\sim 3 \text{ \AA}$ /cycle at 145°C.²⁵ The BET surface area for the complex 3D network measured using N₂ adsorption may be larger than the surface area that can be reached by the SiH₄ and WF₆ precursors. Figure 7 shows the effective conductivity for the same samples in Figure 6 prepared with various SiH₄ and WF₆ exposures at 145°C, and we find that the conductivity is nearly constant at $\sim 1,000$ S/cm when the precursor doses produce sufficient deposition.

Reactant Species Transport through the 3D Fiber Network

It is important to understand if the growth on the fibers is limited by reactant species transport through the fiber network. That is, we want to know if the ALD process sequence is

sufficient for the reactants to fully reach all exposed surface area within the nonwoven fiber mat during the specified gas pulse times. The TEM images in Figure 5 show good conformal coverage over the areas examined, demonstrating complete exposure at the sites imaged. The mass change after ALD coating, however, can give insight into the extent of reaction over the entire surface area of the fiber. Mass change analysis with W ALD works particularly well because of the high density of the W metal. Working specifically in the sub-saturation gas exposure region, i.e. where the extent of reaction is sensitive to the amount of reactants reaching the growth surface, we can use the mass change to explore the extent of reaction and thereby probe reactant transport effects. To probe reactant transport, we introduce a reactant ‘hold’ step into the process sequence. Specifically, after a 10 s SiH₄ dose, we closed the reactor valves to cease the gas flow for some period of time (20 – 120 seconds) then opened the valves to purge for 30 s. The cycle then finished with the same 1 s WF₆ exposure and 30 s N₂ purge. The reaction sequence for a 10 s silane dose with a 60 s SiH₄ hold, for example, is denoted as SiH₄/N₂/WF₆/N₂ = 10(60)/30/1/30 seconds. This ‘hold’ step provides time for gas that is in the chamber to diffuse and move through the tortuous fiber structure. This differs from a longer pulse time, where gas flow continues to supply reactant. If the growth is limited by the reactant transport through the fiber network structure, the hold steps will give reactants more time to reach reactive sites, leading to a net increase in film growth. If species transport is facile through the network, the reaction will go to completion during the pulse time and the hold time will not significantly affect the overall mass uptake.

For this analysis, we also consider the total fiber surface area. The fiber mat has a basis weight of 70 g/m² and the BET surface area is 2.5 m²/g so the surface area per unit 2D area of fabric sample is ~175 m²/m². This surface area value can be roughly related to a trench aspect ratio, where 175 m²/m² corresponds to a set of equally spaced vertical trenches with aspect ratio of ~87:1. This aspect ratio is reasonable for conformal coating by ALD. However, unlike vertical trenches on a fabricated semiconductor wafer, the fiber mat surface includes many ‘hidden’ regions with variable sizes and shapes, well outside the line-of-sight. This complex 3D structure will likely affect the growth, and the hold sequence may help improve uniformity.

We test effects of species transport through the fiber mat by comparing changes in mass when we change: i) silane gas pulse time; or ii) silane hold time with fixed silane pulse time. We started with silane pulse times less than the full saturation exposure where mass uptake will be sensitive to the number of reactant/surface interactions. Using the same conditions as used for the data in Figure 6, we performed 100 ALD cycles at 145°C with and without hold steps, and results are shown in Figure 8.

The data shows that increasing the silane gas flow time from 15 to 120 seconds without the hold sequence leads to increased mass, whereas the silane hold step after a fixed 10 s silane flow does not increase mass uptake. This indicates that the relatively short gas dose time is sufficient for silane to reach reactive sites throughout the fiber matrix under the conditions investigated. Different growth conditions, or different fiber size, density or composition will affect reactant transport, so we sometimes use reaction hold steps to help ensure uniform surface reaction.

Mechanical Response of W-Coated Nylon-6 Nonwovens

We are also interested in the mechanical response of the W-coated nylon fiber samples. After coating, the micro-fiber mat still retains the “soft” feel of the uncoated fabric, suggesting that the W-coated fibers retain flexibility. To test the flexibility of the coated fibers, we measured conductivity after bending the fiber mats around radii of increasing curvature. We first measuring conductivity with the sample laid flat in our test apparatus then we molded the mat around a large cylinder. The sample was then laid flat again to measure conductivity. This was repeated several times for the same fiber sample bent around cylinders of decreasing radius, and the results are shown in Figure 9.

Also shown are results from similar analysis³⁰ of a conductive ZnO layer conformally deposited by ALD onto a polypropylene fiber mat. The results show that the W-coated nylon retains ~90% of its conductivity after bending around a radius as small as 3 mm, and the performance is much better than ZnO material. This suggests that W-coated nylon may be a good material for future flexible electronic systems integrated with textiles.

A1.1.5 Summary and Conclusions

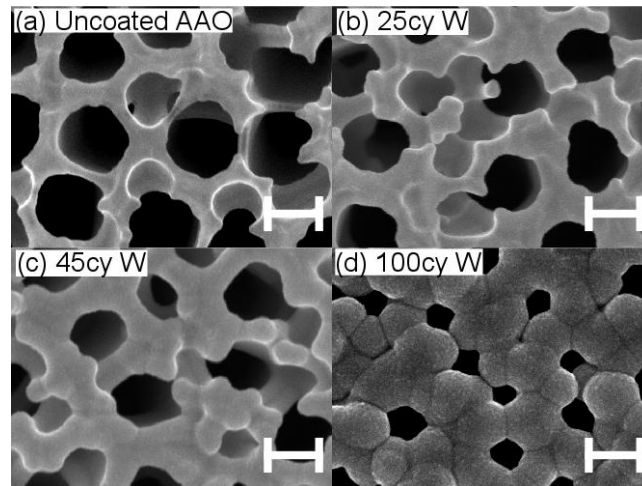
We successfully used WF_6 and 2% SiH_4 in Ar in an ALD sequence to produce conductive coatings on nylon-6 fiber mats at 145°C. Pretreating the fiber mats with 25 cycles of TMA/ H_2O ALD helps promote W nucleation. The W mass uptake on the nylon fiber mats shows saturated behavior with increasing silane and WF_6 exposure. The process offers good thickness control and produces conformal coatings on fiber mats and on nanoporous and high aspect ratio alumina structures. High surface area winged nylon-6 samples coated with W

ALD show very high effective conductivities in the 1,000 S/cm range, and the conductivity remains high even after bending around a small diameter. Good conductivity can be achieved with less than ~20% mass loading. The conductivity values we measure greatly exceed those reported in previous studies using electrospinning, injection forming, and bulk treatment techniques.³¹⁻³³ Results demonstrate that the dilute SiH₄/WF₆ process is suitable for producing high quality conductive nylon-6 nonwoven fiber mats which may enable electronic structures to be integrated into nonwoven or textile media. Potential applications for conductive fibrous media include chemical sensing, wearable electronics, biomedical devices, and energy conversion and storage.

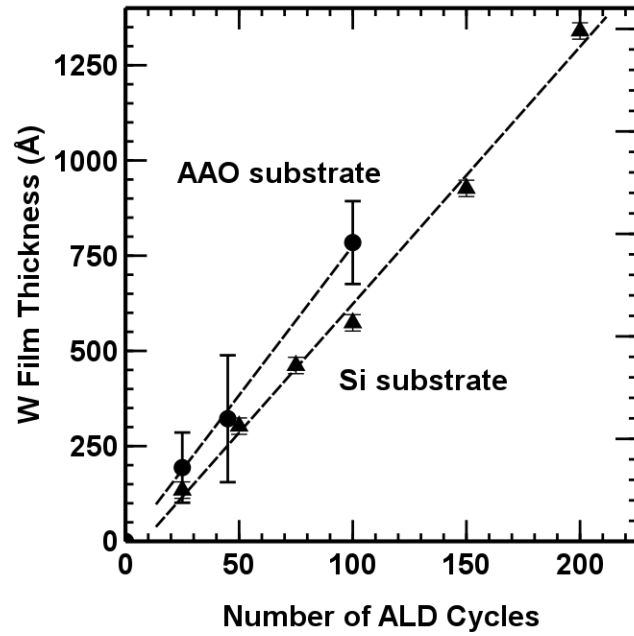
A1.1.6 Acknowledgment

We acknowledge the Nonwovens Cooperative Research Center at North Carolina State University (NCRC) Project 09-118 for support for W.J.S., and the US Dept. of Education GAANN project #P200A100014 for support of B.K.

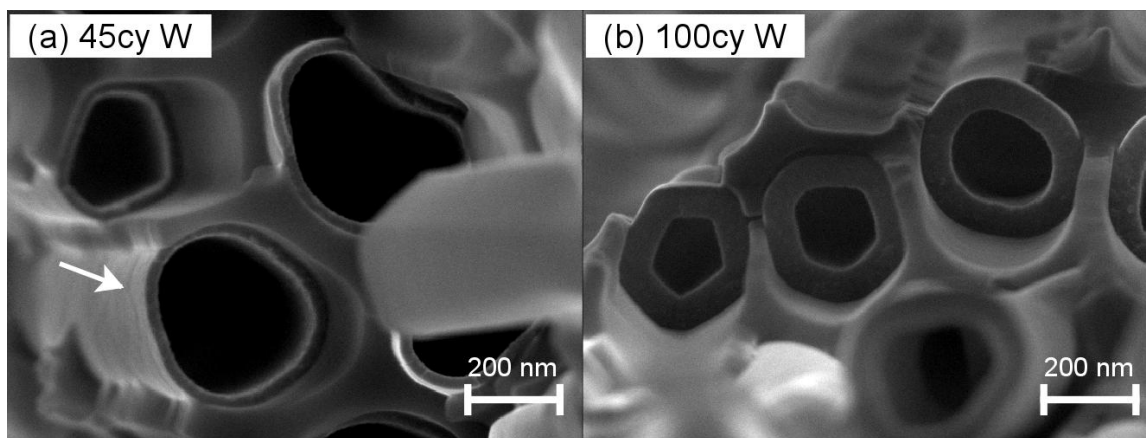
We thank Christina Devine for helping with SEM imaging performed at Duke University, and Dr. Jess Jur of NC State College of Textiles who helped with the construction of the first version of the ALD reactor. We acknowledge Allasso Industries Inc. for supplying the PA-6 fibers and for SEM images of the untreated fiber cross-sections.



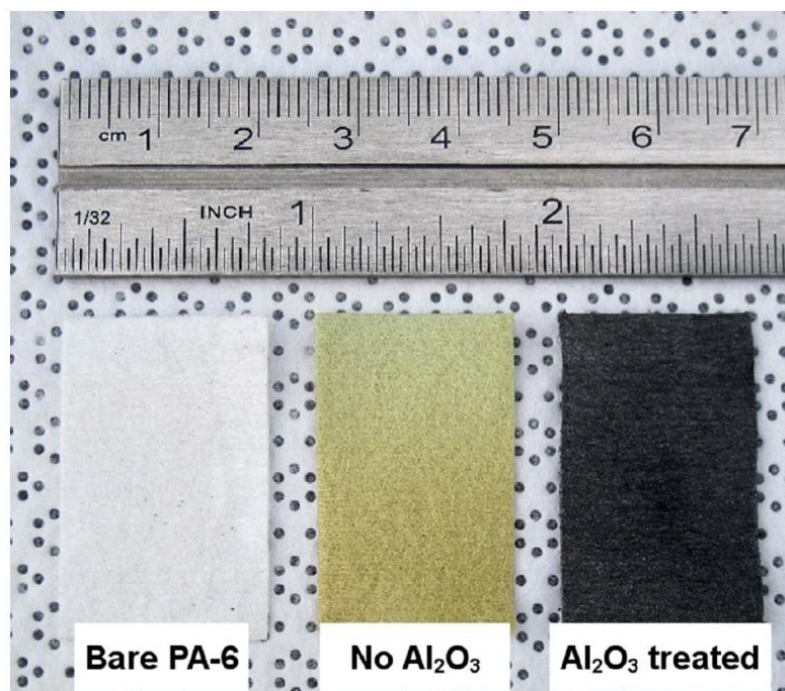
Appendix A1.1 Figure 1. Top-down SEM micrographs of anodic aluminum oxide samples treated with different thicknesses of ALD tungsten at 250,000X magnification (scale bars are 200 nm). The imaged AAO substrates have approximately 250 nm diameter pores. Image (a) is an uncoated substrate. Image (b), (c), and (d) were collected after 25 cycles of Al_2O_3 and 25, 45, and 100 cycles of W respectively at 200°C . These images show pore shrinkage due to increasing ALD coating thicknesses. Samples coated with higher cycle numbers show increasingly rounded edges and softer features in the nanometer scale due to the conformality of the coatings.



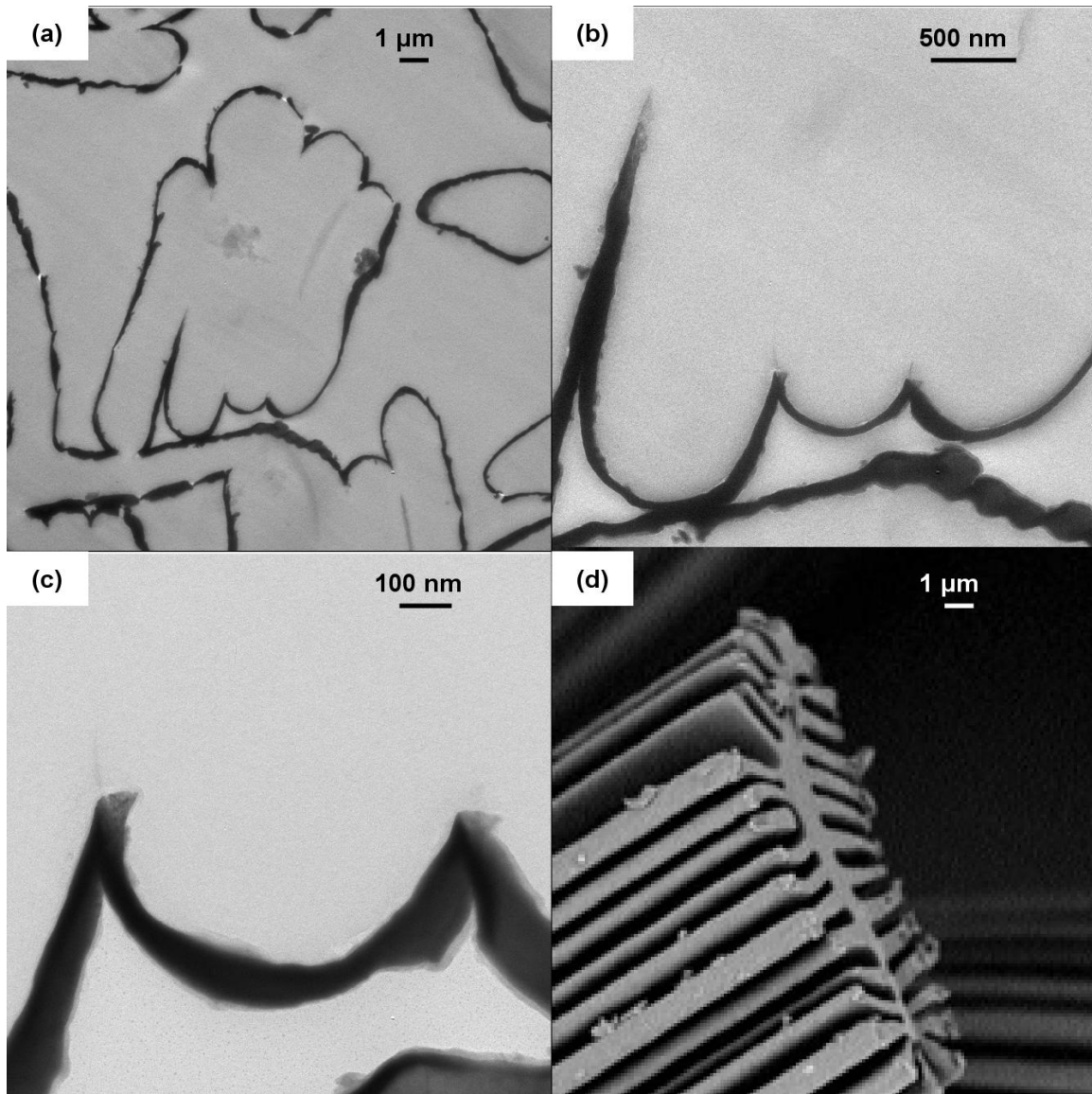
Appendix A1.1 Figure 2. Tungsten film thickness versus ALD cycle number on AAO and silicon substrates. Samples are pre-treated with 25 cycles of Al_2O_3 and processed at 200°C . Film thickness on the AAO were extracted from top-down SEM images of AAO pores shown in Figure 1.



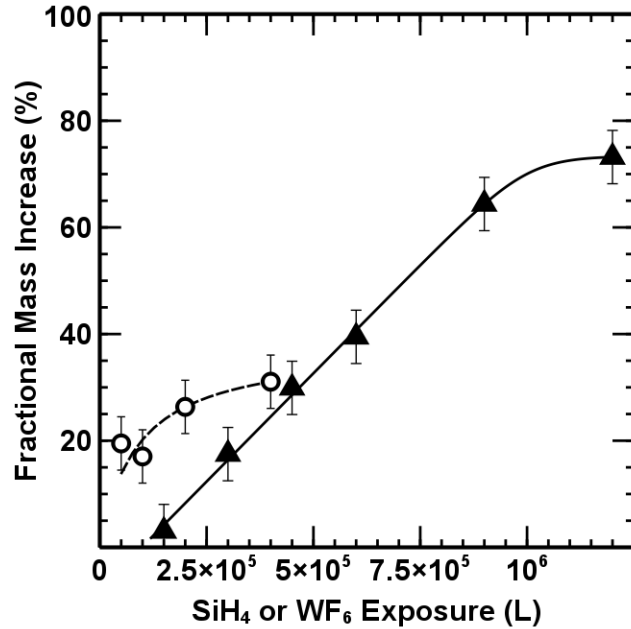
Appendix A1.1 Figure 3. Cross-sectional view of AAO pores with: (a) 45 cycles; and (b) 100 cycles of W ALD after breaking the coated AAO. The AAO templates are pre-treated with 25 cycles of Al_2O_3 and processed at 200°C . In each image, an inner tube of tungsten is surrounded by an outer AAO substrate shell, and the W thickness increases with ALD cycle number. The arrow in image (a) points to the outer side-wall of a W tube where the AAO shell was removed.



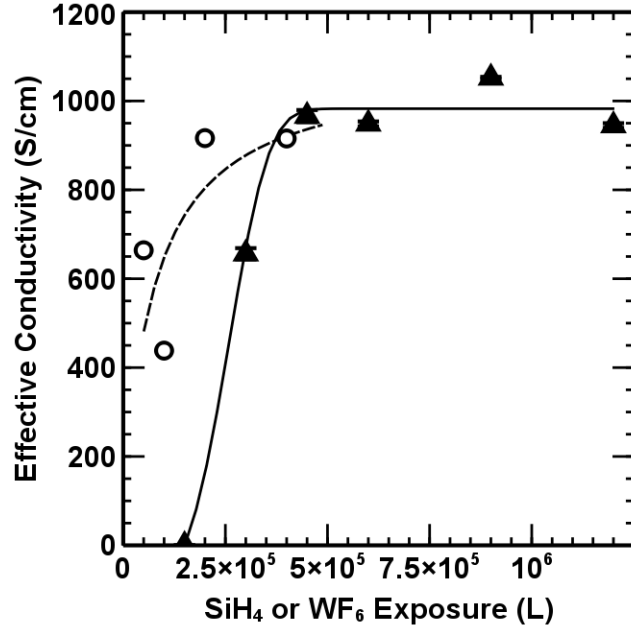
Appendix A1.1 Figure 4. Photograph showing nonwoven nylon-6 fiber mats after coating with 100 cycles of W ALD at 140°C. The sample on the left is not treated with Al₂O₃, resulting in poor tungsten nucleation on the fibers, whereas the sample on the right shows proper W nucleation as a result of pre-treatment with 25 cycles of Al₂O₃ at 140°C.



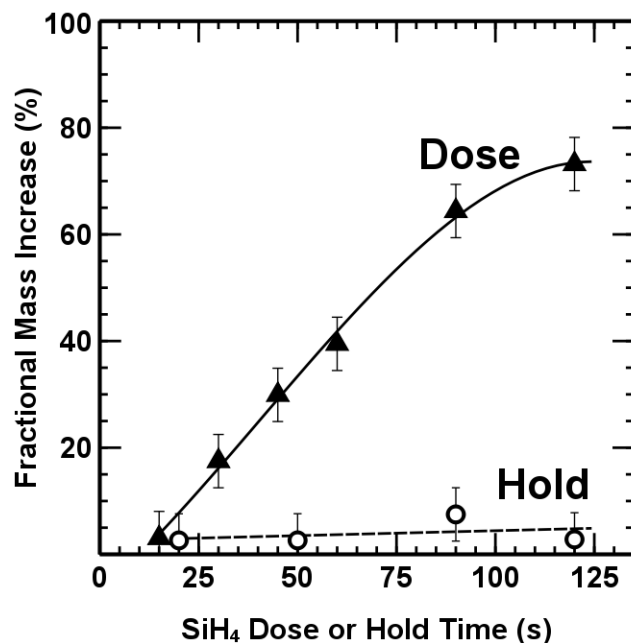
Appendix A1.1 Figure 5. Micrographs of nylon-6 fibers (Allasso, Winged FibersTM) coated with 25 cycles of Al₂O₃ followed by 100 cycles of W at 160°C. The dark contrast is from the tungsten coating, which grows conformally around the fiber wings. The Al₂O₃ deposition is not visible at these magnifications. A cross-sectional SEM image of a PA-6 fibril is shown in (d), reproduced with permission from Allasso Industries Inc.



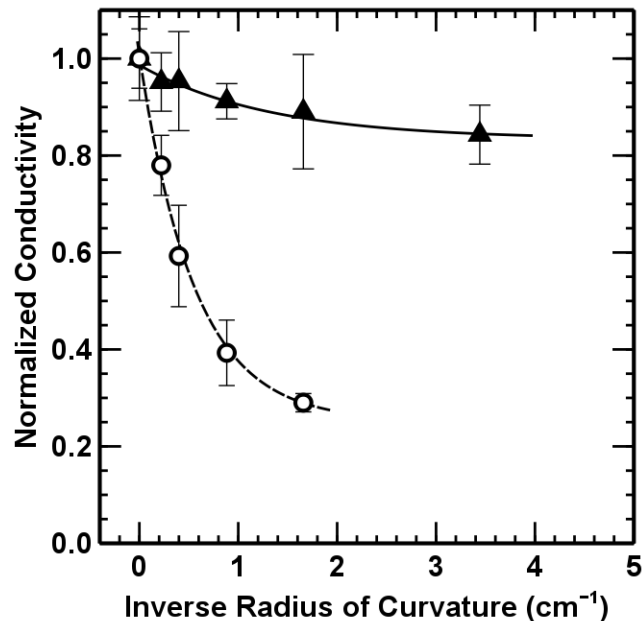
Appendix A1.1 Figure 6. Effect of SiH₄ and WF₆ exposure on substrate mass gain after 25 Al₂O₃ cycles and 100 W ALD cycles at 145°C. The data points show mass uptake on the nylon fiber mat for: (open triangles) increasing silane exposure with fixed WF₆ exposure (= ~2×10⁵ L); and (closed squares) increasing WF₆ with fixed silane exposure (= ~4.5×10⁵ L). The pressure change during silane and WF₆ doses was 0.5 and 0.2 Torr, respectively. For films with 20% or more mass loading, the maximum error of the mean for fractional mass increase was ±5%, as shown by the error bars. The lines are a guide for the eye.



Appendix A1.1 Figure 7. Fiber mat effective conductivity as a function of SiH₄ and WF₆ exposure for 25 cycles of Al₂O₃ and 100 cycles of W deposition at 145°C. The data symbols correspond to the samples shown in Figure 6. The conductivity is approximately 1000 S/cm, independent of exposure conditions when sufficient coating thickness is present. The data points show effective conductivity on the nylon fiber mat for: (open triangles) increasing silane exposure with fixed WF₆ exposure (= ~2×10⁵ L); and (closed squares) increasing WF₆ with fixed silane exposure (= ~4.5×10⁵ L). The lines are a guide for the eye. Each data point represents an average of 7 measurements for each sample. The standard error of the mean is smaller than the size of the data points.



Appendix A1.1 Figure 8. Effect of varying silane dose times and short silane doses combined with varying hold times on W mass uptake on nylon-6 fiber mats. All samples were coated with 25 Al₂O₃ and 100 W cycles at 145°C. For the “hold” sequence, the silane dose time is set at 10 seconds after which the reactor is closed for a set hold time between 20 and 120 seconds. The remainder of the ALD cycle proceeded unchanged. We also compare runs done with different silane dose times without the hold step (triangle symbols, data from Figure 6). With the 10 second silane exposure, the hold step does not enhance W mass uptake on the fiber mat substrates. The error bars represent an uncertainty of ±5% in the mass loading analysis.



Appendix A1.1 Figure 9. Change in conductivity for conducting layers deposited on fiber substrates when the fiber mats are bent around increasingly smaller cylinders. The conductivity of ZnO on polypropylene fibers is approximately 20 S/cm as prepared, but it decreases substantially upon bending. Similar experiments for the W-coated nylon studied here shows ~90% conductivity retention upon bending. Data from ZnO coated polypropylene is from reference 20. Tungsten-coated samples were prepared with 25 Al₂O₃ and 100 W cycles at 145°C. Each data point represents the mean of two conductivity values collected from each sample, and the error bars show typical variation.

A1.1.7 Appendix - Supplemental Items Not Published

Tensile testing was performed for tungsten coated nylon-6 nonwoven substrates to determine how they withstand tensile forces, for example, compared to Al-doped ZnO coated nylon-6.

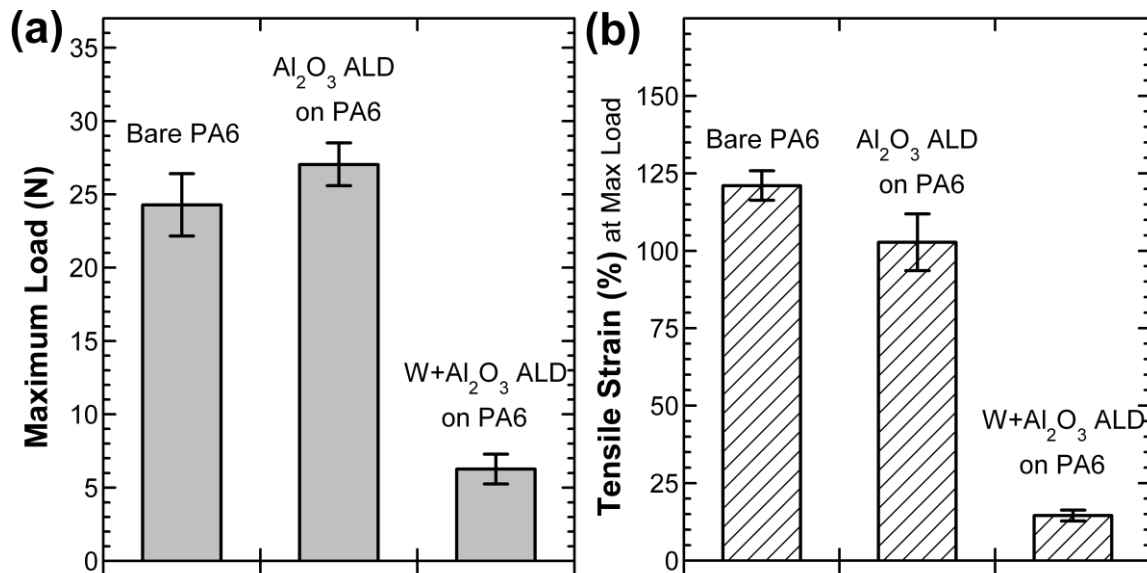
Bare nylon-6 nonwoven samples, Al₂O₃ ALD coated nylon-6 nonwoven samples, and tungsten/Al₂O₃ ALD coated nylon-6 nonwoven samples were subjected to tensile testing, the results of which are plotted in Figure A.1, depicting the force (tensile stress) performance in (a), and the tensile strain performance in (b).

The tungsten coated substrates have lower tensile strength and strain than either the uncoated or Al₂O₃ coated substrates, which was an unexpected finding. It was anticipated that the ductile nature of the metal coating might impart strength onto the nylon-6 substrate, or at the very least, not weakening the underlying material.

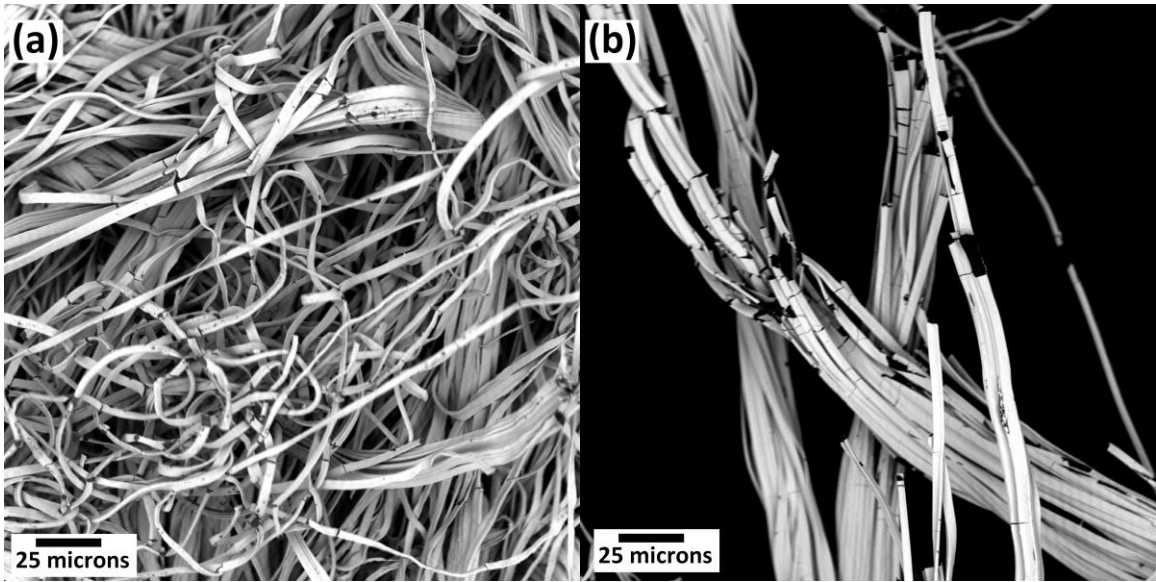
Prior to depositing the 100 cycles of tungsten ALD, a 25 cycle Al₂O₃ base layer was deposited on the bare nylon-6 to help promote nucleation and growth of the W film on the nylon-6 fibers. To control for the potential impact of the Al₂O₃ base layer coating, samples with 25 Al₂O₃ ALD cycles were also tested. As can be seen in Figure A.1, the lower tensile performance of the tungsten coated fibers substrates cannot be attributed to the underlying Al₂O₃ base layer, since no decrease in the tensile properties is observed for the Al₂O₃ coated control samples. All the samples show in Figure A.1 were cross direction oriented, but a smaller sample set of machine direction oriented nylon-6 substrates shows similar results.

Figure A.2 shows SEM images of the (a) as-deposited and the (b) tensile tested tungsten ALD coated samples, which are representative of the samples tested and plotted in

Figure A.1. Some cracking can be seen in the as-deposited tungsten coated nylon-6 fibers, perhaps due to laboratory handling, although much of the substrate remains pristine. The tensile tested sample shows significantly more cracking (which appear as dark lines in the SEM image), as well as significant delamination of the tungsten ALD coating, as indicated by the dark patches along a fiber axial direction.



Appendix A1.1 Figure A.1. (a) The maximum force achieved during the tensile test is plotted for each of the three types of tested substrates. (b) The tensile strain at maximum load is plotted for the three types of substrates. Error bars indicate one standard deviation.



Appendix A1.1 Figure A.2. SEM images of (a) as-deposited, and (b) tensile tested tungsten ALD coated nylon-6 fibers. The as-deposited tungsten coated fibers show limited cracking from normal lab handling. The tensile tested tungsten coated nylon-6 shows much more significant cracking, as well as patches of delaminated coating which appear as dark spots in the image.

A1.1.8 References

- (1) Fox, R. T.; Wani, V.; Howard, K. E.; Bogle, A.; Kempel, L. *J. Appl. Polym. Sci.* **2008**, *107*, 2558–2566.
- (2) Devaux, E.; Koncar, V.; Kim, B.; Campagne, C.; Roux, C.; Rochery, M.; Saihi, D. *Trans. Inst. Meas. Control* **2007**, *29*, 355–376.
- (3) Burger, C.; Hsiao, B. S.; Chu, B. *Annu. Rev. Mater. Res.* **2006**, *36*, 333–368.
- (4) Jur, J. S.; Sweet, W. J.; Oldham, C. J.; Parsons, G. N. *Adv. Funct. Mater.* **2011**, *21*, 1993.
- (5) Wakuda, D.; Suganuma, K. *Appl. Phys. Lett.* **2011**, *98*, 073304.
- (6) Varesano, A.; Tonin, C. *Text. Res. J.* **2008**, *78*, 1110–1115.
- (7) Xiang, C.; Lu, W.; Zhu, Y.; Sun, Z.; Yan, Z.; Hwang, C.-C.; Tour, J. M. *ACS Appl. Mater. Interfaces* **2012**, *4*, 131–136.
- (8) Invernale, M. A.; Ding, Y.; Sotzing, G. A. *ACS Appl. Mater. Interfaces* **2010**, *2*, 296–300.
- (9) Li, D.; McCann, J. T.; Xia, Y. *Small* **2004**, *1*, 83–86.
- (10) Norris, I. D.; Shaker, M. M.; Ko, F. K.; MacDiarmid, A. G. *Synth. Met.* **2000**, *114*, 109–114.
- (11) Chen, D.; Miao, Y.-E.; Liu, T. *ACS Appl. Mater. Interfaces* **2013**, *5*, 1206–1212.
- (12) Ding, Y.; Invernale, M. A.; Sotzing, G. A. *ACS Appl. Mater. Interfaces* **2010**, *2*, 1588–1593.

- (13) Ge, J. J.; Hou, H.; Li, Q.; Graham, M. J.; Greiner, A.; Reneker, D. H.; Harris, F. W.; Cheng, S. Z. D. *J. Am. Chem. Soc.* **2004**, *126*, 15754–15761.
- (14) Little, B. K.; Li, Y.; Cammarata, V.; Broughton, R.; Mills, G. *ACS Appl. Mater. Interfaces* **2011**, *3*, 1965–1973.
- (15) Klaus, J. .; Ferro, S. .; George, S. . *Thin Solid Films* **2000**, *360*, 145–153.
- (16) Kim, S.-H.; Hwang, E.-S.; Kim, B.-M.; Lee, J.-W.; Sun, H.-J.; Hong, T. E.; Kim, J.-K.; Sohn, H.; Kim, J.; Yoon, T.-S. *Electrochem. Solid-State Lett.* **2005**, *8*, C155–C159.
- (17) Kim, S.-H.; Kwak, N.; Kim, J.; Sohn, H. *J. Electrochem. Soc.* **2006**, *153*, G887.
- (18) Fabreguette, F. H.; Wind, R. A.; George, S. M. *Appl. Phys. Lett.* **2006**, *88*, 013116.
- (19) Fabreguette, F. H.; George, S. M. *Thin Solid Films* **2007**, *515*, 7177–7180.
- (20) Wilson, C. A.; Goldstein, D. N.; McCormick, J. A.; Weimer, A. W.; George, S. M. *J. Vac. Sci. Technol., A* **2008**, *26*, 430–437.
- (21) Cavanagh, A. S.; Wilson, C. A.; Weimer, A. W.; George, S. M. *Nanotechnology* **2009**, *20*, 255602.
- (22) Palmer, R. J. In *Encyclopedia of Polymer Science and Technology*; John Wiley & Sons, Inc., 2002.
- (23) Grubbs, R. K.; Nelson, C. E.; Steinmetz, N. J.; George, S. M. *Thin Solid Films* **2004**, *467*, 16–27.
- (24) Wilson, C. A.; McCormick, J. A.; Cavanagh, A. S.; Goldstein, D. N.; Weimer, A. W.; George, S. M. *Thin Solid Films* **2008**, *516*, 6175–6185.
- (25) Kalanyan, B.; Oldham, C., J.; Losego, M. D.; Parsons, G., N. *Chem. Vap. Deposition* **2013**, *19*.

- (26) Spagnola, J. C.; Gong, B.; Arvidson, S. A.; Jur, J. S.; Khan, S. A.; Parsons, G. N. *J. Mater. Chem.* **2010**, *20*, 4213.
- (27) Oldham, C. J.; Gong, B.; Spagnola, J. C.; Jur, J. S.; Senecal, K. J.; Godfrey, T. A.; Parsons, G. N. *J. Electrochem. Soc.* **2011**, *158*, D549–D556.
- (28) Jur, J. S.; Spagnola, J. C.; Lee, K.; Gong, B.; Peng, Q.; Parsons, G. N. *Langmuir* **2010**, *26*, 8239–8244.
- (29) Elam, J. .; Nelson, C. .; Grubbs, R. .; George, S. . *Surf. Sci.* **2001**, *479*, 121–135.
- (30) Sweet, W. J.; Jur, J. S.; Parsons, G. N. *J. Appl. Phys.* **2013**, *Submitted*.
- (31) Chronakis, I. S.; Grapenson, S.; Jakob, A. *Polymer* **2006**, *47*, 1597–1603.
- (32) Xia, Y.; Yun Lu *Compos. Sci. Technol.* **2008**, *68*, 1471–1479.
- (33) Miyauchi, M.; Miao, J.; Simmons, T. J.; Lee, J.-W.; Doherty, T. V.; Dordick, J. S.; Linhardt, R. J. *Biomacromolecules* **2010**, *11*, 2440–2445.

APPENDIX

APPENDIX A1. Co-Authored Work

Appendix A1.2. is a reprint of a co-authored article published in *Advanced Functional Materials*, 2011, 21, 1993-2002, DOI: 10.1002/adfm.201001756.

Appendix A1.2 Atomic Layer Deposition of Conductive Coatings on Cotton, Paper, and Synthetic Fibers: Conductivity Analysis and Functional Chemical Sensing using “All-Fiber” Capacitors

*Jesse. S. Jur, * William J. Sweet III, Christopher J. Oldham and Gregory N. Parsons*

Department of Chemical and Biomolecular Engineering

North Carolina State University, Raleigh, North Carolina 27695 USA

*My contribution to this work included depositing ZnO ALD coatings on various substrates, and measuring the effective conductivity of samples including those plotted in Figures 2, 5 and 6.

A1.2.1 Abstract

Conductive coatings on complex fibrous systems are attracting interest for new electronic and other functional systems. This work describes a procedure to quantify the effective electrical conductivity of conductive coatings on non-conductive fibrous networks, and the values are compared to the conductivity of uniform planar thin film coatings. Furthermore, we demonstrate the functional importance of conductive coatings on fibers by examining an “all-fiber” metal-insulator-metal capacitor as a liquid chemical sensor. Usually, the effective conductivity of a fiber mat is not readily defined. We show that a normal force orthogonal to the current and field direction improves fiber/fiber contact, permitting consistent conductance values to be measured. Nylon fibers coated with an electroless silver plating shows effective conductivity up to 1950 S cm^{-1} when a normal compressive force of 2000 g is applied to the sample of 6 cm^2 in size. Quartz fibers coated with tungsten by atomic layer deposition (ALD) show values up to $\sim 1150 \text{ S cm}^{-1}$, and cotton fibers and paper coated with ZnO by ALD show effective conductivity up to 24 S cm^{-1} under applied normal force. The effective conductivity of the ALD ZnO was approximately the same on the woven cotton and paper substrates over a range of deposited film thicknesses, demonstrating that the effective conductivity values can be directly compared for coatings on different fiber materials. Results also indicate that the effective conductivity value can depend upon the substrate and coating process. Relatively thick fiber coatings cracked under applied normal force and the cracking is detected by a conductance decrease. The ability to reliably analyze the effective

conductivity of coatings on complex fiber systems will be important to design and improve performance of capacitance sensors and other electronic textiles structures.

A1.2.2 Introduction

Natural cellulose-based materials, such as woven cotton and paper, are widely available at low cost. The all-time high for pulp has never been $> \$1/\text{kg}$ and the 15 year high for cotton is $\sim \$0.40/\text{kg}$. Emerging research is exploring new means to provide added electrical, magnetic,¹⁻⁷ microwave, and photo functionality^{8,9} to cellulose structures with high surface area.^{10,11} Highly conformal nanoscale coatings on cellulose materials could enable advances in fiber-based batteries, capacitors, as well as photoactive electrochemical and sensing devices. Conducting and semiconducting thin film coatings are particularly interesting for many of these and other applications.

Existing methods of electronic functionalization of cellulose material include direct printing of metallic particles,¹²⁻¹⁶ infusion of conductive fillers¹⁷⁻¹⁹ and thin film coating.^{2,3,20-25} Paper is particularly well suited for printing due to its porous structure, which enhances the capillary force for ink penetration and subsequent adhesion. The use of metallic or carbon fillers in cellulose¹²⁻¹⁹ or synthetic fiber composites²⁶⁻²⁸ typically requires a high fill fraction to surpass the percolation threshold for electrical conductivity, which can degrade mechanical response. Conductivity of 0.15 S cm^{-1} was reported for cellulose-based composites containing copper formed by electroless plating.¹⁹ Soaking cotton fabrics in carbon nanotube inks also produced conductive coatings, and conductivity was observed to increase from ~ 5 to 125 S cm^{-1} under an applied compressive load.¹⁴ Thin film coatings

using layer-by-layer assembly^{2,23,24} can include polyelectrolytes, inorganic nanoparticles, carbon nanotubes, and biomolecules. Conductivity of 6-10 S cm⁻¹ has been reported² for films deposited using (polyethylene dioxythiophene):PSS and poly(ethyleneimine) on single wood fibers, and 0.25 S cm⁻¹ when deposited in wood fiber mats. Liquid-based sol-gel chemistry can form relatively thick (>100 nm) inorganic films on fibers, but solvent and surface wetting effects make it difficult to achieve good conformality.^{3,20-22} Sol-gel indium tin oxide films on cellulose have shown conductivity as high as 16 S cm⁻¹ after annealing at 450°C for 6 hours (which damaged the fiber matrix).³

Atomic layer deposition (ALD) has also been investigated as a method to produce inorganic coatings on natural fiber systems.^{8,29-33} Atomic layer deposition is a vapor phase thin film growth process where a metal organic precursor and a reactant are sequentially exposed to a surface, resulting in a complementary sequence of self-limiting reactions. Many ALD processes are known for oxides, nitrides and conducting thin films.^{34,35} For several materials, the ALD process operates readily at temperatures less than 150°C, making it amenable to deposition on thermally sensitive polymers, including cellulose paper.³³ The surface of natural cellulose fibers presents many surface hydroxyl groups, which can simplify nucleation of water-based ALD processes, including diethyl zinc/water for ZnO ALD. This article presents analysis of conductive ZnO coatings formed by ALD on cellulose cotton substrates, including woven cotton fiber and cotton paper. In addition, the conductivity of tungsten thin films formed by ALD on woven quartz fiber at 200°C is also evaluated.

While the conductivity of individual thin films can be characterized in many geometries using four-probe methods, analyzing the conductivity of films on a set or bundle of multiple

fibers is expected to be complicated by field uniformity, fiber/fiber contact resistance and other issues. Typical methods for analysis of conductive fiber systems involve simple two-probe current/voltage measurement to determine resistance,^{36,37} or 4-probe techniques to obtain volume resistivity.³⁸ The current flow through a conductive fiber system, made up of a large number of parallel or randomly directed fibers, is expected to depend on the number and conductivity of individual conductive pathways, the extent of interconnectivity between fibers, as well as the resistance and distribution of resistance between interconnecting fibers. This problem could be modeled, for example, to estimate local electric fields and the effective contributions from the through-fiber and cross-fiber conductance pathways distributed in the network. A key problem, however, is a reliable and direct means to quantify and compare conductive coatings formed on different complex fibrous substrate structures.

In this work, we apply a 4-probe measurement method to quantify the effective conductivity of inorganic thin film coatings on natural and synthetic fibrous structures, where the focus is on substrates comprised of a large number of individual fibers. The contact electrodes span across the sample width and establish an approximately linear field along the sample length between the electrodes. We quantify the effect of an applied normal compressive force on the through-fiber conductance, and conclude that compressive force enhances fiber/fiber contact and minimizes internal contact resistance within the fiber structure. We show that this approach provides reliable estimates for coating conductivity on a range of different fiber structures, and values obtained with this method produce consistent results for films of different thickness deposited on different fibrous substrates. Deviations in

the expected trends are noted for some material systems, and we find that these deviations provide insight to other important processes such as substrate/coating interactions or cracking due to mechanical failure. We also show that coated materials can perform in simple device architectures. An “all fiber” capacitor is demonstrated, where the measured values of capacitance versus frequency are sensitive to the composition of liquids that penetrate the dielectric between the conductive fiber electrodes.

A1.2.3 Results and Discussion

2.1 Electrical evaluation of coated fibrous substrates

The four-probe apparatus developed to characterize conductivity of fiber mats is shown in Figure 1. For the analysis, all coated fiber mat samples, including the ALD-coated substrates, were cut into strips 30 mm long and 20 mm wide. The samples were placed on the central region of the 4-probe apparatus, sufficiently far from the edge of the parallel lines. A glass slide with dimensions of 5 cm × 5 cm × 6.25 mm and mass of 18 g was placed on the sample and measurements were conducted by incrementally loading calibrated weights (10 – 2000 g) to the top of the glass slide. In a measurement, current is supplied to the outer electrode pair and voltage is measured between the inner electrodes. Ideally, the inner electrodes for voltage measurement should be as narrow as possible to avoid any local disturbance of the lateral electric field. For our measurement system, we chose 0.2 cm as the inner electrode width which enables good contact with a large number of fibers with minimal lateral field interaction. The narrow electrode width compared with the 1.9 cm outer

electrode spacing suggests that the assumption of uniform field in our analysis introduces an error of a few percent, which is within our expected uncertainty.

Using the known sample width (W) and inner electrode spacing (s), Ohm's law can be used to determine the effective conductivity of a coated fiber mat:

$$\sigma_{eff} = \frac{J}{E} = \frac{I/A}{V/s} = \frac{s}{RA} (S \cdot cm^{-1}) \quad (1)$$

where J is the current density, E is the electric field, R is the measured resistance (V/I), and A is the total cross sectional area of the conducting coating evaluated with normal direction parallel to the macroscopic applied field (i.e. perpendicular between the electrodes). For the case of interest here, where a conductive coating covers an otherwise non-conducting fibrous mat, the net cross sectional area is best evaluated in terms of the total volume of the coating, $V_{(coating)}$, which is related to the net coating mass, $m_{(coating)}$:

$$A = \frac{V_{(coating)}}{L} = \frac{m_{(coating)}}{\rho L} (cm^2) \quad (2)$$

where L is the length of the fibrous substrate and ρ is the density of the material coated onto the fiber. The analysis presumes that the density of the coating material is uniform, and it is known or can be evaluated. We also note that this analysis does not require the fiber coating to be conformal on the fibers, but it does assume that the conductive material is uniformly distributed across the fiber mat, with a constant net cross sectional area at any point between the electrodes. The coating mass can be estimated by comparing sample weight before and after deposition (taking into consideration any possible changes in substrate mass due to sample heating or other processes), or by selectively removing the fiber substrate after

deposition (by calcination or chemical etching, for example) and directly measuring the remaining coating mass. The substrate removal approach must consider possible changes in coating mass due to oxidation or other chemical modification during heating or exposure to chemical etchant species. With these considerations, the net effective conductivity value is then given by:

$$\sigma_{eff} = \frac{sL\rho}{m_{(coating)}} \frac{1}{R} (S \cdot cm^{-1}) \quad (3)$$

This value of σ_{eff} therefore reflects the net conductivity of the coating on an otherwise non-conductive fiber mat substrate. For a given uniformly distributed coating material, the value for σ_{eff} should be independent of coating thickness and fiber substrate dimension, and may be compared to expected bulk conductivities of the coating materials.

Several mechanisms in fiber and thin film systems are expected to influence the measured effective conductivity and produce values that differ from the bulk conductivity of the coated material. For example, surface and grain boundary scattering is known to reduce the conductivity of thin films compared to the same material in bulk form, and this has been observed in thin (< ~100 nm) silver films formed by electroless plating.³⁹ Moreover, it is likely that in a conductive fiber mat, where all fibers may not actively carry current, equivalent current will not flow uniformly through all fibers. Therefore, the measured total mass of the coating will exceed the mass of the active conductive material, and the effective conductivity will therefore be less than the bulk or thin film value. Also, even though a four-probe method avoids probe/sample contact resistance, fiber/fiber contact resistance will be present throughout the sample volume. The importance of these contacts depends on the

nature of the fiber sample under investigation. Fiber/fiber contact resistance may be less important, for example, in woven samples measured parallel to the weave or warp direction, where most fibers extend directly along the entire sample length. On the other hand, fiber/fiber contact resistance will likely be significant in samples such as paper or nonwovens, where individual fibers are either shorter than the electrode spacing or do not follow a well defined straight path between electrodes. Current flow in coated paper or nonwovens therefore requires substantial charge transport from one fiber to another, rather than along an individual filament. A compressive force applied in the sample normal surface direction during electrical measurement will increase connectivity between fibers and minimize fiber/fiber contact resistance effects. The applied normal force will also help maximize the amount of conductive material in the sample contributing to the measured effective conductivity. An increase in conductivity by applied force has been noted previously for cotton fibers coated with conductive carbon nanotubes.¹⁴ By analyzing the effective conductivity as a function of mass loading, we find that for some material systems studied (such as silver on nylon fibers) the measured effective conductivity increases and saturates at a value consistent with the coating bulk conductivity. However, for other materials, such as ZnO on polypropylene fibers, mass loading results in mechanical cracking of the coating and fibers which reduces the measured effective conductivity. Never-the-less, the value for the effective conductivity provides a viable means to characterize and compare various conductive thin film coatings on fiber structures.

2.2 Characterization and analysis of silver coated nylon

Silver coated fabrics are developed commercially for antimicrobial and conductive fiber applications. Images of silver coated nylon fiber show a smooth and uniform coating. Some minor abrasion of the coating on the top-most fibers typically occurred during sample handling and was difficult to avoid. The fiber mat has a random fiber orientation, typical of a nonwoven material. The fabric material has good flexibility and no cracks were observed under moderate SEM magnification ($\sim 5000\times$). The resistance of the silver and ZnO coated paper was evaluated in both 2-probe and 4-probe geometries, and results are provided in Figure 1c and d. For the 2-probe geometry, voltage was applied and current was measured across the two inner probes, resulting in a measured resistance of $15\ \Omega$ for the Ag-coated fibers. In the 4-probe geometry, current was applied across the outer probes and voltage was measured across the two inner probes resulting in a resistance of $0.24\ \Omega$ for the same materials, consistent with elimination of fiber/probe contact resistance in the 4-probe geometry. For the case of ZnO-coated fibers, the difference was more pronounced, showing a 2-probe resistance of $12\ \text{k}\Omega$ compared to a 4-probe resistance of $75\ \Omega$. All subsequent measurements were performed using the 4-probe configuration.

The net coating mass can be readily adjusted either by controlling the extent of deposition coating, or by vertically stacking multiple fiber sheets. With other parameters held constant, the conductance (in Siemens, S) is expected to scale linearly with mass of the coating:

$$1/R = \frac{\sigma_{eff}}{sL\rho} \cdot m_{(coating)}(S) \quad (4)$$

Electrical characterization was first tested using the silver-coated nylon samples. The total mass of silver was adjusted by stacking multiple sheets, and good fiber/fiber contact was promoted by applying a constant large mass force (1700 g) onto the 6 cm² sample surface area. The net mass of silver was determined by polymer calcination and was found to be ~15% of the starting sample mass, consistent with the 15-17% mass loading reported by the supplier. The conductance determined from the measured current and applied voltage is plotted versus the net coating mass in Figure 2a. The trend is linear and extends through the origin, consistent with equation (4). The conductance data was then used in equation (3) to evaluate the effective conductivity. The silver showed no discoloration upon calcination, indicating minimal oxidation. Therefore, the bulk density value for silver, ~10.5 g/cm³, was used for the analysis. The resulting effective conductivity data plotted versus coating mass in Figure 2b. The average value is independent of mass, with a net value of $1.8 \times 10^3 \text{ S cm}^{-1}$. This value is less than bulk silver conductivity ($1 \times 10^6 \text{ S cm}^{-1}$), but corresponds well with reported values for thin ~100 nm Ag films.³⁹

The effect of applied normal force on the conductance and effective conductivity of stacks of silver coated fiber mats was also evaluated, and results are shown in Figure 2c and d. At all values of applied force, the conductance values (Fig. 2c) were found to increase as the number of mats increased. For the stacks of 3 or 4 mats, the conductance increases markedly as the normal force (loading mass) is applied, with saturation in conductance observed upon loading with several hundred grams. As the applied force was removed, the conductance decreased following the same trend line. The effective conductivity values extracted from the data in Figure 2c are plotted versus loading mass in Figure 2d. The effective conductivity

saturates between ~ 1700 and 1950 S cm^{-1} , similar to the data in Figure 2b. The results show a slightly larger effective conductivity for the single fiber mat compared to the stacks of multiple mats. This trend is likely due to the increasing number of fiber/fiber contacts present (and therefore increased total fiber/fiber contact resistance) as the number of mats being measured is increased. Even so, the four-probe mass-compression methodology provides reasonable values for the effective conductivity of fiber mats, and the values follow the trends expected for samples with different total coating mass.

2.3 Atomic layer deposition of ZnO on woven cotton and paper substrates

In order to evaluate the conductivity of other films on fiber systems, ALD ZnO films were formed at 115°C on fiber and planar silicon substrates. The thickness of ZnO films on silicon increased linearly with the number of ALD cycles, with a growth rate of $\sim 2.1 \text{ \AA/cycle}$ in agreement with prior reports.^{40,41} The coating mass for ZnO deposited on cotton and paper under the same ALD conditions also showed a linear mass increase with number of ALD cycles. A different mass uptake per cycle was observed on the two substrates and was ascribed to a different surface area for the starting samples. For the paper substrates, a linear fit to mass gain versus cycle number extrapolates to the origin, indicating a constant film growth rate. On the cotton fiber, a linear fit shows a somewhat reduced growth rate during the first 50-60 ALD cycles. A quantitative relation between fractional mass change and film growth thickness requires information regarding growth uniformity, net active surface area of the fiber structure, fiber density, and coating film density. Even though the ALD film can be uniformly coated through the fiber matrix,^{31,42} the uncertainty of the other parameters precludes a good estimation of the deposited film thickness from the mass change data.

2.4 Electrical analysis ZnO-coated woven cotton

Scanning electron micrographs of the woven cotton fiber sample before and after ZnO ALD at 115°C are shown in Figure 3a and 3b, respectively. The woven fiber consists of parallel sets of micron-scale fibers that intersect orthogonally in the weave structure. Cellulose cotton is a hollow-shell cylinder structure with a shell diameter between 12 and 22 μm , and has significant mechanical resiliency and compressibility. Atomic layer deposition of ZnO produces a conformal layer on the fibers, retaining the smooth fiber surface texture. For the samples coated with a large number of ALD cycles, some increase in physical stiffness is observed during sample handling. Calcination of the coated fibers at 450°C for 90 min results in hollow ZnO tube structures with size and texture similar to the uncoated fibers, indicative of the conformal coating provided by the ALD process.

Woven cotton fibers coated with different amounts of ZnO by ALD were analyzed using the same procedure used for electrical analysis of the silver coated nylon, and results are also displayed in Figure 3. The conductance values in Figure 3c increase as the number of ALD cycles increase, consistent with increasing film coating thickness. Most samples also show a large change in conductance with applied loading mass. For the sample with 600 cycles of coating, the sharp conductance decrease with applied loading is due to mechanical cracking of the thin film coating which is visible in SEM images after sample measurement. The effective conductivity is plotted in Figure 3d versus applied loading weight. For this analysis, although the bulk density of low temperature ALD ZnO is expected to be somewhat less than the bulk value of 5.71 g/cm^3 , the bulk value was used as an approximation in equation (3), resulting in an estimated error of $<\sim 10\%$. Similar to that observed with the silver coated

nylon, the measurements produce a range of conductivity values, in this case between about 7 and 24 S cm⁻¹. The trend in conductivity is also similar to the silver samples in that the largest conductivity value is obtained from the smallest mass measured. In this case, the trend occurs because the cracking is more prevalent in the thicker film coatings.

Non-linear trends in conductivity with film thickness are also expected in thinner ZnO films. For a charge state density of 10¹⁷-10¹⁸ cm⁻³, a depletion layer on the order of ~3-10 nm thick is expected at the surface of the as-formed metal oxide.⁴³ The ZnO films studied here are between ~20 and 200 nm thick, and therefore, a depletion layer on the order of ~10 nm in width will substantively affect the measured conductance in the thinner films. A thin Al₂O₃ layer on the surface of the ZnO will affect surface defects and can reduce the effective band bending.⁴⁴ Such surface passivation may be useful for further studies of conductive coatings on fibers.

The conductivity of planar ZnO films formed by ALD on oxidized silicon wafers at 115°C was also measured, and values ranged from 84 S cm⁻¹ for a ~35 nm thick film, to 148 S cm⁻¹ for a ~82 nm thick film. Other researchers have reported similar values for conductivity of ALD ZnO films, and with similar film thickness dependence. Schuisky *et al.* measured 125 S cm⁻¹ for a 40 nm thick film,⁴¹ and Guziewicz *et al.* obtained 431 S cm⁻¹ for a much thicker film processed at a higher temperature.⁴⁵

The smaller conductivity obtained for the ZnO coated fibers compared to bulk ZnO is likely due to a combination of two effects: i) the ZnO coating on the fibers (especially thicker coatings) are prone to cracking; and ii) depletion layers at the ZnO/air surface (most apparent in thinner coatings). For example, we found that a woven cotton fiber sample coated with a

thin ZnO layer (180 cycles) showed a saturated effective conductivity of 7 S cm^{-1} , compared to 24 S cm^{-1} for a fiber coated with 240 cycles, consistent with surface charge depletion affects in the thinner film coating.

2.5 Electrical analysis of ZnO-coated cotton paper

Cotton paper coated with ALD ZnO was also examined, and SEM images of the paper microstructure and resulting coating are shown Figure 4. Cotton paper is commonly described as a two dimensional random fiber network with fiber lengths on the order of 2 mm.¹² As shown in Figure 4a, the paper investigated in this work consists of randomly oriented fibers that are $\sim 20 \text{ }\mu\text{m}$ in diameter. Fibers in paper are arranged into multiple stacked layers, with some individual fibers extending into multiple layers. The production process produces a more dense fiber network near the finished surface with a less dense network in the middle of an individual sheet. The paper fabrication process also produces smaller microfibrils that connect between the larger fibers, resulting in small film-like structures (likely nanofibers) near the exposed paper surface. The smaller fibers may also contribute to an apparent increase in surface texture on the larger fibers compared to the smooth surface seen on the woven cotton fibers. In general, cotton paper has low compressibility and is not mechanically robust under shear. After ALD coating of the paper, no significant change in fiber structure is observed (Figure 4b), although the film-like texture may be visible, along with some surface smoothening. The starting paper is more mechanically rigid than the starting woven cotton, and during paper sample handling no significant change in mechanical behavior was noted after film coating. After calcination,

the original fiber structure appears degraded, with more of a crumpled or folded film structure remaining.

The electrical results for the cotton paper coated with ALD ZnO are provided in Figure 4c and 4d. The conductance again increases with amount of deposited coating. Several samples show a rapid increase in conductance with applied mass, followed by saturation. It is interesting to note that the change in conductance with loading mass is completely reversible over many loading/unloading cycles for mass loading up to 2000 g studied here. The conductance of some samples increased by a factor of 10^4 upon mass loading, and the conductance change reversed back to the starting value upon mass unloading. As noted above, paper typically consists of a lower density fiber layer between two higher density layers. It is possible that applying a small mass results in collapse of the middle layer, allowing the more dense upper layer to contribute to the conductance. This middle layer may be flexible enough, even with a relatively thick oxide coating, to spring back up after mass is removed, resulting in a sharp conductance drop. The unique structure and flexibility of the ALD-coated paper substrate may provide novel opportunities, for example, for physical pressure sensors or other simple devices.

A comparison of the saturated conductance and saturated effective conductivity data collected for ZnO ALD coatings on woven cotton and paper is presented in Figure 5. The data shows that the measured conductance depends strongly on the substrate and coating thickness, but the effective conductivity, as determined by equation (3), is reasonably consistent for different substrates and different film thicknesses. We therefore can conclude

that the scaling methodology outlined above provides a practical approach to reliably quantify the effective conductivity of coated fiber network systems.

2.6 Electrical analysis of ZnO-coated nonwoven polypropylene

Conducting thin films were also examined on other fiber systems and some irregular effects were sometimes observed that can be related to details of ALD processing on polymers.³² Figure 6a shows, for example, an ALD ZnO coating on nonwoven polypropylene fibers. While the ZnO surface appears smooth, recent results show that during aluminum oxide ALD at elevated temperature (90°C) on polypropylene, significant sub-surface reaction occurs during initial growth cycles, creating isolated oxide particles in the polymer fiber.³² Similar sub-surface growth for the ZnO studied here would lead to isolated ZnO particles that would contribute to the overall ZnO mass, but would not contribute to the overall conductance. This means that the trend described by equation (4) would not hold, and the effective conductivity would increase with number of ALD cycles. Surface band bending is also known to affect conductance of ZnO films,⁴³ which could also produce an increase in effective conductance as the film is deposited. The effective conductivity data shown in Figure 6b for ZnO ALD on polypropylene does not follow the trend of equation (3), but conductivity does increase with increasing number of ALD cycles, consistent with non-uniform growth or conductance with thickness. Therefore, the effective conductivity data that does not scale with the expected trends in equation (3) can give insight into the material properties or fiber coating mechanism. The ZnO precursors are expected to readily react with surface –OH groups on the cotton substrates, minimizing sub-surface growth and affecting the oxide surface potential, permitting the conductance to scale with equation (3).

Thicker ZnO coatings on polypropylene are also susceptible to cracking under applied load. Figure 6c shows an SEM image of SEM image of ZnO coated polypropylene after 2000 g loading, showing significant cracking in the fiber structure. Sample cracking leads to dramatic decreases in film conductance.

2.7 Electrical analysis of W-coated quartz fiber

In order to further demonstrate the applicability of the conductance analysis system, and to obtain materials with higher conductivity, we chose to evaluate the electrical properties of woven quartz fiber mats coated with a tungsten thin film by ALD. The W coating is expected to result in effective conductivity intermediate between the highly conducting silver coating (with $\sigma_{\text{eff}} \sim 1800\text{-}2000 \text{ S cm}^{-1}$) and the less conducting ZnO coating (with $\sigma_{\text{eff}} \sim 15\text{-}20 \text{ S cm}^{-1}$), and would therefore present another range for quantitative evaluation. The W ALD coating could also provide an alternative material choice for applications such as electrochemical sensors and high surface-area electrodes for advanced energy collection and storage applications.

The quartz fiber substrates had a uniform diameter of $\sim 10 \mu\text{m}$, and they were mechanically stiffer than the other substrates studied. The tungsten was deposited at 200°C for either 100 or 200 ALD cycles, and a growth rate of $\sim 5 \text{ \AA/cycle}$ as observed on planar silicon substrates processed simultaneously. Analysis of film thickness versus number of ALD cycles showed that a 10-20 cycle nucleation period was required under the conditions used to achieve steady-state growth on the silicon wafer. An SEM image of the W-coated quartz fiber is shown in Figure 7a. The W film completely covered the quartz fibers, and the woven configuration is evident by the perpendicular fiber orientation. The effective

conductivity as a function of mass loading, is presented in Figure 7b. The saturated effective conductivity is $\sim 1150 \text{ S cm}^{-1}$, consistent with other reports of W thin films,^{41,46} but less than the bulk conductivity of W ($1.85 \times 10^5 \text{ S cm}^{-1}$). The conductivity saturates with only a small applied mass, consistent with the stiffer starting substrate fibers.

To demonstrate the feasibility of the conductive fibers in functional devices, the W-coated quartz fiber samples were used as conducting electrodes in a fiber-based metal-insulator-metal (MIM) capacitor, shown in Figure 7c. Two quartz fiber electrodes coated with 200 ALD cycles of tungsten were separated by an insulating nonwoven polypropylene fiber mat, $\sim 0.5 \text{ mm}$ thick, and the structure was secured together with cotton thread. The active area of the capacitor was $\sim 3 \text{ cm}^2$. Control capacitors using solid copper electrodes separated by the same fibrous insulator were also fabricated, where the capacitor was compressed tightly between two glass plates which decreased the thickness of the nonwoven insulator to $0.12\text{-}0.15 \text{ mm}$. Capacitance values for the control and test samples were recorded as a function of frequency at an applied voltage of 1 V . The capacitance density of the control capacitor was $\sim 16.5 \text{ pF/cm}^2$, independent of frequency between 1 kHz and 1 MHz . The capacitance value corresponded to a relative permittivity, ϵ_r , of $\sim 2.2\text{-}2.8$, which is reasonably close to the expected low frequency permittivity of a polypropylene film ($\epsilon_r = 2.2$). The same analysis of the fiber test capacitor gave $\sim 3.45 \text{ pF/cm}^2$ at 1 kHz , also approximately independent of frequency in the range studied. Using the effective capacitor area defined by the outside edge of the fiber electrode the measured capacitance density for the conducting fiber test sample was a factor of 3 to 4 less than expected in comparison to the Cu electrode control capacitor. This low capacitance value is not unreasonable. The all-fiber

capacitor was not compressed as tightly during measurement, resulting in more air in the nonwoven insulator. In addition, because of the overall structure of the woven conductive fiber electrode, some parts of the electrode will have additional space between the electrode and the insulator, effectively increasing the overall separation, and decreasing the net capacitance. A recent report of a capacitor made using conductively coated cellulosic fiber electrodes² suggested that conducting electrode fibers could penetrate into the insulating layer, effectively increasing the overall capacitance compared to planar control samples. While such a process cannot be ruled out in our samples, we believe that the overall smaller capacitance for the test sample relative to the control is consistent with our conducting fiber electrode structure. Moreover, the conductivity analysis presented above shows that mechanical compression can increase overall fiber mat conductance, which in turn will also affect the total measured capacitance.

The fibrous capacitor structure shown here is unique because it can allow liquids to readily penetrate through the porous conducting electrodes and be absorbed into the nonwoven insulating layer. We have measured the cell capacitance upon exposure to various liquids, and the results are shown in Figure 7d. As expected, exposing the capacitor to more polarizable liquids such as water (H_2O , $\epsilon_r = 80.4$), ethyl alcohol ($\text{C}_2\text{H}_5\text{OH}$, $\epsilon_r = 24.3$), and isopropyl alcohol ($(\text{CH}_3)_2\text{CHOH}$, $\epsilon_r = 18.3$) produced increases in capacitance, and at low frequency, the magnitude of the capacitance increase follows the trend expected from the relative permittivities of the liquids tested. The capacitance decreases with frequency due to dielectric relaxation in the liquid dipole medium, resulting in decreased polarization at higher measurement frequency. The function and performance of this all-fiber capacitor sensor is

consistent with the high conductivity of the tungsten on the fibrous substrates, and such structures could be used to analyze other vapor or liquid materials in a flow-through sensor geometry.

A1.2.4 Conclusions

The effective conductivity of coated fiber systems can be readily characterized, and values obtained are consistent with values expected from the respective thin film conductivity. Nylon fibers coated with an electroless silver coating resulted in the highest values measured, up to 1950 S cm^{-1} when a normal compressive force of 2000 g was applied to the sample of $\sim 6 \text{ cm}^2$. Quartz fibers coated with tungsten by atomic layer deposition produced saturated conductivity of $\sim 1150 \text{ S cm}^{-1}$, and cotton fibers and paper coated with ZnO by ALD showed effective conductivity up to 24 S cm^{-1} . The effective conductivity of the ALD ZnO was the approximately the same on the woven cotton and paper substrates, demonstrating that the same effective conductivity values could be extracted for coatings on different fiber materials. However, results also show the effective conductivity value can be readily influenced by the substrate and coating process. For some coated fibers samples, the conductance increased with applied loading mass, which is likely due to improved fiber/fiber contacts, while physical cracking produced a conductance decrease.

Tungsten coatings on quartz fibers were shown to be sufficiently conductive for use as electrodes in all-fiber capacitor structures. Preliminary results demonstrate that fiber-based capacitors are sensitive to the chemical composition of fluids that penetrate through the electrodes and become absorbed in the insulating layer. The conductivity analysis method

described here provides a basis for consistent evaluation of conductive fibrous materials. The consistent results obtained from the analysis demonstrates that ALD is a viable method to achieve well-controlled conductive and semiconductive coatings on woven textiles and fibrous nonwoven materials. Moreover, the analysis of conductivity and mechanical response will be important to design and optimize the capacitor sensors shown here, as well as other fiber-based electronic and sensing devices.

A1.2.5 Experimental

The four-probe electrical measurement apparatus was fabricated onto a ~3 mm thick 10 × 10 cm quartz plate using a lift-off photoresist. After resist patterning, a ~10 nm Ti adhesion layer and a ~100 nm Au gold electrode layer were formed using electron-beam deposition, the resist was removed to reveal the electrode pattern. The probe design consists of four parallel Au lines with a width of 0.2 cm, spacing of 0.5 cm, and length of 5 cm.

Nylon fiber mats coated with ~100 nm thick silver films formed by electroless plating (resulting in ~15-17 weight % Ag) were attained from Marktek Corporation (SPB15), and measured as received. In addition, woven cotton fiber, cotton paper, and nonwoven polypropylene fiber mats were coated using ZnO by low temperature atomic layer deposition. The paper substrates were archival and acid-free 24 lb cellulose 100 % cotton, obtained from Crane & Co. The woven cotton fiber was a 3 × 1 twill weave obtained from Textile Innovators Inc. The as-received woven cotton had previously been bleached and mercerized in sodium hydroxide solution to produce primarily β -cellulose. Spunbond nonwoven polypropylene fiber mats, obtained from the Nonwoven Cooperative Research

Center at NC State University, had a fiber diameter between ~1 and 10 micrometers and were also used as substrates for ZnO ALD.

Zinc oxide thin films were deposited on the cotton paper and fiber mat using diethylzinc (DEZ) and water in an atomic layer deposition (ALD) sequence.³¹ The ALD reactor consisted of a flow-tube, 24 inches in length and 2 ¾ inches in diameter, and the heated growth zone was extended through a Lindberg/Blue tube furnace. Ultra-high purity argon flowing at 200 standard cubic centimeters per minute (sccm) was used for gas purging and as a precursor carrier gas. The system was pumped by a rotary mechanical pump and pressure was controlled near 2 Torr using a downstream butterfly valve with pressure feedback control.

To prepare polymer fiber substrates for ZnO ALD, the fibers were often coated first using trimethylaluminum (TMA) and water ALD cycles to form thin aluminum oxide coatings, where the typical deposition sequence followed: TMA/Ar/H₂O/Ar = 1/30/1/60 seconds at 60 °C. Previous studies have demonstrated that ALD Al₂O₃ nucleates well on the surface of woven cotton fibers, with growth rates similar to that on planar substrates.^{30,31}

Following the Al₂O₃ growth, the deposition chamber temperature was increased to 115°C for the ALD ZnO growth. The precursors for ZnO growth, DEZ (98% purity, STREM Chemicals) and H₂O (UV-deionized), were held at room temperature, and the external gas lines were heated to 60°C. The precursors were sequentially delivered to the Ar carrier gas stream, followed by Ar purge. The precursor dose and purge times for one cycle was DEZ/Ar/H₂O/Ar = 2/50/2/50 seconds, resulting in exposures of ~0.2 Torr sec for both the DEZ and H₂O. Thin film ZnO was deposited with 180-600 ALD cycles, and after deposition

the thickness of the ZnO was evaluated on a silicon monitor substrate using spectroscopic ellipsometry (Alpha SE, J.A. Woollam). The mass gain due upon ZnO coating was also characterized. The aluminum oxide has a smaller density and a smaller expected growth per cycle than the ZnO, so the 50 cycles of aluminum oxide coating before the 200 or more cycles of ZnO adds a nearly negligible contribution to the total coating mass.

The woven quartz fiber mats were obtained from 3M Corporation with a fiber diameter of ~10 micrometers and were used as received. Tungsten ALD was performed on these quartz fibers mats in a flow-tube reactor design, 24 inches in length and 2 ¾ inches in diameter. This reactor was heated with resistive heating tape and the temperature was stabilized with integral controllers. For a purge gas, Ar was delivered at a flow rate of 250 sccm and the system was pumped with a rotary mechanical pump using Fomblin® oil that was constantly flushed with > 500 sccm N₂. A water-based scrubber was located on the output of the pump, prior to the exhaust. In this work, W thin films were deposited at a temperature of 200 °C directly on the quartz fiber mat. The precursors for W growth, SiH₄ (2% in Ar balance, Custom Gas Solutions) and WF₆ (98%, Sigma Aldrich), were held at room temperature, and the external gas lines were heated between 60-75 °C. The precursor dose and purge times for one cycle was SiH₄/Ar/WF₆/Ar = 2/30/2/30 seconds, resulting in exposures of ~1 and ~0.4 Torr sec for SiH₄ and WF₆, respectively. After deposition, the film thickness was evaluated using step profilometry (Veeco D-150).

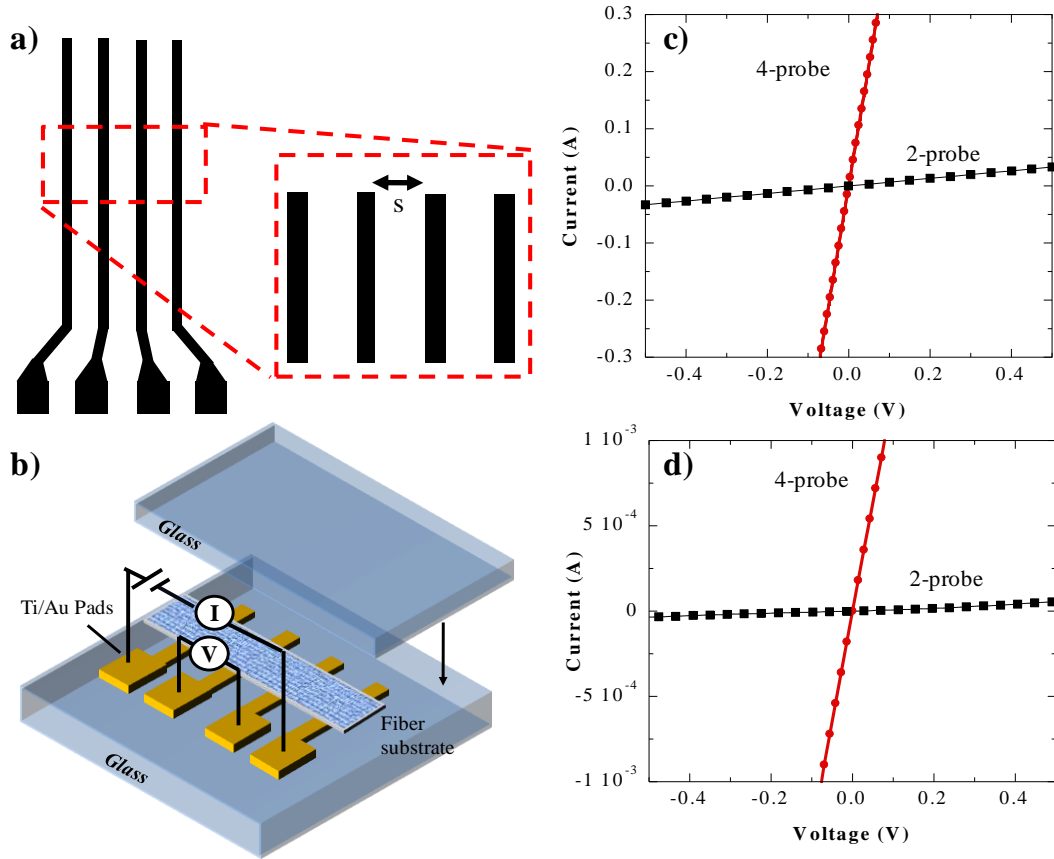
In order to estimated the mass of the ALD (ZnO and W) film deposited on fiber substrates, the fiber substrates were measured before and after ALD deposition using a mass balance. The fiber samples were imaged using a FEI Phenom scanning electron microscope

(SEM) operating at 5 kV accelerating voltage. The conductivity of planar ZnO samples deposited on a silicon wafer with a thermal oxide layer was measured with a 4-point probe (Jandel Multi -height probe with RM3-AR test unit). Electrical measurements were conducted with the 4-probe apparatus discussed above. A Keithley 2605 sourcemeter was used for data collection. Data points were collected after the measured resistance stabilized, typically after 10 to 15 s. The applied current was maintained so that the measured voltage was < 200 mV. Samples were measured 8 to 10 times, and the standard deviation, plotted as error bars, was typically a few percent of the average value.

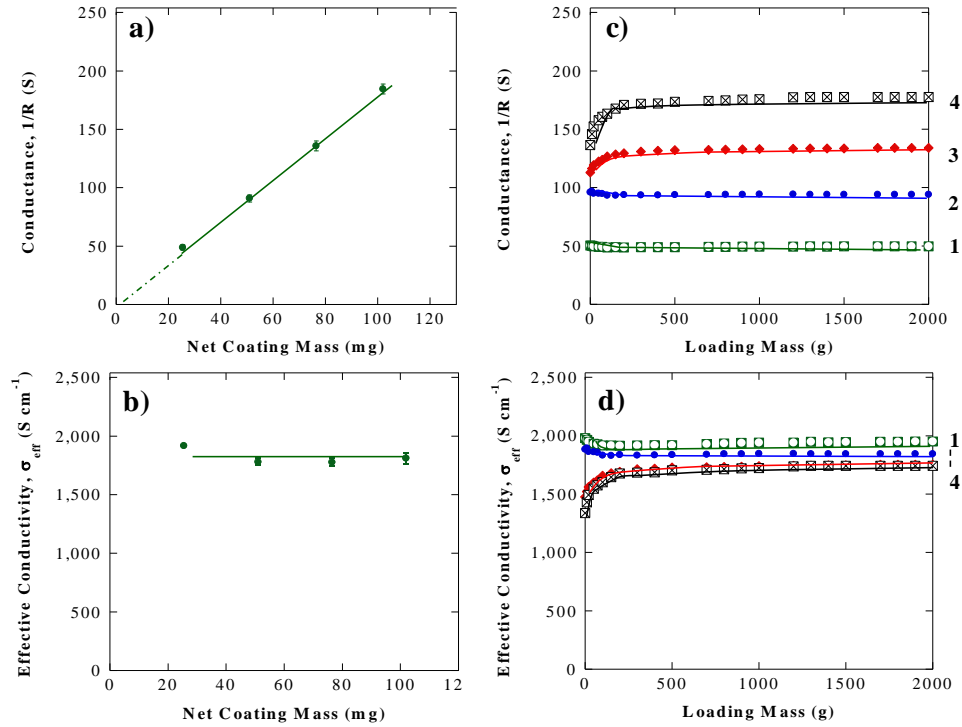
Metal-insulator-metal capacitor structures were fabricated based on tungsten-coated woven quartz fiber as the outer electrodes and nonwoven polypropylene as the middle insulator. The fiber layers were made in contact by sewing the layers with cotton thread. Electrical contact to the outer electrodes was made by sewing extension wires to the corner of the electrodes. Capacitance measurements were performed using an Agilent 4284A Precision LCR Meter. The MIM devices were also analyzed in dry air and while submersed in solutions of deionized water, ethyl alcohol (200 proof, Aaper Alcohol & Chemical Co.), and isopropyl alcohol (99.9%, Fisher Scientific).

A1.2.6 Acknowledgments

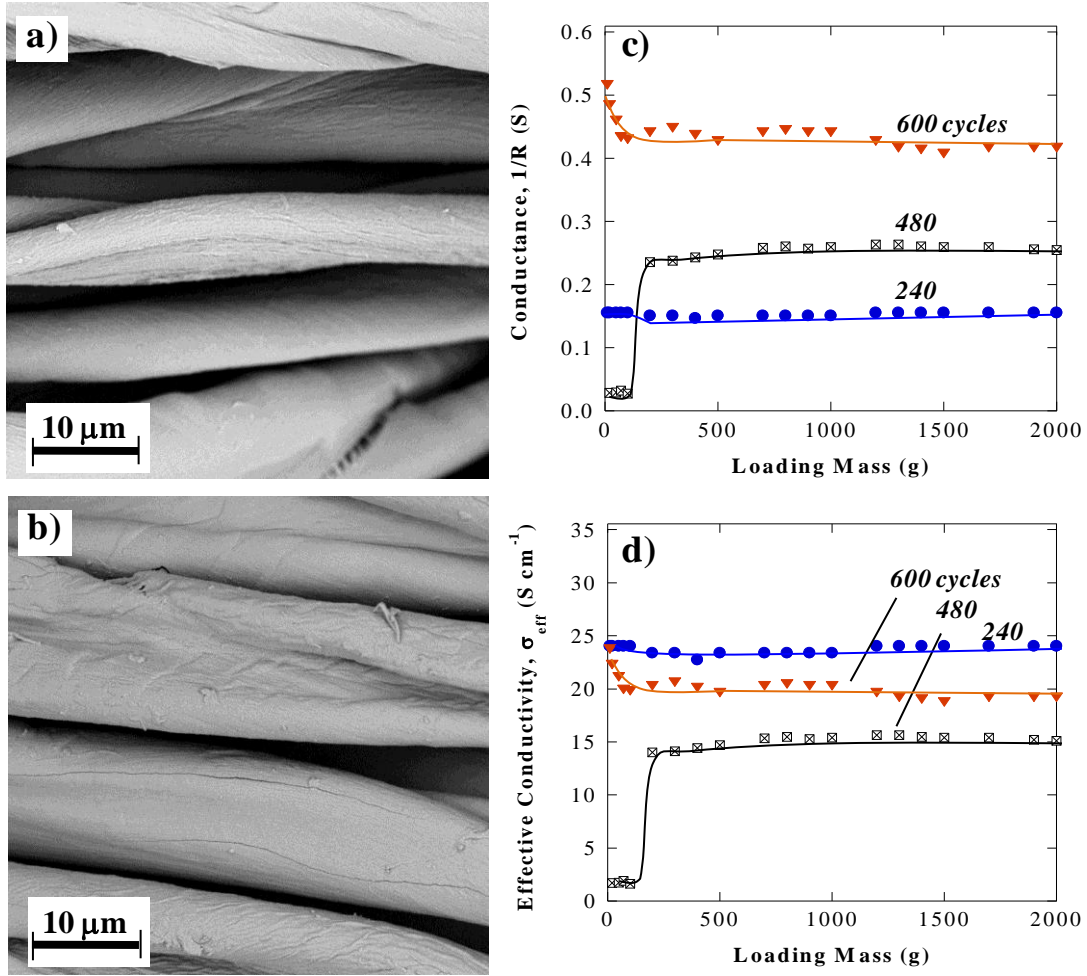
The authors acknowledge support from DOE Project No.08NT0001925 and the Nonwoven Cooperative Research Center at NC State University, Project No. 09-118. The authors would also like to thank Thomas Godfrey at the US Army Natick Soldier RD&E Center for providing the silver samples for this work.



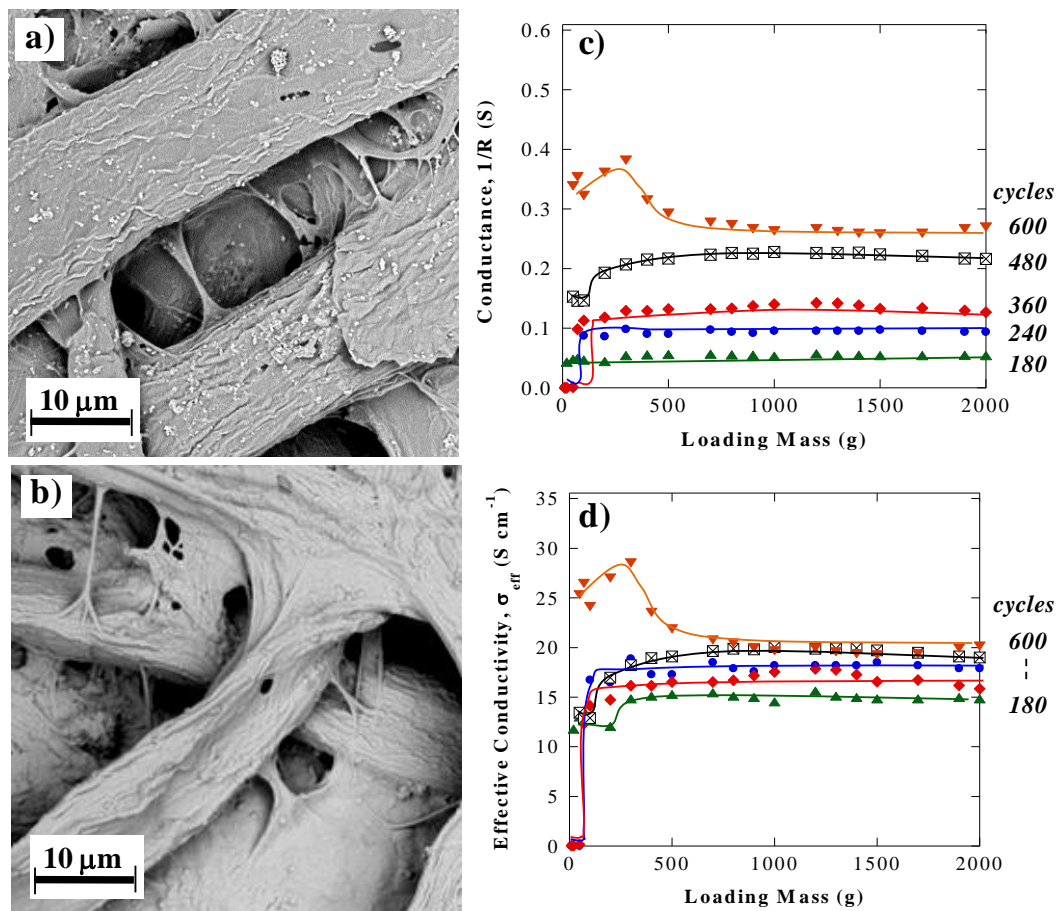
Appendix A1.2 Figure 1. A schematic of the 4-probe (a) line features and (b) experimental apparatus used to measure the resistivity of fiber systems. In this design, the outer electrode spacing is 1.9 cm and the inner probe spacing, $s = 0.5$ cm. The probe pads are fabricated by e-beam deposition of 200 nm of Au with a 10 nm Ti adhesion layer onto a glass slide. Another glass slide is used to apply a uniform compression onto the fiber substrate. Plots of current-voltage (c) for silver coated nylon nonwoven fiber mat and (d) ALD ZnO coated paper with a 2-probe apparatus and the 4-probe apparatus introduced in this work. For the 4-probe method, current was applied across the outer probes and voltage was measured across the two inner probes. For the 2-probe method, voltage was applied and current was measured across the two inner probes.



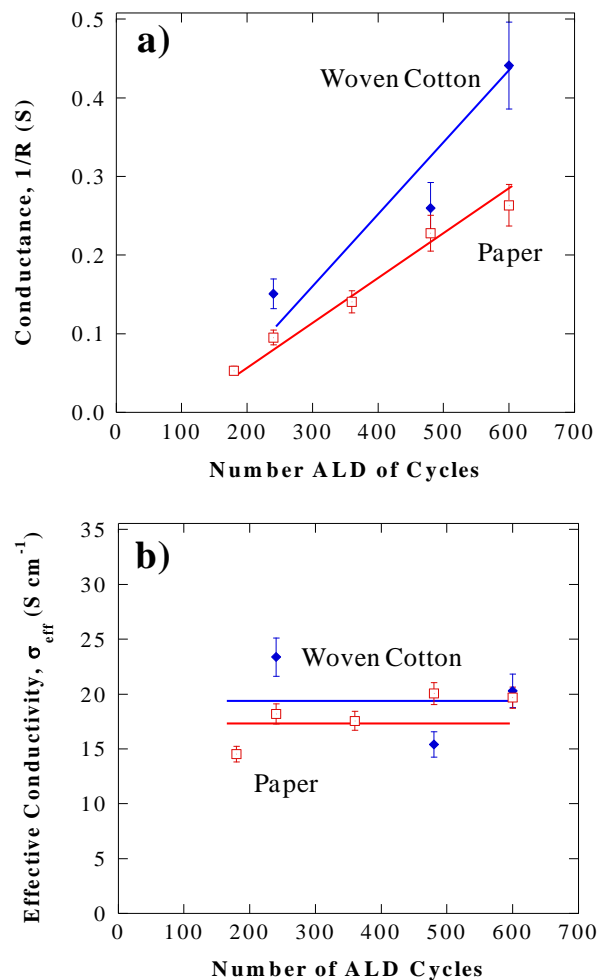
Appendix A1.2 Figure 2. Plots of (a) conductance vs. coating mass; and (b) effective conductivity vs. coating mass for the silver coated nylon nonwoven fiber mat. The 4-probe measurements were conducted with a loading weight of 1700 g. Error bars reflect one standard deviation of the measured values. (c) Plot of conductance measured through silver-coated fiber mats as a function of applied loading mass. Increasing the loading mass compresses the fiber mats and generally increases conductance. The numbers on the right refer to the number of coated mats stacked during the measurement. Stacking multiple mats increases the amount of silver available for conductance. (d) Effective conductivity values obtained from the data in panel (c) after normalizing using equation (3). A somewhat larger value of saturated effective conductivity is obtained with one fiber mat which contained the fewest total number of fiber/fiber contact points.



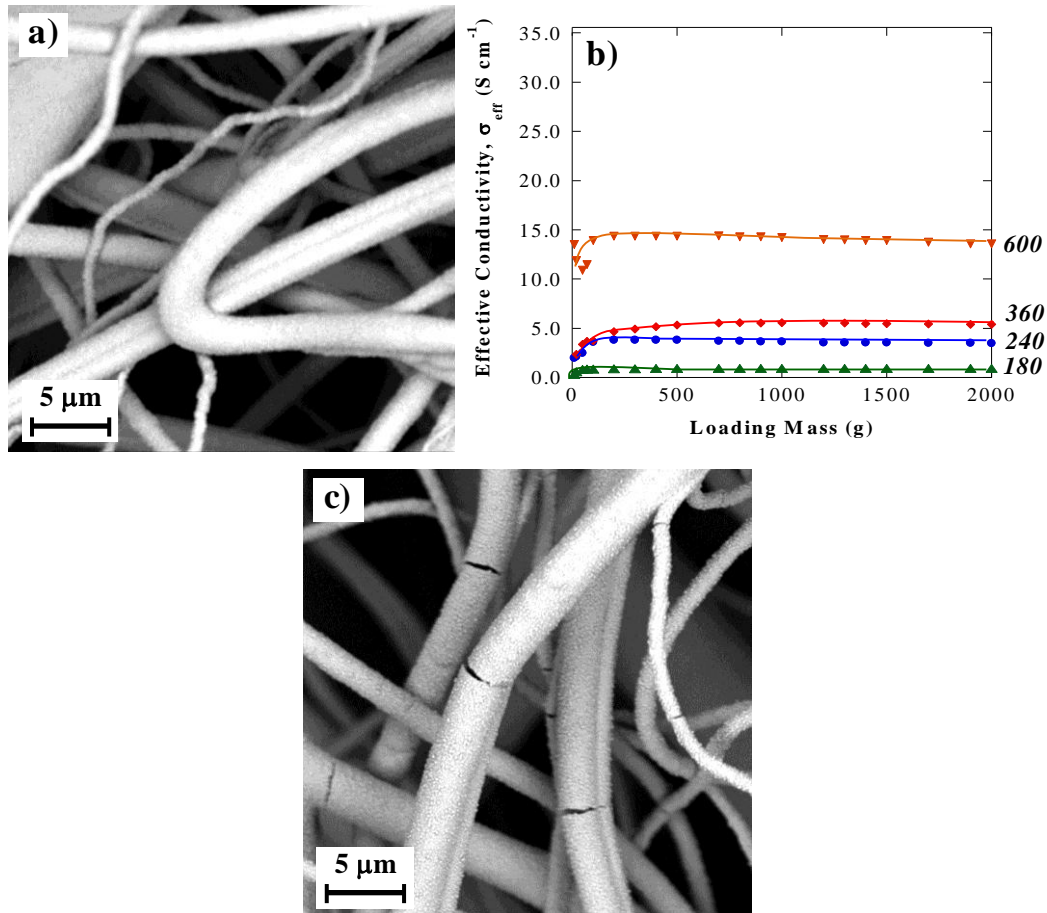
Appendix A1.2 Figure 3. SEM images of woven cotton (a) before ALD processing; and (b) after 480 ALD cycles of ZnO grown at 115°C. Plots of (c) conductance vs. loading mass; and (d) effective conductivity vs. loading mass for woven cotton fiber with 240-600 ALD cycles of ZnO coating grown at 115°C. The number of ZnO ALD cycles used for each sample is indicated. Prior to the ALD ZnO, 50 cycles of aluminum oxide was deposited at a temperature of 60°C.



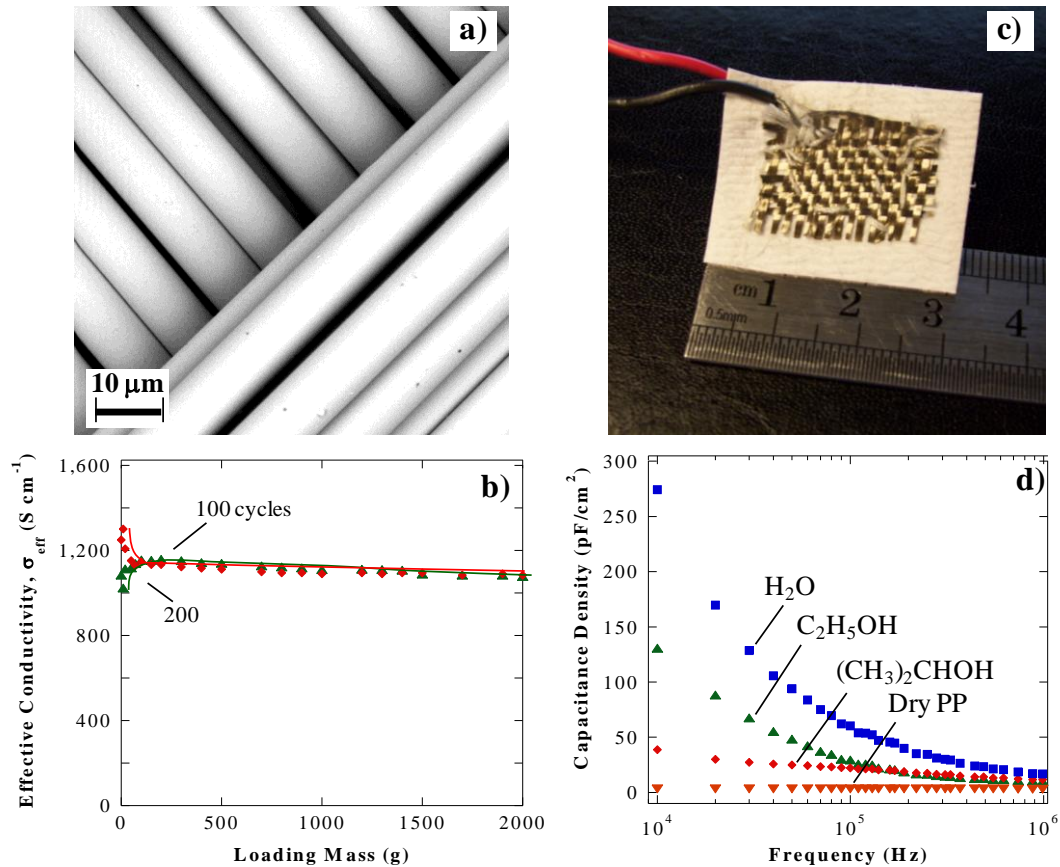
Appendix A1.2 Figure 4. SEM images of cotton paper (a) prior to ALD processing; and (b) after 480 ALD cycles of ZnO grown at 115°C; Plots of (c) conductance; and (d) conductivity vs. loading mass for cotton paper after ZnO ALD at 115°C. The number of ZnO ALD cycles is indicated on the right. Similar to the woven cotton in Figure 3, 50 cycles of aluminum oxide was deposited at 60°C prior to the ZnO ALD.



Appendix A1.2 Figure 5. Values of (a) conductance; and (b) conductivity of ZnO coated woven cotton fiber and cotton paper as a function of ZnO ALD cycles measured with 1000 g loading mass. The conductance values are not expected to be the same on the two substrates. However, normalization of the data using equation (3) produces an effective conductivity value that is approximately independent of substrate and extent of film coating.



Appendix A1.2 Figure 6. (a) SEM image of polypropylene fiber with 480 ALD cycles of ZnO grown at 115°C before mass loading. Plot of (b) conductivity vs. loading weight for nonwoven polypropylene fiber mats with 50 cycles of ALD aluminum oxide followed by 180 to 600 cycles of ALD ZnO. The values do not show a consistent result in this case due to non-cohesive ALD film deposition on the polypropylene fibers. (c) SEM image of polypropylene fiber with 480 ALD cycles of ZnO grown at 115°C after loading with 2000 g, showing film cracking.



Appendix A1.2 Figure 7. (a) SEM image; and (b) effective conductivity vs. loading mass obtained from quartz fibers coated with 200 cycles of ALD W at 200°C. A consistent effective conductivity of 1150 S cm⁻¹ is observed. (c) Picture of an all fiber-based metal–insulator–metal (MIM) capacitor fabricated with tungsten-coated quartz fiber (metal contacts) and polypropylene (insulator). A plot of (d) capacitance density vs. frequency evaluation of the MIM capacitor exposed to various chemical solutions.

A1.2.7 References

- [1] M. A. Dinderman, W. J. Dressick, C. N. Kostelansky, R. R. Price, S. B. Qadri, P. E. Schoen, *Chemistry of Materials* 2006, *18*, 4361.
- [2] M. Agarwal, Y. Lvov, K. Varahramyan, *Nanotechnology* 2006, *17*, 5319.
- [3] Y. Aoki, J. G. Huang, T. Kunitake, *Journal of Materials Chemistry* 2006, *16*, 292.
- [4] P. Sarrazin, L. Valecce, D. Beneventi, D. Chaussy, L. Vurth, O. Stephan, *Advanced Materials* 2007, *19*, 3291.
- [5] L. B. Hu, J. W. Choi, Y. Yang, S. Jeong, F. La Mantia, L. F. Cui, Y. Cui, *Proceedings of the National Academy of Sciences of the United States of America* 2009, *106*, 21490.
- [6] G. Nystrom, A. Razaq, M. Stromme, L. Nyholm, A. Mihranyan, *Nano Letters* 2009, *9*, 3635.
- [7] A. Varesano, A. Aluigi, L. Florio, R. Fabris, *Synthetic Metals* 2009, *159*, 1082.
- [8] M. Kemell, V. Pore, M. Ritala, M. Leskela, *Chemical Vapor Deposition* 2006, *12*, 419.
- [9] R. Pelton, X. L. Geng, M. Brook, *Advances in Colloid and Interface Science* 2006, *127*, 43.
- [10] M. Kemell, M. Ritala, M. Leskela, R. Groenen, S. Lindfors, *Chemical Vapor Deposition* 2008, *14*, 347.
- [11] Y. S. Shin, X. H. S. Li, C. M. Wang, J. R. Coleman, G. J. Exarhos, *Advanced Materials* 2004, *16*, 1212.
- [12] M. Alava, K. Niskanen, *Reports on Progress in Physics* 2006, *69*, 669.
- [13] J. H. He, T. Kunitake, A. Nakao, *Chemistry of Materials* 2003, *15*, 4401.

- [14] L. B. Hu, M. Pasta, F. La Mantia, L. F. Cui, S. Jeong, H. D. Deshazer, J. W. Choi, S. M. Han, Y. Cui, *Nano Letters* 2010, *10*, 708.
- [15] A. Rida, L. Yang, R. Vyas, M. M. Tentzeris, *IEEE Antennas and Propagation Magazine* 2009, *51*, 13.
- [16] S. Zakaria, B. H. Ong, S. H. Ahmad, M. Abdullah, T. Yamauchi, *Materials Chemistry and Physics* 2005, *89*, 216.
- [17] R. E. Anderson, J. W. Guan, M. Ricard, G. Dubey, J. Su, G. Lopinski, G. Dorris, O. Bourne, B. Simard, *Journal of Materials Chemistry* 2010, *20*, 2400.
- [18] J. Jang, S. K. Ryu, *Journal of Materials Processing Technology* 2006, *180*, 66.
- [19] D. Zabetakis, M. Dinderman, P. Schoen, *Advanced Materials* 2005, *17*, 734.
- [20] R. A. Caruso, *Angewandte Chemie-International Edition* 2004, *43*, 2746.
- [21] J. Huang, N. Matsunaga, K. Shimanoe, N. Yamazoe, T. Kunitake, *Chemistry of Materials* 2005, *17*, 3513.
- [22] J. G. Huang, T. Kunitake, *Journal of the American Chemical Society* 2003, *125*, 11834.
- [23] C. Q. Peng, Y. S. Thio, R. A. Gerhardt, *Nanotechnology* 2008, *19*.
- [24] I. Wistrand, R. Lingstrom, L. Wagberg, *European Polymer Journal* 2007, *43*, 4075.
- [25] B. Huang, G. J. Kang, Y. Ni, *Pulp & Paper-Canada* 2006, *107*, 38.
- [26] L. M. Gao, E. T. Thostenson, Z. Zhang, T. W. Chou, *Advanced Functional Materials* 2009, *19*, 123.
- [27] N. Grossiord, J. Loos, L. van Laake, M. Maugey, C. Zakri, C. E. Koning, A. J. Hart, *Advanced Functional Materials* 2008, *18*, 3226.
- [28] H. Yoon, J. Jang, *Advanced Functional Materials* 2009, *19*, 1567.

- [29] G. K. Hyde, S. D. McCullen, S. Jeon, S. M. Stewart, H. Jeon, E. G. Lobo, G. N. Parsons, *Biomedical Materials* 2009, 4.
- [30] G. K. Hyde, K. J. Park, S. M. Stewart, J. P. Hineostroza, G. N. Parsons, *Langmuir* 2007, 23, 9844.
- [31] G. K. Hyde, G. Scarel, J. C. Spagnola, Q. Peng, K. Lee, B. Gong, K. G. Roberts, K. M. Roth, C. A. Hanson, C. K. Devine, S. M. Stewart, D. Hojo, J. S. Na, J. S. Jur, G. N. Parsons, *Langmuir* 2009, 26, 2550.
- [32] J. S. Jur, J. C. Spagnola, K. Lee, B. Gong, Q. Peng, G. N. Parsons, *Langmuir* 2010, 26, 8239.
- [33] M. Kemell, V. Pore, M. Ritala, M. Leskela, M. Linden, *Journal of the American Chemical Society* 2005, 127, 14178.
- [34] M. Leskela, M. Ritala, *Angewandte Chemie-International Edition* 2003, 42, 5548.
- [35] S. M. George, *Chemical Reviews* 2010, 110, 111.
- [36] B. Y. Deng, Q. F. Wei, W. D. Gao, *Journal of Coatings Technology and Research* 2008, 5, 393.
- [37] N. J. Pinto, P. Carrion, J. X. Quinones, *Materials Science and Engineering a-Structural Materials Properties Microstructure and Processing* 2004, 366, 1.
- [38] American Society for Testing and Materials ASTM Designation: D-4496-04, 2006.
- [39] Y. Shacham-Diamand, A. Inberg, Y. Sverdlov, N. Croitoru, *Journal of the Electrochemical Society* 2000, 147, 3345.
- [40] J. S. Na, Q. Peng, G. Scarel, G. N. Parsons, *Chemistry of Materials* 2009, 21, 5585.
- [41] M. Schuisky, J. W. Elam, S. M. George, *Applied Physics Letters* 2002, 81, 180.

- [42] Q. Peng, X. Y. Sun, J. C. Spagnola, G. K. Hyde, R. J. Spontak, G. N. Parsons, *Nano Letters* 2007, 7, 719.
- [43] J. S. Na, G. Scarel, G. N. Parsons, *Journal of Physical Chemistry C* 2010, 114, 383.
- [44] J. P. Richters, T. Voss, D. S. Kim, R. Scholz, M. Zacharias, *Nanotechnology* 2008, 19.
- [45] E. Guziewicz, M. Godlewski, T. A. Krajewski, L. Wachnicki, G. Luka, W. Paszkowicz, J. Z. Domagala, E. Przewdziecka, E. Lusakowska, B. S. Witkowski, *Acta Physica Polonica A* 2009, 116, 814.
- [46] J. W. Klaus, S. J. Ferro, S. M. George, *Thin Solid Films* 2000, 360, 145.